

**Novel Dynamics and Control Formulations for
Multi-Spacecraft Formation Flying, Rendezvous, and
Proximity Operations**

by

E. R. Burnett

B.S., University of Arizona, 2016

M.S., University of Arizona, 2018

A thesis submitted to the
Faculty of the Graduate School of the
University of Colorado in partial fulfillment
of the requirements for the degree of
Doctor of Philosophy

Ann and H.J. Smead Department of Aerospace Engineering Sciences

2021

Committee Members:

Prof. Hanspeter Schaub

Prof. Daniel Scheeres

Prof. Marcus Holzinger

Prof. Jay McMahon

Dr. Andrew Sinclair

Burnett, E. R. (Ph.D., Aerospace Engineering Sciences)

Novel Dynamics and Control Formulations for Multi-Spacecraft Formation Flying, Rendezvous,
and Proximity Operations

Thesis directed by Prof. Hanspeter Schaub

Technological progress has facilitated an increase in investigations of multi-spacecraft solutions for science and commercial applications. Future space missions will require that spacecraft operate in close proximity autonomously, for applications such as rendezvous and docking, servicing and inspecting, and also for distributed space systems. For such things to take place beyond low-Earth orbit, the traditional means of spacecraft formation flying must be extended to develop techniques that work in a variety of dynamical environments. This dissertation aims to demonstrate novel dynamics and control methods for close-proximity satellite relative motion in a variety of settings.

First, a procedure is developed and applied for accurately deriving approximate linear models (and their analytic solutions) for spacecraft relative motion under the influence of non-Keplerian perturbations. This is used for computationally efficient modeling of relative motion under the influence of low degree and order gravitational harmonics and solar radiation pressure. The models derived are used for closed-loop spacecraft relative motion control with differential solar radiation pressure and closed-loop orbit control in an asteroid environment. The concept of linear sensitivity dynamics is then used for developing control that is insensitive to various uncertain dynamical parameters, and also for efficient study of uncertainty propagation in the relative motion problem. Finally, the idea of modal decomposition of close-proximity spacecraft relative motion is introduced, for which the relative state can be represented as a linear sum of simpler motions that are chosen for geometric convenience. The concept extends beyond Keplerian relative motion and into more exotic environments, providing a unifying and simplifying view of the close-proximity spacecraft relative motion problem. It also enables elegant rendezvous and relative orbit control solutions.

Dedication

To my parents, Elizabeth and Dwayne.

Acknowledgements

Many people supported me before and during the development of this dissertation. First, I'd like to thank my advisor Dr. Hanspeter Schaub for his continued support and guidance. His commitment to his students is obvious, and his talent for teaching reaches far beyond Boulder. The first course I ever took in spaceflight was a spacecraft attitude dynamics and controls course in Arizona in 2015, and we used his book. It was an influential read, and part of what first ignited my interest in spaceflight mechanics and astrodynamics.

I would also like to thank the professors and mentors who helped me along the way, especially my M.S. advisor, Dr. Eric Butcher, and my AFRL mentor, Dr. Andy Sinclair. They taught me a lot, and provided me with many early opportunities to succeed. Additionally I owe thanks to Dr. Paul Hayne at CU Boulder, who introduced me to various opportunities in planetary science. I also thank the U.S. Air Force Office of Scientific Research for funding me via the NDSEG Fellowship.

When I first started grad school, at the University of Arizona in 2016, my office mates Mohammad Maadani and Bharani Malladi were constant companions, and I'll always remember my first two years of grad school as a particularly exciting and joyous time. I'd also like to thank Morad Nazari and Arman Dabiri for their guidance at that time.

My time at CU Boulder has been greatly enhanced by the companionship of the many excellent students in CCAR. There is not enough space here to name them all. I additionally acknowledge the support of other friends in Boulder, back home in Tucson, and beyond.

Finally, this work wouldn't have been possible without the love and support of my family, nor without the guidance and example of the many great teachers I've had in my life.

Contents

Chapter	
1	Introduction 1
1.1	Motivation 1
1.2	Related Work 5
1.2.1	Satellite Relative Motion Modeling 5
1.2.2	Use of Solar Radiation Pressure for Spacecraft Propulsion and Control 7
1.2.3	Sensitivity Dynamics, Desensitized Control, and Uncertain Relative Motion . 8
1.2.4	Modal Decomposition of Spacecraft Relative Motion 9
1.3	Contributions of this Work 10
1.4	Publications 14
2	Preliminaries 18
2.1	Spacecraft Relative Motion 18
2.1.1	Fundamentals 18
2.1.2	Clohessy-Wiltshire Dynamics 21
2.2	Perturbed Orbits 24
2.2.1	Representing the Perturbed Two-Body Problem 24
2.2.2	Common Orbital Perturbations 25
2.3	Perturbation Methods 30
2.4	Relative Motion Approximation 33

2.4.1	Fundamentals	33
2.4.2	Local Cartesian Coordinates	35
2.4.3	Orbit Element Differences	36
2.5	Linear Differential Equations, Reducibility, and Lyapunov-Floquet Theory	37
3	Spacecraft Relative Motion Modeling	42
3.1	Modeling J_2 -Perturbed Relative Motion	42
3.1.1	Derivation of Base Model	43
3.1.2	Solution Improvement by Calibration	51
3.1.3	Solution Improvement by Accounting for Radial Variations	53
3.1.4	Numerical Simulations	55
3.2	Model for Oblateness, Ellipticity, and Solar Radiation Pressure	59
3.2.1	Further Analysis of the Linear Model	65
3.2.2	Identifying Important Parameters for Numerical Simulations	65
3.2.3	Angular Momentum of the Relative Orbital State	66
3.2.4	Numerical Simulations	67
3.3	Additional Work in Relative Motion Modeling	72
3.3.1	The J_2 Perturbed Orbit Revisited	73
3.3.2	Modeling the Orbital Effects of Oblateness and Ellipticity	77
3.4	Conclusions	78
4	Relative Motion Control with Differential Solar Radiation Pressure	80
4.1	Solar Radiation Pressure as a Control Parameter	80
4.2	Spacecraft Relative Motion Dynamics with Solar Radiation Pressure	84
4.2.1	Problem Geometry and Coordinate Frames	86
4.2.2	Linearized Attitude-based SRP Control	87
4.2.3	Linearized Relative Motion Dynamics under SRP	90
4.3	Spacecraft Relative Motion Control	94

4.3.1	Linear SRP-Based Formation and Rendezvous Control	94
4.3.2	Controllability Analysis	95
4.3.3	Testing the SRP-Perturbed Relative Motion Model	97
4.3.4	Simulation Results	98
4.4	Conclusions	103
5	Spacecraft Relative Motion Sensitivities	104
5.1	Desensitized Optimal Spacecraft Rendezvous Control	105
5.1.1	Dynamical Uncertainty in the Spacecraft Relative Motion Problem	105
5.1.2	Dynamic Model	107
5.1.3	Low-Sensitivity Optimal Control Design	107
5.1.4	Notes on System Nonlinearity and Orbit Control	112
5.1.5	Orbit Control around Asteroids	113
5.1.6	Low-Thrust Control Simulations	114
5.1.7	Monte Carlo Simulations Using Low-Thrust	118
5.1.8	Discussion	123
5.2	Satellite Relative Motion in the Vicinity of a Poorly Tracked Target Object	124
5.2.1	Relative State Uncertainty	124
5.2.2	Sensitivity Dynamics	126
5.2.3	The Clohessy-Wiltshire Case	133
5.2.4	Numerical Simulations	138
5.2.5	Discussion	150
5.3	Conclusions	151
6	Modal Decomposition of Spacecraft Relative Motion	153
6.1	Motivating Example	154
6.2	General Formulation	158
6.3	Analytic Results for the General Keplerian Relative Motion Problem	160

6.3.1	Relative Motion Dynamics	160
6.3.2	The Lyapunov-Floquet Transformation in any Coordinates	162
6.3.3	Orbit Element Differences	164
6.3.4	Cartesian Coordinates	167
6.3.5	Spherical Coordinates	171
6.3.6	Numerical Simulations for the Keplerian Problem	177
6.4	Weakly Perturbed Orbits	184
6.5	Conclusions	185
7	Applications of the Relative Motion Modal Decomposition	187
7.1	Numerical Application to Analytic Model of Oblateness, Ellipticity, and SRP Perturbations	187
7.2	Implementation for General Almost-Periodic Orbits	193
7.2.1	Almost-Periodic Linear Systems	196
7.2.2	Persistence and Robustness of Modes	199
7.2.3	Dynamics of the Deviation	200
7.2.4	Spacecraft Relative Motion Near Terminator Orbits	201
7.2.5	Mode-Computing Algorithm Validation	206
7.2.6	Applying the Mode-Computing Algorithm to Ryugu Terminator Orbits	208
7.3	Relative Motion Dynamics and Control Using the Fundamental Solution Constants	210
7.3.1	The Modal Constants as State Variables	210
7.3.2	Continuous Control Using the Fundamental Solution Constants	212
7.3.3	Impulsive Control Using the Fundamental Solution Constants	213
7.3.4	Using the Modal Constants to Explore Relative Orbits	216
7.3.5	Effects of Perturbations – Modeling with J_2	220
7.3.6	Impulsive Maneuver Control in the Keplerian Relative Motion Problem	221
7.4	Modal Decomposition and Modal Control in the Earth-Moon Three-Body Problem	225

7.4.1	The Circular Restricted Three Body Problem	225
7.4.2	Relative Motion Modes and Modal Control in the CR3BP	233
7.4.3	Example Simulations	237
7.5	Conclusions	242
8	Conclusions and Future Work	244
8.1	Overview and Contributions of this Work	244
8.2	Recommendations for Future Work	246
	Bibliography	249

Tables

Table

3.1	Unique O Matrix Terms in Eq. 3.17, $O_{ij} = O_{ji}$	47
3.2	J_2 Model Test, Variable Chief Inclination: 0° to 90°	56
3.3	Initial Conditions for Simulation with Large J_2 and J_3	58
3.4	Simulation Parameters for Asteroid Relative Motion Model	68
4.1	SRP Control Simulation 1 Physical Parameters	97
4.2	Control and Optical Parameters for SRP Control Simulation 1	98
4.3	SRP Control Simulation 2 Physical Parameters	102
4.4	Control and Optical Parameters for SRP Control Simulation 2	102
5.1	Asteroid Physical Parameters for Desensitized Control Simulations	114
5.2	Recurring Control Parameters for LQR and Low-Sensitivity Cases	114
5.3	Desensitized Control Simulation Initial Conditions	115
5.4	Eccentric Target Orbit, Unforced Relative Motion	138
5.5	Simulation Parameters, CW Control Example 1	143
5.6	Simulation Parameters, CW Control Example 2	146
7.1	Physical Parameters for Modal Parameter Study	188
7.2	Physical Parameters for Ryugu Simulation	205
7.3	Spacecraft Relative Motion Modal Data for Terminator Orbit, $\Gamma = 3$	209
7.4	Simulation Parameters – Final Keplerian Modal Example	216

7.5	Stability Properties of L_2 Halo Orbits vs. Orbit Period	231
7.6	Halo Orbit Control Simulation Parameters, Example 1	238
7.7	Halo Orbit Control Simulation Parameters, Example 2(a)	240
7.8	Halo Orbit Control Simulation Parameters, Example 2(b)	241

Figures

Figure

1.1	ESA’s RACE Close-Proximity Formation Flying Mission (Credit: GomSpace)	2
1.2	Solar Radiation Pressure Perturbation	4
1.3	Spacecraft Formation Flying Guidance and Control in Perturbed Environments . . .	11
1.4	Near-Earth Asteroids Bennu (L) and Ryugu (R) (Credit: ESA)	13
2.1	Spacecraft Relative Motion in the LVLH Frame	20
2.2	Orbital Effects of J_2 [127]	28
3.1	Model Error Norm vs. Chief Inclination	56
3.2	Error Norm for Various J_2 Models for $i = 10^\circ$	57
3.3	Benefits of Solution Calibration and Correction	58
3.4	Problem Geometry, Asteroid Orbiter	60
3.5	Maximum Deviation of AMROS in One Orbit	69
3.6	Perturbed Relative Motion with $\Gamma = 1.25$, $i = 75^\circ$	70
3.7	Perturbed Relative Motion with $\Gamma = 2.0$, $i = 95^\circ$	72
4.1	Problem Geometry for SRP-based Control, with Attitude-Dependent Resultant Force	84
4.2	SRP-Perturbed Relative Motion	99
4.3	SRP-Based Control of Relative Motion, Case 1	99
4.4	Position, SRP Control Case 1	100
4.5	Control Signals, SRP Control Case 1	100

4.6	SRP-Based Control of Relative Motion, Case 2	100
4.7	Controlled Position, SRP Control Case 2	101
4.8	Control Signals, SRP Control Case 2	101
5.1	Controlled Relative Motion (LQR)	116
5.2	Relative Position vs. Time (LQR)	116
5.3	Control Signals (LQR)	116
5.4	C'_{20} Relative Position Sensitivity (LQR)	117
5.5	C'_{22} Relative Position Sensitivity (LQR)	117
5.6	SRP Relative Position Sensitivity (LQR)	117
5.7	Controlled Relative Motion (Low-Sensitivity Control)	119
5.8	Relative Position vs. Time (Low-Sensitivity Control)	119
5.9	Control Signals (Low-Sensitivity Control)	119
5.10	C'_{20} Relative Position Sensitivity (Low-Sensitivity Control)	120
5.11	C'_{22} Relative Position Sensitivity (Low-Sensitivity Control)	120
5.12	SRP Relative Position Sensitivity (Low-Sensitivity Control)	120
5.13	Controlled Relative Motion, Monte Carlo Results (LQR)	121
5.14	Controlled Relative Motion, Monte Carlo Results (Low-Sensitivity Control)	121
5.15	Total Δv (LQR)	122
5.16	Total Δv (Low-Sensitivity Control)	122
5.17	Nonlinearity Index vs. Time, Monte Carlo Results	123
5.18	Relative Position from Estimated and True Target Spacecraft Locations	126
5.19	Relative Position Sensitivities to Target Semimajor Axis	139
5.20	Relative Position Sensitivities to Target Initial Argument of Latitude	140
5.21	Relative Position Sensitivities to Target R.A.A.N and Inclination	140
5.22	Relative Position Sensitivities to Target q_1, q_2	140
5.23	Sensitivity-Propagated Relative State Uncertainty Distribution	141

5.24	Controlled Relative State, Naïve Control Example	143
5.25	Sensitivity to Semimajor Axis, Naïve Control Example	144
5.26	Sensitivities to Target Orbit Element Angles, Naïve Control Example	144
5.27	Relative Motion Trajectory, Augmented Control Example	146
5.28	Relative Position, Augmented Control Example	147
5.29	Controlled Sensitivity to θ_0 , Augmented Control Example	147
5.30	Stationary Sensitivity to Ω , Augmented Control Example	148
5.31	Control Accelerations, Augmented Control Example	149
6.1	Example Satellite Relative Motion as a Sum of Individual Modes	154
6.2	Planar Relative Motion Modes for the Clohessy-Wiltshire Problem	157
6.3	In-plane Normalized Relative Motion Modes, $e = 0.74$, $f_0 = 90^\circ$	177
6.4	Out-of-plane Normalized Relative Motion Modes, $e = 0.74$, $f_0 = 90^\circ$	178
6.5	Example Relative Orbit, $e = 0.74$, $f_0 = 90^\circ$, $\delta e = 0.002$, $\delta i = 0.2^\circ$, $\delta f_0 = 0^\circ$	178
6.6	Example Modal Decomposition (Planar), $e = 0.74$, $f_0 = 90^\circ$, $\delta e = 0.002$, $\delta i = 0.2^\circ$	179
6.7	Bounded Planar Motion with (x_0, y_0) specified, $e = 0.74$, $f_0 = 90^\circ$	179
6.8	Normalized Relative Motion Modes vs. Eccentricity, Cartesian Coordinates	180
6.9	Normalized Relative Motion Modes, $e = 0.74$, $f_0 = 145^\circ$	182
6.10	Example Modal Decomposition, Cartesian, $e = 0.74$, $f_0 = 145^\circ$, $\delta e = 0.002$, $\delta i =$ $\delta f_0 = 0.2^\circ$	183
6.11	Example Modal Decomposition, Spherical, $e = 0.74$, $f_0 = 145^\circ$, $\delta e = 0.002$, $\delta i =$ $\delta f_0 = 0.2^\circ$	183
7.1	Modulus of Largest Floquet Multiplier	190
7.2	Relative Orbital Motion Modal Data	191
7.3	Relative Motion Modes for $\Gamma = 2$	191
7.4	Long-Term Stable Relative Motion Mode	193
7.5	Transformation Between \mathbf{x} and \mathbf{z} Spaces	198

7.6	Nominal and Perturbed Terminator Orbits at Ryugu	205
7.7	Modal Results for Formations in $\Gamma = 3$ Terminator Orbit	209
7.8	Select Component of Plant Matrix, $\Gamma = 3$, $[\bar{A}(t)]$ Computed from Interval \mathcal{I}_1	210
7.9	Example Relative Orbit	217
7.10	Cartesian Planar Modes	217
7.11	Spherical Planar Modes	218
7.12	Variations of the Planar Relative Motion with c_1	218
7.13	Variations of the Planar Relative Motion with c_3 (Re-scaled)	218
7.14	Variations of the Planar Relative Motion with c_5 (Re-scaled)	219
7.15	Variation of Modal Constants with J_2	222
7.16	Two-Burn Maneuver, Modal Constants	223
7.17	Two-Burn Maneuver, Local Cartesian Coordinates	223
7.18	Five-Burn Maneuver, Modal Constants	223
7.19	Five-Burn Maneuver, Local Cartesian Coordinates	224
7.20	Relative Orbit Transfer Using Modal Constants	224
7.21	L_2 Northern Halo Orbits	230
7.22	Stability Index s_1 , L_2 Halo Orbit Family	232
7.23	Stability Index s_2 , L_2 Halo Orbit Family	232
7.24	Trivial Mode and Drift Mode in Vicinity of L_2 Halo Orbit	235
7.25	Stable L_2 Halo Orbit	238
7.26	Center Modes, Stable L_2 Northern Halo Orbit	238
7.27	Halo Orbit Relative Motion with Impulsive Control, Example 1	239
7.28	Unstable L_2 Northern Halo Orbit and a Center Mode	240
7.29	Halo Orbit Relative Motion with Impulsive Control, Example 2(a)	241
7.30	Halo Orbit Relative Motion with Impulsive Control, Example 2(b)	242

Chapter 1

Introduction

1.1 Motivation

Recent trends in spaceflight anticipate a future where many missions will adopt fractionated multi-spacecraft architectures. The inherent flexibility, robustness, serviceability, and expanded capabilities of this approach have been discussed extensively [5, 86, 101], but the concept has advanced beyond the point of speculation. Missions are in various stages of study, design, or deployment where a multi-spacecraft architecture has been chosen over a more traditional single-spacecraft framework. Multiple demonstrator missions are planned for close-proximity coordination of small, modular spacecraft. Figure 1.1 depicts one example: ESA’s upcoming Rendezvous Autonomous CubeSats Experiment (RACE) double CubeSat mission. This mission will demonstrate relative motion control between two CubeSats built on the standard GomSpace 6U platform. The increased interest in multi-spacecraft solutions is facilitated by the need for expanded capability, and further enabled by recent technological progress. Via miniaturization and maturation of spacecraft components, hardware can be packaged on smaller and more modular platforms [5]. Secondary payload adapters have become a common feature accompanying NASA science missions, and allow multiple small spacecraft to be launched to a destination more quickly. Additionally, the new NASA SIMPLEx program enables SmallSats to conduct stand-alone science missions. These developments are normalizing the small multi-spacecraft mission design concept for destinations more challenging and more scientifically interesting than low-Earth orbit (LEO). As these trends continue, future missions will increasingly find the need to safely regulate and coordinate the operation of multiple

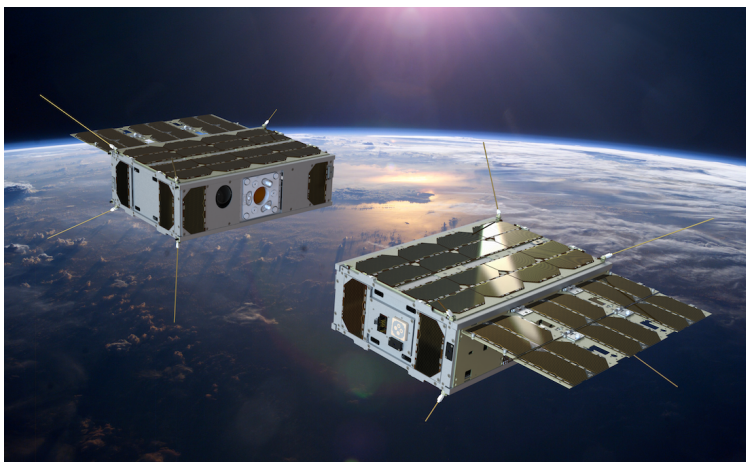


Figure 1.1: ESA’s RACE Close-Proximity Formation Flying Mission (Credit: GomSpace)

spacecraft in distant and dynamically challenging environments. This will sometimes take place in close-proximity – especially whenever rendezvous, coordinated remote sensing, formation flying, or servicing are part of the mission design. Efficiently modeling and understanding the natural dynamics of close-proximity spacecraft relative motion is a necessary undertaking to facilitate these missions [3, 1]. This dissertation considers multiple aspects of the combined problems of modeling, planning, and controlling spacecraft formation flying and proximity operations in highly perturbed environments. Topics of interest and relevance are now briefly discussed, before an extensive review of past work and a concluding summary of the contributions of this dissertation.

The forces at work in most orbital environments are well-understood theoretically, and the relative motion of multiple spacecraft can be numerically simulated in high-fidelity physical models. However, this approach does not readily offer insights into the dynamics and is not a workable implementation for traditional spacecraft control and estimation applications. As a result, many works have addressed the concept of accurately modeling the dynamics of spacecraft relative motion in formulations that are expressed in coordinates centered on one of the spacecraft in close-proximity. If the relative motion dynamics of N spacecraft are linearized about a true or virtual *chief* spacecraft motion, the formation translational dynamics are reduced from a coupled $6N$ degree-of-freedom (DOF) problem to $N - 1$ decoupled 6-DOF problems that share a common approximate dynami-

cal structure. This massive reduction in complexity is particularly useful for spacecraft formation flying, rendezvous, and servicing applications, with the caveat that suitable coordinates for accurate linearization must be identified [67, 70], and the chief orbit must be propagated in parallel or reasonably well-approximated.

In some instances, the dominant environmental dynamics are modeled, but the values of certain parameters are not well known. For example, consider orbits about small bodies, for which it is known that the low degree and order gravitational harmonics will be dynamically important, but a gravity model might be unavailable or untrustworthy. Or, solar radiation pressure forces on a spacecraft might be important but only approximately modeled. For these situations it is necessary to develop control whose performance is relatively predictable and robust despite dynamical unknowns. Various approaches have been proposed for doing this, including strategies where the true nature of the dynamics is discerned over time, such as in adaptive control techniques [69]. Another approach is to explicitly model the sensitivity of the system states to the poorly-known dynamical parameters [72]. If the relative motion dynamics are rendered in an analytic form, the sensitivity has its own analytic linear equations of motion which are additionally linearly forced by the relative state. In this case, linear control designs may be naturally adapted to additionally consider the system sensitivity, yielding an elegant approach for mitigating the effects of dynamic uncertainties.

Aerodynamic drag and solar radiation pressure are two common perturbations which vary with the attitude of the spacecraft. If these forces are strong enough to produce noticeable effects on the relative motion of uncontrolled formations over reasonably short timespans, they can also be used for differential state control. The differential drag formulation is in an advanced state of development, and even flies on some missions in LEO [48], but an SRP control formulation is also potentially promising and is comparatively less explored. The differential SRP acceleration between two spacecraft scales with differences in illuminated spacecraft area, while most other differential accelerations scale with separation. Figure 1.2 depicts the solar radiation pressure perturbation acting on a spacecraft. SRP-based control also presents a feasible fuel-free formation control option

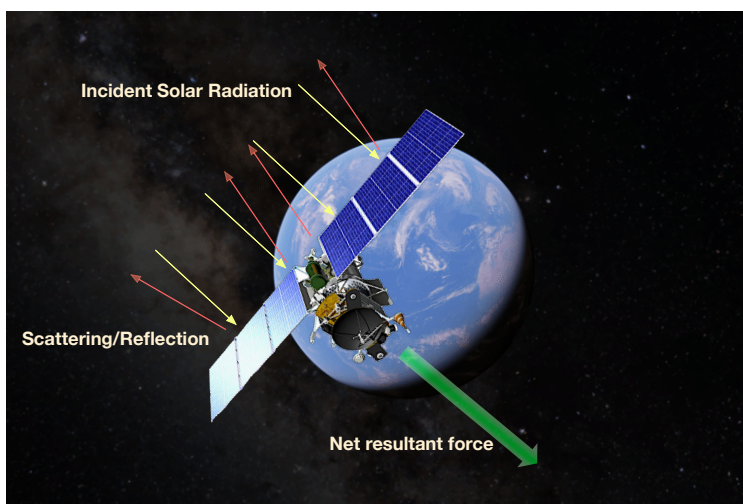


Figure 1.2: Solar Radiation Pressure Perturbation

for orbits in GEO, or around small bodies such as asteroids and comets. For sail-like structures or high area-to-mass ratio spacecraft, a linear feedback controller works well. For more traditional spacecraft geometry, one might seek a controller that properly takes advantage of the full range of solar radiation pressure differences between spacecraft for large attitude differences.

For more general perturbed formation flying problems, it is possible to compute and target desired natural relative motion solutions if the perturbations are sufficiently well-modeled. The linearized plant matrix used to approximate the relative motion tends to be time-varying for many problems, but for bounded and regularly repeating orbits, it is almost-periodic, and this enables interesting transformations (or approximate transformations) to study stability and linearized relative motion solutions using tools from Floquet theory [120]. It also enables a modal decomposition in a transformed space for which the dynamics are linear time-invariant (LTI). From this, conditions for desired relative motion (such as long-term boundedness) can be identified easily, and such solutions can serve as an initial guess for identifying various useful motions. The modal analysis can be performed with an analytic model or with one obtained by numerical linearization in a nonlinear dynamic simulation. Such approaches that combine numerical techniques and appropriate analytical tools are potentially useful for practical design of safe and efficient formation flying and proximity operations in highly perturbed orbital environments. Critically, this approach ac-

counts for the influence of perturbations in the formation design itself instead of treating them as a disturbance to be rejected.

1.2 Related Work

1.2.1 Satellite Relative Motion Modeling

Spacecraft relative motion dynamics have been a topic of study for over 60 years, since the introduction of the well-known Clohessy-Wiltshire (CW) linearized model [36]. This model is valid for cases of small separation between two spacecraft in near-circular Keplerian orbits. The differential equations are very simple, with constant coefficients, and the resulting time-explicit solutions of the evolving Cartesian relative state are extremely compact. This model is used extensively in formation flying to this day, despite its limited accuracy. By neglecting the effects of orbital perturbations, the CW model is useful in practice only for a limited timespan, the length of which is determined by fidelity requirements and the magnitude of the orbital perturbations. While most spacecraft are in near-circular orbits, the circular orbit assumption is also limiting. The Tschauner-Hempel equations [126] are another set of linear differential equations, developed for studying satellite relative motion in the vicinity of eccentric Keplerian orbits. These equations notably use true anomaly as the independent variable instead of time.

Two of the most popular sets of solutions of the Tschauner-Hempel equations are found in the work of Carter [34] and Yamanaka and Ankersen [129]. There is quite a bit of literature on the solutions of the Tschauner-Hempel equations due to difficulties in developing singularity-free solutions, and in developing useful geometric interpretations. The interested reader can find a discussion in Reference 123. Other notable literature on the topic of relative motion in eccentric Keplerian orbits includes References 43, 73, and 93, which discuss time-explicit representations of relative motion in eccentric orbits and nonlinear Keplerian relative motion models. There has also been a lot of work examining the Keplerian relative motion problem through orbit element differences instead of Cartesian coordinates. See for example References 108, 109, and chapter

14 of Reference 111 and references therein. Also relevant is work modeling the relative state in curvilinear coordinates [29, 31], which have a larger region of validity than the Cartesian coordinate relative motion models, but not as large as the orbit element differences. Relative orbital elements (ROEs) in particular are of note because they describe relative motion similarly to orbit elements, but with more of a local geometric interpretation [40].

In addition to exploring relative motion of orbits of general eccentricity, another useful area of research has been in modeling spacecraft relative motion under the influence of various perturbations. Authors have considered the effects of various perturbations common in planetary orbits, including atmospheric drag [33, 76], zonal gravity [11, 116], and solar radiation pressure [53, 102]. In the context of this dissertation, modeling relative motion perturbed by Earth's oblateness is of particular relevance. The most well-known and widely adopted state transition matrix (STM) model of J_2 -perturbed relative motion is the Gim-Alfriend STM (GA-STM) [50]. It is highly accurate, using propagation of the J_2 effect in orbit element differences facilitated by Brouwer-Lyddane theory, and a geometric transformation back to local Cartesian coordinates. It is also extremely complex, and other authors have sought simpler solutions, particularly for control and maneuver planning purposes.

One of the most well-known linear models of relative motion subject to J_2 was developed by Schweighart and Sedwick. Their approach was to time-average the gradient of the J_2 potential to obtain constant coefficient linearized equations. They noted that such averaging resulted in a loss of some information about the perturbed relative motion, and made efforts to correct for this. Their procedure introduced analytic corrections to an initially unperturbed chief orbit, instead of treating the kinematics of the perturbed local vertical-local horizontal (LVLH) frame in the more formal manner of describing the angular velocity of the frame in terms of the perturbed orbit element rates, outlined in Prussing and Conway [104] and implemented also by Casotto [35]. Casotto's implementation still did not result in a stand-alone model, but his work provides very important insights to the general perturbed relative motion problem in local Cartesian coordinates. Another useful read on this topic can be found in Kechichian [76]. Also relevant is the work of Riggi and

D’Amico [106], who proposed a modified STM mapping orbit element differences for J_2 -perturbed relative motion using a new set of elements to separate the in-plane and out-of-plane motion. There is also related work by Koenig et al. [78], as well as very recent work by Willis and D’Amico in exploring the J_2 -perturbed relative motion problem for eccentric orbits using a local Cartesian coordinate formulation [128].

1.2.2 Use of Solar Radiation Pressure for Spacecraft Propulsion and Control

The most frequent exploration of using solar radiation pressure (SRP) for control has been in the solar sailing literature. See e.g. Reference 89 or 38 for a discussion of the basics of solar sailing. Applications of solar sailing have been frequently explored in literature for use in and near the Earth system, particularly by McInnes [87, 90] and others [86, 107]. Parsay notably explored formation flying with solar sails, with and without electric propulsion [101, 102, 103].

Outside of the context of solar sailing, the topic of natural SRP-perturbed orbital dynamics has been frequently studied, especially in the vicinity of small bodies [114]. Many works use a cannonball SRP model, and focus on finding stable orbits while assuming the force variation with attitude is not significant [41, 32]. Some works also discuss orbit-attitude coupling in the uncontrolled dynamics, or the coupled effects of multiple perturbations [77, 82, 94]. Recent work by Kenshiro Oguri and Jay McMahon focuses on SRP-based orbit control around asteroids [99]. The optical force SRP model used in their work is essentially equivalent to the one used in this dissertation, but their approach is otherwise quite different. Their work studies orbit control via a chosen subset of the orbit elements, namely semimajor axis and inclination. The optimal attitude for control is parameterized by two angles, whose values are obtained numerically based on the current system state.

The use of SRP for spacecraft control has already been demonstrated in flight. The K2 mission was able to make use of SRP effects to extend the life of the Kepler space telescope mission, which was suffering from attitude control under-actuation due to reaction wheel failure. This was done by achieving and maintaining an orientation to passively minimize the SRP disturbance along the

roll axis [62]. The Messenger mission to Mercury used SRP for precision orbit control, which is particularly notable and relevant to this work. In that mission, pre-planned attitude and solar array articulations were used to improve the accuracy of Mercury flybys [100]. This was done in an open-loop fashion.

1.2.3 Sensitivity Dynamics, Desensitized Control, and Uncertain Relative Motion

One topic explored in this dissertation is the dynamics and control of the linear sensitivities for linear dynamic systems with uncertain parameters in the dynamics. This makes use of a technique first developed by Kahne [72] in the 1960s, and fundamentally similar methods have been applied in trajectory design [117] and optimal landing guidance [118]. Similar work has also been done in desensitized optimal filtering, in which the estimator is designed to be tolerant of poorly known dynamical parameters [74]. Application of this concept in the context of the spacecraft relative motion problem has not been previously done. Reference 55 explored differential drag control in the presence of an uncertain atmospheric density. This work is related to the other work presented in this dissertation in [chapter 5](#).

Part of this dissertation explores the spacecraft relative motion problem in the context that the chief spacecraft is not observable and its orbit is additionally poorly known. The sensitivities to chief orbit elements have their own dynamics, and these are used to propagate the resulting relative motion uncertainty distribution efficiently. This is a small contribution to the larger study of uncertainty propagation in spaceflight. One relevant work for this is Reference 84, which derives analytic uncertainty propagation for the relative motion problem in elliptic orbits. Under the assumption of a Gaussian white noise process, the authors explore the computation of the evolving mean and covariance matrix of the relative states using Tschauner-Hempel equations [126]. Some work has focused on designing guidance and control to mitigate collision risks in the presence of uncertainties, both with active and passive methods. A classic passive means of minimizing impact risk in formation flying is through the safe ellipse, which ensures that in the presence of along-track drift in the relative motion, the spacecraft will not collide [83]. In Reference 13, Breger and

How investigate tradeoffs between active and passive approaches to safety. They also develop a strategy for generating safe, fuel-optimized rendezvous trajectories that guarantee collision avoidance for a large class of anomalous behaviors. Reference 59 develops a Receding Horizon Control (RHC) approach that enforces passive safety in the presence of common navigation or propulsive system failures. They identify that adding cross-track relative motion also greatly reduces collision probability.

There are several works which explore the problem of rendezvous and proximity operations when the target orbit is uncertain, which leads to uncertainty in the linearized model. In these works, the spacecraft relative state is assumed to be directly and accurately measured, but the effects of dynamic uncertainty need to be mitigated. Reference 85 studies reliable impulsive state-feedback control for autonomous spacecraft rendezvous under target orbital uncertainty with the possibility of thruster faults. This is accomplished using Lyapunov theory and genetic algorithms. Reference 130 addresses robust H_∞ control for spacecraft rendezvous with a noncooperative target, specifically for the case of CW dynamics, in which the target semimajor axis is uncertain. The control design enables rendezvous in the presence of this dynamical uncertainty, while also allowing for control input saturation. In both References 85 and 130, the uncertainty in the target orbit manifests only as dynamic uncertainty in the linearized models. The relative position and velocity are assumed to be observable.

1.2.4 Modal Decomposition of Spacecraft Relative Motion

One interesting line of work is in determining the simplest and most convenient parameterizations of natural relative motion. Largely a question of the choice of coordinates, this also involves factoring the resultant solution in a given set of coordinates in a manner convenient or illuminating for the astrodynamicist. The state transition matrix is an unwieldy means by which to explore relative motion. Instead, other sets of fundamental linear solutions can be chosen to serve as a functional basis. Custom geometric interpretations of the solutions might also be possible, in which the relative motion solution is factored into a more concise or workable form. One example

of this is the nonsingular relative orbit element set for the Clohessy-Wiltshire solution [10, 111]. The pursuit of desirable parameterizations of relative motion is a solved problem for the Clohessy-Wiltshire case, a manageable problem for more general elliptic orbits, but is largely unexplored for the wide variety of periodic and almost-periodic orbits in multi-body and small-body applications. This dissertation uses the idea of the modal decomposition to efficiently parameterize the relative motion problem, and the modal decomposition is a core concept in the theory of vibrations. See Reference 92 or an equivalent introductory text on vibrations for discussion.

To compute the relative motion modal decomposition, this dissertation employs Lyapunov-Floquet theory [97], whose application to the relative motion problem has seen relatively limited study thus far. In Reference 120, an approximate Lyapunov-Floquet (LF) transformation relating the Clohessy-Wiltshire and Tschauner-Hempel dynamics is exploited for relative motion control design. In Reference 98, the authors apply the LF transformation to the Tschauner-Hempel problem with cubic nonlinearities and examine the effect of the nonlinearities on the dynamical variables via averaging theory. Additionally, a simple LF transformation is used in Reference 78 when incorporating the secular effect of the J_2 perturbation on orbit element differences. Floquet theory has also been applied to the study and control of motion of spacecraft in the vicinity of Lagrange points and periodic orbits in cislunar space. See e.g. References 51 and 61. The LF transformation is applied to control design elsewhere in literature. Reference 42 studies control design for dynamical systems with time-periodic coefficients using the LF transformation and the backstepping technique. This is applied to control of a system with two statically coupled pendula subject to periodic forcing. In Reference 95, control of systems with periodic coefficients is discussed and LF theory is applied to control of an industrial mechanism.

1.3 Contributions of this Work

This dissertation contributes to the study and practice of close-proximity satellite relative motion in several related areas. Specifically, the work develops new analytic and semi-analytic methods of understanding and exploiting or mitigating the influence of non-Keplerian disturbances

in close-proximity spacecraft formation flying and rendezvous applications. There is also some new study of spacecraft relative motion dynamics and control in the presence of dynamic and navigational uncertainties. Additionally, the work provides new insights into the nature of relative motion solutions in perturbed and unperturbed orbits, with elegant control applications.

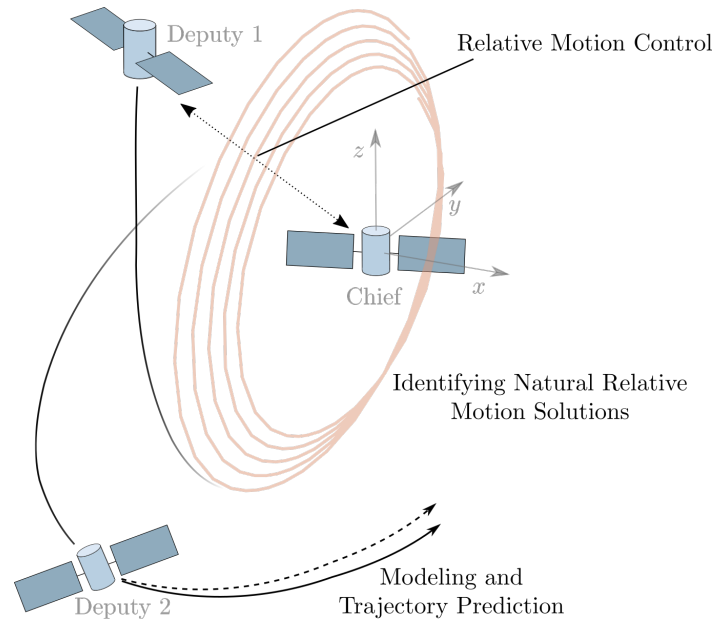


Figure 1.3: Spacecraft Formation Flying Guidance and Control in Perturbed Environments

This work focuses on techniques that apply to fractionated space systems, which can be easily adapted for tasks as varied as short-term rendezvous and docking operations or long-term high-precision close-proximity formation control. Figure 1.3 illustrates the concept of operations and summarizes the general scope. Often, the techniques rely on the linearization simplification, for which the complex formation design problem is reduced to having multiple agents obeying the same linear dynamics. This work combines elements of astrodynamics, dynamics, control, and approximation theory to accomplish the various research goals, which are given below:

- (1) Develop approximations of perturbed relative orbital motion dynamics (Chapter 3)
- (2) Derive, investigate, and demonstrate formation control using differential solar radiation pressure (Chapter 4)

- (3) Investigate robust formation flying/rendezvous control techniques subject to significant disturbances (Chapter 5)
- (4) Develop, test, and apply a methodology for modal decomposition approximations of spacecraft relative motion in a variety of orbital scenarios (Chapters 6, 7)

After a review of necessary fundamentals in [chapter 2](#), the novel contributions of this work begin with [chapter 3](#). This chapter focuses on deriving accurate state transition matrix (STM) models of relative motion subject to various perturbations such as J_2 , with a focus on low-complexity high-accuracy models. The efficacy of these models is compared with others in literature for the J_2 problem. The same techniques are used to derive corrective terms for the J_3 perturbation as well. Additionally, [chapter 3](#) discusses various tools and techniques that can be used to further improve relative motion model accuracy. The chapter also derives a linear model of relative motion subject to some of the dominant disturbances encountered in orbits about large asteroids. The model enables efficient exploration of the parameter space of possible chief orbits, and is revisited in [chapter 7](#). Lastly, the chapter briefly explores the problem of approximating the J_2 -perturbed chief orbit in more general orbital settings, which is necessary for more accurate and globally valid J_2 -perturbed relative motion models.

The same principles discussed in [chapter 3](#) are further applied in [chapter 4](#) to study the SRP-perturbed satellite relative motion problem in detail. A simple analytic linear model of relative motion is obtained and tested numerically. This chapter also explores satellite relative motion control with differential SRP accelerations. The chapter includes controllability analysis and insights for achieving full regulation control with the differential SRP in a closed-loop fashion.

The dissertation pivots to the topic of relative motion sensitivities in [chapter 5](#). This chapter explores the dynamics of sensitivities of the relative state to error in dynamical parameters and in the chief orbit. The main accomplishments of this chapter are spacecraft orbit control in asteroid environments using the linear model developed in [chapter 3](#), including both Linear Quadratic Regulator (LQR) and a desensitized control approach, expected to be more robust to poorly known

dynamical parameters. Also in this chapter is a study in efficient propagation of satellite relative state uncertainty in the vicinity of a poorly tracked target object. This approach could have applications to on-board uncertainty-aware control strategies.

Chapters 6 and 7 explore a very promising topic – the modal decomposition of close-proximity spacecraft relative motion in a variety of applicable orbits. In [chapter 6](#), the theory is introduced, and exact analytic Lyapunov-Floquet (LF) transformations are computed for spacecraft relative motion in Cartesian and curvilinear coordinates. Some of the fundamental modal solutions connect to earlier solutions of the Tschauner-Hempel equations explored previously in literature. Chapter 6 also includes discussion of the analytic extension to weakly-perturbed orbits such as orbits perturbed by J_2 . Chapter 7 explores other applications of the modal decomposition, including satellite relative motion modes in an asteroid orbital environment, with some new contributions for how to apply the modal decomposition procedure numerically in orbits that are not exactly periodic. Additionally, the modal constants (affiliated with the fundamental modes) are used to design a highly computationally efficient impulsive maneuver-based control strategy that switches between desired relative motion modes or combinations of modes. This is demonstrated for relative motion analysis and control in the Keplerian problem and in the Earth-Moon circular restricted three-body problem (CR3BP).

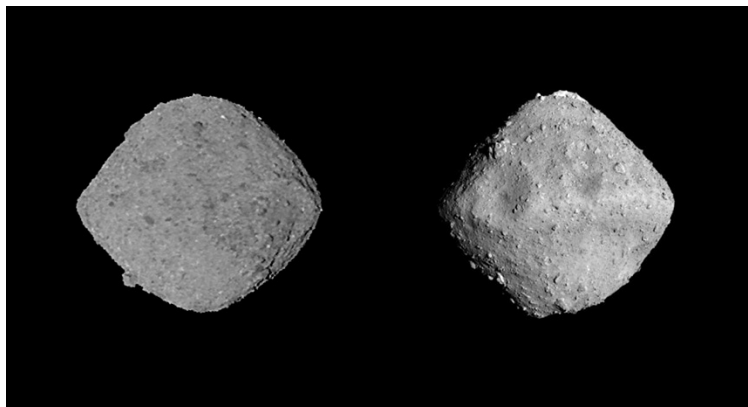


Figure 1.4: Near-Earth Asteroids Bennu (L) and Ryugu (R) (Credit: ESA)

Overall, the concepts developed and explored in this dissertation are all expected to be

of relevance for future multi-spacecraft operations in a variety of complex environments. The applications range from accurate relative motion and rendezvous planning in low-Earth orbits, to multi-spacecraft missions to cislunar space and near-Earth asteroids, such as 101955 Bennu or 162173 Ryugu (depicted in Figure 1.4). Most of the techniques and concepts explored in this dissertation are generally applicable in or extendable to a variety of orbital regimes, contextualizing the traditionally Earthly study of close-proximity spacecraft relative motion within the broader realm of all applicable environments, known and unknown.

1.4 Publications

All publications from my graduate career are listed below. Publications whose content does not appear in this dissertation are marked with a dagger symbol.

Journal Publications

- (1) E. Burnett and H. Schaub, “Approximating Orbits in a Rotating Gravity Field with Oblateness and Ellipticity Perturbations,” *Celestial Mechanics and Dynamical Astronomy*. *Submitted May 6, 2021. Revised and under review.*
- (2) E. Burnett and H. Schaub, “Geometric Perspectives on Fundamental Solutions in the Linearized Satellite Relative Motion Problem,” *Acta Astronautica*, Vol 190, pp. 48-61, January 2022. DOI: 10.1016/j.actaastro.2021.09.028
- (3) † A. Harris, E. Burnett, and H. Schaub, “Desensitized Optimal Attitude Guidance for Differential-Drag Rendezvous,” *Journal of Spacecraft and Rockets*. *Submitted March 18, 2021. Under review.*
- (4) † E. Burnett and P. Hayne, “Europa’s hemispheric color dichotomy as a constraint on non-synchronous rotation,” *Icarus*, Vol 364, Article No. 114438, August 2021. DOI: 10.1016/j.icarus.2021.114438
- (5) E. Burnett and H. Schaub, “Spacecraft Formation and Orbit Control Using Attitude-Dependent Differential Solar Radiation Pressure,” *Advances in Space Research*, Special

Issue: Satellite Constellations and Formation Flying. Vol 67, Issue 11, pp. 3396-3408, June 1 2021. DOI: 10.1016/j.asr.2020.03.047

- (6) E. Burnett and H. Schaub, "Study of Highly Perturbed Spacecraft Formation Dynamics via Approximation," *Advances in Space Research*, Special Issue: Satellite Constellations and Formation Flying. Vol 67, Issue 11, pp. 3381-3395, June 1 2021. DOI: 10.1016/j.asr.2020.02.030
- (7) † E. Burnett, A. J. Sinclair, and C. C. Fisk, "Unit Sphere-Constrained and Higher Order Interpolations in Laplace's Method of Initial Orbit Determination," *Journal of Astronautical Sciences*, Vol 67, pp. 1116-1138, 2020. DOI: 10.1007/s40295-019-00196-x

Conference Papers

- (1) † E. Burnett, S. Albert, and H. Schaub, "A New Guidance Technique for Discrete-Event Drag Modulation for Aerocapture Missions," 2022 AAS Rocky Mountain GNC Conference. Breckenridge, CO. *Submitted August 26, 2021*
- (2) E. Burnett and H. Schaub, "Spacecraft Relative Motion Dynamics and Control Using Fundamental Solution Constants," 2022 AAS Spaceflight Mechanics Meeting. San Diego, CA. *Submitted June 1, 2021*
- (3) † M. J. Grace, E. Burnett, and J. McMahon, "Quasi-Initial Conditions as a State Representation for Aerocapture," 2022 AIAA SciTech Forum: Hypersonic and Spacecraft Flight Mechanics Group. San Diego, CA. *Submitted June 1, 2021*
- (4) E. A. Butcher, E. Burnett, and H. Schaub, "Spherical Coordinate Analytic Approximations for J_2 -Perturbed Eccentric Relative Motion with Quadratic Corrections," 2022 AAS Spaceflight Mechanics Meeting. San Diego, CA. *Submitted June 1, 2021*
- (5) E. Burnett and H. Schaub, "Satellite Relative State Uncertainty Dynamics in the Vicinity of a Poorly Tracked Target Object," AAS 21-511, 2021 AAS Astrodynamics Specialist Conference. Virtual.

- (6) E. Burnett and H. Schaub, “Modal Decomposition of Spacecraft Relative Motion in Quasi-Periodic Orbits,” AAS 20-506, 2020 AAS Astrodynamics Specialist Conference. Virtual.
- (7) E. Burnett and H. Schaub, “Analytic Approximations of Orbit Geometry in a Rotating Higher Order Gravity Field,” AAS 19-684, 2019 AAS Astrodynamics Specialist Conference. Portland, ME.
- (8) E. Burnett, A. Harris, and H. Schaub, “Desensitized Optimal Spacecraft Rendezvous Control with Poorly Known Gravitational and Solar Radiation Pressure Perturbations,” AAS 19-685, 2019 AAS Astrodynamics Specialist Conference. Portland, ME.
- (9) A. Harris, E. Burnett, and H. Schaub, “Desensitized Optimal Attitude Guidance for Differential-Drag Rendezvous,” AAS 19-651, 2019 AAS Astrodynamics Specialist Conference. Portland, ME.
- (10) E. Burnett and H. Schaub, “Spacecraft Formation and Orbit Control Using Attitude-Dependent Solar Radiation Pressure,” IWSCFF 19-28, 2019 International Workshop on Satellite Constellations and Formation Flying. Glasgow, Scotland.
- (11) E. Burnett and H. Schaub, “Study of Highly Perturbed Spacecraft Formation Dynamics via Approximation,” IWSCFF 19-27, 2019 International Workshop on Satellite Constellations and Formation Flying. Glasgow, Scotland.
- (12) † E. Burnett, A. J. Sinclair, and E. A. Butcher, “Coordinate-Invariant Linear Quadratic Control,” GAMM 2019, 90th Annual Meeting of the International Association of Applied Mathematics and Mechanics. Vienna, Austria.
- (13) E. Burnett and E. A. Butcher, “Linearized Relative Motion Dynamics in a Rotating Second Degree and Order Gravity Field,” AAS 18-232, 2018 AAS Astrodynamics Specialist Conference. Snowbird, UT.
- (14) E. Burnett, E. A. Butcher, A. J. Sinclair, and T. A. Lovell, “Linearized Relative Orbital Motion Model About an Oblate Body Without Averaging,” AAS 18-218, 2018 AAS Astrodynamics Specialist Conference. Snowbird, UT.

- (15) † E. Burnett and A. J. Sinclair, “Interpolation on the Unit Sphere in Laplace’s Method,” AAS 17-793, 2017 AAS Astrodynamics Specialist Conference. Stevenson, WA.
- (16) † K. Drozd, E. Burnett, E. Sahr, D. McNeely, V. Franzese, N. R. Morón, “Block-Like Explorer of a near-Earth Body by achieving Orbital Proximity (BEEBOP),” AAS 17-846, 2017 AAS Astrodynamics Specialist Conference . Stevenson, WA.
- (17) † E. A. Butcher, E. Burnett, J. Wang, and T. A. Lovell, “A New Time-Explicit J2-Perturbed Nonlinear Relative Orbit Model with Perturbation Solutions,” AAS 17-758, 2017 AAS Astrodynamics Specialist Conference. Stevenson, WA.
- (18) † E. A. Butcher, E. Burnett, and T. A. Lovell, “Comparison of Relative Orbital Motion Perturbation Solutions in Cartesian and Spherical Coordinates,” AAS 17-202, 2017 AAS Spaceflight Mechanics Meeting. San Antonio, TX.

Chapter 2

Preliminaries

In order to better understand the methodologies used in this research, this chapter provides an introductory review of important concepts. First, the spacecraft relative motion problem is introduced. Then, there is a discussion of common orbital perturbations, which are important phenomena to consider in modern spacecraft formation flying and relative motion control. Afterwards, perturbation methods are briefly discussed, which enable mathematically rigorous approximation of the behavior of complex systems. This set of tools is used for general spacecraft relative motion approximation, which is then discussed. Finally, this chapter discusses the basics of linear differential equations and reducibility of linear differential equations, which includes Lyapunov-Floquet theory for reducing linear systems with periodic coefficients. This chapter draws on a large body of literature to review mainly fundamental concepts. The novel contributions of this dissertation begin with [chapter 3](#). Note that this dissertation presupposes that the reader is familiar with fundamental orbital mechanics, so there is no review of those concepts. The interested reader should consult References [7](#), [8](#), [37](#), or equivalent.

2.1 Spacecraft Relative Motion

2.1.1 Fundamentals

The spacecraft formation flying nomenclature used in this dissertation is as follows. The chief satellite is a spacecraft about which all other nearby satellite motions are referenced. The other satellites are referred to as “deputies”. The chief spacecraft is also sometimes referred to as the

target spacecraft, in which case the deputy is typically called the chaser. Note that the chief orbit need not be occupied by a physical spacecraft – it can be empty. This is referred to as a virtual chief.

To describe the motion of the deputy spacecraft in the vicinity of the chief, the Local Vertical-Local Horizontal (LVLH) or Hill frame is typically used. This is a coordinate frame with the origin centered on the chief spacecraft, defined by the right-handed set of orthonormal basis vectors $\hat{\mathbf{e}}_r$, $\hat{\mathbf{e}}_t$, and $\hat{\mathbf{e}}_n$, which are defined in terms of the instantaneous chief position and velocity vectors \mathbf{r} and \mathbf{v} :

$$\hat{\mathbf{e}}_r = \frac{\mathbf{r}}{r} \quad (2.1a)$$

$$\hat{\mathbf{e}}_n = \frac{\mathbf{r} \times \mathbf{v}}{\|\mathbf{r} \times \mathbf{v}\|} \quad (2.1b)$$

$$\hat{\mathbf{e}}_t = \hat{\mathbf{e}}_n \times \hat{\mathbf{e}}_r \quad (2.1c)$$

In cases where disambiguation is necessary, quantities belonging to the deputy are denoted by subscript “d”, and quantities with subscript “c” belong to the chief. The relative position vector is always resolved in LVLH frame components:

$$\boldsymbol{\rho} = x\hat{\mathbf{e}}_r + y\hat{\mathbf{e}}_t + z\hat{\mathbf{e}}_n = {}^H(x, y, z)^\top \quad (2.2)$$

Figure 2.1 depicts the chief, deputy, and instantaneous relative position. The relative velocity of the deputy with respect to the chief is the derivative of the relative position as seen in the LVLH frame:

$$\boldsymbol{\rho}' = \dot{x}\hat{\mathbf{e}}_r + \dot{y}\hat{\mathbf{e}}_t + \dot{z}\hat{\mathbf{e}}_n = {}^H(\dot{x}, \dot{y}, \dot{z})^\top \quad (2.3)$$

where $(\)' = {}^H\frac{d}{dt}(\)$ generally denotes the derivative of a quantity as seen in the rotating LVLH frame, unless otherwise indicated. In some sections, a prime denotes the derivative with respect to an independent variable other than time (such as an angle), but this is always explicitly specified. Together, the relative position and velocity vectors form the relative state $\mathbf{x} = (\boldsymbol{\rho}^\top, \boldsymbol{\rho}')^\top$. Some sections denote the relative position and velocity by $\Delta\mathbf{r}$ and $\Delta\mathbf{r}'$ instead of $\boldsymbol{\rho}$ and $\boldsymbol{\rho}'$, and this is particularly common in sections where $\rho = r/a$ appears, to avoid ambiguity with the relative range $\|\boldsymbol{\rho}\|$.

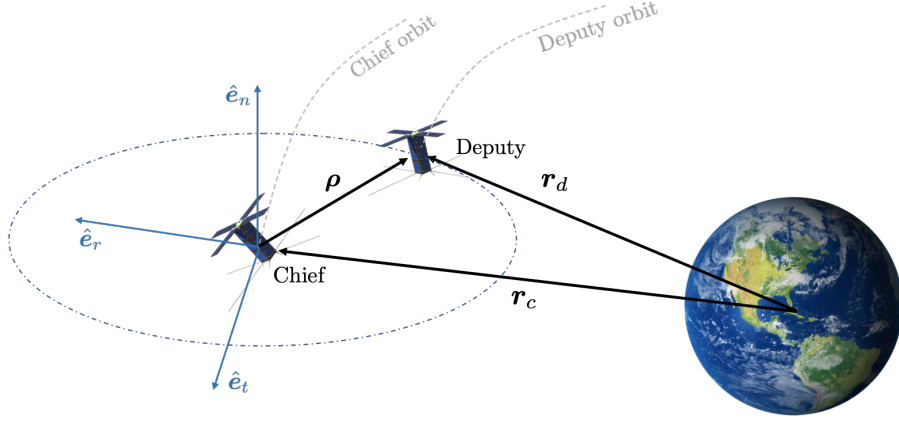


Figure 2.1: Spacecraft Relative Motion in the LVLH Frame

Also, Figure 2.1 depicts, by the dotted line, the *relative orbit* traced by the deputy position vector over the course of one chief orbit. This type of bounded relative motion occurs only when certain conditions are specified, depending on the problem dynamics. With this in mind, the most common case is now explored: The case of *Keplerian dynamics*, where the two-body equation applies to both the chief and deputy. The nonlinear (and exact) Keplerian equations of relative motion are given below. See Reference 111 for the full derivation, which makes use of elementary expressions from orbital mechanics, the two-body equation $\ddot{\mathbf{r}} = -\frac{\mu}{r^3}\mathbf{r}$, and the transport theorem.

$$\ddot{x} - 2\dot{f}\left(\dot{y} - \frac{\dot{r}_c}{r_c}y\right) - \dot{f}^2x - \frac{\mu}{r_c^2} = -\frac{\mu}{r_d^3}(r_c + x) \quad (2.4a)$$

$$\ddot{y} + 2\dot{f}\left(\dot{x} - \frac{\dot{r}_c}{r_c}x\right) - \dot{f}^2y = -\frac{\mu}{r_d^3}y \quad (2.4b)$$

$$\ddot{z} = -\frac{\mu}{r_d^3}z \quad (2.4c)$$

For the Keplerian problem, regardless of the separation between the chief and deputy, the deputy will trace a bounded relative orbit with respect to the chief (as seen in the LVLH frame) if the two spacecraft have the same orbit period, $T_d = T_c$. Equivalently, this requires that the two spacecraft possess the same semimajor axis, $\delta a = a_d - a_c = 0$.

The complexity of Eq. (2.4) is a function of the coordinate representation. If the state were expressed in terms of orbit element differences $\delta\mathbf{oe} = \mathbf{oe}_d - \mathbf{oe}_c$, then for the Keplerian problem, the relative state vector will be constant for all elements, or for all except one, depending on the

choice of the anomaly in \mathbf{oe} . In this case, the complexity of the relative motion dynamics is greatly simplified, but direct geometric interpretation and convenience of the coordinate set is somewhat reduced. With this in mind, some authors have derived alternative coordinate representations such as Relative Orbit Elements (ROEs) [39], to try and recover a state representation that is dynamically convenient but possesses simple geometric interpretation.

Because much of spacecraft formation flying and spacecraft relative motion control happens in scenarios where the chief and deputy are in fairly close proximity, one major simplifying assumption is to linearize the equations of relative motion. Such linearized expressions are the most common focus of the work in this dissertation. By far the most popular linearized relative motion equations in formation flying are the Clohessy-Wiltshire equations. These are derived next.

2.1.2 Clohessy-Wiltshire Dynamics

The Clohessy-Wiltshire (CW) dynamics [36] apply to close proximity of a deputy and chief spacecraft in the case that the chief orbit is very nearly circular, and perturbations are small enough to be ignored for the timespan of interest. First, the kinetics of the problem are treated, by subtracting the two-body accelerations acting on the chief from those acting on the deputy:

$$\ddot{\boldsymbol{\rho}} = -\frac{\mu}{r_d^3}\mathbf{r}_d + \frac{\mu}{r_c^3}\mathbf{r}_c \quad (2.5)$$

Noting $\mathbf{r}_d = \mathbf{r}_c + \boldsymbol{\rho}$, expand the equation:

$$\ddot{\boldsymbol{\rho}} = -\frac{\mu}{((\mathbf{r}_c + \boldsymbol{\rho}) \cdot (\mathbf{r}_c + \boldsymbol{\rho}))^{\frac{3}{2}}}\mathbf{r}_c + \frac{\mu}{r_c^3}\mathbf{r}_c \quad (2.6)$$

Factoring the denominator of the deputy acceleration term, and keeping only terms linear in $\boldsymbol{\rho}$:

$$\ddot{\boldsymbol{\rho}} \approx -\frac{\mu}{r_c^3} \left(1 + 2\frac{(\boldsymbol{\rho} \cdot \mathbf{r}_c)}{r_c^2} \right)^{-\frac{3}{2}} \mathbf{r}_c + \frac{\mu}{r_c^3}\mathbf{r}_c \quad (2.7)$$

Note that linearization renders the *equality* in Eq. (2.6) as an *approximation* in Eq. (2.7), but the approximation notation will be dropped. Using a binomial expansion $(1 + \epsilon)^k \approx 1 + k\epsilon$ to linearize the exponential term, and factoring:

$$\ddot{\boldsymbol{\rho}} = -\frac{\mu}{r_c^3} \left(\left(1 - 3\frac{(\boldsymbol{\rho} \cdot \mathbf{r}_c)}{r_c^2} \right) (\mathbf{r}_c + \boldsymbol{\rho}) - \mathbf{r}_c \right) \quad (2.8)$$

Expanding the expression in parentheses and keeping only terms linear in $\boldsymbol{\rho}$, dropping the subscript notation so $\mathbf{r}_c = \mathbf{r}$:

$$\ddot{\boldsymbol{\rho}} = -\frac{\mu}{r^3} \left(\boldsymbol{\rho} - 3 \frac{(\boldsymbol{\rho} \cdot \mathbf{r})}{r^2} \mathbf{r} \right) \quad (2.9)$$

Noting $\hat{\mathbf{r}} = \mathbf{r}/r$ and expressing this in matrix-vector form:

$$\ddot{\boldsymbol{\rho}} = -\frac{\mu}{r^3} \left([I_{3 \times 3}] - 3\hat{\mathbf{r}}\hat{\mathbf{r}}^\top \right) \boldsymbol{\rho} \quad (2.10)$$

Resolving $\boldsymbol{\rho}$ into its LVLH components as $\boldsymbol{\rho} = x\hat{\mathbf{e}}_r + y\hat{\mathbf{e}}_t + z\hat{\mathbf{e}}_n$, and noting $\hat{\mathbf{r}} = \hat{\mathbf{e}}_r$, obtain the linear terms due to the difference in acceleration felt by the deputy and chief:

$$\ddot{\boldsymbol{\rho}} = \frac{\mu}{r^3} (2x\hat{\mathbf{e}}_r - y\hat{\mathbf{e}}_t - z\hat{\mathbf{e}}_n) \quad (2.11)$$

For a circular chief orbit, $r = a$, so this can be rewritten using the definition of the mean motion:

$$\ddot{\boldsymbol{\rho}} = 2n^2x\hat{\mathbf{e}}_r - n^2y\hat{\mathbf{e}}_t - n^2z\hat{\mathbf{e}}_n \quad (2.12)$$

The inertial acceleration of the relative position vector must be resolved into the LVLH frame as well, which rotates with angular velocity $\boldsymbol{\omega}_H$. This is done by applying the transport theorem twice:

$$\ddot{\boldsymbol{\rho}} = \frac{H_d^2 \boldsymbol{\rho}}{dt^2} + \dot{\boldsymbol{\omega}}_H \times \boldsymbol{\rho} + 2\boldsymbol{\omega}_H \times \frac{H_d \boldsymbol{\rho}}{dt} + \boldsymbol{\omega}_H \times (\boldsymbol{\omega}_H \times \boldsymbol{\rho}) \quad (2.13)$$

If the chief spacecraft is in a circular orbit, $\boldsymbol{\omega}_H = n\hat{\mathbf{e}}_n$ is constant:

$$\ddot{\boldsymbol{\rho}} = \frac{H_d^2 \boldsymbol{\rho}}{dt^2} + 2\boldsymbol{\omega}_H \times \frac{H_d \boldsymbol{\rho}}{dt} + \boldsymbol{\omega}_H \times (\boldsymbol{\omega}_H \times \boldsymbol{\rho}) \quad (2.14)$$

Resolving this in LVLH components and simplifying:

$$\ddot{\boldsymbol{\rho}} = (\ddot{x} - n^2x - 2n\dot{y}) \hat{\mathbf{e}}_r + (\ddot{y} - n^2y + 2n\dot{x}) \hat{\mathbf{e}}_t + \ddot{z} \hat{\mathbf{e}}_n \quad (2.15)$$

Setting the vector Eq. (2.15) equal to Eq. (2.12), simplifying, and separating by component, the three well-known CW equations are obtained:

$$\ddot{x} = 3n^2x + 2n\dot{y} \quad (2.16a)$$

$$\ddot{y} = -2n\dot{x} \quad (2.16b)$$

$$\ddot{z} = -n^2z \quad (2.16c)$$

The solution to this set of linear ODEs can be shown to be [104]:

$$x(t) = (4 - 3 \cos nt) x_0 + \frac{\sin nt}{n} \dot{x}_0 + \frac{2}{n} (1 - \cos nt) \dot{y}_0 \quad (2.17a)$$

$$y(t) = 6 (\sin nt - nt) x_0 + y_0 - \frac{2}{n} (1 - \cos nt) \dot{x}_0 + \frac{4 \sin nt - 3nt}{n} \dot{y}_0 \quad (2.17b)$$

$$z(t) = \cos nt z_0 + \frac{\sin nt}{n} \dot{z}_0 \quad (2.17c)$$

Taking the time derivative of these equations, one can easily obtain $\dot{x}(t)$, $\dot{y}(t)$, $\dot{z}(t)$ as well:

$$\dot{x}(t) = 3n \sin nt x_0 + \cos nt \dot{x}_0 + 2 \sin nt \dot{y}_0 \quad (2.18a)$$

$$\dot{y}(t) = -6n (1 - \cos nt) x_0 - 2 \sin nt \dot{x}_0 + (4 \cos nt - 3) \dot{y}_0 \quad (2.18b)$$

$$\dot{z}(t) = -n \sin nt z_0 + \cos nt \dot{z}_0 \quad (2.18c)$$

Since these solutions to the CW equations are linear in the initial conditions, they can be rearranged to obtain a state transition matrix. There are many uses for the resulting STM for spacecraft relative motion, including linear impulsive rendezvous for bringing two spacecraft in similar near-circular orbits close enough for docking or other proximity operations.

By collecting terms linear in time from $y(t)$ in Eq. (2.17), one obtains $-3(2nx_0 + \dot{y}_0)t$, which isolates a “no-drift” condition when set to zero:

$$2nx_0 + \dot{y}_0 = 0 \quad (2.19)$$

If the initial conditions (x_0, \dot{y}_0) satisfy this equation, then the CW equations yield completely bounded periodic relative motion. It can be shown that this condition is essentially a linearized approximation of $\delta a = a_d - a_c = 0$, which ensures that both the chief and deputy orbit have the same orbit period and their relative motion will remain bounded under two-body dynamics [111]. Since it is only an approximation of the no-drift condition, true non-drifting relative orbit initial conditions will not exactly agree with Eq. (2.19).

2.2 Perturbed Orbits

2.2.1 Representing the Perturbed Two-Body Problem

Formation flying in the presence of orbital perturbations is a common focus of this dissertation. In the context of this dissertation, the dynamics are generally expressed in the following form:

$$\ddot{\mathbf{r}} = -\frac{\mu}{r^3}\mathbf{r} + \mathbf{a}_p \quad (2.20)$$

where \mathbf{a}_p is the perturbing acceleration, often sub-dominant from the two-body acceleration. In this set of coordinates (position and velocity), the coordinates vary rapidly, and the influence of the perturbation is difficult to geometrically or analytically discern.

Commonly in this dissertation, the influence of perturbations on the orbital elements are considered. These quantities are constant (typically except for an anomaly), but their behavior for the perturbed system can be computed via variation-of-parameters [111]. For small perturbations, the variations induced in these quantities from their unperturbed values are typically small. The variations in the orbit elements are given below by Gauss' form of the variational equations [8]:

$$\dot{\Omega} = \frac{r \sin \theta}{h \sin i} a_n \quad (2.21a)$$

$$\dot{i} = \frac{r \cos \theta}{h} a_n \quad (2.21b)$$

$$\dot{\omega} = \frac{1}{he} (-p \cos f a_r + (p+r) \sin f a_t) - \frac{r \sin \theta \cos i}{h \sin i} a_n \quad (2.21c)$$

$$\dot{a} = \frac{2a^2}{h} \left(e \sin f a_r + \frac{p}{r} a_t \right) \quad (2.21d)$$

$$\dot{e} = \frac{1}{h} (p \sin f a_r + ((p+r) \cos f + re) a_t) \quad (2.21e)$$

$$\dot{M} = n + \frac{b}{ahe} ((p \cos f - 2re) a_r - (p+r) \sin f a_t) \quad (2.21f)$$

where $\mathbf{a} = a_r \hat{\mathbf{e}}_r + a_t \hat{\mathbf{e}}_t + a_n \hat{\mathbf{e}}_n$ and $\theta = \omega + f$ is the argument of latitude. Note that only the mean anomaly rate \dot{M} remains nonzero in the absence of perturbations. An alternative parameterization is to use the initial mean anomaly M_0 as an element, for which $M = M_0 + nt$, and then the set of all elements $\mathbf{oe} = (a, e, i, \omega, \Omega, M_0)$ is time-invariant, and the state $\mathbf{X} = (\mathbf{r}^\top, \mathbf{v}^\top)^\top$ can be

recovered by specifying \mathbf{oe} and time t . For example, Reference 114 uses the element $\sigma = -nt_p$ in lieu of an anomaly, where t_p is the time of periapsis passage, and $M = n(t - t_p) = nt - \sigma$. Also commonly used in this dissertation, in place of the mean anomaly, are the true anomaly or argument of latitude, whose variational equations are given below:

$$\dot{f} = \frac{h}{r^2} + \frac{1}{eh} (p \cos f a_r - (p + r) \sin f a_t) \quad (2.22)$$

$$\dot{\theta} = \dot{\omega} + \dot{f} = \frac{h}{r^2} - \frac{r \sin \theta \cos i}{h \sin i} a_n \quad (2.23)$$

Note that for any perturbed orbit problem, the orbit elements almost always remain a valid state description (with the sole exception of the rare violation of geometric singularities). Eqs. (2.21)-(2.23) can be applied in any setting, with any acceleration \mathbf{a}_p acting on the system. However, in the case that the perturbing acceleration is sub-dominant, all elements (except for the anomaly) will generally vary slowly in most circumstances. This is notably not true for the classical orbit element description in perturbed near-circular orbits – the quantities ω and f will fluctuate rapidly due to the small denominator e . In these circumstances, it is better to use the quasi-nonsingular orbit elements, which replace e , ω , and f with $q_1 = e \cos \omega$, $q_2 = e \sin \omega$, and $\theta = \omega + f$. This set of elements is frequently used in this dissertation. It has its own variational equations, which can be easily obtained by direct differentiation, using Eqs. (2.21)-(2.23).

2.2.2 Common Orbital Perturbations

This dissertation focuses on the effects of several different perturbations: non-spherical gravity, third-body gravity, and solar radiation pressure (SRP). Each of these is now briefly introduced.

2.2.2.1 Non-spherical gravity

In reality, the isotropic two-body potential $U(r) = \mu/r$ is not representative of the true gravity field of a body. For small bodies such as asteroids and comets, the non-spherical symmetry of the

gravity field becomes quite important. Even for the Earth and the other planets, the non-spherical gravity effects are noticeable, particularly in low orbits.

The overall body potential U is given by integrating the potential of a differential mass element over the entire body:

$$U(\mathbf{r}) = G \int_B \frac{dm(\boldsymbol{\rho})}{\|\mathbf{r} - \boldsymbol{\rho}\|} \quad (2.24)$$

where B is the collection of all mass elements in the body, $\boldsymbol{\rho}$ is the position vector for the differential mass element dm , and G is the gravitational constant. The gravitational potential satisfies Laplace's equation outside of the body: $\nabla^2 U = 0$. For a homogeneous sphere with constant density, mass M , and radius R , Eq. (2.24) yields $U = GM/r$.

Laplace's equation can be resolved in spherical coordinates:

$$\frac{1}{r^2} \frac{\partial}{\partial r} \left(r^2 \frac{\partial U}{\partial r} \right) - \frac{1}{r^2 \cos \phi} \frac{\partial}{\partial \phi} \left(\cos \phi \frac{\partial U}{\partial \phi} \right) + \frac{1}{r^2 \cos^2 \phi} \frac{\partial^2 U}{\partial \lambda^2} = 0 \quad (2.25)$$

The spherical coordinates can be defined for the position vector $\mathbf{r} = x\hat{\mathbf{e}}_x + y\hat{\mathbf{e}}_y + z\hat{\mathbf{e}}_z$: $r = \sqrt{x^2 + y^2 + z^2}$, $\lambda = \tan^{-1}(y/x)$ is the longitude, and $\phi = \sin^{-1}(z/r)$ is the latitude. Solution of Eq. (2.25) via separation of variables yields the spherical harmonics, which are an orthogonal set of solutions that form a basis for describing any other function satisfying Laplace's equation [75]. The potential for any arbitrary physical gravity field can thus be expressed in a series in terms of the spherical harmonics:

$$U(r, \phi, \lambda) = \frac{\mu}{r} \sum_{l=0}^{\infty} \sum_{m=0}^l \left(\frac{R}{r} \right)^l P_{lm}(\sin \phi) [C_{lm} \cos m\lambda + S_{lm} \sin m\lambda] \quad (2.26)$$

where R is the radius of the Brillouin sphere and μ is the gravitational parameter. P_{lm} are the associated Legendre functions, and C_{lm} and S_{lm} are the gravity field harmonic coefficients, which are defined by the mass distribution of the body. Note that this expansion is only valid outside of the Brillouin sphere of radius R .

In Eq. (2.26), $m = n = 0$ gives the "zeroth degree and order term" $C_{00} = 1$. This is the largest contribution to the gravitational potential; a spherically symmetric "bulk" term equivalent to assuming that the body is replaced by a homogeneous sphere of equal mass. The higher-order

gravitational terms add and subtract “mass” to particular regions of the body to account for local departures from a spherical shape. However, a few of the additional terms can be eliminated with prudent choice of the body-fixed coordinate system. First, if the origin of the coordinate system is chosen to coincide with the body center of mass, it can be shown that the first degree and order terms are all zero: $C_{11} = S_{11} = C_{10} = 0$. Next, choosing the body-fixed coordinate system to be aligned with the principal axes of inertia, one can eliminate some of the second degree and order gravity coefficients: $C_{21} = S_{21} = S_{22} = 0$. Thus, a simple second degree and order gravitational potential can be described with just the coefficients C_{20} and C_{22} – which together account for first-order effects of the *oblateness* and *ellipticity* of a body. The resulting disturbance acceleration is obtained by $\ddot{\mathbf{r}} = \frac{\partial}{\partial \mathbf{r}} (U(\mathbf{r}, t))$ for the potential with just C_{00} , C_{20} , and C_{22} :

$$\ddot{\mathbf{r}} = -\frac{\mu}{r^3} \mathbf{r} + \mathbf{a}_{C_{20}} + \mathbf{a}_{C_{22}} \quad (2.27)$$

$$\mathbf{a}_{C_{20}} = \frac{3\mu C_{20} R^2}{2r^4} \left(\left(1 - 5(\hat{\mathbf{e}}_r \cdot \hat{\mathbf{a}}_3)^2\right) \hat{\mathbf{e}}_r + 2(\hat{\mathbf{e}}_r \cdot \hat{\mathbf{a}}_3) \hat{\mathbf{a}}_3 \right) \quad (2.28a)$$

$$\mathbf{a}_{C_{22}} = \frac{3\mu C_{22} R^2}{r^4} \left(-5 \left((\hat{\mathbf{e}}_r \cdot \hat{\mathbf{a}}_1)^2 - (\hat{\mathbf{e}}_r \cdot \hat{\mathbf{a}}_2)^2 \right) \hat{\mathbf{e}}_r + 2(\hat{\mathbf{e}}_r \cdot \hat{\mathbf{a}}_1) \hat{\mathbf{a}}_1 - 2(\hat{\mathbf{e}}_r \cdot \hat{\mathbf{a}}_2) \hat{\mathbf{a}}_2 \right) \quad (2.28b)$$

where $\hat{\mathbf{a}}_i$ denotes the i^{th} principal axis of the primary body. The C_{20} and C_{22} disturbances are particularly important for modeling spacecraft orbits around asteroids.

Large bodies like the Earth and Venus are very nearly symmetric about their axis of rotation. The gravitational potential of an axially symmetric body can be expressed in terms of the so-called *zonal* gravitational harmonics $J_l = -C_{l0}$ alone. These describe contributions to the gravitational potential that vary with latitude but not longitude. However, more accurate models of the Earth’s gravity field will include additional harmonics: the *sectoral* harmonics C_{ll} , which vary with longitude but not latitude, and the *tesseral* harmonic, which trace a “checkerboard” pattern with dependence on both latitude and longitude. For an excellent depiction of these three types of terms in the spherical harmonic expansion, see Reference 127. For Earth, the J_2 term, which accounts for the oblateness of the Earth, is particularly important, and is given by Eq. (2.28), where $J_2 = -C_{20}$.

The J_2 perturbation produces short-period variations in all orbit elements, but its primary effects are via the two secular variations induced, in the argument of periaapsis and R.A.A.N:

$$\frac{d\bar{\Omega}}{dt} = -\frac{3}{2}J_2 \left(\frac{R}{p}\right)^2 n \cos i \quad (2.29a)$$

$$\frac{d\bar{\omega}}{dt} = \frac{3}{4}J_2 \left(\frac{R}{p}\right)^2 n (5 \cos^2 i - 1) \quad (2.29b)$$

These two effects are respectively called the *regression of the node* and the *rotation of the line of apsides*. These combine to produce a precession of the angular momentum vector. This is illustrated in Figure 2.2, borrowed from Reference 127. Note that the magnitude of J_2 was increased by a factor of 20 to produce this figure.

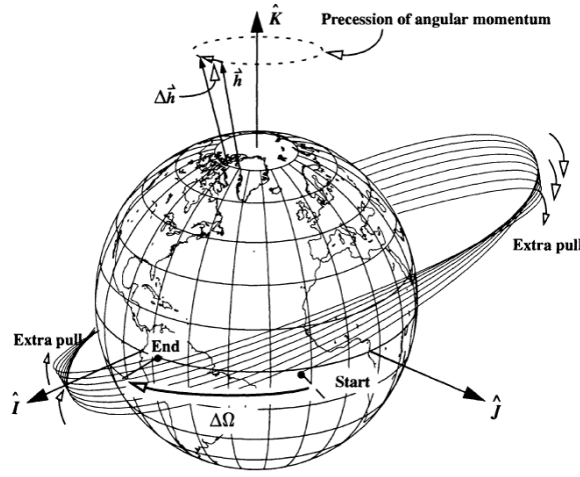


Figure 2.2: Orbital Effects of J_2 [127]

2.2.2.2 Third-body effects

For a third body, such as the sun, with position vector \mathbf{d} relative to the central body, the perturbing acceleration due to its gravity is given as the difference between the acceleration that the spacecraft feels and the acceleration that the nearby primary body feels, as below [114]:

$$\mathbf{a}_g = -\mu_s \left(\frac{(\mathbf{r} - \mathbf{d})}{\|\mathbf{r} - \mathbf{d}\|^3} + \frac{\mathbf{d}}{d^3} \right) \quad (2.30)$$

For orbits in the vicinity of small asteroids, this effect and the disturbance acceleration due to solar radiation pressure are quite important. Together, these two disturbances combine to compete with

the gravitational pull of the asteroid. In this dynamical system, terminator orbits are a natural stable periodic orbit that can arise. These orbits track the sun and are fixed in the asteroid's Hill frame. These will be discussed in [chapter 7](#).

2.2.2.3 Solar radiation pressure

The force due to solar radiation pressure on a general body surface element A_i is given below [\[91, 112\]](#):

$$\mathbf{F}_{S_i} = -P(R)H_i(\hat{\mathbf{u}})A_i \left[\left(\rho_i s_i \left(2\hat{\mathbf{n}}\hat{\mathbf{n}}^\top - [I_{3 \times 3}] \right) + [I_{3 \times 3}] \right) \hat{\mathbf{u}} (\hat{\mathbf{u}} \cdot \hat{\mathbf{n}}_i) + a_{2i} \hat{\mathbf{n}}_i (\hat{\mathbf{n}}_i \cdot \hat{\mathbf{u}}) \right] \quad (2.31)$$

with

$$P(R) \approx \frac{G_1}{R^2} \quad (2.32)$$

$$a_{2i} = B(1 - s_i)\rho_i + (1 - \rho_i)B \quad (2.33)$$

The function $P(R)$ is the solar radiation pressure at distance R , and G_1 is the solar radiation force constant at 1 AU. The specular and diffuse reflectivity coefficients are s_i and ρ_i , and B is the Lambertian scattering coefficient, $\hat{\mathbf{u}}$ is the unit vector to the sun, $\hat{\mathbf{n}}_i$ is the normal vector of the surface element, and $H(\hat{\mathbf{u}})$ is a visibility delta function, equal to 1 or 0, depending on whether or not the face is directly illuminated by sunlight. Neglecting secondary reflections, the total disturbance acceleration felt by a spacecraft will be simply the sum of all facet forces divided by the mass:

$$\mathbf{a}_S = \frac{1}{m} \sum_i \mathbf{F}_{S_i} \quad (2.34)$$

A common representation of SRP encountered in orbital simulations is the simple ‘‘cannonball’’ model, which neglects geometric characteristics of the spacecraft [\[80\]](#):

$$\mathbf{a}_S = -C_R \frac{A \Phi}{m c} \hat{\mathbf{u}} \quad (2.35)$$

where C_R is a radiation pressure coefficient, Φ is the solar flux, and c is the speed of light.

2.3 Perturbation Methods

Many of the problems facing mathematicians, physicists, and engineers include difficulties such as nonlinear governing equations and complex boundary conditions that preclude an exact solution from being found. In these situations, it is often beneficial to find an approximate solution to a problem. This is frequently accomplished by starting with the exact solution of a simpler related problem, and exploring the effects of the troubling terms order-by-order in a small parameter, hence the name “perturbation methods”. What is recovered is a “precise approximation” – an analytic approximation whose error is understood and controllable [58]. Perturbation methods have numerous applications in celestial mechanics, fluid mechanics, the theory of vibrations, quantum mechanics, and in other fields. Examples can be found in References 9, 58, 96, and 97. Note that the modern proliferation of numerical methods has not eliminated the usefulness of perturbation methods – indeed, the two practices are often complementary. Various examples of this complementary relationship can be found in References 9 and 58.

In this dissertation, the perturbed relative motion problem is often analyzed using perturbation methods, because the problem lacks an analytic solution. In particular, two methods are frequently used: (1) the straightforward perturbation expansion and (2) the Lindstedt-Poincaré method. A simple example quickly illustrates the application of these two methods. Consider the undamped, unforced weakly nonlinear Duffing equation given below:

$$\ddot{x} + x + \varepsilon x^3 = 0 \tag{2.36}$$

While this equation is not solvable in terms of standard analytic functions, there are some important insights that can be gained. First, there exists an energy integral for this system:

$$E = \frac{1}{2}\dot{x}^2 + \frac{1}{2}x^2 + \frac{1}{4}\varepsilon x^4 \tag{2.37}$$

Using conservation of energy, it can be shown that the maximum extension is:

$$|x| \leq \sqrt{\frac{-1 + \sqrt{1 + 4\varepsilon E}}{\varepsilon}} \tag{2.38}$$

Furthermore, the period of the oscillation is a function of the amplitude, and can be obtained as below in terms of the maximum extension \tilde{x} :

$$T = 2 \int_{-\tilde{x}}^{\tilde{x}} \frac{1}{\sqrt{2(E - F(x))}} dx \quad (2.39)$$

where $F(x) = \frac{1}{2}x^2 + \frac{1}{4}\varepsilon x^4$.

Consider the case $x(0) = 1$, $\dot{x}(0) = 0$. Examining Eq. (2.36), it is clear that as $\varepsilon \rightarrow 0$, the solution should behave like the unperturbed solution, $x(t) = \cos(t)$. With this in mind, a straightforward perturbation solution poses that the perturbed solution behaves as below:

$$x(t) = x_0(t) + \varepsilon x_1(t) + \varepsilon^2 x_2(t) + \dots \quad (2.40)$$

where $x_0(t) = \cos(t)$ is the unperturbed solution, and the small perturbation-induced deviations are sought. This is achieved by substituting Eq. (2.40) into Eq. (2.36), and isolating terms grouped by their order in ε , stopping after $\mathcal{O}(\varepsilon^2)$:

$$(\ddot{x}_0 + \varepsilon \ddot{x}_1 + \varepsilon^2 \ddot{x}_2) + x_0 + \varepsilon x_1 + \varepsilon^2 x_2 + \varepsilon (x_0^3 + 3\varepsilon x_0^2 x_1) = 0 \quad (2.41)$$

$$\mathcal{O}(\varepsilon^0) : \ddot{x}_0 + x_0 = 0 \quad (2.42a)$$

$$\mathcal{O}(\varepsilon^1) : \ddot{x}_1 + x_1 = -x_0^3 \quad (2.42b)$$

$$\mathcal{O}(\varepsilon^2) : \ddot{x}_2 + x_2 = -x_0^2 x_1 \quad (2.42c)$$

Solving Eq. (2.42) order-by-order, successively substituting, and specifying the constraints on the deviations $x_j(0) = \dot{x}_j(0) = 0$, $j \neq 0$, the following result is obtained:

$$\begin{aligned} x(t) \approx & \cos(t) + \frac{1}{32}\varepsilon (\cos(3t) - \cos(t) - 12t \sin(t)) \\ & + \frac{1}{1024}\varepsilon^2 ((23 - 72t^2) \cos(t) - 24 \cos(3t) + \cos(5t) + 96t \sin(t) - 36t \sin(3t)) \end{aligned} \quad (2.43)$$

There are three things worth noting from the perturbation solution in Eq. (2.43). First, the perturbation affects the frequency of the oscillation, as expected, and as seen by examining the first $\mathcal{O}(\varepsilon)$ term. Second, note that the corrective terms tend to become longer with higher order

in ε . This is a common characteristic of such solutions, and it is quite common to stop with the $\mathcal{O}(\varepsilon)$ correction. Third, note from Eqs. (2.38) and (2.39) that a bounded solution was expected, but there are *secular terms* in Eq. (2.43) – terms that grow without bound, and do not match the true physical behavior of the solution. These terms arise because the straightforward perturbation expansion doesn't have a mechanism for consideration of the frequency-amplitude relationship induced by the nonlinearity. Nonetheless, the approximation given by Eq. (2.43) remains valid for a finite time $t \in [0, 1/\varepsilon]$, dictated by the time for the secular corrective terms to grow too large. It is quite a common problem in perturbation theory to develop solutions that are only accurate for some limited timespan.

The Lindstedt-Poincaré method is specifically designed to remove non-physical secular terms. This method is limited to autonomous weakly nonlinear differential equations with bounded oscillatory solutions. In addition to expressing the solution as an asymptotic series, an alternate timescale with frequency ω is introduced, and the frequency itself is expanded:

$$\tau = \omega t \tag{2.44a}$$

$$x = x_0(\tau) + \varepsilon x_1(\tau) + \varepsilon^2 x_2(\tau) + \dots \tag{2.44b}$$

$$\omega = \omega_0 + \varepsilon \omega_1 + \varepsilon^2 \omega_2 + \dots \tag{2.44c}$$

Transforming Eq. (2.36) via the new independent variable τ , noting $(\)' = \frac{d}{d\tau}(\)$:

$$\omega^2 x'' + x + \varepsilon x^3 = 0 \tag{2.45}$$

Substituting Eq. (2.44) only to $\mathcal{O}(\varepsilon)$, noting $\omega_0 = 1$ from $x_0(t) = \cos(t)$:

$$(1 + 2\varepsilon\omega_1)(x_0'' + \varepsilon x_1) + x_0 + \varepsilon x_1 + \varepsilon x_0^3 = 0 \tag{2.46}$$

$$\mathcal{O}(\varepsilon^0) : x_0'' + x_0 = 0 \tag{2.47a}$$

$$\mathcal{O}(\varepsilon^1) : x_1'' + x_1 = -2\omega_1 x_0'' - x_0^3 \tag{2.47b}$$

Solving Eq. (2.47) and applying the initial conditions yields:

$$x_0 = \cos \tau \tag{2.48a}$$

$$x_1 = \frac{1}{32} (-\cos \tau + \cos 3\tau + 4(8\omega_1 - 3)\tau \sin \tau) \tag{2.48b}$$

From Eq. (2.48), the choice $\omega_1 = \frac{3}{8}$ eliminates the secular term. Thus, the solution, to first order in ε , is given below:

$$x(t) \approx \cos \left(\left(1 + \frac{3}{8}\varepsilon \right) t \right) + \frac{1}{32}\varepsilon \left(-\cos \left(\left(1 + \frac{3}{8}\varepsilon \right) t \right) + \cos \left(3 \left(1 + \frac{3}{8}\varepsilon \right) t \right) \right) \tag{2.49}$$

Note the slight change of the fundamental frequency induced by the nonlinear perturbation, and the secular term has been removed. The application of these techniques to the three-dimensional nonlinear perturbed relative motion problem is more complicated, but the fundamental principles discussed above remain relevant. One of the most important takeaways from this exercise is the systematically uniform treatment of expressions at various orders in the small parameters. It is critical that all terms linear in the perturbative term be accounted for, otherwise the accuracy of the approximation is compromised. There is also the additional challenge of having multiple small parameters of different scales. Other techniques and insights from perturbation theory are discussed as they appear in this dissertation.

2.4 Relative Motion Approximation

2.4.1 Fundamentals

The general orbit problem is a nonlinear dynamic problem of the following form:

$$\dot{\mathbf{X}} = \mathbf{f}_0(\mathbf{X}) + \sum_{i=1}^m \alpha_i \mathbf{f}_i(\mathbf{X}, t) \tag{2.50}$$

where \mathbf{X} is a 6-element state vector of augmented position and velocity vectors, or a set of orbit elements. The function \mathbf{f}_0 is the two-body component of the dynamics, and the $\alpha_i \mathbf{f}_i$ are perturbations with factored scaling terms α_i such that $\|\mathbf{f}_i\| \sim \|\mathbf{f}_0\|$, and typically $|\alpha_i| \ll 1$. This formulation explicitly considers the influence of m distinct perturbations. In the case of N bodies in neighboring orbits, their equations of motion are expressed by N independent nonlinear vector differential

equations of the form given by Eq. (2.50), and this is not a particularly useful or insightful arrangement. An alternative arrangement is obtained by linearizing about one of the orbits – one of the solutions $\mathbf{X}_c(t)$ to Eq. (2.50), and studying the dynamics of the deviation, $\delta\mathbf{X} = \mathbf{X} - \mathbf{X}_c$. For brevity, let $\mathbf{x} \equiv \delta\mathbf{X}$. Subtracting the dynamics and keeping only the terms linear in \mathbf{x} , we obtain a model valid for all spacecraft orbits in the vicinity of $\mathbf{X}_c(t)$ that are close enough to justify the linearization approximation:

$$\dot{\mathbf{x}} = \left(\left. \frac{d\mathbf{f}_0(\mathbf{X})}{d\mathbf{X}} \right|_{\mathbf{X}_c} + \sum_{i=1}^m \alpha_i \left. \frac{d\mathbf{f}_i(\mathbf{X}, t)}{d\mathbf{X}} \right|_{\mathbf{X}_c} \right) \mathbf{x} \quad (2.51)$$

The size and shape of the domain of validity of Eq. (2.51) is a consequence of the choice of coordinates used to parameterize \mathbf{X} . In the case that \mathbf{X} is given in terms of orbit elements, this domain can be quite large. The plant matrix in Eq. (2.51) can be computed numerically, but analytic approximations prove useful for control applications. In practice, if the chief orbit solution can be explicitly approximated to reasonable accuracy by the vector function $\tilde{\mathbf{X}}_c(t)$ for some timespan $t \in [t_0, t_u]$ and the $n \ll m$ dominant perturbations are identified, we obtain an approximation of the relative motion dynamics that is a function of only $\mathbf{X}_c(t_0)$ and the dominant terms in the Jacobian matrices in Eq. (2.51):

$$\dot{\mathbf{x}} = \left(\left. \frac{d\mathbf{f}_0(\mathbf{X})}{d\mathbf{X}} \right|_{\tilde{\mathbf{X}}_c} + \sum_{i=1}^n \alpha_i \left. \frac{d\mathbf{f}_i(\mathbf{X}, t)}{d\mathbf{X}} \right|_{\tilde{\mathbf{X}}_c} \right) \mathbf{x} = [A(\mathbf{X}_c(t_0), t)] \mathbf{x} \quad (2.52)$$

The result that is obtained is a linear time-varying approximation of the relative motion dynamics that requires no updates on knowledge of the chief orbit for the duration of time $t_u - t_0$ and can be used to study the relative motion dynamics of all spacecraft in the vicinity of the chief. In principal, this equation can also be solved (or approximately solved) analytically. In this work, that is typically done via a perturbation expansion [58, 96]. The resulting solution is a time-explicit or anomaly-explicit model of relative motion that is linear in the initial relative state \mathbf{x}_0 . This is a relative motion STM model of the form $\mathbf{x}(t) = [\Phi(t, t_0)]\mathbf{x}_0$, completely analogous to the STM model obtained by Clohessy and Wiltshire [36], but adapted for the specified perturbed problem. It is a very useful result to obtain, enabling rendezvous and relative motion control via impulsive

maneuvers in a manner that explicitly accounts for the influence of the dominant perturbations. If the perturbations exert significant effects in the time between impulsive maneuvers, then impulsive control strategies using Keplerian relative motion STMs can fail altogether.

The LTV equations given by Eq. (2.52) are still highly useful in and of themselves for linear formation control applications, by providing an analytic approximation of the relative motion plant matrix. Possible strategies include the commonly used Linear Quadratic Regulator (LQR), or an extension of LQR for which one uses Eq. (2.52) to derive develop dynamic equations for the system sensitivity to variations in important but uncertain dynamic parameters. Interestingly, the effect of uncertainty in the chief orbit itself can be compensated for in this way, because the initial chief orbit parameters appear in the plant matrix in Eq. (2.52). This is discussed with [chapter 5](#). In the case of SRP-perturbed relative motion, the resulting plant matrix is also useful for linear control using the differential SRP acceleration.

2.4.2 Local Cartesian Coordinates

Developing a linear dynamic approximation of the perturbed relative motion problem in local chief-centered Cartesian or spherical coordinates involves computing the differential accelerations induced by the two-body acceleration and the perturbation (the *kinetics* of the problem) and also computing the Coriolis and centripetal terms induced by the time-varying angular velocity of the perturbed LVLH frame (the *kinematics*). The governing equations for the general perturbed linear problem are given below [35]:

$$\dot{\mathbf{x}} = \begin{bmatrix} 0_{3 \times 3} & I_{3 \times 3} \\ \frac{\partial}{\partial \boldsymbol{\rho}} (\ddot{\mathbf{r}}_d - \ddot{\mathbf{r}}) - [\dot{\boldsymbol{\omega}}] - [\boldsymbol{\omega}] [\boldsymbol{\omega}] & -2[\boldsymbol{\omega}] + \frac{\partial}{\partial \boldsymbol{\rho}} (\ddot{\mathbf{r}}_d - \ddot{\mathbf{r}}) \end{bmatrix} \mathbf{x} \quad (2.53)$$

$$\boldsymbol{\omega} = \frac{r}{h} (\dot{\mathbf{r}} \cdot \hat{\mathbf{e}}_n) \hat{\mathbf{e}}_r + \frac{1}{r} (\dot{\mathbf{r}} \cdot \hat{\mathbf{e}}_t) \hat{\mathbf{e}}_n \quad (2.54)$$

$$\begin{aligned} \dot{\boldsymbol{\omega}} = & \frac{r}{h} \left(\frac{\dot{r}}{r} (\dot{\mathbf{r}} \cdot \hat{\mathbf{e}}_n) - 2 \frac{r}{h} (\ddot{\mathbf{r}} \cdot \hat{\mathbf{e}}_t) (\dot{\mathbf{r}} \cdot \hat{\mathbf{e}}_n) + (\ddot{\mathbf{r}} \cdot \hat{\mathbf{e}}_n) \right) \hat{\mathbf{e}}_r \\ & + \frac{1}{r} \left((\ddot{\mathbf{r}} \cdot \hat{\mathbf{e}}_t) - 2 \frac{\dot{r}}{r} (\dot{\mathbf{r}} \cdot \hat{\mathbf{e}}_t) \right) \hat{\mathbf{e}}_n \end{aligned} \quad (2.55)$$

where the tilde on a symbol denotes the transformation of its vector into the cross-product matrix, and all matrices appear in square brackets. Alternatively, the perturbed angular velocity can be expressed directly in terms of orbit element rates, and this is typically a simpler approach. This will be discussed more in [chapter 3](#).

Computing a perturbed relative motion state transition matrix from the above linear equations involves approximating the perturbed chief orbit using the perturbation methods discussed earlier. A stand-alone linear model that is only a function of the chief initial conditions and time must be developed. Then, the perturbed relative motion solution is modeled as a small deviation from the corresponding unperturbed problem. For example, for perturbed relative motion in the vicinity of a near-circular orbit, the relative motion model will be given as $\mathbf{x}(t) = \mathbf{x}_0(t) + \varepsilon \mathbf{x}_1(t)$, where $\mathbf{x}_0(t)$ is the Clohessy-Wiltshire solution, $\mathbf{x}_1(t)$ is a time-explicit perturbation-induced deviation, and ε is a small term from the perturbed dynamics.

2.4.3 Orbit Element Differences

As opposed to approximating the perturbed dynamics in local Cartesian coordinates, the perturbed dynamics in orbit element differences are more straightforward. These are obtained directly by linearizing the Lagrange planetary equations in their Gaussian form:

$$\dot{\mathbf{oe}} = \mathbf{f}(\mathbf{oe}, \mathbf{a}_p) \quad (2.56)$$

$$\delta \dot{\mathbf{oe}} = \left. \frac{d\mathbf{f}(\mathbf{oe}, \mathbf{a}_p)}{d\mathbf{oe}} \right|_{\mathbf{oe}_c} \delta \mathbf{oe} \quad (2.57)$$

Depending on the choice of orbit elements, at least 5 of the 6 elements in \mathbf{oe} are constant for the unperturbed problem. Noting that in many contexts, the perturbing acceleration is sub-dominant to the two-body dynamics, Eq. (2.56) can be rewritten:

$$\dot{\mathbf{oe}} = \mathbf{f}_0(\mathbf{oe}) + \varepsilon \mathbf{f}_1(\mathbf{oe}, \mathbf{a}_p) \quad (2.58)$$

Thus, Eq. (2.57) can also be rewritten:

$$\delta \dot{\mathbf{oe}} = \left(\left. \frac{d\mathbf{f}_0(\mathbf{oe})}{d\mathbf{oe}} \right|_{\mathbf{oe}_c} + \varepsilon \left. \frac{d\mathbf{f}_1(\mathbf{oe}, \mathbf{a}_p)}{d\mathbf{oe}} \right|_{\mathbf{oe}_c} \right) \delta \mathbf{oe} \quad (2.59)$$

The first matrix in the parentheses in Eq. (2.59) will be quite sparse, and the second matrix will be rather complex. In this context, averaging of the perturbed part of Eq. (2.59) is often used to simplify the analysis. A resulting relative motion solution in the orbit element differences would be of the form $\delta\mathbf{oe} = \delta\mathbf{oe}_0(t) + \varepsilon \delta\mathbf{oe}_1(t)$, where most of the elements in $\delta\mathbf{oe}_0$ will be stationary. This dissertation does not focus heavily on relative motion modeling with orbit element differences, but this approach and inspired ideas do appear in later chapters.

2.5 Linear Differential Equations, Reducibility, and Lyapunov-Floquet Theory

This dissertation makes extensive use of linear time-varying (LTV) differential equations, such as below:

$$\dot{\mathbf{x}} = [A(t)]\mathbf{x} \quad (2.60)$$

These are generally obtained by linearizing about an orbit or trajectory of interest, which is the fundamental generalization of the close-proximity spacecraft formation-flying problem. Not only are the linearized dynamics important for applications such as control and estimation, but in this dissertation, the solution of Eq. (2.60) is also of interest. In chapters 6 and 7, this dissertation explores the problem of efficiently representing the unperturbed and perturbed satellite relative motion problems. This is done by identifying a convenient basis of fundamental solutions $\boldsymbol{\xi}(t)$, for which the relative motion can be expressed as a linear sum $\mathbf{x}(t) = \sum_{i=1}^6 c_i \boldsymbol{\xi}_i(t)$, where the vector of constants $\mathbf{c} = (c_1, \dots, c_6)^\top$ is a function of the initial conditions \mathbf{x}_0 . Obtaining these fundamental solutions involves finding the solutions of Eq. (2.60), which is often challenging to do analytically for multidimensional LTV systems. Note that it can always be done numerically by integrating $[\dot{\Phi}(t, t_0)] = [A(t)][\Phi(t, t_0)]$ with initial condition $[\Phi(t_0, t_0)] = [I]$. In this case the fundamental solution matrix obtained is the state transition matrix, so $\boldsymbol{\xi}_i = \boldsymbol{\phi}_i$ and $\mathbf{c} = \mathbf{x}_0$. However, a systematic analytic means of obtaining fundamental solutions $\boldsymbol{\xi}_i(t)$ is obtained if Eq. (2.60) can be related via an analytic linear time-varying transformation to another set of coordinates with an LTI dynamic form. This enables the modal decomposition approach, to be discussed in chapters 6

and 7.

This section discusses the basics of the *reducibility* of Eq. (2.60) when the plant matrix $[A(t)]$ satisfies various properties, drawing mainly from References 105 and 119. An equation such as Eq. (2.60) is said to be *reducible* if there exists a linear time-varying, non-singular, and invertible change of variables $[P(t)]$ called the *Lyapunov-Perron* or *reducing* transformation satisfying the following:

$$\mathbf{x} = [P(t)]\mathbf{z} \quad (2.61)$$

$$\dot{\mathbf{z}} = [\Lambda]\mathbf{z} \quad (2.62)$$

where $[\Lambda]$ is a constant matrix. Whenever a system is reducible to a system with a constant plant matrix like Eq. (2.62), many properties of the system in \mathbf{z} (including growth/decay of the solutions and their boundedness) are retained in \mathbf{x} . In the context of reducibility, only three particular cases of the temporal variations in $[A(t)]$ are relevant to this dissertation: (1) the plant matrix is periodic, (2) the plant matrix is quasi-periodic, and (3) the plant matrix is almost-periodic, such that there exists some time T for which $[A(t)] \approx [A(t + T)]$ to some satisfactorily small error. Each of these cases will now be introduced and discussed.

In the case that the plant matrix is periodic $[A(t)] = [A(t + T)]$, Lyapunov-Floquet theory applies. To motivate this discussion, consider the following identity with the state transition matrix for the system with periodic plant matrix with period T :

$$[\Phi(t + T, t_0)] = [\Phi(t + T, t_0 + T)][\Phi(t_0 + T, t_0)] = [\Phi(t, t_0)][\Phi(t_0 + T, t_0)] \quad (2.63)$$

The constant matrix $[\Phi(t_0 + T, t_0)]$ is referred to as the monodromy matrix. This matrix encodes the stability of the linearized motion. In particular, any eigenvalues less than unit norm are “stable” (corresponding to convergent modal motion), any outside are “unstable” (corresponding to modal motion that departs from the origin), and any of unit norm correspond to oscillatory modes. The monodromy matrix can be written as below:

$$[\Phi(t_0 + T, t_0)] = [P_0]e^{[\Lambda]T}[P_0]^{-1} \quad (2.64)$$

where $[\Lambda]$ is a constant matrix and $[P_0]$ is constant and invertible. Rewriting Eq. (2.63) using Eq. (2.64):

$$[\Phi(t+T, t_0)] = [\Phi(t, t_0)][P_0]e^{[\Lambda]T}[P_0]^{-1} \quad (2.65)$$

Now, the matrix $[P(t)]$ is defined as below:

$$[P(t)] = [\Phi(t, t_0)][P_0]e^{-[\Lambda](t-t_0)} \quad (2.66)$$

Evaluating Eq. (2.66) at t_0 yields $[P(t_0)] = [P_0]$. Additionally, Eq. (2.66) can be shown to be T -periodic by expanding and using Eqs. (2.63) - (2.65). Inverting this expression leads to a traditional general definition of Floquet theory:

$$[\Phi(t, t_0)] = [P(t)]e^{[\Lambda](t-t_0)}[P(t_0)]^{-1} \quad (2.67)$$

Lyapunov's extension of Floquet theory directly relates the system with linear time-periodic plant matrix to a system that is LTI via the periodic transformation $[P(t+T)] = [P(t)]$:

$$\mathbf{x} = [P(t)]\mathbf{z} \quad (2.68)$$

$$\dot{\mathbf{z}} = [\Lambda]\mathbf{z} \quad (2.69)$$

The Lyapunov-Floquet (LF) transformation and the LTI matrix are any pair of matrices $[P(t)]$, $[\Lambda]$ satisfying the following matrix differential equation, which can be obtained using Eqs. (2.60), (2.68), and (2.69):

$$[P(t)]^{-1} \left([A(t)][P(t)] - [\dot{P}(t)] \right) = [\Lambda] \quad (2.70)$$

In analytically solving this equation, which can be challenging, one seeks periodic solutions for the individual elements of $[P(t)]$ while also requiring the elements of $[\Lambda]$ to be constant. In practice, the periodicity conditions for all non-trivial elements of $[P(t)]$ constrain the admissible forms of $[\Lambda]$, but still allow for variations in the values of elements in $[\Lambda]$ depending on the form of $[P(t_0)]$. As a result, there can be more than a single pair of matrices satisfying Eq. (2.70). However, a unique definition of the LF transformation is given below using the monodromy matrix. This

transformation conveniently equals identity at the epoch time:

$$[P(t)] = [\Phi(t, t_0)]e^{-[\Lambda](t-t_0)} \quad (2.71)$$

$$[P(t_0)] = [P(t_0 + kT)] = [I] \quad (2.72)$$

$$[\Lambda] = \frac{1}{T} \ln (\Phi(t_0 + T, t_0)) \quad (2.73)$$

This definition will be used frequently in chapters 6 and 7 with the modal decomposition and with other related analysis. The modal decomposition explores factoring the relative motion in \boldsymbol{x} in terms of a linear sum of the transformed individual stable, oscillatory, and unstable modes from \boldsymbol{z} .

Given the above definitions for the case that $[A(t)] = [A(t + T)]$, it is natural to ask if reducibility can be obtained for other conditions. Consider for example the case that $[A(t)]$ is quasi-periodic. In other words, $[A(t)]$ is characterized by d distinct frequencies in the frequency vector $\boldsymbol{\omega}$:

$$[A(t)] = [A(\boldsymbol{\omega}t + \boldsymbol{\phi})] \quad (2.74)$$

Significant work has been done in studying the general reducibility of such a linear problem, or constrained versions of it. See e.g. References 105 or 66. For tractable reducibility of $[A(t)]$, these works typically require that, among other things, the frequency vector satisfies a non-resonance or *diophantine* condition. The reducibility of the system is still not trivial when this is satisfied – i.e., computing the transformation $[P(t)]$ is quite challenging. To illustrate the depth of difficulty, note that even the reducibility of the scalar system $\dot{x} = a(t)x$ for quasi-periodic scalar $a(t)$ is not trivial.

With the above challenges in mind, this dissertation includes some work about the perturbative application of standard Lyapunov-Floquet theory to the fairly general case that $[A(t)]$ is almost periodic. In particular, there exists some T such that $[A(t)] \approx [A(t + T)]$ to some satisfactory level. This can be accomplished with quasi-periodic systems when one of the frequencies $\omega_i \in \boldsymbol{\omega}$ is much more important to the behavior of $[A(t)]$ than the others. However, it extends beyond this to more general variations in $[A(t)]$. This is discussed some more in chapter 7, which includes basic analysis of the applicability of modes computed for a similar system with plant matrix

$[\bar{A}(t)] = [\bar{A}(t + T)] = [A(t)] - [\delta A(t)]$, where $[\delta A(t)]$ is a sub-dominant matrix perturbation. The matrix $[\bar{A}(t)]$ can be achieved by Fourier fit of $[A(t)]$ with prudent choice of T , or can additionally be computed simply by omission of higher-order terms in $[A(t)]$, as in References 78 and 24, for example.

Chapter 3

Spacecraft Relative Motion Modeling

This chapter discusses some of the foundational work in this dissertation: Approximating the perturbed spacecraft relative motion problem in a manner that is computationally efficient for onboard operations, but sufficiently accurate for various practical uses. This chapter applies the fundamentals of perturbed relative motion dynamics discussed in [chapter 2](#). First is an in-detail application to the J_2 -perturbed relative motion problem. Some results are shown to demonstrate that the model obtained is quite accurate, even in the context of the many other models obtained for this popular relative motion problem. Then, a similarly obtained model for C_{20} , C_{22} , and solar radiation pressure (SRP) perturbed relative motion is discussed. The derivation of the C_{20} and C_{22} perturbative terms is shown. The SRP perturbative terms are discussed more thoroughly in [chapter 4](#), which studies SRP-perturbed relative motion and SRP-based spacecraft relative motion control in great detail. This model is used to illustrate the benefit of the relative motion approximation procedure for analysis. This method and these models appear repeatedly later in the dissertation, hence their early presentation. Note that much of the work in this chapter also appears in [References 18, 17, and 24, and 25](#).

3.1 Modeling J_2 -Perturbed Relative Motion

As discussed in [chapter 2](#), the gravitational effect of the Earth's oblateness (captured primarily by the J_2 zonal harmonic) is one of the dominant perturbations in low-Earth orbit. Under the action of this perturbation, the analytically elegant predictions of spacecraft relative motion under

Keplerian dynamics lose their validity on long timespans. In particular, drifting of the relative motion becomes a greater problem, and the initial conditions for bounded relative orbits must be modified from the Keplerian case [110]. Additionally, the shape of the relative motion is affected, and the frequency of the relative orbits is altered slightly. For formation flying mission architectures demanding long durations between maneuvers, or requiring very high precision in controlled relative motion, the effects of J_2 must be considered.

This first section explores the application of the methodology discussed in [chapter 2](#) to model the spacecraft relative motion in local Cartesian coordinates with a time-explicit linear model that incorporates the effects of the J_2 perturbation on both the kinetics and kinematics of relative motion. The model is derived to consider near-circular orbits, because the majority of orbits in the J_2 -perturbed LEO region are near-circular. This thus produces a model that is the first-order J_2 -corrected version of the Clohessy-Wiltshire solution. The model is derived in detail, then validated with an application to modeling relative motion in Earth orbits. The results are compared to other models in literature. Additionally, some demonstrations with fictitiously large J_2 and J_3 coefficients illustrate the geometric effects of these perturbations and the power of the relative motion state transition matrix (STM) approximation method to describe the resulting motion efficiently.

3.1.1 Derivation of Base Model

To obtain a linearized relative motion model in terms of the relative position $\Delta \mathbf{r} = \mathbf{r}_d - \mathbf{r}_c = x\hat{\mathbf{e}}_r + y\hat{\mathbf{e}}_t + z\hat{\mathbf{e}}_n$, the procedure is to subtract and linearize the perturbed orbital dynamics of the chief and deputy (the *kinetics* of the problem), and resolve the differential dynamics into the perturbed LVLH frame centered on the chief spacecraft (the *kinematics*). The resulting system of approximate linear differential equations is then solved explicitly.

The kinetics of the problem are straightforward, obtained by linearizing the differential two-body and J_2 -perturbed acceleration, $\Delta \ddot{\mathbf{r}} = \mathbf{a}(\mathbf{r}_d) - \mathbf{a}(\mathbf{r}_c)$, where $\mathbf{r}_d = \mathbf{r}_c + \Delta \mathbf{r}$. The linearized differential accelerations are presented in a compact form below for conciseness, but will later be

expressed in LVLH frame components:

$$\begin{aligned} \Delta \ddot{\mathbf{r}} = & -\frac{\mu}{r^3} \left([I_{3 \times 3}] - 3\hat{\mathbf{r}}\hat{\mathbf{r}}^\top \right) \Delta \mathbf{r} - \frac{3\mu J_2 R^2}{2r^5} \left\{ \left[\left(1 - 5(\hat{\mathbf{a}}_3 \cdot \hat{\mathbf{r}})^2 \right) [I_{3 \times 3}] \right. \right. \\ & + 2\hat{\mathbf{a}}_3\hat{\mathbf{a}}_3^\top + 5 \left(7(\hat{\mathbf{a}}_3 \cdot \hat{\mathbf{r}})^2 - 1 \right) \hat{\mathbf{r}}\hat{\mathbf{r}}^\top \\ & \left. \left. - 10(\hat{\mathbf{a}}_3 \cdot \hat{\mathbf{r}}) \left(\hat{\mathbf{a}}_3\hat{\mathbf{r}}^\top + \hat{\mathbf{r}}\hat{\mathbf{a}}_3^\top \right) \right] \Delta \mathbf{r} \right\} \end{aligned} \quad (3.1)$$

where $\hat{\mathbf{a}}_3$ is the polar axis, $\hat{\mathbf{r}}$ is the chief orbit radial unit vector, and R is the planetary equatorial radius.

To treat the kinematics, the inertial differential acceleration is first equated with the acceleration in the LVLH frame, plus transport terms, because the LVLH frame rotates with angular velocity $\boldsymbol{\omega}_H$:

$$\Delta \ddot{\mathbf{r}} = \frac{H_d^2 \Delta \mathbf{r}}{dt^2} + \dot{\boldsymbol{\omega}}_H \times \Delta \mathbf{r} + 2\boldsymbol{\omega}_H \times \frac{H_d \Delta \mathbf{r}}{dt} + \boldsymbol{\omega}_H \times (\boldsymbol{\omega}_H \times \Delta \mathbf{r}) \quad (3.2)$$

The perturbed angular velocity is defined in a hybrid coordinate system in terms of the rates of change of the orbit element angles [35]:

$$\boldsymbol{\omega}_H = \dot{\Omega} \hat{\mathbf{a}}_3 + \dot{i} \frac{\hat{\mathbf{a}}_3 \times \hat{\mathbf{e}}_n}{\|\hat{\mathbf{a}}_3 \times \hat{\mathbf{e}}_n\|} + \dot{\theta} \hat{\mathbf{e}}_n \quad (3.3)$$

An alternate but fundamentally equivalent expression is given below, illustrating the fundamental geometric constraint $\boldsymbol{\omega}_H \cdot \hat{\mathbf{e}}_t = 0$ [35, 76]:

$$\boldsymbol{\omega}_H = (\dot{\Omega} \sin i \sin \theta + \dot{i} \cos \theta) \hat{\mathbf{e}}_r + (\dot{\theta} + \dot{\Omega} \cos i) \hat{\mathbf{e}}_n \quad (3.4)$$

Successful treatment of the kinematics requires a careful accounting of all first-order J_2 effects in the right-hand side of Eq. (3.2). This requires the perturbed orbit element rates $\dot{\Omega}$, \dot{i} , and $\dot{\theta}$, and will be shown to also require approximation of the J_2 -perturbed variations in r . The derivation starts with the angular rates $\dot{\Omega}$ and \dot{i} , which are given below in terms of the perturbing acceleration [8], along with the J_2 perturbing acceleration in LVLH radial, transverse, and orbit-normal components.

$$\dot{\Omega} = \frac{r \sin \theta}{h \sin i} N_{J_2} \quad (3.5a)$$

$$\dot{i} = \frac{r \cos \theta}{h} N_{J_2} \quad (3.5b)$$

$$\mathbf{a}_{J_2} = R_{J_2} \hat{\mathbf{e}}_r + T_{J_2} \hat{\mathbf{e}}_t + N_{J_2} \hat{\mathbf{e}}_n \quad (3.6)$$

$$R_{J_2} = - \frac{3\mu J_2 R^2}{2r^4} (1 - 3 \sin^2 i \sin^2 \theta) \quad (3.7a)$$

$$T_{J_2} = - \frac{3\mu J_2 R^2}{2r^4} (2 \sin^2 i \sin \theta \cos \theta) \quad (3.7b)$$

$$N_{J_2} = - \frac{3\mu J_2 R^2}{2r^4} (2 \sin i \cos i \sin \theta) \quad (3.7c)$$

Substituting N_{J_2} into equation 3.5, the following is obtained:

$$\dot{\Omega} = - \frac{3\mu J_2 R^2}{hr^3} \cos i \sin^2 \theta \quad (3.8a)$$

$$\dot{i} = - \frac{3\mu J_2 R^2}{4hr^3} \sin 2i \sin 2\theta \quad (3.8b)$$

Now, the angular rate $\dot{\theta}$ is obtained. First, Eq. (3.4) indicates the following:

$$\dot{\theta} = \omega_n - \dot{\Omega} \cos i \quad (3.9)$$

where ω_n is the instantaneous orbit-normal component of the angular velocity. An estimate for this term can be obtained starting with the radial component of Newton's second law in spherical coordinates:

$$\ddot{r} - \omega_n^2 r = -\frac{\mu}{r^2} + R_{J_2} \quad (3.10)$$

Isolating ω_n and factoring and binomial-expanding the square root of the other terms, the following is obtained:

$$\omega_n \approx n\rho^{-3/2} \left(1 - \frac{\rho^3}{2rn^2} R_{J_2} + \frac{\rho^3 \ddot{r}}{2rn^2} \right) \quad (3.11)$$

where $\rho = r/a$. The last term exerts a small influence for near-circular orbits and is neglected.

Then, substituting Eq. (3.7) into Eq. (3.11):

$$\omega_n = n\rho^{-3/2} \left(1 + \frac{3}{4} J_2 \left(\frac{R}{r} \right)^2 (1 - 3 \sin^2 i \sin^2 \theta) \right) \quad (3.12)$$

Then an approximation for $\dot{\theta}$ is given by Eqs. (3.12), (3.9) and (3.8). For now, the model is derived making the pure circular orbit assumption $r \approx a$, as is done in the Clohessy-Wiltshire derivation.

Later, an improvement on this model will be introduced, accounting for small radial variations induced by two-body gravity and J_2 – demonstrating a more correct approach. This exercise illustrates the importance of correctly capturing all first-order perturbative terms.

In LVLH components, Eq. 3.2 becomes:

$$\begin{aligned} \Delta \ddot{\mathbf{r}} = & (\ddot{x} - \dot{\omega}_n y - 2\omega_n \dot{y} - \omega_n^2 x + \omega_n \omega_r z) \hat{\mathbf{e}}_r \\ & + (\ddot{y} + \dot{\omega}_n x + 2\omega_n \dot{x} - (\omega_n^2 + \omega_r^2) y - \dot{\omega}_r z - 2\omega_r \dot{z}) \hat{\mathbf{e}}_t \\ & + (\ddot{z} + \omega_n \omega_r x + \dot{\omega}_r y + 2\omega_r \dot{y} - \omega_r^2 z) \hat{\mathbf{e}}_n \end{aligned} \quad (3.13)$$

where $\omega_r = \dot{\Omega} \frac{\sin i}{\sin \theta} = \frac{r}{h} N_{J_2}$, $\omega_t = 0$, and ω_n was given previously. At this point, it is necessary to resolve Eq. (3.1) in LVLH components, noting the following:

$${}^H \hat{\mathbf{r}} = \begin{pmatrix} r \\ 0 \\ 0 \end{pmatrix} \quad (3.14)$$

$${}^H \hat{\mathbf{a}}_3 = \begin{pmatrix} \sin \theta \sin i \\ \cos \theta \sin i \\ \cos i \end{pmatrix} \quad (3.15)$$

Eq. (3.1) is now resolved in LVLH frame components and expressed in a matrix-vector form as

$$\Delta \ddot{\mathbf{r}} = \Delta \ddot{\mathbf{r}}_{J_0} + \Delta \ddot{\mathbf{r}}_{J_2}:$$

$$\Delta \ddot{\mathbf{r}}_{J_0} = \frac{\mu}{r^3} \begin{pmatrix} 2x \\ -y \\ -z \end{pmatrix} \quad (3.16)$$

$$\Delta \ddot{\mathbf{r}}_{J_2} = \frac{-\mu J_2 R^2}{r^5} \begin{bmatrix} O_{11} & O_{12} & O_{13} \\ O_{21} & O_{22} & O_{23} \\ O_{31} & O_{32} & O_{33} \end{bmatrix} \begin{pmatrix} x \\ y \\ z \end{pmatrix} \quad (3.17)$$

where $O_{ij} = O_{ji}$ with all unique elements defined in Table 3.1. At this point, all components are needed for constructing the base linear model. Eqs. (4.32) and (3.17) are used with Eq. (3.13), with all angular velocity terms given previously. To first order in J_2 , assuming $r \approx a$, $\dot{a} \approx 0$ and

Table 3.1: Unique O Matrix Terms in Eq. 3.17, $O_{ij} = O_{ji}$

$O_{11} = -6 + 9 \sin^2 i (1 - \cos 2\theta)$	$O_{12} = -6 \sin^2 i \sin 2\theta$
$O_{13} = -6 \sin 2i \sin \theta$	$O_{22} = \frac{3}{2} - \frac{\sin^2 i}{4} (9 - 21 \cos 2\theta)$
$O_{23} = \frac{3}{2} \sin 2i \cos \theta$	$O_{33} = \frac{3}{2} + 3 \cos^2 i - \frac{15}{2} \sin^2 \theta \sin^2 i$

$\dot{e} \approx 0$, it can be shown that the only nonzero angular acceleration term is $\dot{\omega}_r$, given below with a the nonzero angular velocity squared terms:

$$\dot{\omega}_r = n \frac{\sin i}{\sin \theta} \left(\frac{d}{d\theta} (\dot{\Omega}) - \dot{\Omega} \frac{\cos \theta}{\sin \theta} \right) \quad (3.18)$$

$$\omega_n \omega_r = n \rho^{-3/2} \dot{\Omega} \frac{\sin i}{\sin \theta} \quad (3.19)$$

$$\omega_n^2 = n^2 \rho^{-3} \left(1 + \frac{3}{2} J_2 \left(\frac{R}{r} \right)^2 (1 - 3 \sin^2 i \sin^2 \theta) \right) \quad (3.20)$$

For deriving the base model, the circular orbit assumptions $r \approx a$, $\rho = r/a = 1$, and $e = 0$ are substituted everywhere. The effect of J_2 is still incorporated in the perturbed angular velocity and in the differential acceleration, but its effect on the orbit radius is ignored for now. After applying the necessary substitutions into Eq. (3.13) and collecting the small dimensionless scaling parameter $\alpha = J_2 \left(\frac{R}{a} \right)^2$, the linear model is given below in matrix-vector form:

$$\begin{pmatrix} \ddot{x} \\ \ddot{y} \\ \ddot{z} \end{pmatrix} = n^2 \begin{bmatrix} Q_{11} & Q_{12} & Q_{13} \\ Q_{21} & Q_{22} & Q_{23} \\ Q_{31} & Q_{32} & Q_{33} \end{bmatrix} \begin{pmatrix} x \\ y \\ z \end{pmatrix} + \begin{bmatrix} 0 & 2\omega_n & 0 \\ -2\omega_n & 0 & 2\omega_r \\ 0 & -2\omega_r & 0 \end{bmatrix} \begin{pmatrix} \dot{x} \\ \dot{y} \\ \dot{z} \end{pmatrix} \quad (3.21)$$

The terms in the Q matrix are given below, followed by the angular velocity terms ω_n and ω_r .

$$Q_{11} = 3 + \frac{15}{2}\alpha (1 - 3 \sin^2 i \sin^2 \theta) \quad (3.22a)$$

$$Q_{12} = 6\alpha \sin^2 i \sin 2\theta \quad (3.22b)$$

$$Q_{13} = 15\alpha \cos i \sin i \sin \theta \quad (3.22c)$$

$$Q_{21} = Q_{12} \quad (3.22d)$$

$$Q_{22} = -3\alpha \cos 2\theta \sin^2 i \quad (3.22e)$$

$$Q_{23} = -6\alpha \cos i \sin i \cos \theta \quad (3.22f)$$

$$Q_{31} = Q_{13} \quad (3.22g)$$

$$Q_{32} = 0 \quad (3.22h)$$

$$Q_{33} = -1 + \frac{3}{2}\alpha (5 \sin^2 i \sin^2 \theta - 2 \cos^2 i - 1) \quad (3.22i)$$

$$(3.22j)$$

$$\omega_n = n \left(1 + \frac{3}{4}\alpha (1 - 3 \sin^2 i \sin^2 \theta) \right) \quad (3.23)$$

$$\omega_r = -3\alpha n \cos i \sin i \sin \theta \quad (3.24)$$

3.1.1.1 Deriving a Perturbed Relative Motion STM

A time-explicit solution is obtained, via straightforward perturbation expansion [96], after converting to a non-dimensional form of the model for the case of near-circular orbits. The difference between the dimensional and non-dimensional forms is simple. First, all variables with distance units are divided by the chief semimajor axis. The normalized time is $\tau = nt$, so the time derivative transformation is $\frac{d}{dt}(\cdot) = n \frac{d}{d\tau}(\cdot)$, where differentiation with respect to normalized time is represented by $(\cdot)'$. Thus, normalized velocity terms are obtained via division by the mean motion n . Finally, the model should be rearranged into a form separating the linear J_2 perturbations (constituting

F_1) from the dimensionless Clohessy-Wiltshire (CW) ODE equations:

$$\begin{pmatrix} x'' - 2y' - 3x \\ y'' + 2x' \\ z'' + z \end{pmatrix} = F_1(\tau, x, y, z, x', y', z', \alpha) \quad (3.25)$$

The solutions to the dimensionless $\mathcal{O}(\alpha)$ equations can be found efficiently using symbolic software to evaluate the following inverse Laplace transform:

$$\begin{pmatrix} x_2(\tau) \\ y_2(\tau) \\ z_2(\tau) \end{pmatrix} = \mathcal{L}^{-1} \left(\begin{bmatrix} s^2 - 3 & -2s & 0 \\ 2s & s^2 & 0 \\ 0 & 0 & s^2 + 1 \end{bmatrix}^{-1} \mathcal{L}(F_1(\tau)) \right) \quad (3.26)$$

where the inverted matrix is the transfer matrix of the CW system and $F_1(\tau)$ is obtained by substituting the normalized CW solution (3.27) into the right side of Eq. (3.25). The resulting perturbation solution to Eq. (3.25) is the sum of Eq. (3.27) and the corrective terms in Eqs. (3.28) - (3.30), where $\tau - \tau_n$ is the normalized time since node crossing.

$$\begin{aligned} x_1(\tau) &= 4x_0 + 2y'_0 - (3x_0 + 2y'_0) \cos \tau + x'_0 \sin \tau \\ y_1(\tau) &= -3\tau (2x_0 + y'_0) - 2x'_0 + y_0 + 2x'_0 \cos \tau + 2(3x_0 + 2y'_0) \sin \tau \\ z_1(\tau) &= z_0 \cos \tau + z'_0 \sin \tau \end{aligned} \quad (3.27)$$

$$\begin{aligned} x_\alpha(\tau) &= \frac{1}{64} \alpha \left((768 - 1152 \sin^2 i) x_0 + (288 - 432 \sin^2 i) y'_0 + 24 (3 \sin^2 i - 2) (16x_0 + x'_0 \tau + 6y'_0) \cos \tau \right. \\ &\quad - 12 \sin^2 i (41x_0 + x'_0 \tau + 20y'_0) \cos(\tau - 2\tau_n) + 37 \sin^2 i (3x_0 + 2y'_0) \cos(3\tau - 2\tau_n) \\ &\quad - 96 \cos i \sin iz'_0 \cos(\tau - \tau_n) + 80 \sin^2 i (2x_0 + y'_0) \cos(2(\tau - \tau_n)) + 32 \cos i \sin iz'_0 \cos(2\tau - \tau_n) \\ &\quad + 96 \cos i \sin iz'_0 \cos \tau_n + 160 \sin^2 i (3x_0 + y'_0) \cos 2\tau_n - 32 \cos i \sin iz'_0 \cos(\tau + \tau_n) \\ &\quad - 37 \sin^2 i (7x_0 + 2y'_0) \cos(\tau + 2\tau_n) + 24 (3 \sin^2 i - 2) (3x_0 \tau - x'_0 + 2y'_0 \tau) \sin \tau \\ &\quad + 12 \sin^2 i (3x_0 \tau - 12x'_0 + 2y'_0 \tau) \sin(\tau - 2\tau_n) - 37 \sin^2 i x'_0 \sin(3\tau - 2\tau_n) \\ &\quad - 384 \cos i \sin iz_0 \sin(\tau - \tau_n) + 64 \sin^2 i (2x'_0 - y_0 + 3\tau (2x_0 + y'_0)) \sin(2(\tau - \tau_n)) \\ &\quad - 32 \cos i \sin iz_0 \sin(2\tau - \tau_n) - 864 \cos i \sin iz_0 \sin \tau_n - 64 \sin^2 i (x'_0 + 3y_0) \sin 2\tau_n \\ &\quad \left. + 448 \cos i \sin iz_0 \sin(\tau + \tau_n) + \sin^2 i (11x'_0 + 128y_0) \sin(\tau + 2\tau_n) \right) \end{aligned} \quad (3.28)$$

$$\begin{aligned}
y_\alpha(\tau) = & \frac{1}{32} \alpha \left(-912\tau x_0 + 1368 \sin^2 i \tau x_0 - 144x'_0 + 216 \sin^2 i x'_0 - 384\tau y'_0 + 576 \sin^2 i \tau y'_0 \right. \\
& + 24(-2 + 3 \sin^2 i)(3\tau x_0 - 3x'_0 + 2\tau y'_0) \cos \tau + 12 \sin^2 i(3\tau x_0 - 8x'_0 + 2\tau y'_0) \cos(\tau - 2\tau_n) \\
& + 13 \sin^2 i x'_0 \cos(3\tau - 2\tau_n) - 384 \cos i \sin i z_0 \cos(\tau - \tau_n) \\
& + 8 \sin^2 i(2x'_0 - y_0 + 3\tau(2x_0 + y'_0)) \cos(2(\tau - \tau_n)) \\
& + 32 \cos i \sin i z_0 \cos(2\tau - \tau_n) - 96 \cos i \sin i(z_0 + 2\tau z'_0) \cos \tau_n \\
& - 8 \sin^2 i(-7x'_0 + 15y_0 + 15\tau(3x_0 + y'_0)) \cos(2\tau_n) \\
& + 448 \cos i \sin i z_0 \cos(\tau + \tau_n) + \sin^2 i(11x'_0 + 128y_0) \cos(\tau + 2\tau_n) \\
& - 24(-2 + 3 \sin^2 i)(22x_0 + \tau x'_0 + 10y'_0) \sin \tau + 12 \sin^2 i(29x_0 + \tau x'_0 + 12y'_0) \sin(\tau - 2\tau_n) \\
& + 13 \sin^2 i(3x_0 + 2y'_0) \sin(3\tau - 2\tau_n) + 96 \cos i \sin i z'_0 \sin(\tau - \tau_n) \\
& - 112 \sin^2 i(2x_0 + y'_0) \sin(2(\tau - \tau_n)) + 32 \cos i \sin i z'_0 \sin(2\tau - \tau_n) + 96 \cos i \sin i(8\tau z_0 + z'_0) \sin \tau_n \\
& - 16 \sin^2 i(6x_0 - 3\tau(x'_0 + 3y_0) + y'_0) \sin(2\tau_n) \\
& \left. + 32 \cos i \sin i z'_0 \sin(\tau + \tau_n) + 37 \sin^2 i(7x_0 + 2y'_0) \sin(\tau + 2\tau_n) \right)
\end{aligned} \tag{3.29}$$

$$\begin{aligned}
z_\alpha(\tau) = & \frac{1}{64} \alpha \left(24(2 + 4 \cos^2 i - 5 \sin^2 i) \tau z'_0 \cos \tau - 60 \sin^2 i(z_0 + \tau z'_0) \cos(\tau - 2\tau_n) + 15 \sin^2 i z_0 \cos(3\tau - 2\tau_n) \right. \\
& - 96 \cos i \sin i(x'_0 + 4\tau(2x_0 + y'_0)) \cos(\tau - \tau_n) + 32 \cos i \sin i x'_0 \cos(2\tau - \tau_n) + 96 \cos i \sin i x'_0 \cos \tau_n \\
& - 32 \cos i \sin i x'_0 \cos(\tau + \tau_n) + 45 \sin^2 i z_0 \cos(\tau + 2\tau_n) - 24(2 + 4 \cos^2 i - 5 \sin^2 i)(\tau z_0 + z'_0) \sin \tau \\
& - 60 \sin^2 i \tau z_0 \sin(\tau - 2\tau_n) + 15 \sin^2 i z'_0 \sin(3\tau - 2\tau_n) + 192 \cos i \sin i(2x_0 + y'_0) \sin(\tau - \tau_n) \\
& + 32 \cos i \sin i(3x_0 + 2y'_0) \sin(2\tau - \tau_n) + 96 \cos i \sin i(3x_0 + 2y'_0) \sin \tau_n \\
& \left. + 64 \cos i \sin i(3x_0 + y'_0) \sin(\tau + \tau_n) + 15 \sin^2 i z'_0 \sin(\tau + 2\tau_n) \right)
\end{aligned} \tag{3.30}$$

The position components of the J_2 -perturbed relative motion solution are given as a linear correction on the position components of the CW solution:

$$\begin{pmatrix} x(\tau) \\ y(\tau) \\ z(\tau) \end{pmatrix} = \begin{pmatrix} x_1(\tau) \\ y_1(\tau) \\ z_1(\tau) \end{pmatrix} + \begin{pmatrix} x_\alpha(\tau) \\ y_\alpha(\tau) \\ z_\alpha(\tau) \end{pmatrix} \tag{3.31}$$

where the first term on the right is the normalized CW solution and the second term is the $\mathcal{O}(\alpha)$ J_2 correction. Note that both of these terms are linear functions of the relative state, so an STM model can be easily obtained by differentiation of the position component equations, then factorization of the 6 state equations:

$$\mathbf{x}(\tau) = \left([\Phi_{\text{CW}}(\tau)] + [\delta\Phi_{J_2}(\tau, \tau_n)] \right) \mathbf{x}(0) \tag{3.32}$$

The resulting solution is valid for the J_2 -perturbed relative motion problem in the vicinity of a near-circular chief orbit. However, there are some additional strategies that can be applied to this base solution to improve its performance.

3.1.2 Solution Improvement by Calibration

Previous work by Sinclair [122, 121] introduced a technique called *calibration*: using linearized transformations between coordinates of differing dynamical nonlinearity to recover (in a given nonlinear coordinate system) much of the benefit of a less nonlinear coordinate description. This method can be used to improve the performance of the new linearized relative motion models by using the nonlinear and linearized transformations between the Cartesian LVLH relative state $\mathbf{x} = (\Delta \mathbf{r}^\top \Delta \mathbf{v}^\top)^\top$ and the orbit element differences, $\delta \mathbf{oe} = (\delta a, \delta e, \delta i, \delta \omega, \delta \Omega, \delta f)^\top$. An alternate set of orbit elements remains defined for $e = 0$, by replacing e , ω and f with $q_1 = e \cos \omega$, $q_2 = e \sin \omega$, and $\theta = \omega + f$. The nonlinear transformations are typically given in an algorithmic form (see e.g. Vallado [127]), but can be written as $\mathbf{x} = \mathbf{g}(\mathbf{oe}, \delta \mathbf{oe})$ and $\delta \mathbf{oe} = \mathbf{k}(\mathbf{oe}, \mathbf{x})$. These transformations can be linearized to give the approximate transformations $\mathbf{x} = [G(\mathbf{oe})] \delta \mathbf{oe}$ and $\delta \mathbf{oe} = [K(\mathbf{oe})] \mathbf{x}$, where $[G(\mathbf{oe})] = [K(\mathbf{oe})]^{-1}$. These linearized time-invariant transformations are given in ch. 14 of Reference 111. A linearized time-varying transformation (accounting for J_2 effects) is given by Gim and Alfriend [50], but the effect of the time-varying terms is generally quite small.

In Reference 121, it was shown that the linearized propagation of a calibrated Cartesian initial condition $\tilde{\mathbf{x}}(t_0) = [G_0] \mathbf{k}(\delta \mathbf{oe}(t_0), \mathbf{x}(t_0))$ is equivalent to linearized transformation of the propagation of $\delta \mathbf{oe}(t_0)$ in the linearized dynamics of the orbit element differences. Because the degree of dynamical nonlinearity is lower with the orbit element difference description [68], the calibrated initial condition thus allows for more accurate linearized solution behavior than would otherwise be possible using the true initial condition and Cartesian coordinate linearized dynamics. However, the calibration process does introduce small error into the initial condition since $\tilde{\mathbf{x}}(t_0) \neq \mathbf{x}(t_0)$.

Using this calibration strategy, by the equivalence of linearized dynamics in Cartesian and

spherical coordinates [31], the following linearized equivalencies are true without loss of generality:

$$x \equiv \delta r \quad (3.33a)$$

$$y \equiv r_c \delta \theta \quad (3.33b)$$

$$z \equiv r_c \delta \phi \quad (3.33c)$$

$$\dot{x} \equiv \delta \dot{r} \quad (3.33d)$$

$$\dot{y} \equiv r_c \delta \dot{\theta} \quad (3.33e)$$

$$\dot{z} \equiv r_c \delta \dot{\phi} \quad (3.33f)$$

Note that equation 3.33 assumes that there is negligible change in r_c , thus the chief orbit should be nearly circular. Because the spherical coordinates more naturally fit the relative motion geometry, they should have a lower degree of nonlinearity in their dynamics. The nonlinear transformation from spherical coordinates to Cartesian coordinates can thus be exploited to further improve the predicted relative position in Cartesian coordinates:

$$x_n = (r_c + \delta r) \cos \delta \theta \cos \delta \phi - r_c \equiv (r_c + x) \cos \left(\frac{y}{r_c} \right) \cos \left(\frac{z}{r_c} \right) - r_c \quad (3.34a)$$

$$y_n = (r_c + \delta r) \sin \delta \theta \cos \delta \phi \equiv (r_c + x) \sin \left(\frac{y}{r_c} \right) \cos \left(\frac{z}{r_c} \right) \quad (3.34b)$$

$$z_n = (r_c + \delta r) \sin \delta \phi \equiv (r_c + x) \sin \left(\frac{z}{r_c} \right) \quad (3.34c)$$

where the new “corrected” Cartesian components are denoted by subscript n , and these equations again assume that variations in the chief orbit radius are negligible. By differentiating Eq. (3.34) (with the assumption $\dot{r}_c = 0$), one would obtain equations for the “corrected” Cartesian components of the relative velocity: \dot{x}_n , \dot{y}_n , and \dot{z}_n . This procedure is most useful for cases with large separation or significant scale differences in the average radial, along-track, or cross-track separations. For small separations with similarly scaled radial, along track, and cross-track motion, this procedure will often be unnecessary. While this calibration procedure might seem counterintuitive, its usefulness will be unequivocally demonstrated with the numerical results later in this chapter.

3.1.3 Solution Improvement by Accounting for Radial Variations

The previously obtained linear model made the assumption $r = a$ and did not account for small two-body and J_2 -induced effects in the chief orbital radius. Accounting for this variation greatly improves model accuracy. Here, two corrections of orbit radius are discussed. The first is a low-inclination analytic model of the J_2 -perturbed radius, and the second is an all-inclination semi-analytic model. For the first two radial correction models, corrective terms are induced in the STM, and these corrections are later demonstrated in numerical simulations.

For this work, the chief radius variations are approximated at $\mathcal{O}(\alpha)$ via a general function $f(t, \mathbf{oe}_0)$, where \mathbf{oe}_0 are the initial chief orbit elements:

$$r(t) \approx a_0(1 - \alpha f(t, \mathbf{oe}_0)) \quad (3.35)$$

With such an assumption, the corrections to the ODE model given in Eq. (3.48) are quite simple.

The changes are limited to two of the diagonal elements of the $[Q]$ matrix, and ω_n :

$$Q'_{11} = Q_{11} + 9\alpha f(t, \mathbf{oe}_0) \quad (3.36)$$

$$Q'_{33} = Q_{33} - 3\alpha f(t, \mathbf{oe}_0)$$

$$\omega'_n = \omega_n + \frac{3}{2}\alpha n f(t, \mathbf{oe}_0) \quad (3.37)$$

where the the new corrected quantities are denoted by a prime, and the original $[Q]$ matrix elements and ω_n were given in Eqs. (3.22) and (3.23).

3.1.3.1 Low-Inclination Analytic Radial Solution

First, the radial accelerations are balanced with the gradient of the terms in the potential that remain for $i = 0$:

$$\frac{d^2 r}{dt^2} - r\dot{\theta}^2 \approx \frac{\partial}{\partial r} (U_c(\mathbf{r})) = \frac{\partial}{\partial r} \left(\frac{\mu}{r} \left(1 + J_2 \frac{R^2}{2r^2} \right) \right) \quad (3.38)$$

where $U_c(\mathbf{r})$ is the total gravitational potential after neglecting terms that vary with latitude, so as to obtain a central force problem. Next, change spatial variables to $u = 1/r$, and time derivatives

to angular derivatives, such that $\frac{d}{dt} = \frac{d}{d\theta} \frac{d\theta}{dt} = \frac{h}{r^2} \frac{d}{d\theta}$:

$$\frac{d^2 u}{d\theta^2} + u = \frac{\mu}{h^2} \left(1 + \frac{3}{2} J_2 R^2 u^2 \right) \quad (3.39)$$

The solution to this ODE may be described in terms of Jacobi elliptic functions, but these are inconvenient for obtaining an analytic STM. Instead, an $\mathcal{O}(\alpha)$ approximate solution is sought, which will be the sum of approximations of the particular and homogeneous solutions. The particular solution is obtained by straightforward perturbation expansion of the polynomial obtained assuming stationary u in the ODE, and the homogeneous solution can be obtained by the Lindstedt-Poincaré technique [96]. Their sum is given below:

$$u = \frac{\mu}{h^2} + \frac{3}{2} J_2 R^2 \frac{\mu^3}{h^6} + A \cos \theta - \frac{3}{4} \mu J_2 \frac{R^2}{h^2} A^2 \left(\frac{1}{4} \cos 2\theta - 1 \right) \quad (3.40)$$

Since Eq. (3.39) is autonomous (for equatorial orbits), the phase angle in the approximate solution may be set to zero. Furthermore, the first-order frequency re-scaling is unity. The constant A is obtained (to $\mathcal{O}(\alpha)$) from $u(0) = 1/r_0$, noting $h(0) = \sqrt{\mu a_0 (1 - e_0^2)}$:

$$A = \frac{1}{r_0} - \frac{1}{a_0(1 - e_0^2)} \left(1 + \frac{3}{2} J_2 \frac{R^2}{a_0^2 (1 - e_0^2)^2} \right) \quad (3.41)$$

Substituting A , then rearranging u to obtain $r(\theta)$ and retaining only $\mathcal{O}(\alpha)$ terms, an approximate expression is obtained that can be simplified into the desired general form of Eq. (3.35):

$$\begin{aligned} r(\theta) &= a_0 \gamma_0 \left(1 - \left(\frac{3}{2} \alpha \left(\frac{1}{\gamma_0^2} \right) (1 - \cos \theta) + \left(\frac{\gamma_0}{\rho_0} - 1 \right) \cos \theta \right) \right) \\ &\approx a_0 \left(1 - \alpha \left(\frac{3}{2} (1 - \cos \theta) + \frac{\left(\frac{1}{\rho_0} - 1 \right)}{\alpha} \cos \theta \right) \right) \end{aligned} \quad (3.42)$$

where $\alpha = J_2 \left(\frac{R}{a_0} \right)^2$, $\gamma_0 = (1 - e_0^2)$, $\rho_0 = r_0/a_0$, and $\gamma_0 \approx 1$ for near-circular orbits. Then $\theta \approx n_0(t - t_n)$ puts Eq. (3.42) in the form of Eq. (3.35).

3.1.3.2 All-Inclination Semi-analytic Radial Solution

For near-circular orbits, a useful time-explicit approximation for the chief orbit radius may be given in terms of the time since node crossing, $\xi = t - t_n$ (the time since $\theta = 0$):

$$r(\xi) \approx \left(a^* - \Delta a \left| \sin \left(\frac{n^* \xi}{2} \right) \right| \right) + (r_0 - a^*) \cos(n^* \xi) \quad (3.43)$$

The parameter n^* is the J_2 -corrected average mean motion, and a^* is the unperturbed semimajor axis that would result in such mean motion:

$$n^* \approx n_0 \left(1 + \frac{3}{16} \alpha (5 + 7 \cos 2i_0) \right) \quad (3.44)$$

$$a^* = \left(\frac{\mu}{n^{*2}} \right)^{\frac{1}{3}} \approx a_0 \left(1 - \frac{1}{8} \alpha (5 + 7 \cos 2i) \right) \quad (3.45)$$

In the context of this discussion, all initial values of parameters refer to the value of that parameter at $\xi = 0$. Note that the absolute values are unnecessary if the most recent node-crossing time is used, such that $(t - t_n) < T$. The parameter Δa is the magnitude of the deviation of the osculating perturbed semimajor axis. This term appears in Brouwer [16]:

$$\Delta a = \frac{3}{2} \frac{\mu}{n_0^2 a_0^2} J_2 \left(\frac{R}{a_0} \right)^2 \sin^2 i_0 = \frac{3}{2} \alpha a_0 \sin^2 i_0 \quad (3.46)$$

Eq. (3.43) is expanded and simplified and only terms of $\mathcal{O}(\alpha)$ are retained to put it in the form of Eq. (3.35), with the perturbing function given below:

$$f(\xi, \mathbf{oe}_0) = \frac{3}{2} \sin^2 i_0 \left| \sin \left(\frac{n_0 \xi}{2} \right) \right| - \frac{1}{8} (5 + 7 \cos 2i_0) (\cos(n_0 \xi) - 1) - \frac{\left(\frac{r_0}{a_0} - 1 \right)}{\alpha} \cos(n_0 \xi) \quad (3.47)$$

The divisor in the final term implies that the numerator should be at most $\mathcal{O}(\alpha)$, which it is. Note the similarity, to $\mathcal{O}(\alpha)$, of Eqs. (3.42) and (3.47) when $i = 0$.

The resulting STM corrections for both radial approximations are given in Reference 18. Later in this section, the time-explicit relative motion model is tested with both of these incorporated.

3.1.4 Numerical Simulations

Here, the J_2 models previously obtained are tested, and the benefits of the calibration procedure are additionally demonstrated. First, the performances of the derived J_2 models are compared to one another and to the CW model. This is done for a range of inclinations from 0° to 90° . The J_2 value of the Earth is used, $J_2 = 1082.63 \times 10^{-6}$. Below, the initial chief orbit elements and deputy orbit element differences are given. The orbit element differences are kept constant for

Table 3.2: J_2 Model Test, Variable Chief Inclination: 0° to 90°

Parameter	Value
$\mathbf{oe}_0 = (a, e, i, \Omega, \theta)$	7100, 0.0, i , 0.0, 0.0
$\delta\mathbf{oe}_0 = (\delta a, \delta e, \delta i, \delta\Omega, \delta\theta)$	0.0, 0.005, 0.2, 0.0, 0.0
LVLH Initial Conditions (m, m/s)	$\Delta\mathbf{r}_0 = -3550\hat{e}_r, \Delta\mathbf{v}_0 = 75.0\hat{e}_t + 26.3\hat{e}_n$
Unperturbed Relative Orbit Dimensions (km)	$(x, y, z) = \pm (35.5, 71.0, 24.8)$

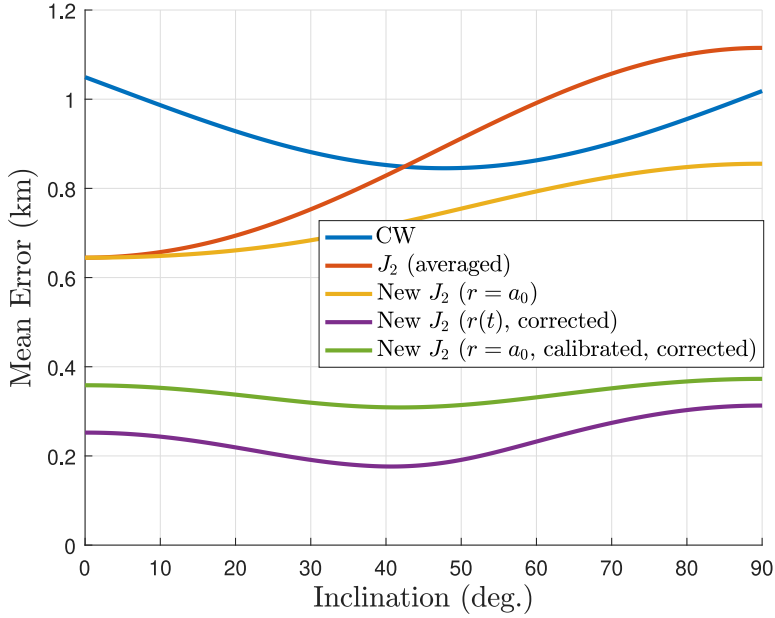


Figure 3.1: Model Error Norm vs. Chief Inclination

all simulations in this study; only the chief inclination is varied. The unperturbed relative orbit dimensions and LVLH frame initial conditions are also given.

In Figure 3.1, the average error norm over one orbit is given vs. inclination for each model, including a J_2 model obtained using averaging in the kinematics [30] and the newly obtained J_2 models, one assuming $r = a_0$ and another using the time-varying approximation for the chief radius, given in Eqs. (3.35) and (3.47). Results are also given for the calibrated and corrected J_2 model assuming $r = a_0$. Coordinate correction offers great improvement for cases with larger separation or with highly unequal radial, along-track, and cross-track relative motion scale. For this case, it offers only small improvement (as $\Delta\mathbf{r} \rightarrow \mathbf{0}$, the transformation Eq. (3.34) approaches identity).

The approximation of the time-varying chief orbit radius greatly reduces the model error, to the lowest curve. Calibrating the initial conditions and using coordinate correction on the model with $r = a_0$ offers almost comparable reductions in error, at least for this type of relative orbit.

Now, the initial conditions from Table 3.2 are used, with $i = 10^\circ$. The position error norm of multiple models is compared for 5 orbits, including the J_2 -only GA-STM [50] and the Schweighart & Sedwick model [116]. The results are given in Figure 3.2.

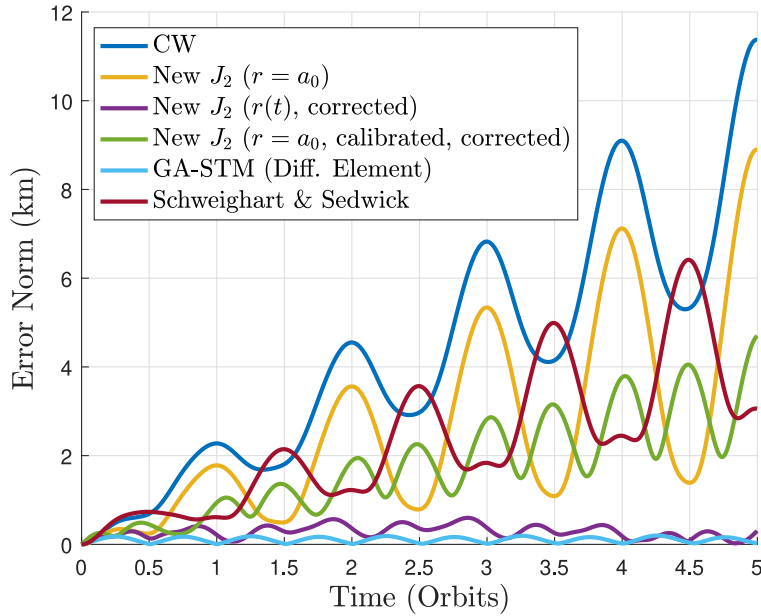


Figure 3.2: Error Norm for Various J_2 Models for $i = 10^\circ$

Figure 3.2 shows that for this case, the J_2 -perturbed model with the approximation of the time-varying chief radius has comparable performance to the GA-STM for 5 orbits, while also outperforming the model obtained by Schweighart and Sedwick. Coordinate-correction was applied to obtain these results, but the benefits are minor at this scale. The differential equinoctial element GA-STM was used to generate these results, with only the J_2 corrections included. This demonstrates the benefits of approximating the variations in the chief radius. The calibrated and corrected zonal model with $r = a_0$ on average also has slightly better performance than the Schweighart and Sedwick model for this case. Note that while the performance of the GA-STM is still slightly better

than the best J_2 model obtained, the latest model is analytically much simpler and computationally much easier to implement than the GA-STM.

An additional case result clearly shows the benefits of solution calibration and coordinate correction. In this case, consider an Earth-mass body with $J_2 = 8 \times 10^{-3}$ and $J_3 = 2 \times 10^{-3}$. The perturbative effects of J_3 are on the same scale as J_2 , and the analytic procedure in this chapter is extended to include the J_3 terms. Those corrective terms are available in Reference 18 and their derivation is not discussed here. The orbit elements and initial conditions are given in Table 3.3. It is clear from the large inclination difference and small eccentricity difference that the out-of-plane motion will be on a different scale from the in-plane motion. This is a situation in which the model performance would clearly benefit from coordinate correction, Eq. (3.34).

Table 3.3: Initial Conditions for Simulation with Large J_2 and J_3

Parameter	Value
$\mathbf{oe}_0 = (a, e, i, \Omega, \theta)$	6800, 0.0, 2.0, 0.0, 0.0
$\delta\mathbf{oe}_0 = (\delta a, \delta e, \delta i, \delta\Omega, \delta\theta)$	0.0, 0.0002, 3.82, 0.0, 0.0
LVLH Initial Conditions (m, m/s)	$\Delta\mathbf{r}_0 = -1360\hat{e}_r, \Delta\mathbf{v}_0 = -14.0\hat{e}_t + 510.2\hat{e}_n$

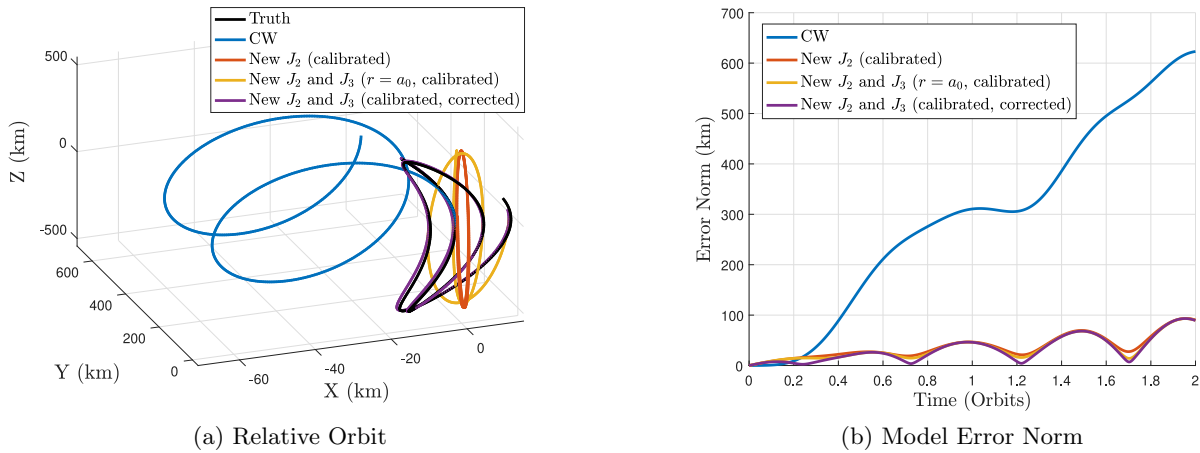


Figure 3.3: Benefits of Solution Calibration and Correction

Figure 3.3 shows the true and model-predicted relative motion (a) and the model error norm (b). In this relative motion case, the CW model completely fails to predict the behavior, and

predicts large along-track drift. Note that the results of the new models without calibration are not shown, since they will diverge much like the CW solution. This figure shows the successive improvements of calibration, inclusion of J_3 terms, and finally coordinate correction. It shows that only coordinate correction allows the model to recover the complex “boomerang” shape of the relative motion with high accuracy. The extension of these linear models simply using coordinate transformations is a significant development, as it greatly extends the region of validity in which these models can be used.

Overall, these simulation results demonstrate that the method of developing linear models of perturbed relative motion offers solutions with significant improvement over the popular Clohessy-Wiltshire (CW) model. The position error scale is generally reduced by 1 - 2 orders of magnitude, enabling computationally efficient modeling of relative motion in situations that classical relative motion models such as the CW model cannot handle. The results with the additional J_3 perturbative terms demonstrate that the procedure can be extended to include more than one perturbation, which facilitates the arguments in the next section – where a linear relative motion model is obtained for oblateness ($C_{20} = -J_2$), ellipticity (C_{22}), and solar radiation pressure (SRP).

3.2 Model for Oblateness, Ellipticity, and Solar Radiation Pressure

In this section, the analytic arguments and techniques developed and reviewed in this chapter are applied to the problem of perturbed formation dynamics in near-circular orbits around large asteroids. In particular, the approximate modeling method is applied to the combined perturbations due to oblateness ($C_{20} = -J_2$), ellipticity (C_{22}), and cannonball solar radiation pressure (SRP). These represent some of the dominant effects for orbits about large asteroids. It is not necessary to repeat the full derivation of this model, which is obtained by applying the same principles as were used in deriving the J_2 model. To see the full derivation for terms accounting for C_{20} and C_{22} , see Reference 17. Note that, as in the first J_2 model introduced in the previous section, the assumption $r = a_0$ is reused in the derivation of these terms. The additional linear perturbative terms due to SRP are discussed in Reference 19. Additionally, the SRP perturbative effect is

discussed extensively in [chapter 4](#).

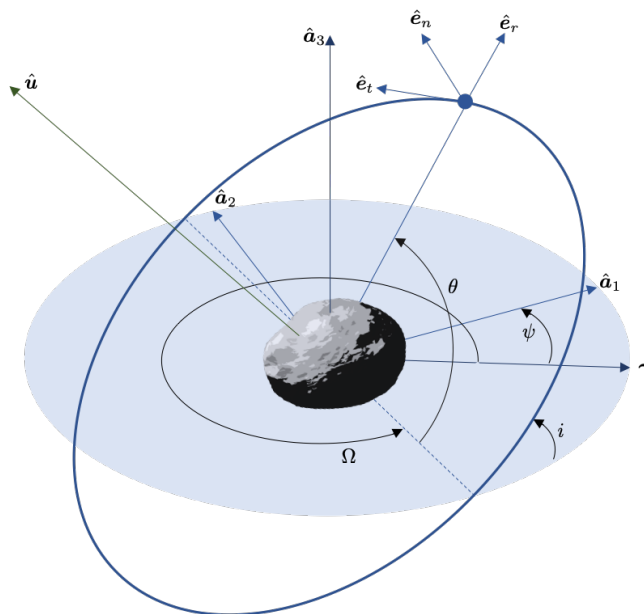


Figure 3.4: Problem Geometry, Asteroid Orbiter

Figure 3.4 shows that the spacecraft orbit is described with respect to the plane perpendicular to the asteroid rotation axis. The axes $\hat{a}_1, \hat{a}_2, \hat{a}_3$ are aligned with the principal axes of inertia of the asteroid, and the asteroid is assumed to be in a spin about the axis of maximum inertia. The right ascension Ω is measured from an inertially fixed reference direction γ in this plane, along with the asteroid rotation angle $\psi = \psi_0 + ct$ tracking the \hat{a}_1 vector. The vector \hat{u} points towards the sun, and the plane perpendicular to this vector is the terminator plane. It is assumed that the formation is centered about a chief in a near-circular orbit, for which the argument of latitude $\theta = \omega + f$ is a convenient angular coordinate.

The dominant effects of the gravity field (captured by coefficients C_{20} and C_{22}) are accounted for by the linearized model, along with the influence of SRP disturbances, using a body-averaged cannonball SRP model. Third-body gravity terms are neglected, as the orbit is assumed to be of a radius such that the dominant gravity perturbations are from low degree and order coefficients of the asteroid gravity field, and not from external bodies or particular surface features. The task of including third-body influence in the linearized model will still often be important, particularly

for high orbits or for orbits about smaller asteroids, but this is left as future work. The effects of the orbit geometry play an important role in the formation dynamics, but the assumptions $r \approx a_0$ and $\theta \approx \theta_0 + nt$ are appropriate for the time span of several orbits, where $n = \sqrt{\mu/a^3}$ is the unperturbed mean motion. The angular rate ratio is defined as $\Gamma = c/n$, R is the Brillouin sphere radius, φ is the asteroid argument of latitude, and h is the orbit angular momentum. The model is given below, in which the kinematics of the perturbed LVLH frame are well-approximated for several orbits, and the perturbed chief orbit parameters a , Ω , and i may be updated as needed:

$$\begin{pmatrix} \ddot{x} \\ \ddot{y} \\ \ddot{z} \end{pmatrix} = n^2 \begin{bmatrix} F_{11} & F_{12} & F_{13} \\ F_{21} & F_{22} & F_{23} \\ F_{31} & F_{32} & F_{33} \end{bmatrix} \begin{pmatrix} x \\ y \\ z \end{pmatrix} + \begin{bmatrix} 0 & 2\omega_n & 0 \\ -2\omega_n & 0 & 2\omega_r \\ 0 & -2\omega_r & 0 \end{bmatrix} \begin{pmatrix} \dot{x} \\ \dot{y} \\ \dot{z} \end{pmatrix} \quad (3.48)$$

$$\begin{aligned} F_{11} = & 3 - \frac{3}{8}C_{20} \left(\frac{R}{a}\right)^2 \left[20(1 - 3\sin^2 i \sin^2 \theta) \right. \\ & + \frac{3}{8}C_{22} \left(\frac{R}{a}\right)^2 \left[30 \cos(2(\Omega - \psi)) ((3 + \cos 2i) \cos 2\theta + 2\sin^2 i) \right. \\ & \left. \left. - 120 \sin(2(\Omega - \psi)) \cos i \sin 2\theta \right] \right] \end{aligned} \quad (3.49a)$$

$$\begin{aligned} F_{12} = & -6C_{20} \left(\frac{R}{a}\right)^2 \sin^2 i \sin 2\theta + \frac{3}{4}C_{22} \left(\frac{R}{a}\right)^2 \left[8 \cos(2(\Omega - \psi)) (3 + \cos 2i) \sin 2\theta \right. \\ & \left. + 32 \sin(2(\Omega - \psi)) \cos i \cos 2\theta \right] \end{aligned} \quad (3.49b)$$

$$\begin{aligned} F_{13} = & -15 \sin i \left(C_{20} \left(\frac{R}{a}\right)^2 \cos i \sin \theta + 2C_{22} \left(\frac{R}{a}\right)^2 \left[\cos(2(\Omega - \psi)) \cos i \sin \theta \right. \right. \\ & \left. \left. + \sin(2(\Omega - \psi)) \cos \theta \right] \right) - \frac{a}{nh} N_{\text{SRP}} \end{aligned} \quad (3.49c)$$

$$F_{21} = F_{12} \quad (3.49d)$$

$$\begin{aligned} F_{22} = & 3C_{20} \left(\frac{R}{a}\right)^2 \sin^2 i \cos 2\theta - \frac{3}{4}C_{22} \left(\frac{R}{a}\right)^2 \left[4 \cos(2(\Omega - \psi)) (3 + \cos 2i) \cos 2\theta \right. \\ & \left. - 16 \sin(2(\Omega - \psi)) \cos i \sin 2\theta \right] \end{aligned} \quad (3.49e)$$

$$\begin{aligned} F_{23} = & 6 \sin i \left(2C_{22} \left(\frac{R}{a}\right)^2 \left[\cos(2(\Omega - \psi)) (\cos i - \Gamma) \cos \theta \right. \right. \\ & \left. \left. + \sin(2(\Gamma - \psi)) (\Gamma \cos i - 1) \sin \theta \right] + C_{20} \left(\frac{R}{a}\right)^2 \cos i \cos \theta \right) + \frac{\dot{\varphi}}{n^2} \frac{a}{h} \frac{d}{d\varphi} (N_{\text{SRP}}) \end{aligned} \quad (3.49f)$$

$$F_{31} = F_{13} \quad (3.49g)$$

$$F_{32} = 12C_{22} \left(\frac{R}{a}\right)^2 \Gamma \sin i (\cos(2(\Omega - \psi)) \cos \theta - \sin(2(\Omega - \psi)) \cos i \sin \theta) - \frac{\dot{\varphi}}{n^2} \frac{a}{h} \frac{d}{d\varphi} (N_{\text{SRP}}) \quad (3.49h)$$

$$F_{33} = -1 + \frac{1}{4}C_{20} \left(\frac{R}{a}\right)^2 [6 + 12 \cos^2 i - 30 \sin^2 i \sin^2 \theta] + \frac{1}{4}C_{22} \left(\frac{R}{a}\right)^2 [\cos(2(\Omega - \psi)) (-15(3 + \cos 2i) \cos 2\theta - 54 \sin^2 i) + 60 \sin(2(\Omega - \psi)) \cos i \sin 2\theta] \quad (3.49i)$$

The angular velocities of the perturbed LVLH frame are given below:

$$\omega_n = n \left(1 - \frac{3}{4} \left(\frac{R}{a}\right)^2 [C_{20} (1 - 3 \sin^2 i \sin^2 \theta) + 6C_{22} (\sin(2(\Omega - \psi)) \cos i \sin 2\theta - \frac{1}{4} \cos(2(\Omega - \psi)) (1 + 3 \cos 2\theta - 2 \cos 2i \sin^2 \theta))] \right) \quad (3.50)$$

$$\omega_r = 3n \left(\frac{R}{a}\right)^2 \sin i (2C_{22} \sin(2(\Omega - \psi)) \cos \theta + [C_{20} + 2C_{22} \cos(2(\Omega - \psi))] \cos i \sin \theta) + \frac{a}{h} N_{\text{SRP}} \quad (3.51)$$

Note that the C_{20} terms in Eq. (3.49) match their J_2 counterparts in Eq. (3.22), and the C_{22} terms are obtained in the same way, but with the added difficulty of accounting for the time-varying geometry relating the asteroid and orbit orientations. The term N_{SRP} is the \hat{e}_n component of the SRP disturbance acceleration acting on the chief spacecraft:

$$N_{\text{SRP}} = -P(R_O) \frac{A}{m} \left(\frac{(1 - \bar{\rho}_s)}{C_{1(1,1)}} + \bar{a}_2 + 2\bar{\rho}_s C_{1(1,1)} \right) C_{1(1,1)} \left(\hat{e}_\xi^\top [C_1(\boldsymbol{\sigma}_r)]^\top \hat{e}_1 \right) \quad (3.52)$$

where A/m is the spacecraft illuminated area-to-mass ratio, $\hat{e}_1 = [1, 0, 0]^\top$ and the unit vector \hat{e}_ξ is not a function of θ due to the problem geometry:

$$\hat{e}_\xi = \begin{pmatrix} \sin \kappa \sin \varphi \cos i - \sin \Omega \cos \varphi \sin i + \cos \Omega \cos \kappa \sin \varphi \sin i \\ \sin \kappa \cos \varphi \cos i + \sin \Omega \sin \varphi \sin i + \cos \Omega \cos \kappa \cos \varphi \sin i \\ \cos \kappa \cos i - \cos \Omega \sin \kappa \sin i \end{pmatrix} \quad (3.53)$$

with solar radiation pressure terms defined below, for a single-plate model of a spacecraft:

$$P(R_O) \approx \frac{G_1}{R_O^2} \quad (3.54)$$

$$\bar{a}_2 = \bar{B}(1 - \bar{s})\bar{\rho} + (1 - \bar{\rho})\bar{B} \quad (3.55)$$

The function $P(R_O)$ is the solar radiation pressure at asteroid orbit distance R_O , and G_1 is the solar radiation force constant at 1 AU. The specular and diffuse reflectivity coefficients are \bar{s} and $\bar{\rho}$, and \bar{B} is the Lambertian scattering coefficient. In this work, resultant SRP acceleration is projected purely along the line from the sun, and the dynamics are thus identical to a cannonball SRP model for chief and deputy. The model also assumes that the spacecraft orbits are near-circular. The model assumes that the chief and deputy spacecraft are subject to similar net resultant SRP acceleration, so the primary relative motion effect from SRP is due to the kinematics of the perturbed LVLH frame. Accounting for the differential SRP acceleration would require introducing independent deputy geometric and optical parameters, as well as tracking the deputy attitude (see [chapter 4](#)). That would not be desirable for this work in studying the deputy-agnostic relative motion dynamics, so it is not done here. Lastly, note that the SRP model does not account for eclipse effects without modification.

The matrix $[C_1(\boldsymbol{\sigma}_r)]$ is the rotation matrix from the asteroid-centered Hill frame to the spacecraft reference orientation. The primary body Hill frame H_P is defined by orthonormal vectors $\{\hat{\mathbf{u}}, \hat{\mathbf{H}} \times \hat{\mathbf{u}}, \hat{\mathbf{H}}\}$, where $\hat{\mathbf{u}}$ points toward the sun and $\hat{\mathbf{H}}$ is out of the orbit plane of the primary body. In all cases studied here, $[C_1(\boldsymbol{\sigma}_r)] = [I_{3 \times 3}]$ and thus $C_{1(1,1)} = 1$ (sun-facing). The angle κ is the obliquity of the ecliptic plane and φ is the argument of latitude, or the rotation angle (in the orbit plane) from the Vernal Equinox to the radial vector from the sun to the planet. This model is derived from the facet-based SRP model given by McMahon and Scheeres [112, 91]. The model assumes that the asteroid is in a circular orbit about the sun, but this could be updated without great difficulty. The timescale of large variations in φ is very slow compared to the spacecraft orbit period. The motion of the asteroid orbit around the sun is not important here, as these studies focus on short-term formation behavior of 1 – 5 spacecraft orbits, a timescale on the order of days to a week. In this context, terms that are functions of φ are examples of long-period terms that can be ignored by assuming $\varphi \approx \varphi_0$ for the timescale of interest.

In Eq. (3.49), the appearance of only the \hat{e}_n component of the SRP disturbance acceleration, N_{SRP} , should be briefly explained. Recall that because the differential SRP acceleration between chief and deputy is assumed to be negligible in this work, the main effect of SRP is in the kinematics of the perturbed chief-centered LVLH frame. The angular velocity of the LVLH frame with respect to the inertial frame may be described in terms of the perturbed orbit element rates, as before [35]:

$$\boldsymbol{\omega}_H = \frac{d\Omega}{dt} \hat{\mathbf{a}}_3 + \frac{di}{dt} \frac{\hat{\mathbf{a}}_3 \times \hat{\mathbf{e}}_n}{\|\hat{\mathbf{a}}_3 \times \hat{\mathbf{e}}_n\|} + \frac{d\theta}{dt} \hat{\mathbf{e}}_n \quad (3.56)$$

where the SRP-perturbed orbit element rates are given below as functions of the orbit geometry and N_{SRP} :

$$\frac{d\Omega}{dt} = \frac{r \sin \theta}{h \sin i} N_{SRP} \quad (3.57a)$$

$$\frac{di}{dt} = \frac{r \cos \theta}{h} N_{SRP} \quad (3.57b)$$

$$\frac{d\theta}{dt} = \frac{d\omega}{dt} + \frac{df}{dt} = \frac{h}{r^2} - \frac{r \sin \theta \cos i}{h \sin i} N_{SRP} \quad (3.57c)$$

If the effect of the SRP disturbance is secondary, then its effect on $r(t)$ and $h(t)$ will not be particularly pronounced over short timespans. Thus, the dominant effect will be in the \hat{e}_n component of the SRP disturbance acceleration, N_{SRP} . More advanced analysis could incorporate approximation of the SRP-induced changes to chief orbit radius and angular momentum in the linear relative motion system matrix, but that level of fidelity is unnecessary for the numerical studies in this work.

Note that unlike in the previous section, an STM will not be obtained for the linear model given by Eqs. (3.48) - (3.51). Instead, simulations are conducted with linear propagation of the model dynamics, without any restarting/update of the chief orbit parameters, to replicate the performance of an STM.

3.2.1 Further Analysis of the Linear Model

Note that as $i \rightarrow 0$, ignoring long-period SRP effects, the equations of motion can be shown to reduce to the following highly simplified form:

$$\begin{aligned}\ddot{x} &= 3n^2 \left(1 + \frac{5}{2}\alpha + 15\beta \cos \Theta\right) x + 24n^2\beta \sin \Theta y + 2n \left(1 + \frac{3}{4}\alpha - \frac{9}{2}\beta \cos \Theta\right) \dot{y} - \frac{a}{nh} N_{\text{SRP}} z \\ \ddot{y} &= 24n^2\beta \sin \Theta x - 12n^2\beta \cos \Theta y - 2n \left(1 + \frac{3}{4}\alpha - \frac{9}{2}\beta \cos \Theta\right) \dot{x} + 2\frac{a}{h} N_{\text{SRP}} \dot{z} \\ \ddot{z} &= -n^2 \left(1 - \frac{9}{2}\alpha + 15\beta \cos \Theta\right) z - 2\frac{a}{h} N_{\text{SRP}} \dot{y}\end{aligned}\quad (3.58)$$

where $\alpha = -C_{20} \left(\frac{R}{a}\right)^2$ and $\beta = C_{22} \left(\frac{R}{a}\right)^2$, and $\Theta = 2((1 - \Gamma)\theta + (\Omega + \Gamma\theta_0 - \psi_0))$. For a purely equatorial orbit $i = 0$, and Ω is undefined, so θ is measured from the reference direction γ , then $\Theta = 2((1 - \Gamma)\theta + (\Gamma\theta_0 - \psi_0))$.

Previous analysis [20] studies these equations without SRP, including their further reduced LTI form for $\Gamma = 1$, and finds that the reduced LTI model can successfully predict the stability properties of the libration points [75] collinear with the $\hat{\mathbf{a}}_1$ and $\hat{\mathbf{a}}_2$ in the rotating asteroid-fixed frame, and the associated eigenvectors can be used to produce the stable and unstable manifolds. This linearized relative motion model can then be viewed as a generalization of the classical problem of studying motion in the vicinity of equilibrium points in the rotating body-fixed frame.

3.2.2 Identifying Important Parameters for Numerical Simulations

The form of Eqs. (3.49) – (3.51) lends some insight into important parameters in the formation dynamics. First, note that all C_{22} associated terms are multiplied by either $\cos(2(\Omega - \psi))$ or $\sin(2(\Omega - \psi))$, representing the importance of the evolution of the relative configuration of the orbit plane and the asteroid orientation. For cases of $\Gamma \approx 1$ these terms change slowly, and the value of $\Omega - \psi_0$ becomes quite important. As the value of Γ is increased (corresponding to a raising of the chief semimajor axis), these terms oscillate more quickly, and the importance of $\Omega - \psi_0$ on formation dynamics is reduced.

Recall that as $i \rightarrow 0$, the in-plane x and y dynamics nearly decouple with the out-of-plane z dynamics, with the exception of kinematic coupling terms due to the SRP disturbance. The fact

that inclination has such an influence on the dynamics suggest that it is also important to consider.

The value of semimajor axis is vitally important to formation dynamics, manifesting through the small parameters premultiplying the time-varying disturbance terms, $C_{2j}(R/a)^2$, $j = 0, 2$. It also affects the magnitude of Γ , determining whether or not the initial relative configuration of the chief orbit and asteroid attitude has an important role.

Lastly, the optical coefficients are important due to their effect on the SRP disturbance, and so is the geometry of the chief orbit with respect to the direction to the sun, captured by the coupled orbit angle terms in \hat{e}_ξ in Eqs. (4.28) – (4.29). For simplicity, the studies in this section assume that the asteroid spin axis orientation is known, along with the spacecraft optical coefficients. The studies consider a family initially near-circular chief orbits (at varying inclinations both near and far from the terminator plane) on which to center the formation. The semimajor axis and inclination are chosen as the main independent parameters for studying the highly perturbed formation dynamics in this problem.

3.2.3 Angular Momentum of the Relative Orbital State

Because the relative motion is characterized by time-varying relative position and velocity, a vector quantity that captures large variations in either of these vectors is sought. The angular momentum of the relative orbital state (AMROS) provides an intuitive view of perturbed formation behavior, defined as the cross-product of the relative position $\Delta\mathbf{r} = (x, y, z)^\top$ and velocity $\Delta\mathbf{r}' = (\dot{x}, \dot{y}, \dot{z})^\top$:

$$\Delta\mathbf{h} = \Delta\mathbf{r} \times \Delta\mathbf{r}' \quad (3.59)$$

It is important to note that this term is not the same as the difference between the angular momentum of the deputy and the chief, $\delta\mathbf{h}$. This term is only the component of the angular momentum difference that is purely associated with the chief-centered relative state, and independent of the chief position and velocity:

$$\delta\mathbf{h} = \mathbf{h}_d - \mathbf{h}_c = \Delta\mathbf{h} + (\mathbf{r}_c \times \Delta\mathbf{r}') + (\Delta\mathbf{r} \times \mathbf{v}_c) \quad (3.60)$$

A simple argument for using this parameter is that it captures large changes in $\Delta\mathbf{r}(t)$ or $\Delta\mathbf{r}'(t)$ that indicate significant change to the nature of the relative motion or relative orbit. However, substitution of the Clohessy-Wiltshire solutions into Eq. (3.59) provides another argument for the rationale of its use. For unperturbed close-proximity formations, satisfaction of the no-drift condition manifests in the solution to the linearized dynamics as periodicity of $\Delta\mathbf{h}$, with the quantity predicted to be constant when the relative motion furthermore has no along-track angular offset, parameterized only by nonzero δe and δi :

$$\Delta\mathbf{h}_{\text{HCW}} = \left(3x_0 + \frac{2}{n}\dot{y}_0\right)\dot{z}_0\hat{\mathbf{e}}_t - \frac{2}{n}(21n^2x_0 + 24nx_0\dot{y}_0 + 7\dot{y}_0^2)\hat{\mathbf{e}}_n \quad (3.61)$$

Any violation of the no-drift condition likewise results in $\Delta\mathbf{h}$ no longer being periodic or conserved. Thus, the CW solution establishes a link between this physical quantity and the linearized approximation of the no-drift constraint. Changes in the value of $\Delta\mathbf{h}(t)$ or its norm Δh using the perturbed linear models will be useful for predicting the degree, timescale, and manner of formation deviation from classical unperturbed non-drifting geometry. It is important to note that under the true dynamics, $\Delta\mathbf{h}$ is not truly constant for unperturbed chief-centered non-drifting relative motion, but instead fluctuates periodically on a small scale. The scale of these unperturbed fluctuations is a small fraction ($\sim 0.1\%$) of the mean value for formations on any scale that permit linearization. However, the effects of perturbations may result in fluctuations on the same order as the mean.

3.2.4 Numerical Simulations

Simulation of linearized relative motion with the model equations allows for efficient exploration of relative motion in a parameter space of various chief orbits. Here, the strengths and limitations of the analytic approximate model are shown by direct comparison with results from nonlinear dynamic simulations. Note that this same model will be revisited for modal analysis of spacecraft relative motion in [chapter 7](#).

3.2.4.1 Simulation Setup

For the results that follow, close-proximity formation dynamics about a rotating asteroid are considered, with important physical parameters given in Table 3.4.

Table 3.4: Simulation Parameters for Asteroid Relative Motion Model

Parameters	Values
Asteroid Physical Parameters	$M = 4.9 \times 10^{14}$ kg, $R = 6$ km, Ellipsoidal semi-axes: 6, 3, 2.5 km
Gravity Parameters	$\mu = 3.271 \times 10^{-5}$ km ³ /s ² , $C_{20} = -0.0903$, $C_{22} = 0.0375$
Asteroid Orbit Radius	$R_O = 3.5904 \times 10^8$ km (2.4 AU)
Configuration Parameters	$\kappa = 15^\circ$, $\varphi_0 = 90^\circ$, $T_r = 18.0$ hr, $\psi_0 = 0$
Spacecraft Optical Constants	$\frac{A}{m} = 0.3$ m ² /kg, $\bar{B} = 0.6$, $\bar{s} = 0.25$, $\bar{\rho} = 0.3$

The parameter R is the Brillouin sphere radius, the maximum extent of the body material from its center of mass. The linearized relative motion model in Eq. (3.48) is used to explore the parameter space for prograde and retrograde near-circular chief orbits. Namely, the inclination of prograde orbits in the terminator plane is $i_T = 75.0^\circ$, and the set of inclinations tested is between 70° and 105° in one degree increments. The range of Γ tested is from $\Gamma = 3/4$ to $\Gamma = 4$, with 25 evenly spaced values. The semimajor axis is related to Γ through the following equation, where $c = 2\pi/T_r$:

$$a = \left(\mu \frac{\Gamma^2}{c^2} \right)^{1/3} \quad (3.62)$$

For simplicity, the initial non-critical chief orbit elements $e_0, \omega_0, \Omega_0, f_0$ are all assumed to be zero. Thus $\theta_0 = 0$ and additionally, the chief orbit is initially circular. Small initial nonzero values of chief eccentricity (e.g. $\mathcal{O}(10^{-3})$) do not significantly affect the results. The osculating chief orbit eccentricity is generally of this scale anyway, and can reach higher values in strongly perturbed cases.

While third body effects are ignored in this study, the radius of the asteroid sphere of influence is estimated assuming $m \ll M$ [8]:

$$r_{\text{SOI}} = R_O \left(\frac{m}{M} \right)^{2/5} \approx 205 \text{ km} \quad (3.63)$$

where M is the mass of the sun. Note that at $a = 38.2$ km (the maximum orbit size tested), the

sun's gravity would be a little less than 3% the strength of the asteroid gravity, so the third-body disturbance should be included in the approximate model for higher fidelity in actual applications.

In the studies that follow, for each point in the parameter space, the state transition matrix is computed using the linearized dynamics for one period of the $[A(t)]$ matrix. This enables any type of close-proximity relative motion to be studied without re-integrating each initial condition of interest.

3.2.4.2 Results

First, the magnitude of the maximum deviation (over one orbit) of the AMROS parameter is computed with results from both the linearized model and the truth model. This involves determining the time t at which $\|\Delta\mathbf{h}(t) - \Delta\mathbf{h}(0)\|$ is maximum, and returning that maximum value. For these results, the relative motion of a single deputy around the chief is considered, with the only nonzero differential elements being $\delta e = 0.003$ and $\delta i = 0.1^\circ$. In the unperturbed case, this would result in periodic bounded planar relative motion with an average separation on the order of 100 meters, with the linear model predicting conservation of $\Delta\mathbf{h}$ and the truth model showing small fluctuations.

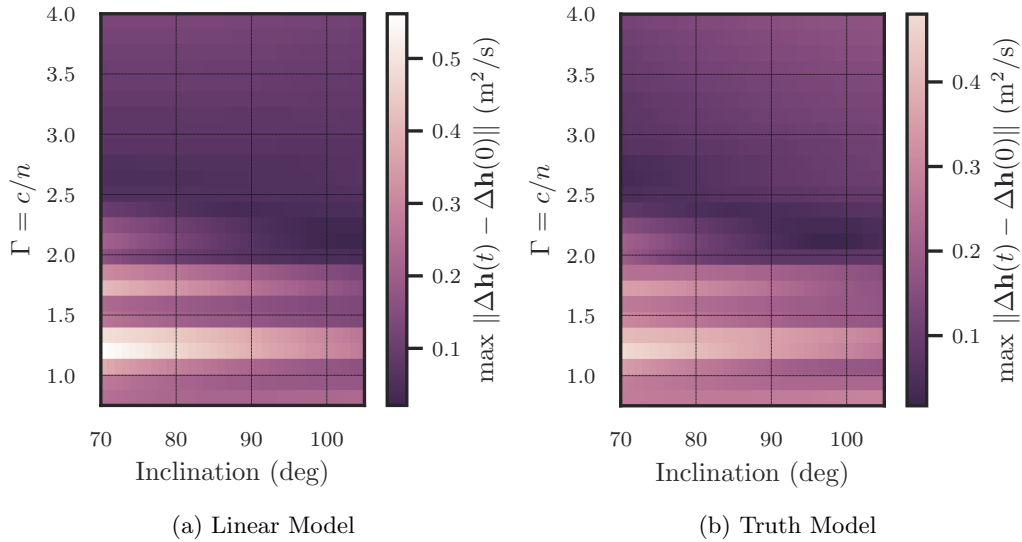


Figure 3.5: Maximum Deviation of AMROS in One Orbit

The results for the highly perturbed asteroid environment are given in Figure 3.5 for one orbit, which is about three days. The results show strong agreement between the linearized model (left) and truth model (right). The results also establish that within one orbit, the orbits for $\Gamma < 2$ are much more significantly perturbed than higher altitude orbits of $\Gamma > 2$.

Since this figure is used to explore and compare behavior throughout the parameter space, the relative values are more important to study than the absolute values. Both plots show two bands of highly perturbed relative motion behavior around $\Gamma = 1.25$ and $\Gamma = 1.75$, with retrograde orbits ($i > 90^\circ$) showing less deviation than prograde orbits, despite their large angular separation from the terminator plane at $i = 75^\circ$. Overall, the deviations in the AMROS parameter are clearly strongly dependent on the value of the angular rate ratio Γ , with larger deviation for small values of Γ . This shows that the largest deviations from classical relative motion are at low altitude.

Two individual cases from the parameter space serve to illustrate the severity of the perturbations. Recall that the initial relative motion conditions parameterized only by small δe and δi would classically result in bounded relative motion in the absence of these perturbations [3]. First, consider the case from $\Gamma = 1.25$ and $i = 75^\circ$. The relative motion is plotted for 4 orbit periods in Figure 3.6. The results show strong agreement for the first orbit, with divergence between the linear and truth model afterwards.

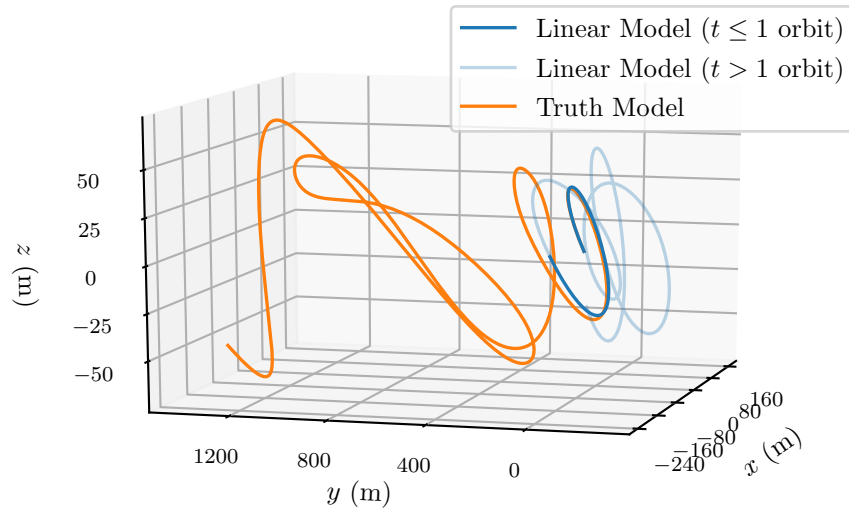


Figure 3.6: Perturbed Relative Motion with $\Gamma = 1.25$, $i = 75^\circ$

The linear model successfully predicts the degree and manner of the deviation for the first orbit. The truth model shows that over the course of the next several orbits, the deputy continues to rapidly drift further away. This long-term behavior is not well captured by the linear model – at least not without periodically updating the chief orbit elements and re-initializing. Such an update and re-initialization procedure would be reasonable in any on-board guidance implementation procedure, but these results evaluate the efficacy of the unaided model. The eventual failure of the model is an unsurprising phenomenon, given the rapid change in geometry and scale of the true motion. What is most surprising is the rapid timescale and manner in which a close-proximity two spacecraft formation is ripped apart by the dynamics of the orbital environment. This is not an isolated case: sampling other bright regions in Figure 3.5 often results in finding similar highly destabilized behavior.

To investigate a region in the parameter space where the maximum deviation of the AMROS parameter is comparatively rather low, the case of $\Gamma = 2$ and $i = 95^\circ$ is chosen. The relative orbital motion is plotted in Figure 3.7. The resulting relative motion is indeed more stable for short time spans, and the behavior is well-approximated (without any re-initialization and chief orbit parameter updates) for 4 orbits. Since the orbit period in this case is 36 hours, this stable behavior persists and is well-approximated for 6 days. The long-term relative motion is however still highly unstable, as can be seen from the truth model results propagated over 10 orbits.

The individual case results in Figures 3.6 and 3.7 reflect general observations that the maximum deviation of the AMROS parameter is a good tool for studying short-term behavior. Additionally, recall that these results were generated via propagation of the analytic approximation linear model without any updating of the chief elements or restarting of the model. As a result, the behavior of these models is similar to what would be expected if a relative motion STM were to be generated from the model.

These results show that the behavior of the linearized dynamics can be used to describe perturbation and destabilization of close-proximity relative motion in the short term, but the long-term behavior is also of interest. The case used to produce Figure 3.7 shows that short-term stable

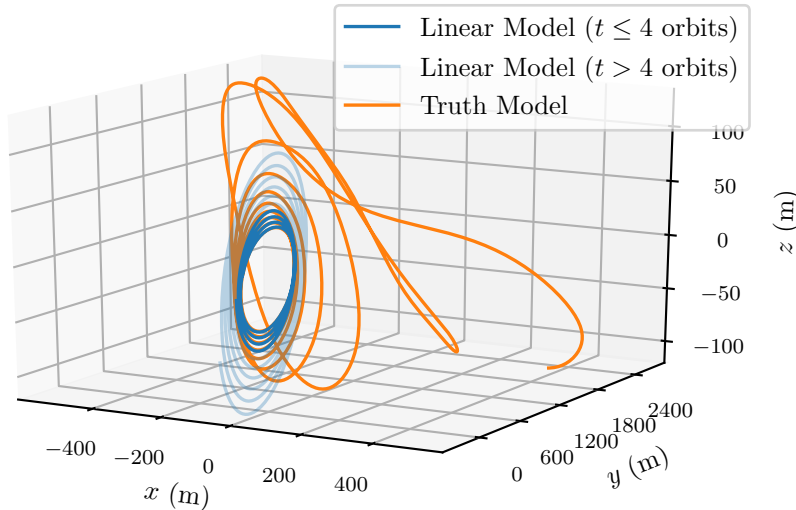


Figure 3.7: Perturbed Relative Motion with $\Gamma = 2.0$, $i = 95^\circ$

behavior can still become destabilized in the long-term. In light of these results, it is natural to ask if the approximate dynamics can be used to easily identify cases where relative motion will be stable for much longer time spans. It turns out that this is also possible. However, such discussion goes beyond the scope of this chapter, and is delayed until the analytic model for oblateness, ellipticity, and SRP is revisited for modal analysis of spacecraft relative motion in [chapter 7](#).

3.3 Additional Work in Relative Motion Modeling

This chapter applies a strategy of developing approximate linearized models of relative motion in local Cartesian coordinates, which will be shown in this dissertation to have extensive application in spacecraft formation flying and relative motion control applications. When an analytic linear model is obtained, it is possible to solve it for a relative motion state transition matrix, which can be applied in the same manner as the classical CW STM. As was demonstrated with the derivation of the J_2 models, the accuracy of the approximation of the chief orbit behavior has a strong effect on the accuracy of the predicted spacecraft relative motion. For situations with many perturbations, it becomes increasingly difficult to approximate the behavior of the perturbed chief orbit. This section discusses recent work in describing the orbital behavior in the J_2 perturbed environment and in

orbits perturbed by primary body oblateness and ellipticity. It also surveys some recent works related to the models obtained here, and discusses alternate approaches to perturbed spacecraft relative motion modeling.

3.3.1 The J_2 Perturbed Orbit Revisited

A new analysis is performed yielding an analytic approximation of the behavior of the J_2 -perturbed orbit radius for all inclinations, with the goal of replacing the earlier semi-analytic expression. First, the important radial equation is restated:

$$\ddot{r} - \omega_n^2 r = -\frac{\mu}{r^2} + R_{C_{20}} \quad (3.64)$$

where $C_{20} = -J_2$ and $R_{C_{20}}$ is given below:

$$R_{C_{20}} = \frac{3\mu C_{20} R^2}{2r^4} (1 - 3\sin^2 i \sin^2 \theta) \quad (3.65)$$

Eq. (3.64) is quite important for the J_2 -perturbed relative motion modeling problem, because it isolates the coupled behavior of two unknowns: $r(t)$ and $\omega_n(t)$. In particular, all occurrences of i and θ are second-order in C_{20} , so an analysis that is accurate to first-order in C_{20} permits the use of the unperturbed values for these quantities. The result is an equation in two unknowns, and the degeneracy can be broken by use of an integral of motion. In particular, using the orbit energy and the substitutions $r(t) \approx r_0(1 + \xi(t))$ where $\xi \sim \mathcal{O}(1/r_0)$ and $\dot{r} \approx r_0 \dot{\xi}$, it is possible to approximate the behavior of the radius given by Eq. (3.64) with a simpler differential equation. Below, the total orbit energy is given, where $U(\mathbf{r})$ is the gravitational potential:

$$E = \frac{1}{2}v^2 - U(\mathbf{r}) \quad (3.66)$$

$$U(\mathbf{r}) = \frac{\mu}{r} + \frac{\mu}{r^3} \left[C_{20} R^2 \left(\frac{3}{4} \sin^2 i (1 - \cos 2\theta) - \frac{1}{2} \right) \right] \quad (3.67)$$

The orbit energy is written in terms of ω_n :

$$E = \frac{1}{2} (r^2 \omega_n^2 + \dot{r}^2) - U(\mathbf{r}) \quad (3.68)$$

Because it is conserved, $E = E_0 \forall t$ and the following may be written:

$$\omega_n^2 = \frac{2(E_0 + U(\mathbf{r})) - \dot{r}^2}{r^2} \quad (3.69)$$

Using the substitution $r(t) = r_0(1 + \xi(t))$, and substituting ω_n^2 using Eqs. (3.67) - (3.69), Eq. (3.64) is expanded about $\xi = 0$, retaining terms linear in ξ :

$$\ddot{\xi} + \left(2 \left(\frac{\mu}{r_0^3} + \frac{E_0}{r_0^2} \right) - 4 \frac{\mu \bar{f}}{r_0^3} \right) \xi - \left(\frac{\mu}{r_0^3} + 2 \frac{E_0}{r_0^2} - \frac{\mu \bar{f}}{r_0^3} \right) = 0 \quad (3.70)$$

where \bar{f} is a function associated with the C_{20} component of the gravitational potential:

$$\bar{f}(t) = C_{20} \frac{R^2}{r_0^2} \left(\frac{3}{4} \sin^2 i_0 (1 - \cos 2\theta) - \frac{1}{2} \right) \quad (3.71)$$

Thus, the problem has been transformed to a study of (assumed small) variations about the initial value $r(0) = r_0$, an approximation which significantly simplifies the problem. The following change of time variables enables the subsequent non-dimensionalization of Eq. (3.70):

$$\tau = \left(\frac{\mu}{r_0^3} \right)^{1/2} t, \quad \frac{d}{dt} = \left(\frac{\mu}{r_0^3} \right)^{1/2} \frac{d}{d\tau} \quad (3.72)$$

$$\xi'' + \left(2 \left(1 + \frac{E_0 r_0}{\mu} \right) - 4 \bar{f} \right) \xi - \left(\left(1 + 2 \frac{E_0 r_0}{\mu} \right) - \bar{f} \right) = 0 \quad (3.73)$$

Note that here we redefine $(\)' = d/d\tau(\)$. The change of time variables renders $\xi(\tau)$, $\xi'(\tau)$, and $\xi''(\tau)$ to all be of the same order. In this derivation, it is assumed that ξ and \bar{f} are both similarly small (e.g. 10^{-2}), denoted $\mathcal{O}(\epsilon)$. This derivation could be modified to accommodate different relative scales. The smallness of ξ depends on the orbit not deviating drastically from the unperturbed geometry, and the scale of \bar{f} depends on the altitude and the size of C_{20} .

This system can be initiated (without loss of generality) with $\theta_0 = 0$, then substitution of $\theta \approx n_0 t$, $n_0 = \sqrt{\mu/a_0^3}$, renders the function \bar{f} as an explicit function of time t . Note that non-circular orbit angular frequency variations would appear pre-multiplied by other small terms (i.e. terms involving C_{20}), and are thus neglected. Finally, the substitution $t = (\mu/r_0^3)^{-1/2} \tau$ renders everything a function of the dimensionless time: $\theta = (r_0^3/a_0^3)^{1/2} \tau$.

Identifying the small parameters ξ and \bar{f} as $\mathcal{O}(\epsilon)$, the $\mathcal{O}(\epsilon)$ part of Eq. (3.73) is given below:

$$\xi'' + 2 \left(1 + \frac{E_0 r_0}{\mu} \right) \xi = \left(1 + 2 \frac{E_0 r_0}{\mu} \right) - \bar{f} \quad (3.74)$$

To first order, ξ obeys simple sinusoidal dynamics with an oscillatory forcing term due to the negative of the C_{20} component of the potential. This first-order equation can be solved using the method of undetermined coefficients, noting that the harmonic forcing term has different frequencies from the homogeneous solution. The solution of Eq. (3.74) is the sum of the homogeneous and particular solutions given below:

$$\xi_h(\tau) = D \cos(\sqrt{2\eta_1}\tau) + E \sin(\sqrt{2\eta_1}\tau) \quad (3.75)$$

$$\xi_p(\tau) = A \cos(\omega_p\tau) + B \sin(\omega_p\tau) + C \quad (3.76)$$

where the quantities η_1 and ω_p are given:

$$\eta_1 = 1 + \frac{E_0 r_0}{\mu}, \quad \omega_p = 2n_0 \left(\frac{\mu}{r_0^3} \right)^{-1/2} \quad (3.77)$$

Substituting the particular solution into Eq. (3.74), the following equations are obtained in terms of the undetermined coefficients A , B , and C :

$$\begin{aligned} A(2\eta_1 - \omega_p^2) &= \frac{3}{4} C_{20} \frac{R^2}{r_0^2} \sin^2 i \\ B &= 0 \end{aligned} \quad (3.78)$$

$$2\eta_1 C = 1 + 2 \frac{E_0 r_0}{\mu} + \frac{1}{2} C_{20} \frac{R^2}{r_0^2} \left(1 - \frac{3}{2} \sin^2 i \right)$$

Letting $\alpha = C_{20}(R/r_0)^2 \sim \mathcal{O}(\epsilon)$, the following values are obtained:

$$A = \frac{3}{4} \alpha \left(\frac{\sin^2 i}{2\eta_1 - \omega_p^2} \right), \quad B = 0, \quad C = \frac{1}{4} \alpha \left(\frac{1 - \frac{3}{2} \sin^2 i}{\eta_1} \right) + \frac{1}{2\eta_1} \left(1 + 2 \frac{E_0 r_0}{\mu} \right) \quad (3.79)$$

The first initial condition is $r(0) = r_0(1 + \xi(0)) = r_0$. The next initial condition on ξ is given from the following expression:

$$r'(0) = \left(\frac{\mu}{r_0^3} \right)^{-1/2} \dot{r}(0) = \left(\frac{\mu}{r_0^3} \right)^{-1/2} r_0 \dot{\xi}(0) = r_0 \xi'(0) \quad (3.80)$$

$$\xi'(0) = \left(\frac{\mu}{r_0^3}\right)^{-1/2} \frac{\dot{r}_0}{r_0} = E\sqrt{2\eta_1} \quad (3.81)$$

Thus, D and E are obtained from the initial conditions:

$$D = -A - C, \quad E = \left(\frac{\mu}{r_0^3}\right)^{-1/2} \frac{\dot{r}_0}{r_0} \left(\frac{1}{\sqrt{2\eta_1}}\right) \quad (3.82)$$

The approximate solution for $\xi(\tau)$ is given by the sum of Eqs. (3.75) and (3.76) with the coefficients given in Eqs. (3.79) and (3.82), thus approximating $r(\tau) = r_0(1 + \xi(\tau))$ to first order:

$$\xi(\tau) = A \cos(\omega_p \tau) + C + D \cos(\sqrt{2\eta_1} \tau) + E \sin(\sqrt{2\eta_1} \tau) \quad (3.83)$$

This simple approximation is accurate for sufficiently small initial eccentricity ($e_0 \sim 10^{-3}$) and for all inclinations. Accuracy is less dependent on the osculating eccentricity, which can generally grow to larger values (10^{-2}) at some points in the orbit. The accuracy for small eccentricity is captured in the terms C , D , and E . For example, setting $\omega = f_0 = 0$, the equation for ξ reduces to:

$$\xi(\tau) = C \left(1 - \cos(\sqrt{2\eta_1} \tau)\right) \quad (3.84)$$

Then, $r(\tau) = a(1 - e)(1 + \xi(\tau))$. Making the necessary substitutions, then expanding to first-order in eccentricity, the classical first-order expansion [8] is recovered:

$$r(t) \approx a(1 - e \cos(n_0 t)) \quad (3.85)$$

Thus, a radial correction is obtained which rigorously accounts for both J_2 and small eccentricity effects. Additionally, because Eq. (3.64) holds for high eccentricities, it is possible to use this equation to approach the same problem for higher eccentricities. However, due to the mixed appearance of time derivatives and the variable θ , it is not analytically straightforward to solve this equation for general inclinations. For problems like this, it is generally known that time is a suitable independent variable for perturbed near-circular orbit approximation, and true anomaly is generally poor, especially for perturbed low-eccentricity orbits [64]. The argument of latitude is a useful independent variable due to its ease of geometric interpretation, but it introduces additional perturbative terms into the transformed form of the previously simple Eq. (3.64). A good discussion

of these types of difficulties can be found in Reference 128. Reference 128 also solves for the radial behavior for the eccentric J_2 -perturbed problem with zero inclination, which is a step towards the goal of developing a J_2 -perturbed relative motion model for eccentric chief orbits. Developing a concise but accurate local coordinate STM for the J_2 -perturbed problem in eccentric orbits is still an unsolved problem, and there are several authors working on it.

3.3.2 Modeling the Orbital Effects of Oblateness and Ellipticity

While the earlier relative motion model for C_{20} , C_{22} , and SRP made the simplifying assumption $r = a_0$, it is possible to develop an accurate expression for the behavior of the chief orbit radius $r(t)$, as well as for the other elements, for the orbit problem perturbed by oblateness and ellipticity. This is done in a similar manner to the previously discussed derivation of near-circular radial motion for J_2 : a conserved quantity (in this case, the Jacobi integral) is used to make the radial equation solvable, and the radial variations are assumed to be small deviations, $r = r_0(1 + \xi(t))$. A linear approximate differential equation for the deviation parameter $\xi(t)$ is derived and then solved. Once the orbit radius $r(t)$ is obtained, it is possible to find the coupled normal component of angular velocity, $\omega_n(t)$. Then, other elements can be obtained by subsequent analysis or direct integration of their Gauss planetary equations, accurate to first order in C_{20} and C_{22} . This is explored more in Reference 25, but the results are only briefly discussed here, and are not repeated for the sake of brevity.

In Reference 25, the choice of coordinates to describe the perturbed orbital state is to use the classical elements Ω and i to describe the orientation of the perturbed orbit plane, and polar coordinates $(r, \theta, \dot{r}, \omega_n)$ to parameterize the remaining state elements. This treatment avoids any direct use of the eccentricity, argument of periapsis, or true anomaly, and any associated difficulties of using elements explicitly derived from these. The results are time-explicit expressions for each of these coordinates. Note that the model given in Eq. (3.48) could be updated and re-derived with these improved approximations of the perturbed chief orbit (neglecting the SRP effect on the orbit radius again) and a more accurate STM could be obtained. However, it is observed that the

number of terms in the relative motion STM grows quickly with the number of terms in the linear model. As a result, the approach of generating an approximate STM model of relative motion in the manner explored in this chapter could have practical limitations for systems with many dominant perturbations.

3.4 Conclusions

This chapter introduces and applies a fundamental method of modeling spacecraft relative motion under the influence of perturbations in an accurate, useful, and computationally efficient manner. Linearized models of spacecraft relative motion allow for efficient analysis and various applications such as local relative motion control. The resulting linear time-varying differential equations can be solved to obtain a state transition matrix of relative motion. This is done using an unperturbed solution as the generating solution and solving for the corrective terms for the non-Keplerian effects using a perturbation technique such as the straightforward perturbation expansion [96]. The chapter begins with an in-depth derivation the commonly studied J_2 perturbation, dominant in Low Earth Orbit. The resulting STM is computed then validated and compared with various other solutions from literature. Then, a linear model accounting for solar radiation pressure and primary body oblateness and ellipticity is introduced, having been derived by similar means. This model is then tested to study spacecraft relative motion in the vicinity of near-circular orbits about a large asteroid. Finally, there is some additional discussion in high-fidelity orbit approximation in perturbed problems.

The applications of the developments in this chapter are numerous. The J_2 -perturbed STM provides much higher accuracy than the popular Clohessy-Wiltshire STM, and can be used for the same applications such as rendezvous and relative motion maneuver planning. The methodology in this chapter is used in [chapter 4](#) for modeling spacecraft relative motion perturbed by solar radiation pressure (SRP), and facilitates the creation of an accurate control model for using differential SRP as a relative motion control parameter. In general, the linearized models enable powerful and robust control using a Linear Quadratic Regulator and Linear Quadratic Tracking control. This

is explored further in [chapter 5](#), along with a related linear control strategy known as desensitized control. Lastly, the asteroid relative motion linear model also finds use in [chapter 7](#) in a modal analysis of perturbed spacecraft relative motion.

Chapter 4

Relative Motion Control with Differential Solar Radiation Pressure

This chapter applies the principles of relative motion dynamic approximation discussed in [chapter 3](#) to the case of spacecraft relative motion perturbed by solar radiation pressure (SRP). This enables the use of the attitude-dependent differential solar radiation pressure acceleration as a control parameter for relative motion control, in a highly realistic framework that accounts for the SRP effects on the motion of both the deputy and the chief spacecraft. This concept is similar to the use of differential drag for formation flying control, which is already done for satellite formations in low-Earth orbit. Differential drag control only allows for in-plane control, but differential SRP allows for full controllability of the relative motion. It is important to account for the effects of SRP on the chief orbit, because these effects alter the relative motion kinematics from the unperturbed case. This chapter concludes with simulated relative motion control results with SRP for spacecraft in geostationary Earth orbit (GEO) and in orbits about a small body. This chapter is based on work also appearing in References [19](#) and [23](#).

4.1 Solar Radiation Pressure as a Control Parameter

Solar radiation pressure (SRP) is the driving force for solar sails, but it is typically viewed as a disturbance force and not a control parameter for typical modern spacecraft. However, in environments where differential solar radiation pressure is sufficiently strong on the scale of the relative motion dynamics, small sustained variations in attitude can be used to harness this perturbation for control – even for spacecraft with realistic optical parameters. While not particularly suitable

in low-Earth orbits, the efficacy of this control method becomes much greater for multi-spacecraft formations sufficiently far from the planet. The geostationary (GEO) region is one example. In this region, the spacecraft are not subject to strong disturbances from higher-order gravitational effects or drag due to the rarefied atmosphere. SRP-based control also becomes a feasible option for formations in orbit around small bodies such as asteroids, comets, and moons.

The possibility of using small attitude changes for formation-keeping is appealing because of the potential for saved thruster fuel. It is also valuable because the differential SRP force between identical spacecraft can achieve the incredibly small values necessary for real-time and high-precision formation-keeping around small asteroids and comets. Even the smallest commercially available ion thrusters are often too powerful for continuous use in station-keeping or high precision formation control in these environments, requiring them to be used in a pulsed control strategy almost like chemical thrusters. This contradicts the nature of their design for very long-duration burns, reducing efficiency and accelerating wear. Other design solutions are available to partially mitigate this issue, such as pulsed plasma thrusters (PPTs), but these are not as efficient as other forms of electric propulsion. In this context, SRP-based control would be preferred over any type of electric propulsion, and can be implemented on spacecraft with traditional geometry and surface materials.

The topic of natural SRP-perturbed orbital dynamics has been frequently studied, especially in the vicinity of small bodies [114]. Many works use a cannonball SRP model, and focus on finding stable orbits while assuming the force variation with attitude is not significant [41, 32]. Some works also discuss orbit-attitude coupling in the uncontrolled dynamics, or the coupled effects of multiple perturbations [77, 82, 94]. Recent work by Kenshiro Oguri and Jay McMahon focuses on SRP-based orbit control around asteroids [99]. The optical force SRP model used in their work is essentially equivalent to the one used here, but their approach is otherwise quite different. Their work studies orbit control via a chosen subset of the orbit elements, namely semimajor axis and inclination. The optimal attitude for control is parameterized by two angles, whose values are obtained numerically based on the current system state. The chapter makes multiple novel analytical arguments that

provide insight about the controlled orbital dynamics – including attitude constraints to prevent orbital escape, and even an analytic upper bound for the time of flight for landing on an asteroid using SRP-based control.

It is worth noting that SRP-based control has also been extensively studied for solar sails, but this work usually makes restrictive assumptions about the spacecraft optical properties. While interesting work has been done to study the natural and controlled orbital dynamics using the SRP force, this chapter is focused on the topic of orbital formation control, for which spacecraft with unremarkable geometry can still produce sufficient differences in SRP force to use it as a relative position and velocity control parameter.

In contrast to the previously mentioned works on the topic of SRP-based control, a desirable approach would be to use a relative motion model that requires only occasional updates of the formation state differences and the spacecraft orbital elements of one or more of the spacecraft. These state differences could be provided directly from measurements in local-vertical local-horizontal (LVLH) components. Ideally, a model accounting for the evolution of the perturbed orbit and the linearized SRP-perturbed differential dynamics will naturally enable sufficiently reliable situational awareness even with low navigation update frequency. Lastly, a linearized approach leverages the smallness of the formation geometry on the scale of the spacecraft orbits. It is also amenable to a linearly optimal LQR control approach – in which the optimal gain schedule can be computed in advance of the maneuver, or in a receding-horizon manner. Developing such a model is the primary focus of this chapter.

This chapter derives an accurate linearized time-varying (LTV) model of formation dynamics subject to attitude-dependent SRP forces. The problem geometry for a single illuminated spacecraft facet is given in Figure 4.1 for a spacecraft that seeks to rendezvous with a nearby chief spacecraft using only the attitude-controlled SRP forces $\sum_i \mathbf{F}_{S_i}$ for control. The relative state is resolved in local radial, transverse, and normal directions, which use the chief position vector \mathbf{r} and angular momentum vector \mathbf{h} as $\hat{\mathbf{e}}_r = \mathbf{r}/r$, $\hat{\mathbf{e}}_t = -\hat{\mathbf{e}}_r \times \hat{\mathbf{e}}_h$, and $\hat{\mathbf{e}}_h = \mathbf{h}/h$. The vector $\hat{\mathbf{u}}$ points towards the sun and $\hat{\mathbf{H}}$ is normal to the planet orbit plane. The model uses the chief-deputy notation commonly

used in spacecraft formation flying, in which the motion of one spacecraft (the deputy) is described with respect to another (the chief), in a local chief-centered frame. The model may be updated with chief orbit elements with any desired frequency. The analytical approach in this chapter naturally allows for the evolution of the spacecraft orbit elements to be approximated for relatively long timespans. This model can easily be combined with components of other models to account for additional system perturbations [17]. While it is assumed that updated relative heading, range, and range-rate data is periodically available for the spacecraft in the formation, the relative position and velocity can be efficiently integrated between measurements using the linearized model. By incorporating accurate and computationally efficient approximation of system evolution into the model, significant decoupling of the tasks of control and navigation is achievable. Overall, the developments in this chapter are a step towards enabling a highly flexible, simple formation control strategy suitable for closed-loop SRP-based spacecraft formation control.

After the linearized model is developed, a linearly optimal control strategy is designed for small attitude departures from a reference orientation. For simplicity in developing the proof-of-concept simulations, the model is implemented with a single facet only, but the approach can be easily generalized to a multi-facet spacecraft model. The model developed in this chapter could be adapted and extended to find use in future multi-spacecraft missions to asteroids and comets, and will also be useful for formation control or orbit maintenance in high-altitude orbits about the Earth, such as the GEO belt.

Lastly, it is important to note that the use of SRP for spacecraft control has already been demonstrated in flight. The K2 mission was able to make use of SRP effects to extend the life of the Kepler space telescope mission, which was suffering from attitude control under-actuation due to reaction wheel failure. This was done by achieving and maintaining an orientation to passively minimize the SRP disturbance along the roll axis [62]. The Messenger mission to Mercury used SRP for precision orbit control, which is particularly notable and relevant to this work. In that mission, pre-planned attitude and solar array articulations were used to improve the accuracy of Mercury flybys [100]. This was done in an open-loop fashion, but closed-loop control would be

highly desirable. Closed-loop control should be readily achievable using SRP models with varying levels of fidelity, and the work in this chapter enables further steps towards that goal.

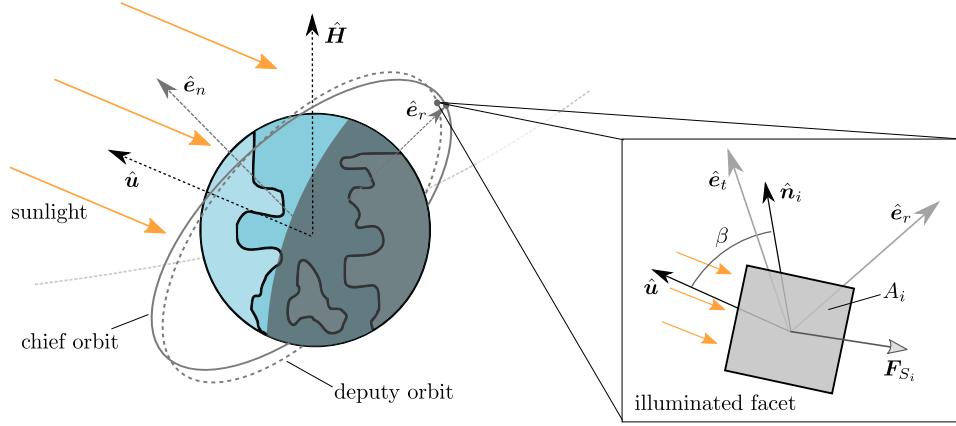


Figure 4.1: Problem Geometry for SRP-based Control, with Attitude-Dependent Resultant Force

4.2 Spacecraft Relative Motion Dynamics with Solar Radiation Pressure

The force due to solar radiation pressure on a general body surface element A_i is given below [112]:

$$\mathbf{F}_{S_i} = -P(R)H_i(\hat{\mathbf{u}})A_i \left[\left(\rho_i s_i \left(2\hat{\mathbf{n}}\hat{\mathbf{n}}^\top - [I_{3 \times 3}] \right) + [I_{3 \times 3}] \right) \hat{\mathbf{u}} (\hat{\mathbf{u}} \cdot \hat{\mathbf{n}}_i) + a_{2i}\hat{\mathbf{n}}_i (\hat{\mathbf{n}}_i \cdot \hat{\mathbf{u}}) \right] \quad (4.1)$$

with

$$P(R) \approx \frac{G_1}{R^2} \quad (4.2)$$

$$a_{2i} = B(1 - s_i)\rho_i + (1 - \rho_i)B \quad (4.3)$$

The function $P(R)$ is the solar radiation pressure at distance R , and G_1 is the solar radiation force constant at 1 AU. The specular and diffuse reflectivity coefficients are s_i and ρ_i , and B is the Lambertian scattering coefficient, $\hat{\mathbf{u}}$ is the unit vector to the sun, $\hat{\mathbf{n}}_i$ is the normal vector of the surface element, and $H(\hat{\mathbf{u}})$ is a visibility delta function, equal to 1 or 0, depending on whether or not the face is directly illuminated by sunlight. Figure 4.1 highlights the important aspects of the problem geometry. For simplicity and generality, this analysis neglects the effects of secondary

reflections from other surfaces. However, a realistic treatment of the body optical properties (B , s_i , ρ_i) is important.

The SRP force can be modeled by considering the sum of the forces on all illuminated facets. The results in this chapter use a single-facet model of a spacecraft for generality and to validate the derivation. However, it is emphasized that this method can be directly generalized to a spacecraft with fixed geometry and multiple illuminated facets. Summing over the contributions of all body area elements, an approximate model of the net SRP force vector on the spacecraft is obtained:

$$\mathbf{F}_S = -P(R)A \left((\bar{a}_2 \cos \beta + 2\bar{\rho}\bar{s} \cos^2 \beta) \hat{\mathbf{n}} + (1 - \bar{\rho}\bar{s}) \cos \beta \hat{\mathbf{u}} \right) \quad (4.4)$$

where $\cos \beta = \hat{\mathbf{u}} \cdot \hat{\mathbf{n}}$, A is a projected area term, and $\hat{\mathbf{n}}$ is the corresponding equivalent normal unit vector. This implementation neglects the eclipse dynamics, but the effect could easily be reintroduced for a higher fidelity control implementation. The terms \bar{a}_2 , $\bar{\rho}$, and \bar{s} are illuminated body-averaged optical parameters. This replaces the multi-facet SRP force model with a single-plate SRP force model at some reference orientation.

It is always possible to obtain an equivalent single-plate model representation of the resultant SRP force acting on a spacecraft, for which the sum of the $\hat{\mathbf{n}}_i$ components of the resultant SRP force acts along $\hat{\mathbf{n}}$, and the total $\hat{\mathbf{u}}$ component is also reproduced. However, the extent to which attitude-dependent SRP force variations of the single plate correctly model the true spacecraft SRP force variations is situation dependent. Accuracy would be highly dependent on spacecraft geometry and the optical properties of the surface facets. For example, for the case of small attitude deviations from a reference orientation that is at or near the transition to shadowing of one or more large facets, the nonlinear effect of facet shadowing could present challenges for applying the linearized control formulation. Other approaches of modeling SRP acceleration variation for small angles are possible, such as a local linearization of the spherical harmonic series representation [47].

4.2.1 Problem Geometry and Coordinate Frames

Before continuing with the derivation of the linearized dynamics and control model, the primary coordinate frames must be defined. First, the rotating frame moving with the primary body is called the planet frame \mathcal{P} , and is defined by orthonormal vectors $\{\hat{\mathbf{u}}, \hat{\mathbf{H}} \times \hat{\mathbf{u}} / \|\hat{\mathbf{H}} \times \hat{\mathbf{u}}\|, \hat{\mathbf{H}}\}$, where $\hat{\mathbf{u}}$ points from the planet toward the sun and $\hat{\mathbf{H}} = \mathbf{h}_p / h_p$ is defined by the planet's orbit angular momentum vector \mathbf{h}_p , normal to its orbit plane.

One can describe the rotation from the planet frame to the primary-centered inertial (\mathcal{N}) frame through two angles:

$$[\mathcal{N}\mathcal{P}] = [R_1(\kappa)] [R_3(\varphi + \pi)]^\top = \begin{bmatrix} -\cos \varphi & \sin \varphi & 0 \\ -\sin \varphi \cos \kappa & -\cos \varphi \cos \kappa & \sin \kappa \\ \sin \varphi \sin \kappa & \cos \varphi \sin \kappa & \cos \kappa \end{bmatrix} \quad (4.5)$$

where $[R_1(\theta)]$ denotes the rotation matrix for a 1-axis rotation by angle θ , and $[R_3(\theta)]$ is the rotation matrix for a 3-axis rotation by angle θ [111]. The angle κ is the obliquity of the ecliptic plane and φ is the argument of latitude, or the rotation angle (in the orbit plane) from the Vernal Equinox to the radial vector from the sun to the planet. For Earth, $\kappa \approx 23.5^\circ$, and the \mathcal{N} frame is the typical Earth-centered inertial (ECI) frame.

Because this chapter is focused on using SRP force for rendezvous and formation control, the controlled relative motion of two or more spacecraft is considered. The motions of one or more deputies relative to the chief are used to describe formation or rendezvous geometry without explicitly considering all individual spacecraft orbits. Recall that one may arbitrarily decide which spacecraft is designated as the chief and which is the deputy. In this chapter, the chosen representation for the relative state is to resolve the relative position

$$\Delta \mathbf{r} = (x, y, z)^\top \quad (4.6)$$

and velocity

$$\Delta \mathbf{r}' = (\dot{x}, \dot{y}, \dot{z})^\top \quad (4.7)$$

in the chief-centered rotating local-vertical, local-horizontal (LVLH) frame. Here, $()'$ denotes the derivative of a state quantity as seen in the LVLH frame. This frame rotates with the spacecraft orbit and is defined by orthonormal radial, along-track, and orbit-normal vectors \mathbf{v} : $\hat{\mathbf{e}}_r = \mathbf{r}/r$ and $\hat{\mathbf{e}}_n = \mathbf{r} \times \mathbf{v} / \|\mathbf{r} \times \mathbf{v}\|$.

Now a final rotation from the inertial frame to an orbiting spacecraft-centered local-vertical local-horizontal (LVLH frame) may be defined. The rotation $[\mathcal{HN}]$ is given below in terms of the chief spacecraft orbit radial and angular momentum vectors \mathbf{r} and \mathbf{h} , and equivalently in a 3–1–3 sequence in terms of the spacecraft orbit elements Ω , i , and θ [111]:

$$[\mathcal{HN}] = \begin{bmatrix} \hat{\mathbf{r}}^\top \\ \frac{1}{rh} (r^2 \mathbf{v} - (\mathbf{v} \cdot \mathbf{r}) \mathbf{r})^\top \\ \hat{\mathbf{h}}^\top \end{bmatrix} \quad (4.8)$$

$$[\mathcal{HN}] = \begin{bmatrix} \cos \Omega \cos \theta - \sin \Omega \sin \theta \cos i & \sin \Omega \cos \theta + \cos \Omega \sin \theta \cos i & \sin \theta \sin i \\ -\cos \Omega \sin \theta - \sin \Omega \cos \theta \cos i & -\sin \Omega \sin \theta + \cos \Omega \cos \theta \cos i & \cos \theta \sin i \\ \sin \Omega \sin i & -\cos \Omega \sin i & \cos i \end{bmatrix} \quad (4.9)$$

Thus, the rotation from \mathcal{P} to \mathcal{H} is:

$$[\mathcal{HP}] = [\mathcal{HN}] [\mathcal{NP}] \quad (4.10)$$

With the system geometry and coordinate descriptions now defined, a control matrix $[B]$ can now be obtained, which maps deputy spacecraft attitude to accelerations in the LVLH frame. The uncontrolled dynamics of an SRP-perturbed multi-spacecraft formation are also considered to obtain the system matrix $[A]$. This complex derivation follows the control matrix derivation.

4.2.2 Linearized Attitude-based SRP Control

Modified Rodrigues Parameters (MRPs) are used to describe the spacecraft attitude, or the attitude of a single-plate model in this chapter. This attitude description is expressed in terms of the principal rotation elements (angle α and axis $\hat{\mathbf{e}}$) [111]:

$$\boldsymbol{\sigma} = \tan \frac{\alpha}{4} \hat{\mathbf{e}} \quad (4.11)$$

The MRP attitude representation has the benefit of linearizing as $\boldsymbol{\sigma} \approx (\alpha/4) \hat{\boldsymbol{e}}$, providing a larger usable range for linear control than an angular representation [111].

The mapping to and from a general rotation matrix $[C]$ is given below:

$$[C] = [I_{3 \times 3}] + \frac{8[\tilde{\boldsymbol{\sigma}}]^2 - 4(1 - \sigma^2)[\tilde{\boldsymbol{\sigma}}]}{(1 + \sigma^2)^2} \quad (4.12)$$

$$\boldsymbol{\sigma} = \begin{pmatrix} \sigma_1 \\ \sigma_2 \\ \sigma_3 \end{pmatrix} = \frac{1}{\zeta(\zeta + 2)} \begin{pmatrix} C_{23} - C_{32} \\ C_{31} - C_{13} \\ C_{12} - C_{21} \end{pmatrix} \quad (4.13)$$

where $\zeta = \sqrt{C_{11} + C_{22} + C_{33} - 1}$, $\sigma^{2n} = (\boldsymbol{\sigma}^\top \boldsymbol{\sigma})^n$, and $[\tilde{\boldsymbol{\sigma}}]$ is the MRP skew-symmetric matrix.

To use the MRP formulation, the rotation of a vector in \mathcal{P} components into the spacecraft body frame (\mathcal{B}) components is defined in terms of two successive rotations. The first is a rotation $[C_1(\boldsymbol{\sigma}_r)]$ to the “reference” attitude, and the second is a rotation $[C_2(\boldsymbol{\sigma}_c)]$ to the current orientation, which is a controlled deviation from this reference attitude:

$${}^{\mathcal{B}}\boldsymbol{r} = [C_2(\boldsymbol{\sigma}_c)][C_1(\boldsymbol{\sigma}_r)]{}^{\mathcal{P}}\boldsymbol{r} \quad (4.14)$$

The attitude deviation $\boldsymbol{\sigma}_c$ is the control parameter for attitude-based position control using SRP. This work assumes that the spacecraft attitude control system is fully capable of enforcing the needed attitude behavior.

From Eq. (4.4), substituting $\hat{\boldsymbol{n}} \cdot \hat{\boldsymbol{u}}$ for all $\cos \beta$ terms, the force due to SRP is rewritten below in its \mathcal{P} components using ${}^{\mathcal{P}}\hat{\boldsymbol{n}} = [C_1(\boldsymbol{\sigma}_r)]^\top [C_2(\boldsymbol{\sigma}_c)]^\top {}^{\mathcal{B}}\hat{\boldsymbol{n}}$ and defining ${}^{\mathcal{B}}\hat{\boldsymbol{n}} = \hat{\boldsymbol{e}}_1$ and ${}^{\mathcal{P}}\hat{\boldsymbol{u}} = \hat{\boldsymbol{e}}_1$, where $\hat{\boldsymbol{e}}_1 = [1, 0, 0]^\top$:

$$\boldsymbol{F}_S = -P(R)A \left(\left(\bar{a}_2 (\hat{\boldsymbol{n}} \cdot \hat{\boldsymbol{u}}) + 2\bar{\rho}\bar{s} (\hat{\boldsymbol{n}} \cdot \hat{\boldsymbol{u}})^2 \right) [C_1(\boldsymbol{\sigma}_r)]^\top [C_2(\boldsymbol{\sigma}_c)]^\top + (1 - \bar{\rho}\bar{s}) (\hat{\boldsymbol{n}} \cdot \hat{\boldsymbol{u}}) [I_{3 \times 3}] \right) \hat{\boldsymbol{e}}_1 \quad (4.15)$$

To obtain the $[B]$ matrix, this equation must be linearized with respect to the control term $\boldsymbol{u} = \boldsymbol{\sigma}_c$. First, all control-associated parts are replaced with their expansions up to $\mathcal{O}(\sigma_c)$:

$$[C_2(\boldsymbol{\sigma}_c)] \approx [I_{3 \times 3}] - 4[\tilde{\boldsymbol{\sigma}}_c] \quad (4.16)$$

$$\hat{\boldsymbol{n}} \cdot \hat{\boldsymbol{u}} = \hat{\boldsymbol{e}}_1^\top [C_2(\boldsymbol{\sigma}_c)][C_1(\boldsymbol{\sigma}_r)]\hat{\boldsymbol{e}}_1 \approx \hat{\boldsymbol{e}}_1^\top ([C_1(\boldsymbol{\sigma}_r)] - 4[\tilde{\boldsymbol{\sigma}}_c][C_1(\boldsymbol{\sigma}_r)]\hat{\boldsymbol{e}}_1) \quad (4.17)$$

$$(\hat{\mathbf{n}} \cdot \hat{\mathbf{u}})^2 \approx \left(\hat{\mathbf{e}}_1^\top [C_1(\boldsymbol{\sigma}_r)]^\top \hat{\mathbf{e}}_1 \right) \hat{\mathbf{e}}_1^\top \left([C_1(\boldsymbol{\sigma}_r)] - 8[\tilde{\boldsymbol{\sigma}}_c][C_1(\boldsymbol{\sigma}_r)]\hat{\mathbf{e}}_1 \right) \quad (4.18)$$

Substituting Eqs. (4.16) – (4.18) into Eq. (4.15), expanding, and retaining only terms up to $\mathcal{O}(\sigma_c)$, the linearization of \mathbf{F}_S is obtained:

$$\begin{aligned} \mathbf{F}_S \approx & -P(R)A \left\{ \left(\bar{a}_2 + 2\bar{\rho}s \hat{\mathbf{e}}_1^\top [C_1(\boldsymbol{\sigma}_r)] \hat{\mathbf{e}}_1 \right) \left(\hat{\mathbf{e}}_1^\top [C_1(\boldsymbol{\sigma}_r)] \hat{\mathbf{e}}_1 \left([C_1(\boldsymbol{\sigma}_r)]^\top ([I_{3 \times 3} + 4[\tilde{\boldsymbol{\sigma}}_c]) \right) \right) \right. \\ & - 4 \left(\bar{a}_2 + 4\bar{\rho}s \hat{\mathbf{e}}_1^\top [C_1(\boldsymbol{\sigma}_r)] \hat{\mathbf{e}}_1 \right) \hat{\mathbf{e}}_1^\top [\tilde{\boldsymbol{\sigma}}_c] [C_1(\boldsymbol{\sigma}_r)] \hat{\mathbf{e}}_1 [C_1(\boldsymbol{\sigma}_r)]^\top \\ & \left. + (1 - \bar{\rho}s) \hat{\mathbf{e}}_1^\top ([I_{3 \times 3}] - 4[\tilde{\boldsymbol{\sigma}}_c]) \hat{\mathbf{e}}_1 [I_{3 \times 3}] \right\} \hat{\mathbf{e}}_1 \end{aligned} \quad (4.19)$$

This equation is linear in $\boldsymbol{\sigma}_c$, and is rearranged below so that the control vector $\boldsymbol{\sigma}_c$ is explicitly isolated:

$$\begin{aligned} \mathbf{F}_S = & -P(R)A \left\{ (\bar{a}_2 + 2\bar{\rho}s C_{1(1,1)}) \left(C_{1(1,1)} [C_1(\boldsymbol{\sigma}_r)]^\top \right) \hat{\mathbf{e}}_1 \right. \\ & - 4 (\bar{a}_2 + 2\bar{\rho}s C_{1(1,1)}) \left(C_{1(1,1)} [C_1(\boldsymbol{\sigma}_r)]^\top [\tilde{\mathbf{e}}_1] \right) \boldsymbol{\sigma}_c \\ & - 4 (\bar{a}_2 + 4\bar{\rho}s C_{1(1,1)}) \left([C_1(\boldsymbol{\sigma}_r)]^\top [\hat{\mathbf{e}}_1 \hat{\mathbf{e}}_1^\top] [C_1(\boldsymbol{\sigma}_r)]^\top [\tilde{\mathbf{e}}_1] \right) \boldsymbol{\sigma}_c \\ & \left. + (1 - \bar{\rho}s) \hat{\mathbf{e}}_1 + 4(1 - \bar{\rho}s) [\hat{\mathbf{e}}_1 \hat{\mathbf{e}}_1^\top] [\tilde{\mathbf{e}}_1] \boldsymbol{\sigma}_c \right\} \end{aligned} \quad (4.20)$$

where the shorthand notation $C_{1(1,1)} = \hat{\mathbf{e}}_1^\top [C_1(\boldsymbol{\sigma}_r)] \hat{\mathbf{e}}_1$ is used. If the reference orientation is sun-facing, then $[C_1(\boldsymbol{\sigma}_r)] = [I_{3 \times 3}]$ and a simpler form is obtained:

$$\mathbf{F}_S = -P(R)A \left\{ (1 + \bar{\rho}s + \bar{a}_2) \hat{\mathbf{e}}_1 - 4(\bar{a}_2 + 2\bar{\rho}s) [\tilde{\mathbf{e}}_1] \boldsymbol{\sigma}_c \right\} \quad (4.21)$$

From this result, the $[B]$ matrix can be isolated for the system resolved in P :

$$[B] = 4 \frac{P(R)A}{m} \begin{bmatrix} \mathbf{0}_{4 \times 3} & & \\ 0 & 0 & -\bar{a}_2 - 2\bar{\rho}s \\ 0 & \bar{a}_2 + 2\bar{\rho}s & 0 \end{bmatrix} \quad (4.22)$$

The $[B]$ matrix for a more general reference orientation can be readily obtained by isolating the control-associated terms in Eq. (4.20). This can also be easily resolved in any desired frame by using the appropriate rotation matrices. Note that in the case of linearization about a sun-facing reference, the $[B]$ matrix for the system resolved in \mathcal{P} predicts zero acceleration will be produced along the $\hat{\mathbf{u}}$ direction due to small controlled attitude variations. In reality, a small acceleration

will be produced, but this is not captured by the linearization. This suggests that motion along the $\hat{\mathbf{u}}$ direction is instantaneously uncontrollable with linear control. However, investigations later in the chapter show that the system is still fully controllable.

4.2.3 Linearized Relative Motion Dynamics under SRP

The SRP-perturbed uncontrolled relative orbital motion behavior of the spacecraft is now derived. Because the SRP-based control is enabled by deviations from a reference attitude that is assumed to be fixed in the \mathcal{P} frame, this analysis assumes that the SRP-based differential acceleration between the deputy and chief spacecraft is negligible. This implicitly assumes that the deputy and chief geometry and optical characteristics are similar. In this case, with both spacecraft at the same reference orientation, the only manifestation of the SRP acceleration is on the kinematics of the chief LVLH frame. Note that depending on the dynamic environment, this effect may be overshadowed by other disturbance accelerations.

The angular velocity of the perturbed LVLH frame with respect to the inertial frame may be described in terms of the perturbed orbit element rates [35]:

$$\boldsymbol{\omega}_H = \frac{d\Omega}{dt} \hat{\mathbf{a}}_3 + \frac{di}{dt} \frac{\hat{\mathbf{a}}_3 \times \hat{\mathbf{e}}_n}{\|\hat{\mathbf{a}}_3 \times \hat{\mathbf{e}}_n\|} + \frac{d\theta}{dt} \hat{\mathbf{e}}_n \quad (4.23)$$

where $\hat{\mathbf{a}}_3$ is the vector pointing along the planet polar axis, the third orthogonal unit vector used for the ECI frame. The angle Ω is the right ascension of the ascending node, i is the inclination, and $\theta = \omega + f$ is the argument of latitude. The orbit element rates are obtained using the variational equations in their Gaussian form to yield the osculating rates due to the SRP perturbation, resolved in local radial, along-track, and cross-track components:

$$\mathbf{a}_{\text{SRP}} = R_{\text{SRP}} \hat{\mathbf{e}}_r + T_{\text{SRP}} \hat{\mathbf{e}}_t + N_{\text{SRP}} \hat{\mathbf{e}}_n \quad (4.24)$$

$$\frac{d\Omega}{dt} = \frac{r \sin \theta}{h \sin i} N_{\text{SRP}} \quad (4.25a)$$

$$\frac{di}{dt} = \frac{r \cos \theta}{h} N_{\text{SRP}} \quad (4.25b)$$

$$\frac{d\theta}{dt} = \frac{d\omega}{dt} + \frac{df}{dt} = \frac{h}{r^2} - \frac{r \sin \theta \cos i}{h \sin i} N_{\text{SRP}} \quad (4.25c)$$

The argument of latitude is used to avoid the possibility of small denominators in the variational equations for near-circular orbits. The argument of latitude rate has two components: the “unperturbed” argument of latitude rate $\dot{\theta}_u = h/r^2$, and a component due to the regression of the node from which θ is measured [104]. The expression for N_{SRP} may be obtained using the rotation from \mathcal{P} to \mathcal{H} , and the SRP disturbance force resolved in \mathcal{P} components, Eq. (4.20), with $\boldsymbol{\sigma}_c = \mathbf{0}$ because the chief attitude is the reference orientation. In this analysis, it is assumed that the chief attitude is fixed in the \mathcal{P} frame.

$$N_{\text{SRP}} = \frac{1}{m} \hat{\boldsymbol{e}}_3^\top [\mathcal{H}\mathcal{N}] [\mathcal{N}\mathcal{P}] \mathbf{F}_S \quad (4.26)$$

$$N_{\text{SRP}} = -P(R) \frac{A}{m} \left(\frac{(1 - \bar{\rho}s)}{C_{1(1,1)}} + \bar{a}_2 + 2\bar{\rho}s C_{1(1,1)} \right) C_{1(1,1)} \left(\hat{\boldsymbol{e}}_3^\top [\mathcal{H}\mathcal{N}] [\mathcal{N}\mathcal{P}] [C_1(\boldsymbol{\sigma}_r)]^\top \hat{\boldsymbol{e}}_1 \right) \quad (4.27)$$

$$N_{\text{SRP}} = -P(R) \frac{A}{m} \left(\frac{(1 - \bar{\rho}s)}{C_{1(1,1)}} + \bar{a}_2 + 2\bar{\rho}s C_{1(1,1)} \right) C_{1(1,1)} \left(\hat{\boldsymbol{e}}_\xi^\top [C_1(\boldsymbol{\sigma}_r)]^\top \hat{\boldsymbol{e}}_1 \right) \quad (4.28)$$

where the unit vector $\hat{\boldsymbol{e}}_\xi$ is not a function of θ due to the problem geometry:

$$\hat{\boldsymbol{e}}_\xi = \begin{pmatrix} \sin \kappa \sin \varphi \cos i - \sin \Omega \cos \varphi \sin i + \cos \Omega \cos \kappa \sin \varphi \sin i \\ \sin \kappa \cos \varphi \cos i + \sin \Omega \sin \varphi \sin i + \cos \Omega \cos \kappa \cos \varphi \sin i \\ \cos \kappa \cos i - \cos \Omega \sin \kappa \sin i \end{pmatrix} \quad (4.29)$$

Assuming the primary body orbit radius R is nearly constant and that the reference orientation is stationary as seen in the \mathcal{P} frame, the only time-varying term in Eq. (4.28) is the primary body’s argument of latitude, φ . Generally, this time scale will be much slower than the spacecraft orbit period about the primary body, and may be slow enough to ignore for sufficiently short-duration rendezvous.

By applying the transport theorem twice with angular velocity given by Eq. (4.23), the kinematics of the perturbed LVLH frame are given in radial, along-track, and cross-track components:

$$\begin{aligned} \Delta \ddot{\mathbf{r}} = & (\ddot{x} - \dot{\omega}_n y - 2\omega_n \dot{y} - \omega_n^2 x + \omega_n \omega_r z) \hat{\boldsymbol{e}}_r \\ & + (\ddot{y} + \dot{\omega}_n x + 2\omega_n \dot{x} - (\omega_n^2 + \omega_r^2) y - \dot{\omega}_r z - 2\omega_r \dot{z}) \hat{\boldsymbol{e}}_t \\ & + (\ddot{z} + \omega_n \omega_r x + \dot{\omega}_r y + 2\omega_r \dot{y} - \omega_r^2 z) \hat{\boldsymbol{e}}_n \end{aligned} \quad (4.30)$$

where the angular velocity has also been resolved into its LVLH components:

$$\omega_r = \dot{\Omega} \frac{\sin i}{\sin \theta} \quad (4.31a)$$

$$\omega_t = 0 \quad (4.31b)$$

$$\omega_n = \dot{\theta}_u = h/r^2 \quad (4.31c)$$

The term $\Delta \ddot{\mathbf{r}}$ represents the differential perturbing accelerations. If only the SRP differential acceleration is considered, then, in the case of the earlier listed assumptions, this term is due only to the differential gravity, which is assumed to be a two-body potential for now:

$$\Delta \ddot{\mathbf{r}}_{J_0} = \frac{\mu}{r^3} \begin{pmatrix} 2x \\ -y \\ -z \end{pmatrix} \quad (4.32)$$

The choice of local Cartesian/curvilinear coordinates for treatment of the perturbed relative motion problem has led to one important limitation: large chief orbit eccentricities introduce significant analytical difficulties to the derivation, for multiple reasons. While such problems are still analytically tractable, this derivation is restricted to cases of $e \approx 0$ (near-circular orbits) and $\dot{a} \approx 0$ (negligible changes to orbit specific energy). This dynamical model can theoretically be adapted for perturbed eccentric orbits, assuming $\dot{e} \approx 0$ still holds, and that all ρ terms are updated to account for the variations in the chief radius. Note that writing $\dot{e} \approx 0$ only implies the assumption that the effects from \dot{e} are small compared to the first-order effects of the solar radiation pressure. However, this will not always be the case. Both the long and short-term effects of solar radiation pressure on eccentricity are discussed extensively by [114]. Relaxing of the aforementioned assumptions and further potential developments of the model are left to future work.

To first order in the SRP terms, assuming $\dot{a} \approx 0$ and $\dot{e} \approx 0$, it can be shown that the only nonzero angular acceleration term is $\dot{\omega}_r$, given below with the nonzero angular velocity squared terms:

$$\dot{\omega}_r = n \frac{\sin i}{\sin \theta} \left(\frac{d}{d\theta} \left(\dot{\Omega} \right) - \dot{\Omega} \frac{\cos \theta}{\sin \theta} \right) + \dot{\varphi} \frac{\sin i}{\sin \theta} \frac{d}{d\varphi} \left(\dot{\Omega} \right) \quad (4.33)$$

$$\omega_n \omega_r = n \rho^{-3/2} \dot{\Omega} \frac{\sin i}{\sin \theta} \quad (4.34)$$

$$\omega_n^2 = \frac{h^2}{r^4} \quad (4.35)$$

where $\rho = r/a$ and n is the orbital mean motion. From the near-circular orbit assumption and the assumption $\dot{a} \approx 0$, it is implied that $r(t) \approx a$, thus $\dot{\theta}_p \approx n$ and $\rho \approx 1$. These assumptions will not be valid for long time spans if the SRP disturbance acceleration is large enough to significantly change the chief orbit. Evaluating Eqs. (4.33) – (4.35), all nonzero kinematic terms are presented below, explicitly in terms of N_{SRP} :

$$\omega_r = \frac{r}{h} N_{\text{SRP}}, \quad \omega_n = \frac{h}{r^2} \quad (4.36)$$

$$\dot{\omega}_r = \dot{\varphi} \frac{r}{h} \frac{d}{d\varphi} (N_{\text{SRP}}) \quad (4.37)$$

$$\omega_n \omega_r = n \rho^{-3/2} \frac{r}{h} N_{\text{SRP}}, \quad \omega_n^2 = \frac{h^2}{r^4} \quad (4.38)$$

The final linearized relative motion equations are obtained and presented below in matrix-vector form, resolved in the chief-centered LVLH frame, \mathcal{H} .

$$\begin{pmatrix} \ddot{x} \\ \ddot{y} \\ \ddot{z} \end{pmatrix} = \begin{bmatrix} h^2/r^4 + 2\frac{\mu}{r^3} & 0 & -n\rho^{-3/2}\frac{r}{h}N_{\text{SRP}} \\ 0 & h^2/r^4 - \frac{\mu}{r^3} & \dot{\varphi}\frac{r}{h}\frac{d}{d\varphi}(N_{\text{SRP}}) \\ -n\rho^{-3/2}\frac{r}{h}N_{\text{SRP}} & -\dot{\varphi}\frac{r}{h}\frac{d}{d\varphi}(N_{\text{SRP}}) & -\frac{\mu}{r^3} \end{bmatrix} \begin{pmatrix} x \\ y \\ z \end{pmatrix} + \begin{bmatrix} 0 & 2\frac{h}{r^2} & 0 \\ -2\frac{h}{r^2} & 0 & 2\frac{r}{h}N_{\text{SRP}} \\ 0 & -2\frac{r}{h}N_{\text{SRP}} & 0 \end{bmatrix} \begin{pmatrix} \dot{x} \\ \dot{y} \\ \dot{z} \end{pmatrix} \quad (4.39)$$

If small variations in the chief orbit radius are known, and any resulting terms are of the same order as linear SRP-associated terms, then the substitution of these variations may be desirable.

Otherwise, if $r \approx a \forall t$, and e is small, the expression may be simplified further:

$$\begin{pmatrix} \ddot{x} \\ \ddot{y} \\ \ddot{z} \end{pmatrix} = \begin{bmatrix} 3n^2 & 0 & -n\frac{a}{h}N_{\text{SRP}} \\ 0 & 0 & \dot{\varphi}\frac{a}{h}\frac{d}{d\varphi}(N_{\text{SRP}}) \\ -n\frac{a}{h}N_{\text{SRP}} & -\dot{\varphi}\frac{a}{h}\frac{d}{d\varphi}(N_{\text{SRP}}) & -n^2 \end{bmatrix} \begin{pmatrix} x \\ y \\ z \end{pmatrix}$$

$$+ \begin{bmatrix} 0 & 2n & 0 \\ -2n & 0 & 2\frac{a}{h}N_{\text{SRP}} \\ 0 & -2\frac{a}{h}N_{\text{SRP}} & 0 \end{bmatrix} \begin{pmatrix} \dot{x} \\ \dot{y} \\ \dot{z} \end{pmatrix} \quad (4.40)$$

The position and velocity-associated matrices in Eq. (4.40) are denoted as $[A_p]$ and $[A_v]$, respectively. Reusing the state representation $\mathbf{x} = [x, y, z, \dot{x}, \dot{y}, \dot{z}]^\top$, for which one may write $\dot{\mathbf{x}} = [A(t)]\mathbf{x}$, the time-varying $[A]$ matrix is:

$$[A] = \begin{bmatrix} 0_{3 \times 3} & I_{3 \times 3} \\ A_p & A_v \end{bmatrix} \quad (4.41)$$

with all components of the linear model defined, the linearized relative orbital motion dynamics can now be expressed in their usual form:

$$\dot{\mathbf{x}} = [A(t)]\mathbf{x} + [B(t)]\mathbf{u} \quad (4.42)$$

The $[A]$ matrix terms are given in Eqs. (4.40) – (4.41). The control-associated $[B]$ matrix is given in Eq. (4.22), with the lower 3×3 sub-matrix now pre-multiplied by $[\mathcal{HP}]$ to resolve the resultant control accelerations in the LVLH frame components.

4.3 Spacecraft Relative Motion Control

This section discusses and demonstrates the implementation of the new SRP-perturbed relative orbital motion model for control.

4.3.1 Linear SRP-Based Formation and Rendezvous Control

Control in this chapter is performed using the Linear Quadratic Regulator (LQR), which is for the design of a control input \mathbf{u} that minimizes the finite-time cost function shown below, under the action of the linearized dynamics $\dot{\mathbf{x}} = [A]\mathbf{x} + [B]\mathbf{u}$ [124].

$$J = \frac{1}{2} \int_{t_0}^{t_f} \left(\mathbf{x}^\top [Q] \mathbf{x} + \mathbf{u}^\top [R] \mathbf{u} \right) dt + \frac{1}{2} \mathbf{x}_f^\top [S_f] \mathbf{x}_f \quad (4.43)$$

where $[Q]$ and $[R]$ are the state and control-associated weight matrices, and $[S_f]$ is the matrix associated with the quadratic final state cost. The solution is given below:

$$\mathbf{u} = -[K_x]\mathbf{x} \quad (4.44)$$

The time-varying gain matrix $[K_x]$ is given in terms of $[S]$, obtained by solving the Riccati differential equation with final condition $[S(t_f)] = [S_f]$:

$$[K_x] = [R]^{-1}[B]^\top[S] \quad (4.45)$$

$$[\dot{S}] + [S][A] + [A]^\top[S] - [S][B][R]^{-1}[B]^\top[S] + [Q] = [0] \quad (4.46)$$

4.3.2 Controllability Analysis

Before the SRP-based control is simulated, controllability analysis provides some insight into the problem. For completeness, the time-varying effects of the SRP perturbation are included in the $[A]$ matrix for the relative motion dynamics.

For an LTV system with n states, if the following is satisfied, the system is controllable [124]:

$$\text{rank}\left([B_0(t), B_1(t), \dots, B_{n-1}(t)]\right) = n \quad (4.47)$$

where $[B_0] = [B]$ and all other elements are given by the following:

$$[B_{i+1}(t)] = [A(t)][B_i(t)] - \frac{d}{dt}[B_i(t)] \quad (4.48)$$

The rank of the controllability matrix, if less than n , determines the dimension of the controllable subspace.

To facilitate this discussion for SRP-based control, the $[B]$ matrix is now resolved into \mathcal{H} :

$$[B] = \begin{bmatrix} 0_{3 \times 3} \\ [\mathcal{HN}][\mathcal{NP}][B_C] \end{bmatrix} \quad (4.49)$$

where $[B_C]$ is the constant part of the $[B]$ matrix:

$$\begin{aligned} [B_C] = 4P(R) \frac{A}{m} & \left((\bar{a}_2 + 2\bar{\rho}s)C_{1(1,1)} C_{1(1,1)}[C_1(\boldsymbol{\sigma}_r)]^\top[\tilde{\mathbf{e}}_1] - (1 - \bar{\rho}s)[\hat{\mathbf{e}}_1\hat{\mathbf{e}}_1^\top][\tilde{\mathbf{e}}_1] \right. \\ & \left. + (\bar{a}_2 + 4\bar{\rho}s)C_{1(1,1)} [C_1(\boldsymbol{\sigma}_r)]^\top[\hat{\mathbf{e}}_1\hat{\mathbf{e}}_1^\top][C_1(\boldsymbol{\sigma}_r)]^\top[\tilde{\mathbf{e}}_1] \right) \end{aligned} \quad (4.50)$$

If the reference orientation is sun-facing, then $[C_1(\boldsymbol{\sigma}_r)] = [I_{3 \times 3}]$ and a much simpler form is obtained for $[B_C]$:

$$[B_C] = 4P(R) \frac{A}{m} (\bar{a}_2 + 2\bar{\rho}s) [\tilde{\mathbf{e}}_1] \quad (4.51)$$

For this controllability analysis, it is assumed that the reference orientation is sun-facing. The rotation from \mathcal{P} to \mathcal{H} is time-varying, and thus the $[B]$ matrix will be time-varying as well. Furthermore, the $[A]$ matrix is time-varying. The time-varying terms in the $[A]$ matrix obtained from Eq. (4.40) can be expected to evolve slowly compared to the time scale of the relative orbital motion dynamics.

Using the SRP-perturbed system $[A]$ matrix, the controllability matrix is obtained in terms of the $[B_i(t)]$ sub-matrices:

$$[B_i(t)] = [B'_i(t)][B_C] = \begin{bmatrix} [B'_{i(u)}(t)] \\ [B'_{i(l)}(t)] \end{bmatrix} [B_C] \quad (4.52)$$

where the time-varying portion $[B'_i(t)]$ can be shown to obey the following recursive relationship and initial values:

$$[B'_{i+1}(t)] = \begin{bmatrix} [B'_{i(l)}(t)] - \frac{d}{dt} \left([B'_{i(u)}(t)] \right) \\ [A_p][B'_{i(u)}(t)] + [A_v][B'_{i(l)}(t)] - \frac{d}{dt} \left([B'_{i(l)}(t)] \right) \end{bmatrix} \quad (4.53)$$

$$[B'_{0(u)}(t)] = [0_{3 \times 3}], \quad [B'_{0(l)}(t)] = [\mathcal{HP}] \quad (4.54)$$

Using Eq. (4.53), and recalling $[B_0(t)] = [B(t)]$, the next two sub-matrices are shown analytically:

$$[B_1(t)] = \begin{bmatrix} [\mathcal{HP}] \\ [A_v][\mathcal{HP}] - [\mathcal{HP}][\tilde{\omega}_{H,P}] \end{bmatrix} [B_C] \quad (4.55)$$

$$[B_2(t)] = \begin{bmatrix} [A_v][\mathcal{HP}] - 2[\mathcal{HP}][\tilde{\omega}_{H,P}] \\ [A_p][\mathcal{HP}] + [A_v]^2[\mathcal{HP}] - 2[A_v][\mathcal{HP}][\tilde{\omega}_{H,P}] + [\mathcal{HP}][\tilde{\omega}_{H,P}]^2 - [\dot{A}_v][\mathcal{HP}] \end{bmatrix} [B_C] \quad (4.56)$$

where $[\tilde{\omega}_{H,P}]$ is an angular velocity term associated with the rotating frames:

$$\frac{d}{dt} ([\mathcal{HP}]) = [\mathcal{HP}][\tilde{\omega}_{H,P}] \quad (4.57)$$

The matrix $[\tilde{\omega}_{H,P}]$ is skew-symmetric, with the components of the angular velocity of frame \mathcal{P} relative to \mathcal{H} , expressed in \mathcal{P} components. Note that it is assumed that angular acceleration terms are zero because the effect of rotating frame angular acceleration terms is quite small for near-circular planetary and spacecraft orbits. Thus, $[\dot{\tilde{\omega}}_{H,P}] \approx [0_{3 \times 3}]$.

The symbolic expressions for each sub-matrix were obtained via MATLAB and saved as functions. To enforce the zero angular acceleration condition, the time-varying angular terms were truncated to their linear approximations, $\theta \approx \theta_0 + nt$ and $\varphi \approx \varphi_0 + \dot{\varphi}t$. The final expression for the controllability matrix is far too long and complex to include here.

Table 4.1 gives hypothetical parameters for evaluating the controllability matrix, and for the first set of simulation results to follow this controllability analysis. The optical parameters for this first result are values corresponding to a completely reflective surface [89], but adding absorption doesn't affect the conclusion of the controllability analysis. This hypothetical simulation data is representative of some high-altitude orbit over a large asteroid. Only two-body gravity and SRP perturbations are implemented in the truth model, since this chapter is primarily concerned with the solar radiation pressure perturbation, which would be a dominant disturbance at this altitude.

Table 4.1: SRP Control Simulation 1 Physical Parameters

Parameter	Value
$\mathbf{ae}_0 = (a, e, i, \Omega, \theta)$	200, 0.0, 86.0°, 0.0°, 0.0°
$\delta\mathbf{ae}_0 = (\delta a, \delta e, \delta i, \delta\Omega, \delta\theta)$	0.0, 0.00125, 0.05°, 0.0°, 0.0°
Optical constants	$\frac{A}{m} = 0.5\text{m}^2/\text{kg}, \bar{B} = 0.8, \bar{s} = 0.7, \bar{\rho} = 0.3$
Primary Body Orbit Radius	$R = 3.5904 \times 10^8\text{km}$ (2.4AU)
Primary Body Orbit Angles	$\kappa = 4^\circ, \varphi_0 = 90^\circ$
Primary Body Physical Parameters	$d = 40\text{km}, \rho = 2.119\text{g}/\text{cm}^3, m = 7.1 \times 10^{16}\text{kg}$

Using the parameters in Table 4.1, the rank of the controllability matrix may be obtained for various times in the simulation. Numerical results show that the rank of the controllability matrix is consistently 6, using the default tolerance in MATLAB. Lowering the tolerance (e.g. to 1×10^{-10}), the rank of the controllability matrix reduces to 4. These numerical results suggest that the system is fully controllable, with kinematic coupling enabling weak controllability of the spacecraft motion along $\hat{\mathbf{u}}$.

4.3.3 Testing the SRP-Perturbed Relative Motion Model

First, results are presented to demonstrate that the dynamical model obtained in this chapter works as expected. Namely, the model given in Eq. (4.40) was simulated for the data given in Table

4.1, along with a nonlinear truth model. The results are given in Figure 4.2. Note that there is close agreement between the SRP model and the nonlinear truth model for the 6 orbits simulated. This shows that the linearized SRP model is properly accounting for the SRP disturbance acceleration's effects.

4.3.4 Simulation Results

With the efficacy of the linearized dynamical model demonstrated, finite-time LQR control is now implemented to obtain the optimal control signals $\mathbf{u}(t) = \boldsymbol{\sigma}_c(t)$. Of particular interest is the full controllability of the system implied by the analysis in the preceding section. It was hypothesized that controllability is weakest in the projection of the motion along $\hat{\mathbf{u}}$. Setting the relative motion to take place near the terminator plane allows the motion along $\hat{\mathbf{u}}$ to be easily investigated. Without treating the out-of-plane associated elements of the $[Q]$ matrix differently from the in-plane associated elements, simulation results show that the motion in the z direction fails to settle. However, by over-weighting the cost of z and \dot{z} in the dynamics, the controller takes a strategy that seeks to minimize the motion in this mode, by delaying the settling of the x and y motion.

The first simulation demonstrates relative motion regulation control to a chief in a terminator orbit. The non-optical physical constants and initial conditions are unchanged from the uncontrolled simulation - thus are given in Table 4.1. The control parameters and the new optical parameters for this simulation are given in Table 5.2.

Table 4.2: Control and Optical Parameters for SRP Control Simulation 1

Parameter	Value
Q	$Q = I_{6 \times 6}$, except $Q(3, 3) = Q(6, 6) = 60$
R	$100I_{3 \times 3}$
S_f	$I_{6 \times 6}$
$t_0, \Delta t, t_f$	$t_0 = 0, \Delta t = 10, t_f = 2581510$ (29.88 days)
Optical constants	$\frac{A}{m} = 0.5\text{m}^2/\text{kg}, \bar{B} = 0.6, \bar{s} = 0.25, \bar{\rho} = 0.3$

The position deviations and control signals are given in Figures 4.4 and 4.5. The results

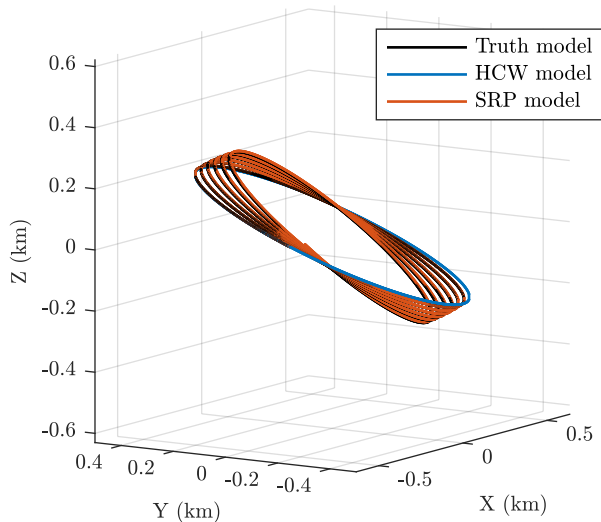


Figure 4.2: SRP-Perturbed Relative Motion

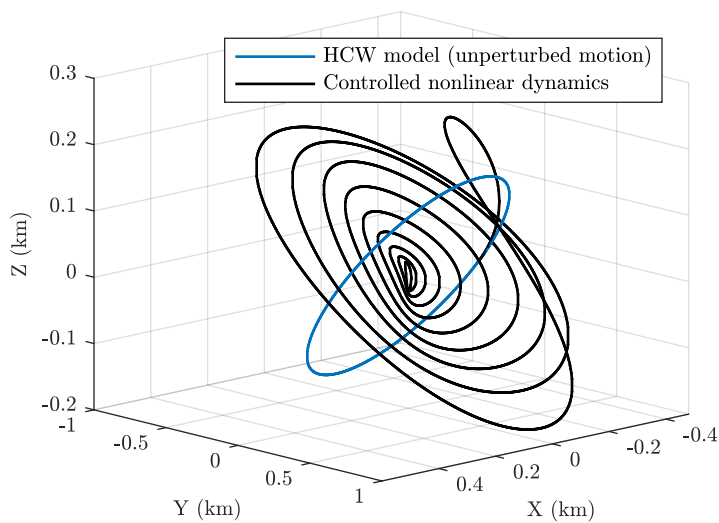


Figure 4.3: SRP-Based Control of Relative Motion, Case 1

show that for this case, the controller functions as intended – successfully controlling the deputy spacecraft to very near the origin of the LVLH frame, over the course of one month. This is done with $< 10^\circ$ attitude deviations from the sun-pointing direction. This is important in the context of this work, because the attitude variations must remain small in order for the single-plate SRP

model to be accurate.

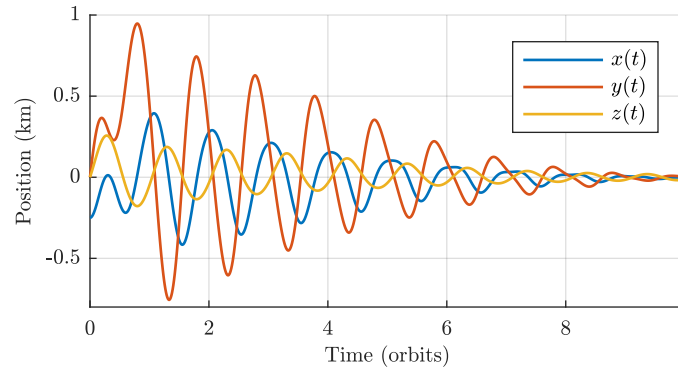


Figure 4.4: Position, SRP Control Case 1

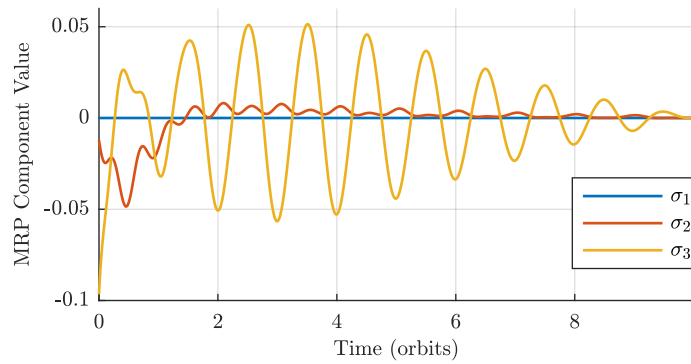


Figure 4.5: Control Signals, SRP Control Case 1

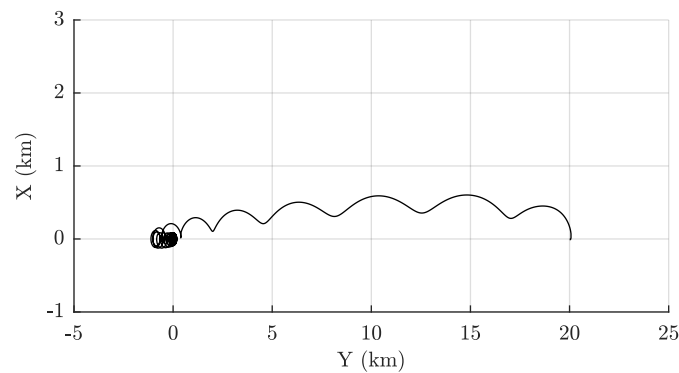


Figure 4.6: SRP-Based Control of Relative Motion, Case 2

The second simulation demonstrates control to change a GEO orbit longitude by 0.544° , or

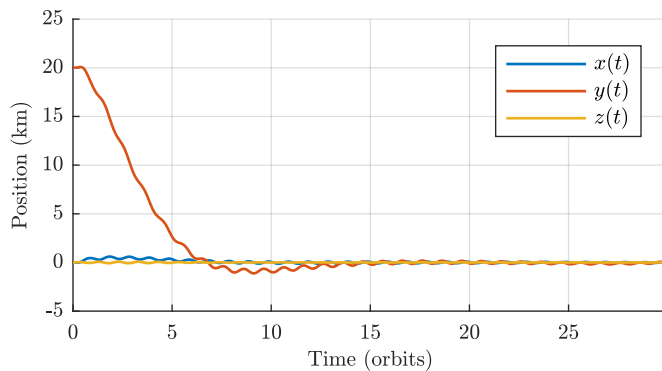


Figure 4.7: Controlled Position, SRP Control Case 2

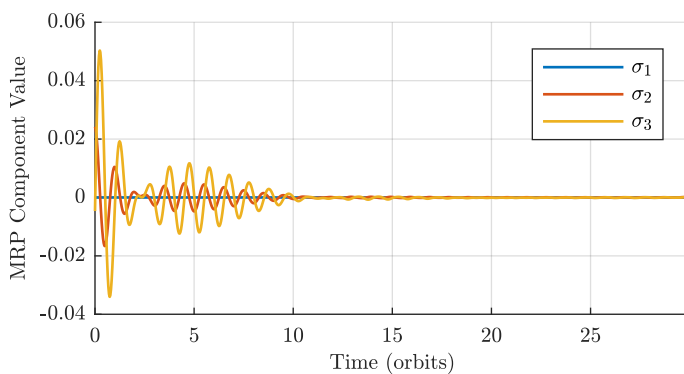


Figure 4.8: Control Signals, SRP Control Case 2

20 km in the along-track direction, over the course of 30 days. The optical parameters are the same as in the first simulation, but the other physical parameters and the new control parameters are different. These are given in Tables 4.3 and 4.4 respectively. This simulation neglects the perturbative effects of lunar and solar gravity, which manifest via a long term (53 year) precession and nutation of the orbit [4]. In this particular case, a scale analysis of the lunar gravity perturbation will show that there would be sufficient control authority to cancel such perturbations in addition to controlling the spacecraft to the desired location.

The motion in LVLH x and y components is given in Figure 4.6. The z motion is quite insignificant in this case, so it is not shown. Note that the scale of the x motion is magnified in the figure to show the bowed nature of the trajectory followed, and to clearly show the oscillations in

the radial direction. Also note the overshoot in the y direction followed by the slow settling behavior around the origin. There are two time scales of the settling behavior. Much of the separation is settled in the along-track direction within 15 orbits, but the control action in the remaining orbits slowly dampens out the oscillations mainly in the x and y components. The large final cost on the relative state ensures that in the final 3-4 orbits, the relative motion is further settled.

Table 4.3: SRP Control Simulation 2 Physical Parameters

Parameter	Value
$\mathbf{oe}_0 = (a, e, i, \Omega, \theta)$	42157, 0.0, 0.0°, 0.0°, 0.0°
$\delta\mathbf{oe}_0 = (\delta a, \delta e, \delta i, \delta\Omega, \delta\theta)$	0.0, 0.0, 0.0°, 0.0°, 0.544°
Primary Body Orbit Radius	$R = 1.496 \times 10^8 \text{km}$ (1.0AU)
Primary Body Orbit Angles	$\kappa = 23.5^\circ, \varphi_0 = 90^\circ$
Primary Body Physical Parameters	$r = 6371 \text{ km}, \mu = 398600 \text{ km}^3/\text{s}^2$

Table 4.4: Control and Optical Parameters for SRP Control Simulation 2

Parameter	Value
Q	$0.5I_{6 \times 6}$
R	$10^5 I_{3 \times 3}$
S_f	$S_f = 10^8 I_{6 \times 6}$, except $S_f(1, 1) = 10^{10}$ & $S_f(4, 4) = 10^{11}$
$t_0, \Delta t, t_f$	$t_0 = 0, \Delta t = 80, t_f = 2584240$ (30 days)
Optical constants	$\frac{A}{m} = 0.5 \text{m}^2/\text{kg}, \bar{B} = 0.6, \bar{s} = 0.25, \bar{\rho} = 0.3$

These results suggest that relatively large maneuvers in the GEO belt are possible with SRP-based linear control, assuming sufficient time is available for such maneuvers. Faster settling results would likely be possible through iteration on the current selection of control parameters, but these results are an adequate demonstration of capability. The results from cases 1 and 2 show that both closed-loop rendezvous control and larger changes to a GEO orbit using a virtual chief are possible using small sustained attitude variations to change the resultant SRP disturbance force. This is simulated for spacecraft with relatively realistic area-to-mass ratios and unremarkable (neither highly reflective or absorptive) optical properties. Simulations with smaller area-to-mass ratios still display the same characteristic behavior, but with longer time spans needed to achieve the same control objectives.

4.4 Conclusions

This chapter derives a new relative motion model accounting for the effects of the solar radiation pressure (SRP) disturbance acceleration on spacecraft relative motion. The kinematics of the SRP-perturbed chief orbit are absorbed into the linearized system $[A(t)]$ matrix to accommodate infrequent updates of the chief orbit parameters. The model demonstrates the feasibility of SRP-based control in multiple environments of interest for spacecraft with unremarkable geometry and surface optical properties. The model is derived from an existing multi-facet model of SRP force, obtaining an illuminated body averaged single-plate model that should be valid for small angular attitude deviations, especially for spacecraft with large solar arrays, or otherwise relatively flat spacecraft. Numerical simulations of SRP-based control for spacecraft with unremarkable geometric and optical properties establish the feasibility of the use of attitude-dependent SRP force for formation and rendezvous control.

Future work could explore refinements to the methods used in this work, and will detail the limitations of the model and control strategy used in this work. Future work could also include higher-fidelity multi-facet spacecraft SRP modeling that is valid for larger attitude variations, and explorations of how to account for independent articulation of solar arrays in a box-wing spacecraft model. A multi-fidelity modeling approach could enable a low-level control strategy (linear or otherwise) to be corrected for high precision SRP-based control. Look-up tables generated in advance (or series fits of such data) could take place of the linearized approximation of the attitude-dependent variations in the magnitude and direction of the resultant SRP acceleration. This work is thus the first step towards a goal of accurate high-fidelity SRP-based formation and orbit control.

Chapter 5

Spacecraft Relative Motion Sensitivities

This chapter explores the use of the linear sensitivities in spacecraft relative motion modeling and control. The sensitivity is the derivative of the spacecraft relative state with respect to an uncertain or mis-modeled parameter in the dynamics:

$$\mathbf{s} = \left. \frac{d\mathbf{x}}{d\alpha} \right|_* \quad (5.1)$$

where the “*” subscript denotes evaluation on a nominal trajectory, and for the nominal case, $\alpha = \alpha^*$. The sensitivity vector also has its own dynamics, obtained by direct differentiation of Eq. (5.1) [72]:

$$\begin{aligned} \dot{\mathbf{s}} &= \frac{d}{dt} \left(\left. \frac{d\mathbf{x}}{d\alpha} \right|_* \right) = \frac{d}{d\alpha} \left(\left. \frac{d\mathbf{x}}{dt} \right|_* \right) \\ &= \frac{d}{d\alpha^*} ([A(\alpha^*)]) \mathbf{x} + [A(\alpha^*)] \mathbf{s} + \frac{d}{d\alpha^*} ([B(\alpha^*)]) \mathbf{u} \end{aligned} \quad (5.2)$$

The true behavior of \mathbf{x} can then be linearly approximated as the sum of the nominal behavior and the product of the sensitivity and the difference between the true and nominal value of the uncertain parameter:

$$\mathbf{x}(t) = \mathbf{x}^*(t) + (\alpha - \alpha^*) \mathbf{s}(t) \quad (5.3)$$

Note lastly that all of the equations above generalize naturally for a system with N independent uncertain parameters, e.g.:

$$\mathbf{x}(t) = \mathbf{x}^*(t) + \sum_{i=1}^N (\alpha_i - \alpha_i^*) \mathbf{s}_i(t) \quad (5.4)$$

Eqs. (5.2) and (5.3) are of critical importance to this chapter. The true behavior of a system with an uncertain parameter is governed by the sensitivities, these sensitivities have their own

simple dynamics, and in some circumstances can be influenced by control. This prompts two explorations: First, the concept of “desensitized control” is explored for the spacecraft relative motion problem, in which control of \boldsymbol{x} is augmented with control of the sensitivities of the relative motion to poorly modeled parameters. Second, the dynamics of uncertainty propagation of the spacecraft relative motion problem are examined through the perspective of the sensitivities for the case that a spacecraft moves and maneuvers in the vicinity of a target object with an uncertain orbit. Much of the work in this chapter can be found in References 21 and 27, and 55 is also relevant.

The sensitivity dynamics and control concepts explored in this chapter have some strong connections to other recent concepts in the literature. Reference 56 poses the aerocapture problem as a robust optimization problem. This work explores multi-objective control simultaneously minimizing mean drift from a desired terminal state \boldsymbol{x}^* along with variation of \boldsymbol{x} about its mean. In the case that the mean objective is exactly satisfied, the problem reduces to minimizing a weighted trace of the final covariance. This approach shares some similarities with desensitized control, because it can be shown from consider-covariance analysis [125] that the linear sensitivities map between parameter covariance and state covariance, so any control to achieve certain goals with the final state covariance matrix will accomplish this via influence on the final sensitivity states.

5.1 Desensitized Optimal Spacecraft Rendezvous Control

5.1.1 Dynamical Uncertainty in the Spacecraft Relative Motion Problem

Uncertainty is a major obstacle to robust spacecraft control. In particular, while the physics of the space environment are often reasonably well understood, the true values of perturbative parameters are frequently poorly known. This is especially true in missions to previously unexplored or dynamically complex bodies. This can also still pose a challenge for more familiar environments with unpredictable variations, such as the constantly changing conditions of the rarefied atmosphere in low-Earth orbits. Controllers that are not designed to account for or be robust to uncertainty

are fundamentally ill-suited for use in such space missions. An active area of research is design of controllers that are naturally robust to poorly-known dynamical parameters. Such controllers still typically use some nominal or expected values for these parameters, but are designed to be operationally desensitized to reasonable deviations from the expected values. Desensitized linear optimal control is one appealing option, due to its relative ease of design, analysis, and implementation. This method was first developed by Kahne [72] in the 1960s, and fundamentally similar methods have been applied in trajectory design [117] and optimal landing guidance [118]. Similar work has also been done in desensitized optimal filtering, in which the estimator is designed to be tolerant of poorly known dynamical parameters [74]. It is possible to develop desensitized control for the spacecraft relative motion problem, which enables more robust control design for rendezvous guidance and formation maintenance.

This section implements a new approach to spacecraft relative motion Linear Quadratic Regulator (LQR) control in a highly uncertain environment, with a modification to design a linearly optimal controller that is minimally sensitive to chosen system perturbations, but otherwise inherits the traditional features of LQR control. This is done by extending the work originally presented by Kahne [72] to enable control design that is desensitized to variations in an arbitrary number of poorly known system dynamical parameters, and applying the method to spacecraft formation/rendezvous control.

As an example application, this section is focused on control design in the highly perturbed environment around small asteroids, in which the gravitational harmonics C_{20} and C_{22} and solar radiation pressure (SRP) constitute the dominant perturbations for a range of orbits potentially desirable for future missions. The decision to truncate the gravitational effects at the second degree and order implicitly assumes that the spacecraft are in high orbits, where individual surface features and higher order gravity field components are dominated by the C_{20} and C_{22} perturbation. Third-body effects may also be important enough to warrant inclusion in the control design, in sufficiently high orbits. This work could be extended to apply in such an environment if the effects of the additional perturbation is accounted for, and the modification is conceptually straightforward.

The control design assumes that the gravitational harmonics are not well-known (such as if they are estimated from light curve data [71]). Uncertainty in the magnitude of the SRP force is also considered. The control model is first derived using the linearized dynamics containing linear perturbation terms due to gravity coefficients C_{20} and C_{22} , and the SRP force, and the controller is then applied in a nonlinear dynamic truth model with differing values of the chosen dynamical parameters to test the performance of the controller. This section investigates the effect of these mis-modeled parameters on the control performance for both standard LQR and desensitized optimal control.

The work presented in this section is directly relevant for mission design to small-body environments, in which after orbital insertion, it is desired to correct to a nominal orbit, maintain a nominal orbit under the presence of perturbations, or even facilitate spacecraft rendezvous in this uncertain environment. However, the given implementation can be easily adapted for robust rendezvous control in Earth orbits as well, and the procedure introduced in this section can be readily adapted to minimize uncertainty to essentially any other poorly known dynamical parameters.

5.1.2 Dynamic Model

This section makes use of the combined C_{20} , C_{22} , and SRP model first presented in [chapter 3](#), without further modification. See Eqs. (3.48) - (3.51) and the associated discussion.

5.1.3 Low-Sensitivity Optimal Control Design

A method of optimal control design is introduced, which minimizes the effect of mis-modeled parameters by augmenting in the sensitivities to these parameters to the cost function:

$$J = \frac{1}{2} \mathbf{x}^\top(t_f)[S]\mathbf{x}(t_f) + \frac{1}{2} \int_0^{t_f} \left(\mathbf{x}^\top(t)[Q(t)]\mathbf{x}(t) + \mathbf{u}^\top(t)[R(t)]\mathbf{u}(t) + \mathbf{s}^\top(t)[E(t)]\mathbf{s}(t) \right) dt \quad (5.5)$$

where $[E]$ is the weight matrix associated with the sensitivity cost and $\mathbf{s}(t)$ is the sensitivity vector:

$$\mathbf{s}(t) = \left. \frac{d\mathbf{x}(t)}{d\alpha} \right|_{\alpha_{nom}} \quad (5.6)$$

and it can be shown to obey

$$\dot{\mathbf{s}}(t) = [A(t)]\mathbf{s}(t) + [C(t)]\mathbf{x}(t) \quad (5.7)$$

where $[C(t)]_{ij} = \left. \frac{d[A]_{ij}}{d\alpha} \right|_{\alpha_{\text{nom}}}$. This elegant modification of the LQR optimal control problem was first performed by Kahne [72]. In order to use this technique to apply to a control problem with three poorly-known parameters, two additional sensitivity vector terms must be added to the cost function, and the same procedure will be followed to derive the modified equations for optimal control that minimizes the controlled trajectory sensitivity to three parameters.

Now, Kahne's procedure is extended to optimal linear control with an arbitrary number of sensitivity vectors augmented into the cost function:

$$J = \frac{1}{2} \mathbf{x}^\top(t_f)[S]\mathbf{x}(t_f) + \frac{1}{2} \int_0^{t_f} \left(\mathbf{x}^\top(t)[Q(t)]\mathbf{x}(t) + \mathbf{u}^\top(t)[R(t)]\mathbf{u}(t) + \sum_{i=1}^p \mathbf{s}_i^\top(t)[E_i(t)]\mathbf{s}_i(t) \right) dt \quad (5.8)$$

where $\mathbf{s}_i(t)$ is the i^{th} sensitivity vector:

$$\mathbf{s}_i(t) = \left. \frac{d\mathbf{x}(t)}{d\alpha_i} \right|_{\alpha_{i,\text{nom}}} \quad (5.9)$$

$$\dot{\mathbf{s}}_i(t) = [A(t)]\mathbf{s}_i(t) + [C_i(t)]\mathbf{x}(t) \quad (5.10)$$

$$[C_{i(jk)}(t)] = \left. \frac{\partial[A_{jk}(t)]}{\partial\alpha_i} \right|_{\alpha_{i,\text{nom}}} \quad (5.11)$$

The Hamiltonian is given below:

$$H = \frac{1}{2} \left(\mathbf{x}^\top [Q] \mathbf{x} + \mathbf{u}^\top [R] \mathbf{u} + \sum_i \mathbf{s}_i^\top [E_i] \mathbf{s}_i \right) + \boldsymbol{\lambda}^\top ([A] \mathbf{x} + [B] \mathbf{u}) + \sum_i \mathbf{q}_i^\top ([A] \mathbf{s}_i + [C_i] \mathbf{x}) \quad (5.12)$$

The necessary conditions for optimality yield the following:

$$\dot{\mathbf{x}} = \frac{\partial H}{\partial \boldsymbol{\lambda}} = [A] \mathbf{x} + [B] \mathbf{u} \quad (5.13)$$

$$\dot{\boldsymbol{\lambda}} = -\frac{\partial H}{\partial \mathbf{x}} = -[Q] \mathbf{x} - [A]^\top \boldsymbol{\lambda} - \sum_i [C_i]^\top \mathbf{q}_i \quad (5.14)$$

$$\dot{\mathbf{s}}_i = \frac{\partial H}{\partial \mathbf{q}_i} = [A] \mathbf{s}_i + [C_i] \mathbf{x} \quad (5.15)$$

$$\dot{\mathbf{q}}_i = -\frac{\partial H}{\partial \mathbf{s}_i} = -[E_i] \mathbf{s}_i - [A]^\top \mathbf{q}_i \quad (5.16)$$

$$\frac{\partial H}{\partial \mathbf{u}} = [R] \mathbf{u} + [B]^\top \boldsymbol{\lambda} = \mathbf{0} \rightarrow \mathbf{u}(t) = -[R]^{-1} [B]^\top \boldsymbol{\lambda}(t) \quad (5.17)$$

The split final and initial conditions are $\mathbf{x}(0) = \mathbf{x}_0$, $\boldsymbol{\lambda}(t_f) = [S]\mathbf{x}(t_f)$, $\mathbf{s}_i(0) = \mathbf{0}$, $\mathbf{q}_i(t_f) = \mathbf{0}$.

To adapt the matrix/vector notation to an arbitrary number (p) of sensitivities, the augmented vector notation $\mathbf{s}_{p \times 1} = (\mathbf{s}_1^\top, \mathbf{s}_2^\top, \dots, \mathbf{s}_p^\top)$ is defined, along with necessary augmented matrix notation given below:

$$[C_{6p \times 6}] = \begin{bmatrix} [C_1] \\ [C_2] \\ \vdots \\ [C_p] \end{bmatrix}, \quad [C_{6p \times 6}]^\top = \begin{bmatrix} [C_1]^\top & [C_2]^\top & \dots & [C_p]^\top \end{bmatrix} \quad (5.18)$$

$$[A_{6p \times 6p}] = \begin{bmatrix} [A] & [0_{6 \times 6}] & \dots \\ [0_{6 \times 6}] & \ddots & \\ \vdots & & [A] \end{bmatrix} \quad (5.19)$$

The augmented system dynamics are given below:

$$\begin{pmatrix} \dot{\mathbf{x}} \\ \dot{\mathbf{s}}_{6p \times 1} \\ \dot{\boldsymbol{\lambda}} \\ \dot{\mathbf{q}}_{6p \times 1} \end{pmatrix} = \begin{bmatrix} [A] & [0_{6 \times 6p}] & -[B][R]^{-1}[B]^\top & [0_{6 \times 6p}] \\ [C_{6p \times 6}] & [A_{6p \times 6p}] & [0_{6p \times 6}] & [0_{6p \times 6p}] \\ -[Q] & [0_{6 \times 6p}] & -[A]^\top & -[C_{6p \times 6}]^\top \\ [0_{6p \times 6}] & -[E_{6p \times 6p}] & [0_{6p \times 6}] & -[A_{6p \times 6p}]^\top \end{bmatrix} \begin{pmatrix} \mathbf{x} \\ \mathbf{s}_{6p \times 1} \\ \boldsymbol{\lambda} \\ \mathbf{q}_{6p \times 1} \end{pmatrix} \quad (5.20)$$

Let $\mathbf{z} = (\mathbf{x}^\top, \mathbf{s}_{6p \times 1}^\top)$, $\boldsymbol{\psi} = (\boldsymbol{\lambda}^\top, \mathbf{q}_{6p \times 1}^\top)$, thus:

$$\begin{pmatrix} \dot{\mathbf{z}} \\ \dot{\boldsymbol{\psi}} \end{pmatrix} = [\Gamma(t)] \begin{pmatrix} \mathbf{z} \\ \boldsymbol{\psi} \end{pmatrix} \quad (5.21)$$

where $[\Gamma(t)]$ is the system matrix in Eq. (5.20). The solution to this system is given in terms of its STM:

$$\begin{pmatrix} \mathbf{z}(t) \\ \boldsymbol{\psi}(t) \end{pmatrix} = [\Phi(t, t_0)] \begin{pmatrix} \mathbf{z}(t_0) \\ \boldsymbol{\psi}(t_0) \end{pmatrix} \quad (5.22)$$

$$\mathbf{z}(t_f) = [\phi_{11}(t_f, t_0)]\mathbf{z}(t_0) + [\phi_{12}(t_f, t_0)]\boldsymbol{\psi}(t_0) \quad (5.23)$$

$$\boldsymbol{\psi}(t_f) = [\phi_{21}(t_f, t_0)]\mathbf{z}(t_0) + [\phi_{22}(t_f, t_0)]\boldsymbol{\psi}(t_0) = [S]\mathbf{x}(t_f) = [G]\mathbf{z}(t_f) \quad (5.24)$$

where $[G]$ is of dimension $6(p+1) \times 6(p+1)$, with all entries zero except the 6×6 upper left sub-matrix, $[S]$. Thus:

$$\boldsymbol{\psi}(t_f) = G([\phi_{11}(t_f, t)]\mathbf{z}(t) + [\phi_{12}(t_f, t)]\boldsymbol{\psi}(t)) \quad (5.25)$$

$$\boldsymbol{\psi}(t) = ([\phi_{22}(t_f, t)] - [G][\phi_{12}(t_f, t)])^{-1} ([G][\phi_{11}(t_f, t)] - [\phi_{21}(t_f, t)])\mathbf{z}(t) \equiv [K(t)]\mathbf{z}(t) \quad (5.26)$$

Applying the final conditions, it can be shown that $[K(t_f)] = [G]$. Partitioning $[K]$ into appropriately dimensioned sub-matrices, the top 6 rows of Eq. (5.26) are isolated:

$$\boldsymbol{\lambda}(t) = [K_{11}(t)]\mathbf{x}(t) + [K_{12}(t)]\mathbf{s}_{6p \times 1}(t) \quad (5.27)$$

The control signal is given in terms of the usual state feedback term, and a new feedback term for the augmented sensitivities:

$$\mathbf{u}(t) = -[R]^{-1}[B]^\top [K_{11}(t)]\mathbf{x}(t) - [R]^{-1}[B]^\top [K_{12}(t)]\mathbf{s}_{6p \times 1}(t) \quad (5.28)$$

Thus, $[K_{12}(t)]$ is a $6 \times 6p$ matrix that maps the augmented sensitivity vectors, and the differential equation for the full $[K]$ matrix will now be derived. First, differentiating Eq. (5.26), and isolating then rewriting the differential equations from the augmented dynamics:

$$\dot{\boldsymbol{\psi}} = [\dot{K}(t)]\mathbf{z}(t) + [K(t)]\dot{\mathbf{z}}(t) \quad (5.29)$$

$$\dot{\mathbf{z}}(t) = [L(t)]\mathbf{z}(t) - [M(t)]\boldsymbol{\psi}(t) \quad (5.30)$$

$$\dot{\boldsymbol{\psi}}(t) = -[N(t)]\mathbf{z}(t) - [P(t)]\boldsymbol{\psi}(t) \quad (5.31)$$

The new matrices in Eqs. (5.30) and (5.31) are directly obtained from the partitioned sub-matrices in Eq. (5.20) using the following definition:

$$[\Gamma(t)] = \begin{bmatrix} [L(t)] & -[M(t)] \\ -[N(t)] & -[P(t)] \end{bmatrix} \quad (5.32)$$

Using Eq. (5.26) in Eq. (5.30):

$$\dot{\mathbf{z}}(t) = ([L(t)] - [M(t)][K(t)])\mathbf{z}(t) \quad (5.33)$$

Eq. (5.33) is substituted into Eq. (5.29):

$$\dot{\boldsymbol{\psi}} = \left([\dot{K}(t)] + [K(t)][L(t)] - [K(t)][M(t)][K(t)] \right) \boldsymbol{z}(t) \quad (5.34)$$

Then, substituting Eq. (5.26) in Eq. (5.31), equating with (5.34) and rearranging:

$$\left([\dot{K}(t)] + [K(t)][L(t)] + [P(t)][K(t)] - [K(t)][M(t)][K(t)] + [N(t)] \right) \boldsymbol{z}(t) = \mathbf{0} \quad (5.35)$$

The ODE for $[K(t)]$ is given below, for which the final condition is $[K(t_f)] = [G]$, or equivalently $[K_{11}(t_f)] = [S]$, $[K_{12}(t_f)] = [0_{6 \times 6p}]$, $[K_{21}(t_f)] = [0_{6p \times 6}]$, $[K_{22}(t_f)] = [0_{6p \times 6p}]$.

$$[\dot{K}(t)] + [K(t)][L(t)] + [P(t)][K(t)] - [K(t)][M(t)][K(t)] + [N(t)] = \mathbf{0} \quad (5.36)$$

Since $[K(t)]$ is symmetric, it is clear that not all elements of the matrix need to be numerically integrated. Eq. (5.36) is expanded and symmetry is used to obtain a smaller set of equations to be integrated, which will result in greater computational efficiency:

$$\begin{aligned} & [\dot{K}_{11}] + [K_{11}][A] + [K_{12}][C_{6p \times 6}] + [A]^\top [K_{11}] + [C_{6p \times 6}]^\top [K_{12}]^\top - [K_{11}][B][R]^{-1}[B]^\top [K_{11}] \\ & + [Q] = [0_{6 \times 6}] \\ & [\dot{K}_{12}] + [K_{12}][A_{6p \times 6p}] + [A]^\top [K_{12}] + [C_{6p \times 6}]^\top [K_{22}] - [K_{11}][B][R]^{-1}[B]^\top [K_{12}] = [0_{6 \times 6p}] \\ & [\dot{K}_{22}] + [K_{22}][A_{6p \times 6p}] + [A_{6p \times 6p}]^\top [K_{22}] - [K_{12}]^\top [B][R]^{-1}[B]^\top [K_{12}] + [E_{6p \times 6p}] = [0_{6p \times 6p}] \end{aligned} \quad (5.37)$$

If the symmetry of $[K]$ is used, then one must solve $18p^2 + 39p + 21$ coupled scalar ODE equations to model the behavior of $[K]$. If the symmetry is not exploited, the number of equations to be solved is $36p^2 + 72p + 36$. This becomes more costly as more sensitivity vectors are added to the cost function, but this problem is still tractable for two uncertain parameters.

To implement this controller, Eq. (5.37) should be solved backwards in time from the given final conditions, to obtain a pre-saved gain schedule. Then, the control should be applied as shown in Eq. (5.28), where the signals $\boldsymbol{s}_{6p \times 1}$ are obtained by integrating $\dot{\boldsymbol{s}}_i(t) = [A(t)]\boldsymbol{s}_i(t) + [C_i(t)]\boldsymbol{x}(t)$ as the system evolves. Lastly, remaining error due to nonlinearity or neglected dynamics can be greatly reduced by feeding back an error integral term. Note that if one sets $[E_{6p \times 6p}] = [0_{6p \times 6p}]$, the effects of system sensitivity are ignored, and the problem reduces to standard LQR with a final cost.

5.1.4 Notes on System Nonlinearity and Orbit Control

Before simulating LQR control and low-sensitivity control in the highly perturbed asteroid orbit environment, this section discusses several necessary topics, which provide justification for the methods, analysis, and results that will follow.

5.1.4.1 Quantifying Nonlinearity

In general, successful application of the linear control law to the nonlinear system is limited to a finite region of space around the virtual chief, and to a finite span of time for which the assumptions of the linearized model hold. This region of space and span of time will be referred to as the linear regime. The amount of acceptable nonlinearity will differ depending on the application, and thus so will this definition. In this section, the scale of system nonlinearity is quantified with a dimensionless index that represents the average spatial deviation between the linearized and nonlinear propagated dynamics:

$$\nu_s(t, t_0) = \frac{1}{t - t_0} \int_{t_0}^t \frac{\|\Delta \mathbf{r}_{nl}(\tau) - \Delta \mathbf{r}_l(\tau)\|}{\|\Delta \mathbf{r}_l(\tau)\|} d\tau \quad (5.38)$$

where $\Delta \mathbf{r} = (x, y, z)^\top$ and the velocity differentials do not need to be directly included in this index. This can be applied to results from both the uncontrolled dynamics and controlled dynamics, however the scale of this parameter can be expected to differ with these two implementations. This parameter may be a misleading representation if $\Delta \mathbf{r}_l \approx \mathbf{0}$ for much of the time range. This should be addressed by de-weighting or excluding such instances from the calculation of this quantity. Alternative nonlinearity measures may also be considered, such as the average spatial distance between the two trajectories:

$$e_s(t, t_0) = \frac{1}{t - t_0} \int_{t_0}^t \|\Delta \mathbf{r}_{nl}(\tau) - \Delta \mathbf{r}_l(\tau)\| d\tau \quad (5.39)$$

5.1.5 Orbit Control around Asteroids

Orbiting around asteroids is not always possible, because these bodies are small enough that solar radiation pressure can easily dominate the gravitational force. Furthermore, the gravitational perturbations due to non-sphericity are often quite large. It is important to bear in mind that orbital motion around asteroids is highly non-Keplerian – complex and chaotic. Despite the complexity, several assumptions about the asteroid and spacecraft are used in this section to enable a study of near-optimal guidance in this environment.

The simulations in this section use a hypothetical asteroid given in Table 5.1. The hypothetical asteroid is rather large. At the operating altitude, it is assumed that the dominant non-spherical gravity perturbations are due to C_{20} and C_{22} [17].

The SRP disturbance on the spacecraft is assumed to be well-modeled by a simple flat-plate model. In this section, it is also assumed to be sun-facing. Since most spacecraft are solar powered, and these panels constitute the majority of the projected surface area, this will often be a reasonable assumption.

The simulations assume that the orientation of the asteroid spin axis, its rotation period, and its gravitational parameter μ are well-known. The first two parameters could be well-estimated by camera data before rendezvous, while the third would be estimated from telemetry data from the initial encounter and orbit insertion. It is possible to extend the methods in this section to account for uncertainty in these parameters as well.

The desired “chief” orbit to rendezvous with is initially a near-circular orbit in the terminator plane. The nominal initial target orbit for the survey phase of the OSIRIS-REx mission is one such orbit. These orbits are naturally quasi-stable, and are an attractive target for initial orbit-targeting maneuvers [57]. However, the highly perturbed and uncertain environment can and will introduce error. The scenario studied in this section is analogous to correcting post-maneuver orbit error with LQR control, using very low thrust.

Lastly, the formation flying rendezvous control problem presumes that the relative position

and velocity of the spacecraft are sufficiently well-known, otherwise the rendezvous would not be attempted. The accuracy of knowledge of the chief orbit is less important. In fact, the desensitized control strategy could be implemented with the initial chief orbit elements chosen as the uncertain parameters. This would enable rendezvous control for a formation whose absolute position is somewhat uncertain, but for which the formation geometry is known from sensors on the individual spacecraft.

5.1.6 Low-Thrust Control Simulations

To test the various optimal control strategies, consider the case of the hypothetical asteroid in Table 5.1 and the initial conditions given in Table 5.3. First, LQR control is tested – in which it is assumed that the SRP and second-order gravitational parameters are accurately known. Then, low-sensitivity optimal control is implemented, and the results from these two strategies are compared. The repeated control parameters (used in both cases) are given in Table 5.2. The initial conditions are given in Table 5.3.

Table 5.1: Asteroid Physical Parameters for Desensitized Control Simulations

Parameters	Values
Asteroid semi-axes, C_{20} & C_{22}	$A = 6, B = 3, C = 2.5, C_{20} = -0.093, C_{22} = 0.0375$
Density, gravitational parameter	$\rho = 2.6 \text{ g/cm}^3, \mu = 3.271 \times 10^4 \text{ m}^3/\text{s}^2$
Asteroid spin axis, orientation	$T_r = 38.5 \text{ hours}, \psi_0 = \pi/8, \kappa = 15^\circ$
Asteroid orbit	$e = 0, R = 2.4 \text{ AU}, \theta_0 = \omega + f_0 = \pi/2$
Spacecraft optical properties	$\frac{A}{m} = 0.3, \bar{B} = 0.6, \bar{s} = 0.25, \bar{\rho} = 0.3$

Table 5.2: Recurring Control Parameters for LQR and Low-Sensitivity Cases

Parameter	Value
$[Q]$	$[Q] = 0_{6 \times 6}$
$[R]$	$(1 \times 10^{12})I_{3 \times 3}$
$[S_f]$	$S_f(1 : 3, 1 : 3) = I_{3 \times 3}, S_f(4 : 6, 4 : 6) = (1 \times 10^9)I_{3 \times 3}$
$[B]$	$B(1 : 3, 1 : 3) = 0_{3 \times 3}, B(4 : 6, 1 : 3) = I_{3 \times 3}$
$[E]$	$[E_1] = [E_2] = 0.1I_{6 \times 6}, [E_3] = 0.01I_{6 \times 6}$
$t_0, \Delta t, t_f$	$t_0 = 0, \Delta t = 200, t_f = 555800$ (2 orbits, 6.43 days)

Table 5.3: Desensitized Control Simulation Initial Conditions

Parameters	Values
Chief Orbit Elements	$\mathbf{oe}_c = [a, e, i, \omega, \Omega, f_0] = [40 \text{ km}, 5 \times 10^{-4}, 75^\circ, 0^\circ, 0^\circ, 0^\circ]$
Deputy Orbit Element Differences	$\Delta\mathbf{oe} = \mathbf{oe}_d - \mathbf{oe}_c = [0 \text{ km}, 0.07, 2.0^\circ, 0^\circ, 0^\circ, 0^\circ]$
Initial Conditions (LVLH)	$\Delta\mathbf{r} = -2800\hat{e}_x \text{ m}, \Delta\mathbf{v} = 0.1285\hat{e}_y + 0.0339\hat{e}_z \text{ m/s}$

5.1.6.1 LQR Control

In this case, $[Q] = [0_{6 \times 6}]$ and it is the final state cost that drives the system to the origin. In Figure 5.1, it is clear that there is significant deviation between the control applied to the linear and nonlinear dynamics. Figure 5.2 shows the relative position vs. time from the control applied to the nonlinear dynamics. Since the LQR control is implemented by solving the matrix Riccati equation for $[K(t)]$ and feeding back $\mathbf{u}(t) = -[R]^{-1}[B]^\top [K(t)]\mathbf{x}(t)$, the deviations do not result in significant final miss distance. This closed-loop control implementation method seems naturally robust, at least in achieving the desired final condition. However, the significant deviation between the designed and actual controlled trajectories indicates that the effect of nonlinearities is non-negligible. This is also clear from the deviation between the designed (L) and actual (NL) control signals in Figure 5.3.

The positional sensitivity associated with C_{20} , C_{22} , and SRP force uncertainty are given in Figures 5.4 - 5.6. These results were propagated using Eq. (5.10) evaluated along the linear and nonlinear trajectories. These results indicate that while the SRP perturbation is largest, it is uncertainty in C_{22} that would result in the greatest deviation from the planned relative motion trajectory. This emphasizes the dynamic importance of C_{22} on relative motion dynamics in the asteroid orbit.

5.1.6.2 Low-Sensitivity Control

For the low-sensitivity control design, the control parameters given in Table 5.2 are unchanged. The sensitivity-associated weight matrices are for C_{20} , C_{22} , and SRP, respectively $E_1 = E_2 = 0.1I_{6 \times 6}$, and $E_3 = 0.01I_{6 \times 6}$. The control applied to the nonlinear dynamics is very

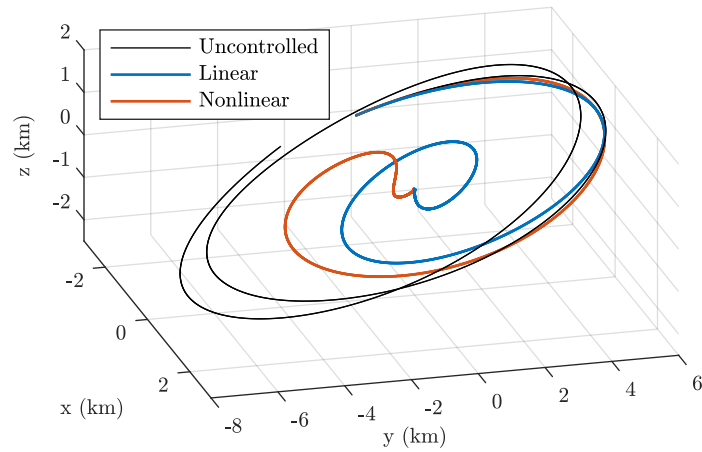


Figure 5.1: Controlled Relative Motion (LQR)

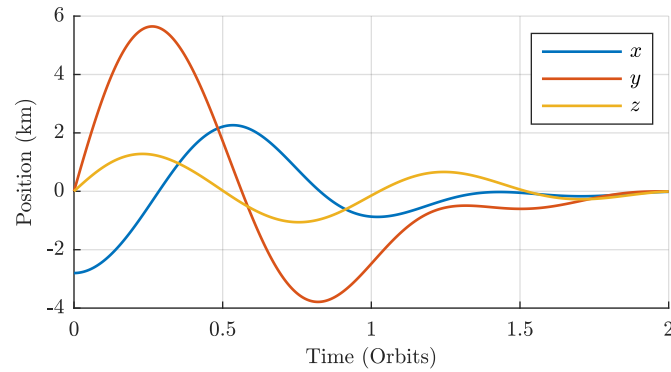


Figure 5.2: Relative Position vs. Time (LQR)

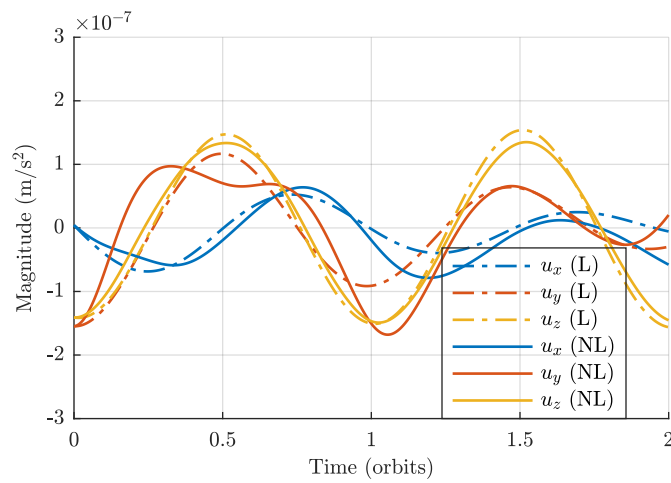


Figure 5.3: Control Signals (LQR)

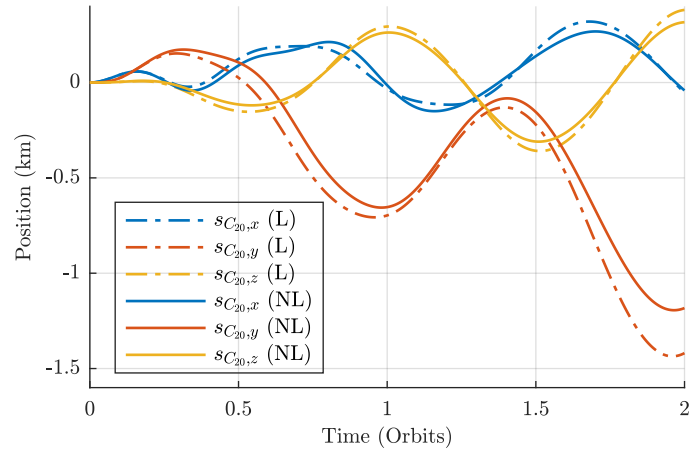
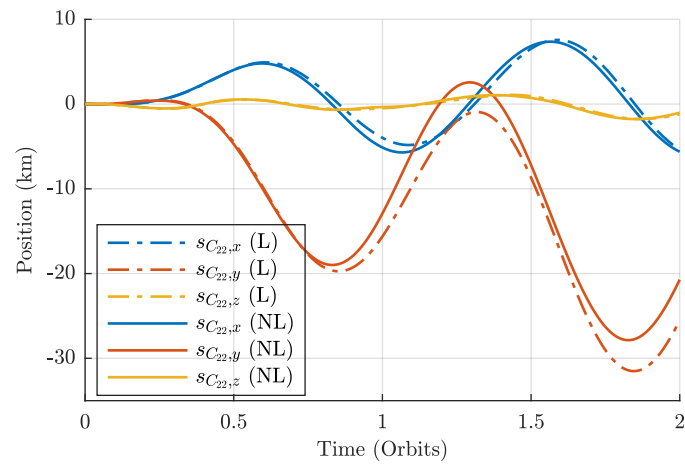
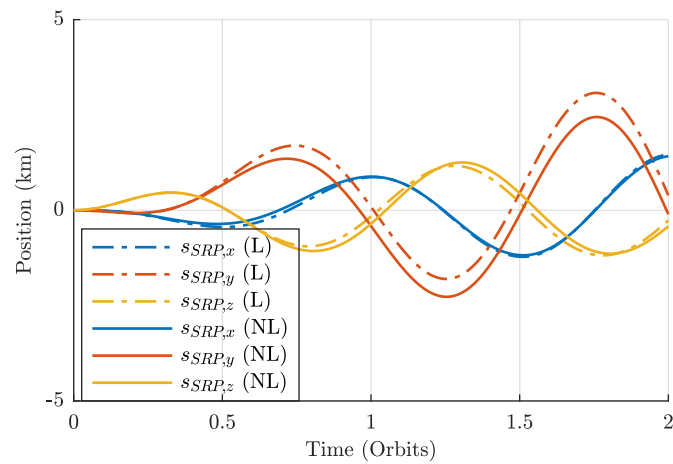
Figure 5.4: C_{20} Relative Position Sensitivity (LQR)Figure 5.5: C_{22} Relative Position Sensitivity (LQR)

Figure 5.6: SRP Relative Position Sensitivity (LQR)

close to the control applied to the linear dynamics. This is evident by comparing the linear and nonlinear results in Figures 5.7 and 5.9. The controller comes quite close to achieving the desired final condition. In addition, it is clear that the sensitivities to the three parameters are greatly reduced from the standard LQR results, which can be seen by comparing Figures 5.10 - 5.12 with Figures 5.4 - 5.6. Note that the y axis limits are greatly reduced for Figures 5.10 - 5.12.

It is worth noting that using poor values for the gravitational coefficients and SRP magnitude will not cause significant change to the trajectory design or control signals, which makes some intuitive sense. To minimize sensitivity to the poorly modeled parameters, the controller sends the deputy spacecraft on a trajectory whose design is minimally sensitive to errors in these parameters. Interestingly, this seems to result in a more close agreement between the control applied to the linear and nonlinear dynamics – suggesting that this control method should effectively expand the size of the linear regime. The effect of mis-modeled and unmodeled parameters on standard LQR control and low-sensitivity control is explored more fully by Monte Carlo analysis in the next section.

In general, this study illustrates that the shape of these low-sensitivity controlled trajectories are quite unintuitive and interesting. It also seems that they generally require more control than the traditional LQR design, compare Figures 5.9 and 5.3, but the required control is quite small (at or below the thrust level of small ion thrusters) in either case for station-keeping or formation control around this asteroid.

5.1.7 Monte Carlo Simulations Using Low-Thrust

In this section, Monte Carlo simulations of 50 runs were performed for both the standard LQR and the low-sensitivity control design from the previous section. All simulation parameters are reused, except the simulations now assume mis-modeled C_{20} and C_{22} with a 30% standard deviation about the nominal computed values, along with mis-modeled SRP force with a 20% standard deviation in magnitude from the expected value.

Figure 5.13 shows the controlled trajectories using standard LQR, and Figure 5.14 shows the

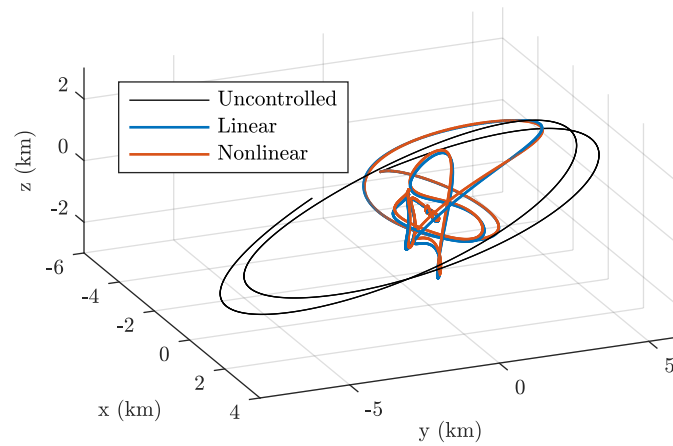


Figure 5.7: Controlled Relative Motion (Low-Sensitivity Control)

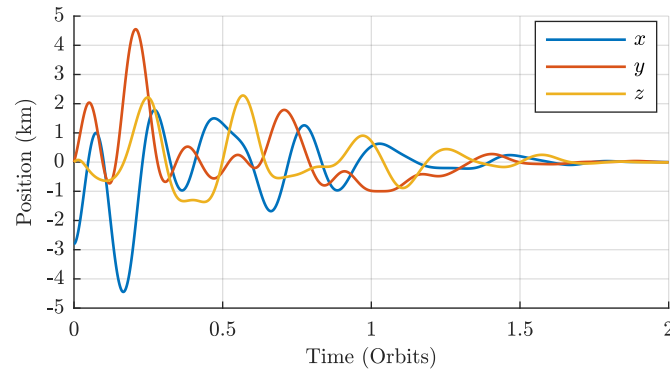


Figure 5.8: Relative Position vs. Time (Low-Sensitivity Control)

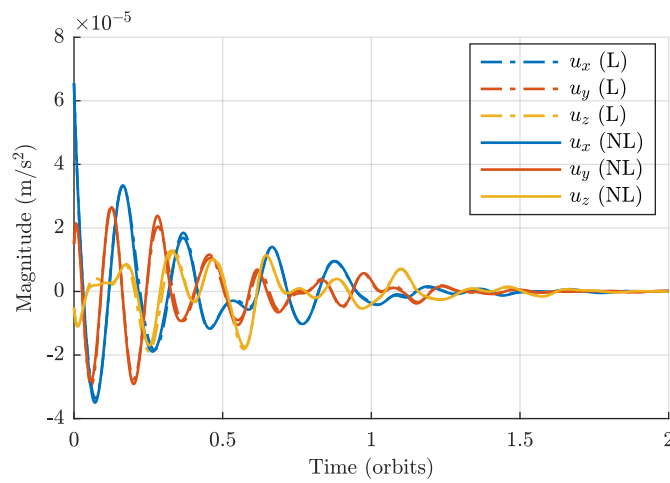


Figure 5.9: Control Signals (Low-Sensitivity Control)

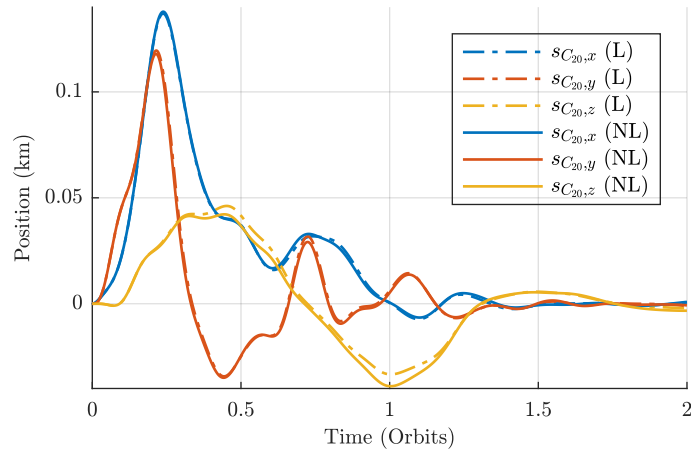
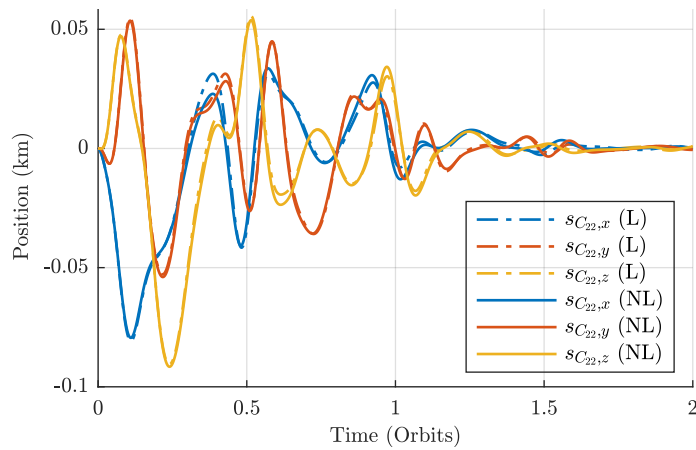
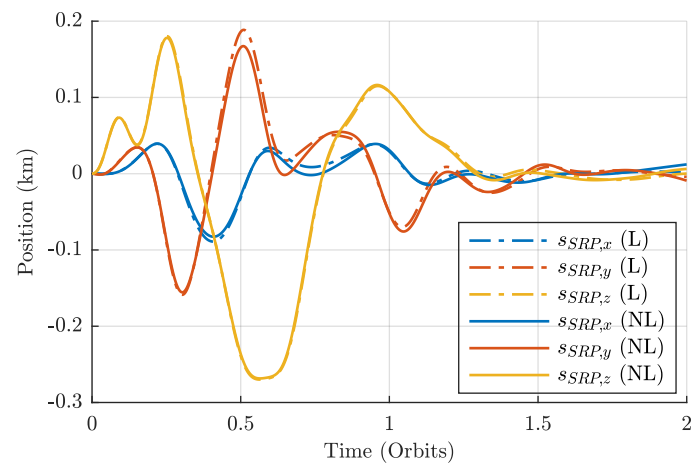
Figure 5.10: C_{20} Relative Position Sensitivity (Low-Sensitivity Control)Figure 5.11: C_{22} Relative Position Sensitivity (Low-Sensitivity Control)

Figure 5.12: SRP Relative Position Sensitivity (Low-Sensitivity Control)

controlled trajectories using low-sensitivity control. It is clear that both controllers successfully reach the origin of the LVLH frame. However, the LQR controller consistently deviates greatly from the trajectory predicted from the controlled linear dynamics given by the black line, while the low-sensitivity controller does not deviate much from the behavior predicted by the linearized model. Furthermore, the true low-sensitivity trajectories are spatially closer together than the true LQR trajectories, as would be expected.

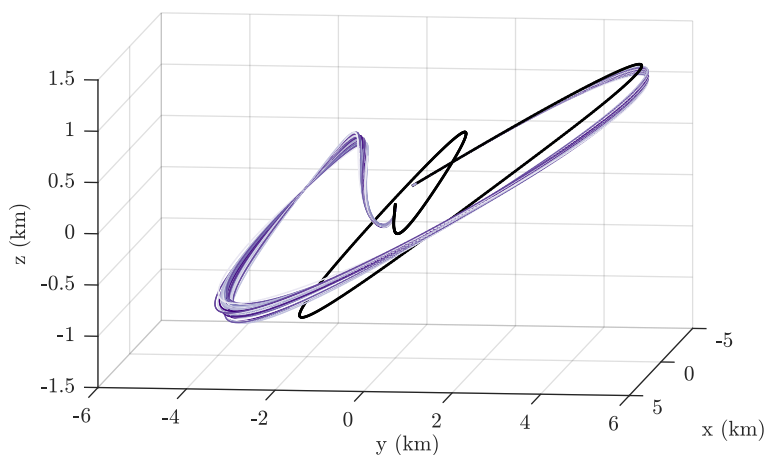


Figure 5.13: Controlled Relative Motion, Monte Carlo Results (LQR)

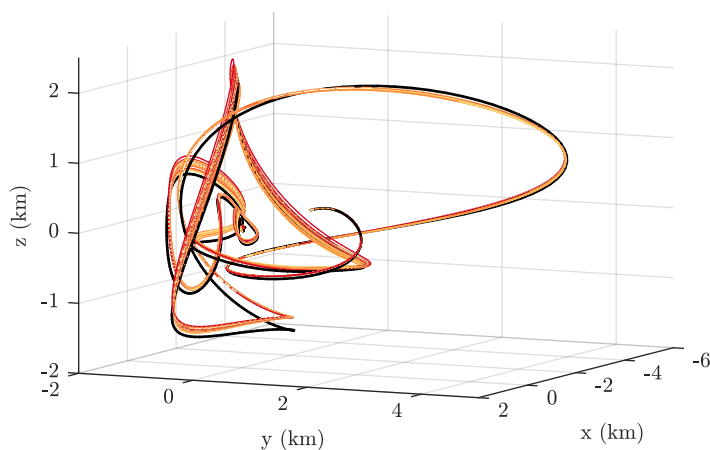


Figure 5.14: Controlled Relative Motion, Monte Carlo Results (Low-Sensitivity Control)

Figures 5.15 and 5.16 show the distributions of total Δv used by both controllers. The cost is higher for the low-sensitivity control, indicating that the low-sensitivity trajectories are generally

more expensive to follow, at least in this current implementation.

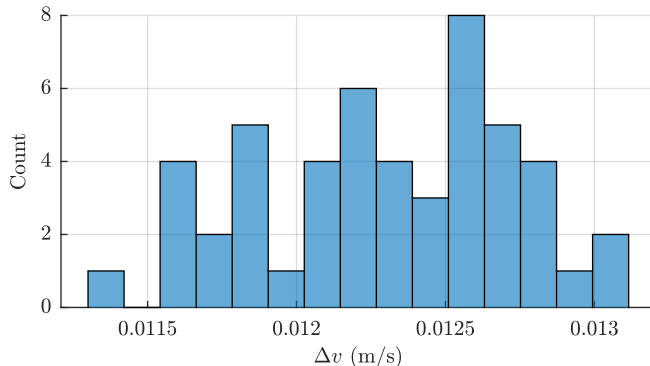


Figure 5.15: Total Δv (LQR)

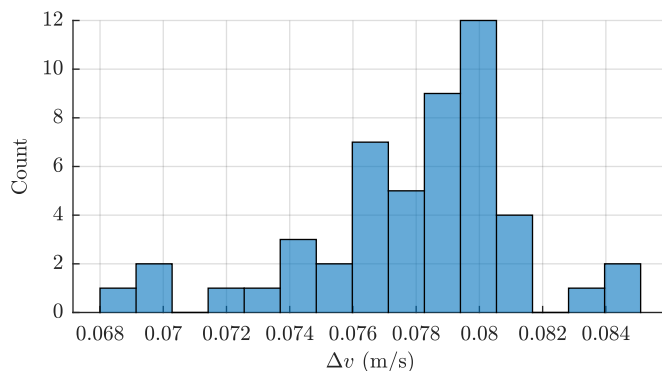


Figure 5.16: Total Δv (Low-Sensitivity Control)

Figure 5.17 shows the nonlinearity index vs. time for both controllers. Since this index is meaninglessly inflated as $\Delta \mathbf{r}_l \rightarrow \mathbf{0}$, the nonlinearity index is only shown while $\|\Delta \mathbf{r}_l\| > 0.15$ km. The difference between the two families of curves emphasizes that the low-sensitivity controller follows the expected linear dynamics much more closely, with its nonlinearity index being an order of magnitude lower than for the standard LQR control. The low-sensitivity controller also reduces the scale of the relative motion much more quickly than the standard LQR controller, a feature that cannot be discerned from looking at the trajectories alone.

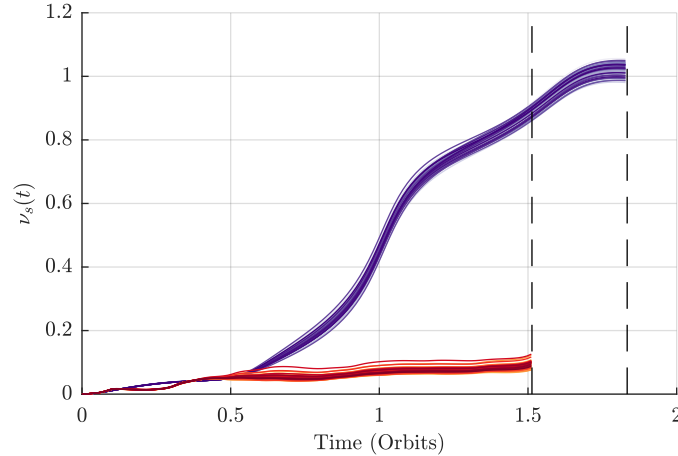


Figure 5.17: Nonlinearity Index vs. Time, Monte Carlo Results

5.1.8 Discussion

In this section, desensitized control is implemented to solve the formation flying rendezvous problem for spacecraft in orbits about asteroids with uncertain parameters. The method first introduced by Kahne [72] is applied and extended to desensitized control with any number of unknown system parameters. For the example application in this section, those parameters are C_{20} , C_{22} and the solar radiation pressure (SRP) disturbance magnitude.

Numerical simulations compare the performance and characteristics of the Linear Quadratic Regulator (LQR) control with desensitized control. The desensitized control enables rendezvous along a trajectory that is much closer to the design trajectory predicted by the linearized dynamics. This is an interesting and useful feature for desensitized control, and a surprising result to obtain from a linear control design. The comparative closeness of the design and actual trajectories would be particularly useful for more complex formation control problems, in which operational and geometric constraints would demand that the design trajectory be followed as closely as possible.

5.2 Satellite Relative Motion in the Vicinity of a Poorly Tracked Target Object

5.2.1 Relative State Uncertainty

A major topic in formation flying and satellite proximity operations is collision avoidance with other space objects. There have been many important works studying the effects of uncertainties in the satellite relative motion problem. Reference 84 derives analytic uncertainty propagation for the relative motion problem in elliptic orbits. Under the assumption of a Gaussian white noise process, they explore the computation of the evolving mean and covariance matrix of the relative states using Tschauner-Hempel equations [126]. Some work has focused on designing guidance and control to mitigate collision risks in the presence of uncertainties, both with active and passive methods. A classic passive means of minimizing impact risk in formation flying is through the safe ellipse, which ensures that in the presence of along-track drift in the relative motion, the spacecraft will not collide [83]. In Reference 13, Breger and How investigate tradeoffs between active and passive approaches to safety. They also develop a strategy for generating safe, fuel-optimized rendezvous trajectories that guarantee collision avoidance for a large class of anomalous behaviors. Reference 59 develops a Receding Horizon Control (RHC) approach that enforces passive safety in the presence of common navigation or propulsive system failures. They identify that adding cross-track relative motion also greatly reduces collision probability.

There are several works which explore the problem of rendezvous and proximity operations when the target orbit is uncertain, which leads to uncertainty in the linearized model. In these works, the spacecraft relative state is assumed to be directly and accurately measured, but the effects of dynamic uncertainty need to be mitigated. Reference 85 studies reliable impulsive state-feedback control for autonomous spacecraft rendezvous under target orbital uncertainty with the possibility of thruster faults. This is accomplished using Lyapunov theory and genetic algorithms. Reference 130 addresses robust H_∞ control for spacecraft rendezvous with a noncooperative target, specifically for the case of CW dynamics, in which the target semimajor axis is uncertain. The

control design enables rendezvous in the presence of this dynamical uncertainty, while also allowing for control input saturation. In both References 85 and 130, the uncertainty in the target orbit manifests only as dynamic uncertainty in the linearized models. The relative position and velocity are assumed to be observable.

Typically, the safe use of translational control in close proximity requires that the relative position and velocity be directly and accurately observed, otherwise there is a fundamental risk of collision or other undesired outcomes. However, sometimes a spacecraft must maneuver in the vicinity of another space object whose position and velocity is not known to a desirable degree of accuracy, due to poor observability conditions or any other factors leading to an inability to make the necessary measurements. In such circumstances, the initial estimates of the relative state are going to have some degree of error, and the resulting relative motion over time will be generally uncertain as well. This is depicted in Figure 5.18, where the nominal relative position $\boldsymbol{\rho}^*$ obtained from the best guess of the target orbit differs from the true relative state $\boldsymbol{\rho}$. In addition to dynamic error due to incorrect linearization, the uncertainty directly affects the relative range and range rate, as well as the orientation of the target-centered LVLH frame. This section studies this problem of relative motion in the vicinity of a poorly tracked target object, from the perspective of the linear sensitivities of the relative state. The sensitivities studied are the derivative of the relative state vector with respect to the individual uncertain orbit elements of the target spacecraft, and they have their own linear forced dynamics if the two spacecraft are in close proximity in similar orbits.

Through the sensitivities, an uncertainty distribution in the initial target orbit elements can be directly mapped to an evolving uncertainty distribution in the relative state. Assuming small target orbit element errors, the problem can be approached by linearization, and the sensitivities progress with their own dynamics influenced only by the nominal relative state and by the control. The action of an estimator has no effect on the sensitivity propagation, and instead changes the uncertainty distribution of the initial target orbit elements. In this manner, the sensitivities act as a scaffolding for the relative state uncertainty distribution, and only need to be propagated once in

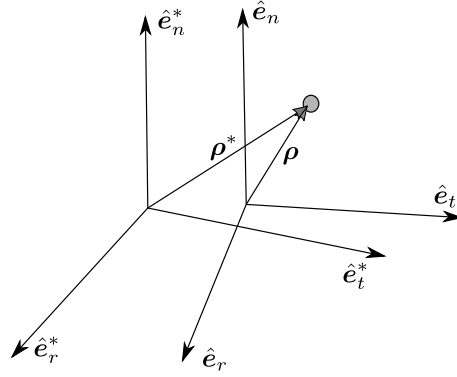


Figure 5.18: Relative Position from Estimated and True Target Spacecraft Locations

parallel with the nominal relative motion dynamics. This framework could allow for uncertainty-conscious linear control to be designed for the relative motion problem that actively reduces the risk of satellite impact due to errors in the target orbit estimate.

5.2.2 Sensitivity Dynamics

5.2.2.1 Fundamentals of the Linear Sensitivities

The relative state of a satellite with respect to another orbiting space object is a function of the orbit elements of the two. Let $\boldsymbol{\alpha}_s$ and $\boldsymbol{\alpha}_t$ denote the controlled spacecraft and the target object's orbit elements at some epoch time. For linearization about an incorrect orbit parameterized by estimated target orbit elements $\boldsymbol{\alpha}_t^*$, the true relative state \boldsymbol{x} can be expressed as a sum of the nominal state \boldsymbol{x}^* and the deviations induced by the product of the sensitivities to the orbit elements and their errors:

$$\boldsymbol{s}_i = \left. \frac{d\boldsymbol{x}}{d\boldsymbol{\alpha}_{t,i}} \right|_* \quad (5.40)$$

$$\check{\boldsymbol{s}}_i = \left. \frac{d\boldsymbol{x}}{d\boldsymbol{\alpha}_{s,i}} \right|_* \quad (5.41)$$

$$\begin{aligned} \boldsymbol{x} &\approx \boldsymbol{x}^* + \left. \frac{d\boldsymbol{x}}{d\boldsymbol{\alpha}_t} \right|_* (\boldsymbol{\alpha}_t - \boldsymbol{\alpha}_t^*) + \left. \frac{d\boldsymbol{x}}{d\boldsymbol{\alpha}_s} \right|_* (\boldsymbol{\alpha}_s - \boldsymbol{\alpha}_s^*) \\ &= \boldsymbol{x}^* + \sum_{i=1}^6 (\alpha_{t,i} - \alpha_{t,i}^*) \boldsymbol{s}_i + \sum_{i=1}^6 (\alpha_{s,i} - \alpha_{s,i}^*) \check{\boldsymbol{s}}_i \end{aligned} \quad (5.42)$$

In this work, the orbit of the maneuvering spacecraft is assumed to be known to much higher precision than the target orbit, so the influence of this uncertainty on the relative state is neglected:

$$\mathbf{x} \approx \mathbf{x}^* + \sum_{i=1}^6 (\alpha_{t,i} - \alpha_{t,i}^*) \mathbf{s}_i \quad (5.43)$$

The “ t ” subscript is dropped, because this work only considers uncertainties in the orbit elements of the unknown target object’s orbit. The associated sensitivity state vectors have their own linear forced dynamics, obtained from the relative motion dynamics.

$$\dot{\mathbf{s}}_i = \frac{d}{dt} \left(\frac{d\mathbf{x}}{d\alpha_i} \right) = \frac{d}{d\alpha_i} \left(\frac{d\mathbf{x}}{dt} \right) = \frac{d}{d\alpha_i} (A_{\mathbf{x}}) \mathbf{x} + A_{\mathbf{x}} \mathbf{s}_i + \frac{d}{d\alpha_i} (B_{\mathbf{x}}) \mathbf{u} \quad (5.44)$$

Note that the concept of sensitivities having their own dynamics is not new, and is explored extensively in Reference 72.

5.2.2.2 Dynamics in Local Cartesian Coordinates

If the relative state \mathbf{x} is in Cartesian coordinates in the LVLH frame, the plant matrix $A_{\mathbf{x}}$ [111] and control matrix $B_{\mathbf{x}}$ are given below for the Keplerian case.

$$A_{\mathbf{x}} = \begin{bmatrix} 0 & 0 & 0 & 1 & 0 & 0 \\ 0 & 0 & 0 & 0 & 1 & 0 \\ 0 & 0 & 0 & 0 & 0 & 1 \\ \dot{\theta}^2 + 2\frac{\mu}{r^3} & \ddot{\theta} & 0 & 0 & 2\dot{\theta} & 0 \\ -\ddot{\theta} & \dot{\theta}^2 - \frac{\mu}{r^3} & 0 & -2\dot{\theta} & 0 & 0 \\ 0 & 0 & -\frac{\mu}{r^3} & 0 & 0 & 0 \end{bmatrix} \quad (5.45)$$

$$B_{\mathbf{x}} = \begin{bmatrix} 0_{3 \times 3} \\ R_3(\theta)R_1(i)R_3(\Omega)R_{\mathcal{NH}}^* \end{bmatrix} \quad (5.46)$$

In Eq. (5.46), the rotation matrix $R_{\mathcal{NH}}^*$ maps from the known nominal LVLH frame to the inertial frame, and the subsequent rotations map from the inertial frame to the true LVLH frame. For small uncertainties in the target orbit, the lower 3×3 sub-matrix in $B_{\mathbf{x}}$ will thus be close to identity. The sensitivity dynamics given by Eq. (5.44) are evaluated using a chosen nominal target orbit and

nominal relative motion, and are not influenced by the uncertainty in the target orbit elements. Note that the last term in Eq. (5.44) is nonzero only for the sensitivities to the orbit element angles parameterizing the rotation $R_{\mathcal{H}\mathcal{N}}$ from the inertial frame \mathcal{N} to the target-centered LVLH frame \mathcal{H} .

The initial values of the sensitivities will typically be nonzero for this problem, and can be directly computed. References 111 and 50 discuss the geometric method, mapping the relative state in orbit element differences to the relative state in local Cartesian or curvilinear coordinates via the linear mapping $\mathbf{x} = [G(\theta)] \delta\mathbf{oe}$. Writing $\mathbf{x}_0^* = [G(\theta_0)] \delta\mathbf{oe}_0^*$, where $\delta\mathbf{oe}_0^* = \mathbf{oe}_s(0) - \mathbf{oe}_t^*(0)$, the initial sensitivities are derived:

$$\mathbf{s}_i(0) = \frac{d\mathbf{x}_0^*}{d\mathbf{oe}_i(0)} = \frac{d}{d\mathbf{oe}_i(0)} (G(\theta_0) \delta\mathbf{oe}_0^*) = \frac{d}{d\mathbf{oe}_i(0)} (G(\theta_0)) \delta\mathbf{oe}_0^* + G(\theta_0) \frac{d\delta\mathbf{oe}_0^*}{d\mathbf{oe}_i(0)} \quad (5.47)$$

$G(\theta)$ is reproduced below from Reference 111 for when \mathbf{x} is in local Cartesian coordinates and $\delta\mathbf{oe}$ is in quasi-nonsingular orbit element differences:

$$G_{\mathbf{x}} = \begin{bmatrix} \frac{r}{a} & \frac{v_r}{v_t} r & 0 & -\frac{r}{p}(2aq_1 + rc\theta) & -\frac{r}{p}(2aq_2 + rs\theta) & 0 \\ 0 & r & 0 & 0 & 0 & rci \\ 0 & 0 & rs\theta & 0 & 0 & -rc\theta si \\ -\frac{v_r}{2a} & \left(\frac{1}{r} - \frac{1}{p}\right)h & 0 & \frac{1}{p}(v_r a q_1 + hs\theta) & \frac{1}{p}(v_r a q_2 - hc\theta) & 0 \\ -\frac{3v_t}{2a} & -v_r & 0 & \frac{1}{p}(3v_t a q_1 + 2hc\theta) & \frac{1}{p}(3v_t a q_2 + 2hs\theta) & v_r ci \\ 0 & 0 & (v_t c\theta + v_r s\theta) & 0 & 0 & (v_t s\theta - v_r c\theta)si \end{bmatrix} \quad (5.48)$$

where $v_r = \dot{r}$, $v_t = r\dot{\theta}$, and c and s denote the cos and sin functions respectively. Because of the definition of $\delta\mathbf{oe}_0^*$, the final term in Eq. (5.47) can be rewritten as $-G(\theta_0)\hat{e}_i$, where \hat{e}_i is a unit vector with six components, with the i^{th} component one and all other components zero. Note from Eq. (5.44) that the sensitivity state vectors behave as an augmented position and velocity vector. In other words, for the elements s_j of a given sensitivity vector, $\dot{s}_j = s_{j+3}$ for $j = 1, 2, 3$.

Denoting $\Delta\mathbf{oe} = \mathbf{oe} - \mathbf{oe}^*$, and writing each \mathbf{s}_i in terms of its associated element \mathbf{oe}_i , Eq. (5.42) is rewritten in terms of the sensitivities to and differences in the initial target quasi-nonsingular orbit elements \mathbf{oe}_0 :

$$\mathbf{x} = \mathbf{x}^* + \mathbf{s}_a \Delta a + \mathbf{s}_{\theta_0} \Delta \theta_0 + \mathbf{s}_i \Delta i + \mathbf{s}_{q_1} \Delta q_1 + \mathbf{s}_{q_2} \Delta q_2 + \mathbf{s}_{\Omega} \Delta \Omega \quad (5.49)$$

Because the target spacecraft orbit is parameterized by epoch orbit elements, an initial statistical distribution in these epoch elements can be directly mapped to a distribution of future relative states via the sensitivities \mathbf{s}_i .

In Eq. (5.49), the relative state is expressed as a time-varying vector sum of scalar random variables. This is interesting because in principle, for the unforced problem, the time-varying vector states can be computed analytically as functions of the nominal target argument of latitude θ for the case of Keplerian orbits. This would enable highly efficient uncertainty propagation for the problem of close-proximity spacecraft relative motion in the vicinity of an uncertain target – at least for the timespan that the majority of the uncertainty distribution lies within the linear regime. Interestingly, from Eq. (5.44) it can be shown that some of the sensitivity terms can be influenced by control. As a result, the action of a controller has some influence on the distribution of possible relative states.

Returning to Eq. (5.44), the relative state sensitivity dynamics to each orbit element are derived:

$$\dot{\mathbf{s}}_a = \left(A_{\mathbf{x},a} + A_{\mathbf{x},\theta} \frac{d\theta}{da} \right) \mathbf{x}^* + A_{\mathbf{x}} \mathbf{s}_a + B_{\mathbf{x},\theta} \frac{d\theta}{da} \mathbf{u} \quad (5.50a)$$

$$\dot{\mathbf{s}}_{\theta_0} = A_{\mathbf{x},\theta} \frac{d\theta}{d\theta_0} \mathbf{x}^* + A_{\mathbf{x}} \mathbf{s}_{\theta_0} + B_{\mathbf{x},\theta} \frac{d\theta}{d\theta_0} \mathbf{u} \quad (5.50b)$$

$$\dot{\mathbf{s}}_i = A_{\mathbf{x}} \mathbf{s}_i + B_{\mathbf{x},i} \mathbf{u} \quad (5.50c)$$

$$\dot{\mathbf{s}}_{q_1} = \left(A_{\mathbf{x},q_1} + A_{\mathbf{x},\theta} \frac{d\theta}{dq_1} \right) \mathbf{x}^* + A_{\mathbf{x}} \mathbf{s}_{q_1} + B_{\mathbf{x},\theta} \frac{d\theta}{dq_1} \mathbf{u} \quad (5.50d)$$

$$\dot{\mathbf{s}}_{q_2} = \left(A_{\mathbf{x},q_2} + A_{\mathbf{x},\theta} \frac{d\theta}{dq_2} \right) \mathbf{x}^* + A_{\mathbf{x}} \mathbf{s}_{q_2} + B_{\mathbf{x},\theta} \frac{d\theta}{dq_2} \mathbf{u} \quad (5.50e)$$

$$\dot{\mathbf{s}}_{\Omega} = A_{\mathbf{x}} \mathbf{s}_{\Omega} + B_{\mathbf{x},\Omega} \mathbf{u} \quad (5.50f)$$

The unintuitive $d\theta/d\alpha_i$ terms appear due to the influence of changes in the orbit elements a , θ_0 , q_1 , and q_2 on the subsequent evolution of $\theta(t)$.

All terms appearing in Eq. (5.50) are directly computed and provided below:

$$A_{\mathbf{x},\alpha_i} = \frac{d}{d\alpha_i} (A_{\mathbf{x}}) = \begin{bmatrix} 0_{3 \times 3} & 0_{3 \times 3} \\ K_{\alpha_i}^{A_{\mathbf{x}}} & \Omega_{\alpha_i}^{A_{\mathbf{x}}} \end{bmatrix} \quad (5.51)$$

$$K_a^{A\mathbf{x}} = \begin{bmatrix} -\frac{3}{a}\dot{\theta}^2 - \frac{6}{a}\frac{\mu}{r^3} & -\frac{3}{a}\ddot{\theta} & 0 \\ \frac{3}{a}\ddot{\theta} & -\frac{3}{a}\dot{\theta}^2 + \frac{3}{a}\frac{\mu}{r^3} & 0 \\ 0 & 0 & \frac{3}{a}\frac{\mu}{r^3} \end{bmatrix} \quad (5.52a)$$

$$\Omega_a^{A\mathbf{x}} = \begin{bmatrix} 0 & -\frac{3}{a}\dot{\theta} & 0 \\ \frac{3}{a}\dot{\theta} & 0 & 0 \\ 0 & 0 & 0 \end{bmatrix} \quad (5.52b)$$

$$K_\theta^{A\mathbf{x}} = \begin{bmatrix} 4\dot{\theta}^2\frac{\kappa'}{\kappa} + 6\frac{\mu}{r^3}\frac{\kappa'}{\kappa} & \frac{2\dot{\theta}^2}{\kappa^2}(4\kappa'^2 - \kappa + \eta^2) & 0 \\ -\frac{2\dot{\theta}^2}{\kappa^2}(4\kappa'^2 - \kappa + \eta^2) & 4\dot{\theta}^2\frac{\kappa'}{\kappa} - 3\frac{\mu}{r^3}\frac{\kappa'}{\kappa} & 0 \\ 0 & 0 & -3\frac{\mu}{r^3}\frac{\kappa'}{\kappa} \end{bmatrix} \quad (5.53a)$$

$$\Omega_\theta^{A\mathbf{x}} = \begin{bmatrix} 0 & 4\dot{\theta}\frac{\kappa'}{\kappa} & 0 \\ -4\dot{\theta}\frac{\kappa'}{\kappa} & 0 & 0 \\ 0 & 0 & 0 \end{bmatrix} \quad (5.53b)$$

$$K_{q_1}^{A\mathbf{x}} = \begin{bmatrix} 2\dot{\theta}^2\beta_1 + 6\frac{\mu}{r^4}\gamma_1 & 4\dot{\theta}^2\beta_1\frac{\kappa'}{\kappa} - 2\dot{\theta}^2\frac{q_2 + \sin\theta}{\kappa^2} & 0 \\ -4\dot{\theta}^2\beta_1\frac{\kappa'}{\kappa} + 2\dot{\theta}^2\frac{q_2 + \sin\theta}{\kappa^2} & 2\dot{\theta}^2\beta_1 - 3\frac{\mu}{r^4}\gamma_1 & 0 \\ 0 & 0 & -3\frac{\mu}{r^4}\gamma_1 \end{bmatrix} \quad (5.54a)$$

$$\Omega_{q_1}^{A\mathbf{x}} = \begin{bmatrix} 0 & \frac{6}{\eta^2}q_1\dot{\theta} + \frac{4}{\kappa}\dot{\theta}\cos\theta & 0 \\ -\frac{6}{\eta^2}q_1\dot{\theta} - \frac{4}{\kappa}\dot{\theta}\cos\theta & 0 & 0 \\ 0 & 0 & 0 \end{bmatrix} \quad (5.54b)$$

$$K_{q_2}^{A\mathbf{x}} = \begin{bmatrix} 2\dot{\theta}^2\beta_2 + 6\frac{\mu}{r^4}\gamma_2 & 4\dot{\theta}^2\beta_2\frac{\kappa'}{\kappa} + 2\dot{\theta}^2\frac{q_1 + \cos\theta}{\kappa^2} & 0 \\ -4\dot{\theta}^2\beta_2\frac{\kappa'}{\kappa} - 2\dot{\theta}^2\frac{q_1 + \cos\theta}{\kappa^2} & 2\dot{\theta}^2\beta_2 - 3\frac{\mu}{r^4}\gamma_2 & 0 \\ 0 & 0 & -3\frac{\mu}{r^4}\gamma_2 \end{bmatrix} \quad (5.55a)$$

$$\Omega_{q_2}^{A_{\mathbf{x}}} = \begin{bmatrix} 0 & \frac{6}{\eta^2} q_2 \dot{\theta} + \frac{4}{\kappa} \dot{\theta} \sin \theta & 0 \\ -\frac{6}{\eta^2} q_2 \dot{\theta} - \frac{4}{\kappa} \dot{\theta} \sin \theta & 0 & 0 \\ 0 & 0 & 0 \end{bmatrix} \quad (5.55b)$$

$$\frac{d\theta}{da} = -\frac{3a\eta \kappa^2}{2r_0^2 \kappa_0^2} n(t - t_0) \quad (5.56a)$$

$$\frac{d\theta}{d\theta_0} = \frac{\kappa^2}{\kappa_0^2} \quad (5.56b)$$

$$\frac{d\theta}{dq_1} = \frac{1}{r^2 \eta^2} (r \sin \theta (r + a(1 - q_1^2)) - r_0 \sin \theta_0 (r_0 + a(1 - q_1^2))) \quad (5.56c)$$

$$+ a q_1 q_2 (r \cos \theta - r_0 \cos \theta_0) + q_2 (r - r_0) (a + r + r_0))$$

$$\frac{d\theta}{dq_2} = \frac{1}{r^2 \eta^2} (-r \cos \theta (r + a(1 - q_2^2)) + r_0 \cos \theta_0 (r_0 + a(1 - q_2^2))) \quad (5.56d)$$

$$- a q_1 q_2 (r \sin \theta - r_0 \sin \theta_0) - q_1 (r - r_0) (a + r + r_0))$$

$$\kappa = 1 + q_1 \cos \theta + q_2 \sin \theta \quad (5.57)$$

$$\kappa_0 = 1 + q_1 \cos \theta_0 + q_2 \sin \theta_0 \quad (5.58)$$

$$\kappa' = -q_1 \sin \theta + q_2 \cos \theta \quad (5.59)$$

$$\eta = \sqrt{1 - q_1^2 - q_2^2} \quad (5.60)$$

$$\beta_1 = \frac{3q_1}{\eta^2} + 2 \frac{\cos \theta}{\kappa} \quad (5.61)$$

$$\beta_2 = \frac{3q_2}{\eta^2} + 2 \frac{\sin \theta}{\kappa} \quad (5.62)$$

$$\gamma_1 = \frac{2aq_1}{\kappa} + \frac{a\eta^2}{\kappa^2} \cos \theta \quad (5.63)$$

$$\gamma_2 = \frac{2aq_2}{\kappa} + \frac{a\eta^2}{\kappa^2} \sin \theta \quad (5.64)$$

$$B_{\mathbf{x}, \Omega} = \frac{dB_{\mathbf{x}}}{d\Omega} = \begin{bmatrix} 0_{3 \times 3} \\ -R_3(\theta) R_1(i) \tilde{e}_3 R_3(\Omega) R_{\mathcal{NH}}^* \end{bmatrix} \quad (5.65a)$$

$$B_{\mathbf{x}, i} = \frac{dB_{\mathbf{x}}}{di} = \begin{bmatrix} 0_{3 \times 3} \\ -R_3(\theta) \tilde{e}_1 R_1(i) R_3(\Omega) R_{\mathcal{NH}}^* \end{bmatrix} \quad (5.65b)$$

$$B_{\mathbf{x},\theta} = \frac{dB_{\mathbf{x}}}{d\theta} = \begin{bmatrix} 0_{3 \times 3} \\ -\tilde{\mathbf{e}}_3 R_3(\theta) R_1(i) R_3(\Omega) R_{\mathcal{NH}}^* \end{bmatrix} \quad (5.65c)$$

where $\tilde{\mathbf{e}}_i$ denotes the skew-symmetric tilde (cross) matrix for the i^{th} basis vector.[111] Eqs. (5.51) - (5.65) are all evaluated on the nominal target orbit, and enable the sensitivity dynamics given in Eq. (5.44) to be computed.

Substituting $R_{\mathcal{NH}}^* = R_3^\top(\Omega^*) R_1^\top(i^*) R_3^\top(\theta^*)$, the directions for the control components u_1, u_2, u_3 track the nominal LVLH frame basis vectors. Then, Eq. (5.65) can be simplified when evaluated on the nominal target orbit:

$$B_{\mathbf{x},\Omega} = \begin{bmatrix} 0_{3 \times 3} \\ -R_3(\theta) R_1(i) \tilde{\mathbf{e}}_3 R_1(i)^\top R_3(\theta)^\top \end{bmatrix} = \begin{bmatrix} 0 & 0 & 0 \\ 0 & 0 & 0 \\ 0 & 0 & 0 \\ 0 & ci & -c\theta si \\ -ci & 0 & sis\theta \\ c\theta si & -sis\theta & 0 \end{bmatrix} \quad (5.66a)$$

$$B_{\mathbf{x},i} = \begin{bmatrix} 0_{3 \times 3} \\ -R_3(\theta) \tilde{\mathbf{e}}_1 R_3(\theta)^\top \end{bmatrix} = \begin{bmatrix} 0 & 0 & 0 \\ 0 & 0 & 0 \\ 0 & 0 & 0 \\ 0 & 0 & s\theta \\ 0 & 0 & c\theta \\ -s\theta & -c\theta & 0 \end{bmatrix} \quad (5.66b)$$

$$B_{\mathbf{x},\theta} = \begin{bmatrix} 0_{3 \times 3} \\ -\tilde{\mathbf{e}}_3 \end{bmatrix} = \begin{bmatrix} 0 & 0 & 0 \\ 0 & 0 & 0 \\ 0 & 0 & 0 \\ 0 & -1 & 0 \\ 1 & 0 & 0 \\ 0 & 0 & 0 \end{bmatrix} \quad (5.66c)$$

Propagating both the nominal relative state \mathbf{x}^* and the sensitivities via Eq. (5.50) once,

uncertainty distributions in the target orbit elements can be rapidly mapped to an evolving distribution in the relative state. This mapping is extremely accurate for close-proximity (km-scale) satellite relative motion and for modest uncertainties in the target orbit.

5.2.3 The Clohessy-Wiltshire Case

The sensitivity dynamics discussed in Section 2 for the general Keplerian relative motion problem are inconvenient to explore analytically due to their complexity. To avoid such a prolonged investigation, this section explores the sensitivity dynamics for the controlled relative motion problem when the target orbit is sufficiently near-circular to use the Clohessy-Wiltshire (CW) model [36]. It is easier to analyze this system and then afterwards investigate if and how fundamental conclusions change for the general-eccentricity case.

For the CW problem, the natural relative motion dynamics assume the following highly simplified linear-time varying form that is a function of the target semimajor axis alone:

$$\dot{\mathbf{x}} = \begin{bmatrix} 0 & 0 & 0 & 1 & 0 & 0 \\ 0 & 0 & 0 & 0 & 1 & 0 \\ 0 & 0 & 0 & 0 & 0 & 1 \\ 3n^2 & 0 & 0 & 0 & 2n & 0 \\ 0 & 0 & 0 & -2n & 0 & 0 \\ 0 & 0 & -n^2 & 0 & 0 & 0 \end{bmatrix} \mathbf{x} \quad (5.67)$$

where $n = \sqrt{\mu/a^3}$. Because the CW problem linearizes about a circular orbit, the orbit element definition from Section 2 is modified. In particular, the target orbit is parameterized by a , $\bar{\theta}$, i , and Ω . The quantity $\bar{\theta}$ is measured from the ascending node, and eccentricity is assumed sufficiently small that one may write $\bar{\theta} \approx \bar{\theta}_0 + nt$. The orbit element differences are $\delta\mathbf{oe} = (\delta a, \delta\theta, \delta e, \delta i, \delta\Omega)^\top$. For this study, the chaser periapsis is located at the chaser's ascending node. Note that it is always possible to define the inertial frame such that the periapsis is at zero latitude, so there is no loss of generality with this approach.

The initial sensitivities are computed in the same manner as before – using Eq. (5.47).

However, the mapping from element differences to local coordinates needs to be modified from Eq.

(6.53):

$$G_{CW} = \begin{bmatrix} 1 & 0 & -a \cos \bar{\theta} & 0 & 0 \\ 0 & a & 0 & 0 & a \cos i \\ 0 & 0 & 0 & a \sin \bar{\theta} & -a \cos \bar{\theta} \sin i \\ 0 & 0 & na \sin \bar{\theta} & 0 & 0 \\ -\frac{3}{2}n & 0 & 2na \cos \bar{\theta} & 0 & 0 \\ 0 & 0 & 0 & na \cos \bar{\theta} & na \sin \bar{\theta} \sin i \end{bmatrix} \quad (5.68)$$

The derivatives of Eq. (5.68) with respect to the target orbit elements are simple and thus are not explicitly provided.

From Eqs. (5.47) and (5.67), only the sensitivity to the target semimajor axis is influenced by the relative state. Its dynamics are given with the other sensitivities below:

$$\dot{\mathbf{s}}_a = A_{CW,a} \mathbf{x}^* + A_{CW} \mathbf{s}_a + B_{\mathbf{x},\theta} \frac{d\bar{\theta}}{da} \mathbf{u} \quad (5.69a)$$

$$\dot{\mathbf{s}}_{\bar{\theta}_0} = A_{CW} \mathbf{s}_{\bar{\theta}_0} + B_{\mathbf{x},\theta} \mathbf{u} \quad (5.69b)$$

$$\dot{\mathbf{s}}_i = A_{CW} \mathbf{s}_i + B_{\mathbf{x},i} \mathbf{u} \quad (5.69c)$$

$$\dot{\mathbf{s}}_{\Omega} = A_{CW} \mathbf{s}_{\Omega} + B_{\mathbf{x},\Omega} \mathbf{u} \quad (5.69d)$$

$$A_{CW,a} = \begin{bmatrix} 0 & 0 & 0 & 0 & 0 & 0 \\ 0 & 0 & 0 & 0 & 0 & 0 \\ 0 & 0 & 0 & 0 & 0 & 0 \\ -\frac{9}{a}n^2 & 0 & 0 & 0 & -\frac{3}{a}n & 0 \\ 0 & 0 & 0 & \frac{3}{a}n & 0 & 0 \\ 0 & 0 & \frac{3}{a}n^2 & 0 & 0 & 0 \end{bmatrix} \quad (5.70)$$

$$\frac{d\bar{\theta}}{da} = -\frac{3}{2a}nt \quad (5.71)$$

Inspecting Eqs. (5.69) – (5.71), the influence of control and the motion of the nominal trajectory are generally sub-dominant in the dynamics of \mathbf{s}_a . In other words, $\dot{\mathbf{s}}_a \approx A_{CW} \mathbf{s}_a$, except for large

magnitudes of the control signal \mathbf{u} , or large values of the components of the nominal relative state \mathbf{x}^* .

Further interpretation of the sensitivity dynamics for the CW case is possible by investigating the initial values of the sensitivities themselves using Eq. (5.47). Note that the uncontrolled dynamics of \mathbf{s}_{θ_0} , \mathbf{s}_i , and \mathbf{s}_Ω are all the same as the CW system. It can be shown that all three are periodic. Consider $\mathbf{s}_{\theta_0}(0)$:

$$\mathbf{s}_{\theta_0}(0) = \begin{pmatrix} a \sin \bar{\theta}_0 \delta e \\ -a \\ a \cos \bar{\theta}_0 \delta i + a \sin \bar{\theta}_0 \sin i \delta \Omega \\ na \cos \bar{\theta}_0 \delta e \\ -2na \sin \bar{\theta}_0 \delta e \\ -na \sin \bar{\theta}_0 \delta i + na \cos \bar{\theta}_0 \sin i \delta \Omega \end{pmatrix} \quad (5.72)$$

The CW no-drift condition is $\dot{y}_0 + 2nx_0 = 0$. From Eq. (5.72), the components $s_{\theta_0,x}(0)$ and $s_{\theta_0,y}(0)$ satisfy this constraint. Additionally, $s_{\theta_0,y}$ is much greater than all other components of \mathbf{s}_{θ_0} and is nearly stationary in the absence of control. A similar result can be shown for \mathbf{s}_i and \mathbf{s}_Ω using their initial components – both of these sensitivities are also periodic in the uncontrolled case. For \mathbf{s}_i , the dominant component is a large periodic oscillation in $s_{i,z}$, with the state components in the x and y directions of a negligible scale by comparison. For \mathbf{s}_Ω , there is a large y component, and the oscillatory z component is also large, whereas the x component is insignificant.

Because the sensitivities directly map static uncertainty distributions in \mathbf{oe}_0 to evolving uncertainty distributions in the relative state, it is of interest to see which sensitivities drive the growth in the distribution in the absence of control. Because all other sensitivities are periodic, it is clear that growth in components of \mathbf{s}_a must be driving the secular growth in uncertainty for uncontrolled relative motion. The unforced behavior of \mathbf{s}_a turns out to be extremely simple. To

start out, the initial value of the sensitivity is given below:

$$\mathbf{s}_a(0) = \begin{pmatrix} -1 - \cos \bar{\theta}_0 \delta e \\ \delta \bar{\theta}_0 + \cos i \delta \Omega \\ \sin \bar{\theta}_0 \delta i - \cos \bar{\theta}_0 \sin i \delta \Omega \\ -\frac{1}{2} n \sin \bar{\theta}_0 \delta e \\ \frac{3}{2} n + \frac{9n}{4a} \delta a - n \cos \bar{\theta}_0 \delta e \\ -\frac{n}{2} \cos \bar{\theta}_0 \delta i - \frac{n}{2} \sin \bar{\theta}_0 \sin i \delta \Omega \end{pmatrix} \quad (5.73)$$

Substituting the initial sensitivity state into the CW solution [111] and keeping only dominant terms, the sensitivity to semimajor displays the following approximate behavior, neglecting small oscillations:

$$\mathbf{s}_a(t) \approx \left(-1, \frac{3}{2} nt, 0, 0, \frac{3}{2} n, 0 \right)^\top \quad (5.74)$$

It is natural to ask what the influence of control on the sensitivities can have – because any permitted purposeful control of the sensitivities enables a corresponding control of some aspect of the evolving relative state uncertainty distribution. To answer this, first recall that the scale of control needed to significantly influence \mathbf{s}_a is of a much larger scale than that needed for the other sensitivities, due to the n/a multiplier on the control \mathbf{u} . Thus, the controllability of the other sensitivities \mathbf{s}_{θ_0} , \mathbf{s}_i , and \mathbf{s}_Ω with lower thrust is considered. For control analyses of this type, the resulting meager effect of control on \mathbf{s}_a is neglected. Furthermore, the z components of the sensitivities are decoupled from the in-plane components and are also neutrally stable, so these will be ignored as well.

Note that it can be determined from Eqs. (5.69) and (5.66) that the simultaneous control of all components of \mathbf{x}^* , \mathbf{s}_{θ_0} , \mathbf{s}_i , and \mathbf{s}_Ω is impossible. However, control of a subset of these states is possible. As a demonstration of control of a subset of the sensitivities, a simple strategy is explored in this section that combines augmented control of the planar \mathbf{x}^* and \mathbf{s}_{θ_0} with stabilization of planar \mathbf{s}_Ω . The out-of-plane components of the nominal relative state and the sensitivities are ignored.

The augmented dynamics are given below:

$$\dot{\mathbf{z}} = \frac{d}{dt} \begin{pmatrix} \mathbf{x}_{2D} \\ \mathbf{s}_{\theta_0, 2D} \end{pmatrix} = \begin{bmatrix} A_{2D} & 0_{4 \times 4} \\ 0_{4 \times 4} & A_{2D} \end{bmatrix} \mathbf{z} + B_{\mathbf{z}} \mathbf{u} \quad (5.75)$$

where the control vector is composed of the in-plane accelerations $\mathbf{u} = (a_x, a_y)^\top$, and A_{2D} and $B_{\mathbf{z}}$ are given below:

$$A_{2D} = \begin{bmatrix} 0 & 0 & 1 & 0 \\ 0 & 0 & 0 & 1 \\ 3n^2 & 0 & 0 & 2n \\ 0 & 0 & -2n & 0 \end{bmatrix} \quad (5.76)$$

$$B_{\mathbf{z}} = \begin{bmatrix} 0 & 0 & 1 & 0 & 0 & 0 & 0 & 1 \\ 0 & 0 & 0 & 1 & 0 & 0 & -1 & 0 \end{bmatrix}^\top \quad (5.77)$$

Stabilization of \mathbf{s}_Ω is achieved by enforcing the no-drift constraint $x_{\text{off}}(\mathbf{s}_\Omega) = 4s_{\Omega,x} + \frac{2}{n}s_{\Omega,y} \approx 0$ to prevent secular growth in the \mathbf{s}_Ω dynamics. This is achieved by the following out-of-plane control component:

$$u_3 = a_z = \frac{\cos i}{\sin i \sin \bar{\theta}} u_1 \quad (5.78)$$

where some maximum $|u_3| < \delta$ is enforced as needed for when $\sin \bar{\theta}$ is small. Computing the controllability matrix $\mathcal{C} = [B \ AB \ A^2B \ \dots \ A^7B]$ for the LTI system given by Eq. (5.75), the rank is 8, thus the augmented planar state and θ_0 sensitivity dynamics are determined to be fully controllable. Most of the secondary effects of the control strategy are small changes in the neutrally stable out-of-plane components of the sensitivities \mathbf{s}_i and \mathbf{s}_Ω , and increases in the out-of-plane motion of \mathbf{x}^* . Additionally, this strategy does have a tendency to grow the small in-plane components of \mathbf{s}_i . Nonetheless, it is a simple demonstration of the possibility of designing control to influence the sensitivities.

5.2.4 Numerical Simulations

5.2.4.1 Efficient Relative State Uncertainty Propagation via the Sensitivities

To demonstrate the successful propagation of the sensitivity dynamics for the general Keplerian case, consider the example given by the information in Table 5.4. For this example, the initial target orbit element error statistics correspond to uncertainty in its initial orbit position on the order of 100 m, with cm/s error in velocity. The chaser spacecraft orbit position is assumed perfectly known, but the relative state is uncertain. The nominal relative state is linearly propagated using the plant matrix given by Eq. (5.45) and the sensitivities are propagated from their initial values – obtained using Eq. (5.47) – through use of Eq. (5.50). This first study is control-free, investigating the behavior of the unforced sensitivities over the course of two nominal target orbit periods. The dominant components of the sensitivities of relative position to each orbit element

Table 5.4: Eccentric Target Orbit, Unforced Relative Motion

Parameters	Values
Nominal Target Orbit	$\mathbf{oe}_{t,0}^* = (a, e, i, \omega, \Omega, f_0) \approx (12600 \text{ km}, 0.3, 63.4^\circ, 27^\circ, 2^\circ, 10^\circ)$ $\theta_0^* = 37^\circ, q_1^* = 0.2673, q_2^* = 0.1362$
Target Orbit Uncertainty	Normal dist., zero-mean, angle deviations $\times 10^{-5}$ degrees: $\sigma_a = 20 \text{ m}, \sigma_e = 2 \times 10^{-6}, \sigma_i = 4, \sigma_\omega = 4, \sigma_\Omega = 1.9, \sigma_{f_0} = 8$
Chaser Spacecraft Orbit	$\delta \mathbf{oe}_{s,0}^* = \mathbf{oe}_{s,0} - \mathbf{oe}_{t,0}^* = (0.4 \text{ km}, 8 \times 10^{-5}, 0.01^\circ, 0.006^\circ, 0^\circ, 0^\circ)$
Nominal Initial Relative State	$\boldsymbol{\rho}_0 = (-724.2, 926.9, 929.7) \text{ m}, \boldsymbol{\rho}'_0 = (0.009, 1.202, 1.097) \text{ m/s}$

are given in Figures. 5.19 - 5.22. The sensitivities of velocity are not explicitly shown but their behavior can be inferred from the position sensitivity curves, because the sensitivities behave like augmented position and velocity state vectors. Inspecting the sensitivity figures, the out-of-plane components of sensitivities to semimajor axis and θ_0 are negligible, and so are the in-plane components of sensitivity to inclination. Note that all sensitivities except \mathbf{s}_a are periodic, thus it is the uncertainty in target semimajor axis that drives secular growth in relative state uncertainty. This finding agrees with intuition, because only an error in the target semimajor axis would correspond to a drift over time.

The effect of the scale of target eccentricity on the sensitivities is straightforward. For low

eccentricity, the growth in $s_{a,y}$ becomes more linear in time, and the oscillations in $s_{a,x}$ are reduced. As $e \rightarrow 0$, $s_{a,x} \rightarrow -1$. Additionally, for low eccentricity, the $s_{\theta_0,x}$ curve is composed of small oscillations about zero, and the $s_{\theta_0,y}$ curve is nearly constant, oscillating about $-a^*$. For larger values of eccentricity, the oscillations in \mathbf{s}_{θ_0} become large, as demonstrated by the large oscillations in the two quantities for $e = 0.3$ in Figure 5.20. The characteristic behavior of \mathbf{s}_i , \mathbf{s}_{q_1} , and \mathbf{s}_{q_2} does not change greatly with the eccentricity except for an increasing sharpness near target periapsis for very high values of eccentricity. For \mathbf{s}_{Ω} , the oscillations in the y component flatten out as eccentricity is decreased.

Note that the scale of components of \mathbf{s}_a is smaller than the components of sensitivities to the target orbit element angles because small variations in angular separation scale with the semimajor axis of the orbit, so even a small error in θ_0 can have large consequences for the relative state in Cartesian components. Rescaling $\underline{\mathbf{s}}_a = a^* \mathbf{s}_a$ might be a superior way of representing the scale of the sensitivities to semimajor axis – mapping small deviations in $(a - a^*)/a^*$ to large variations in the x and y coordinates of the relative state.

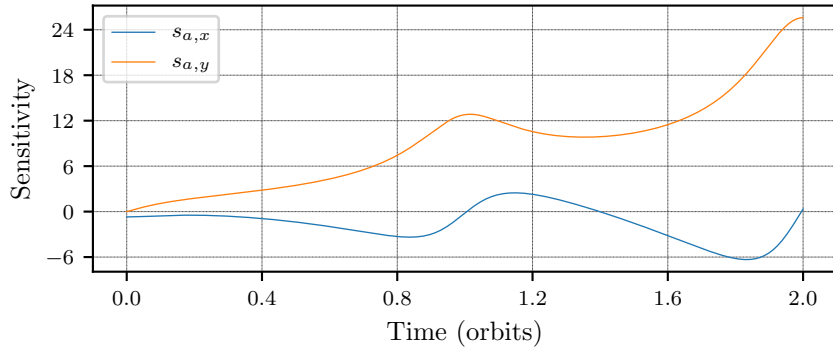


Figure 5.19: Relative Position Sensitivities to Target Semimajor Axis

The real value of propagating the sensitivities is in their use for rapidly and accurately capturing variations in the relative state arising from uncertainty in the target orbit. The sensitivities are propagated once by evaluating their linear equations on a nominal target orbit, and the nominal relative state is also propagated once using the nominal target orbit. Then, dispersions in the target orbit elements from its nominal values can be directly mapped to dispersions in the local

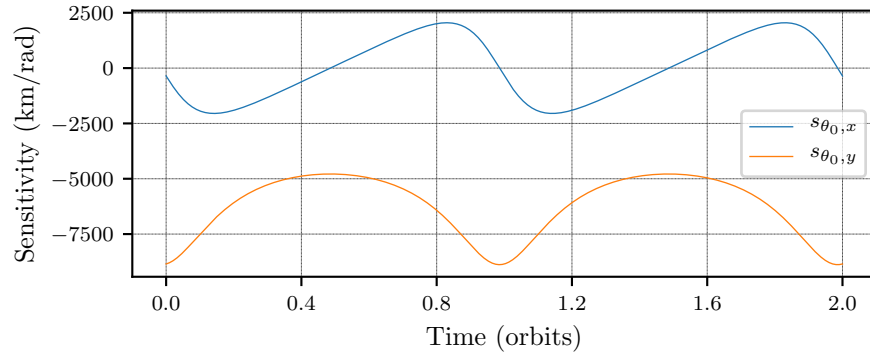


Figure 5.20: Relative Position Sensitivities to Target Initial Argument of Latitude

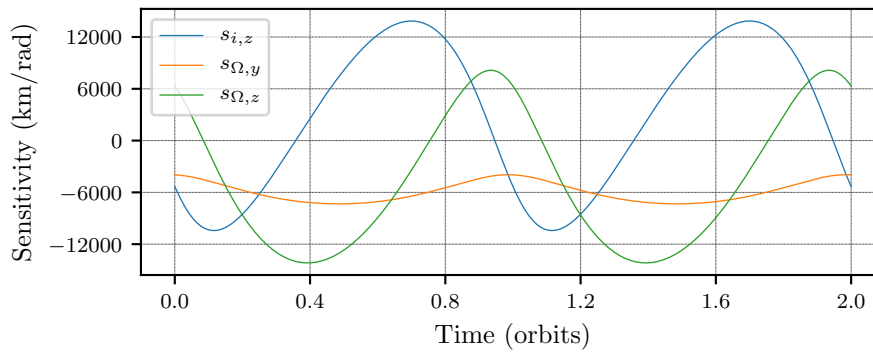
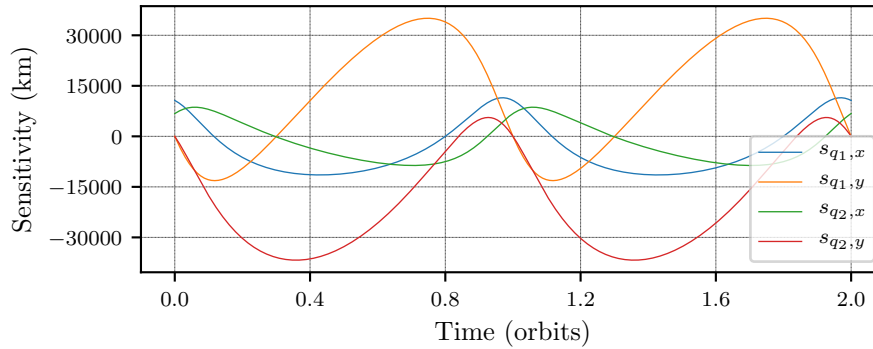


Figure 5.21: Relative Position Sensitivities to Target R.A.A.N and Inclination

Figure 5.22: Relative Position Sensitivities to Target q_1, q_2

relative state using Eq. (5.49). To demonstrate the usefulness of this, the statistical variations in the initial target orbit elements given in Table 5.4 are used to generate a 1000-point Monte Carlo study of the evolution of the relative state. To investigate collision risk, the time of smallest relative distance for the nominal relative trajectory is computed to be $t_{\text{crit}} \approx t_0 + 1.328T^*$. All 1000 points

are given in Figure 5.23 at times t_0 (blue) and t_{crit} (red), along with a subset of their connecting trajectories (gray) and the nominal trajectory (dashed line). This information is all obtained in a matter of seconds, because the individual points do not need to be numerically propagated and are instead mapped directly through the sensitivities. Repeating this study with 10,000 points thus results in minimal increase in runtime. Comparing the sensitivity-mapped relative state solutions to their true values obtained by numerical integration of the individual cases, the sensitivity study is revealed to be highly accurate, with none of the position errors ever exceeding 0.2 cm in the simulated timespan of 1.328 nominal target orbit periods.

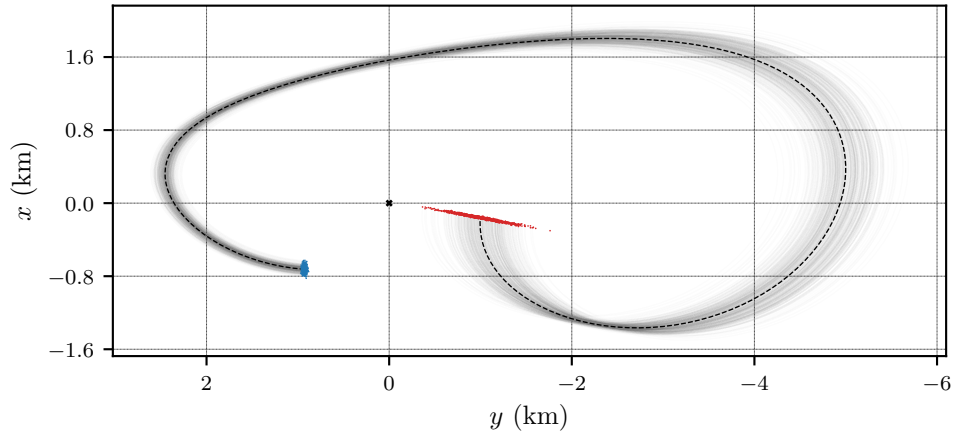


Figure 5.23: Sensitivity-Propagated Relative State Uncertainty Distribution

The relative states depicted in Figure 5.23 are each results for different target orbits – the relative motion is shown in the nominal LVLH frame centered on the uncertain target at $(0, 0)$. The chaser spacecraft orbit is known, but the target-centered relative state is unknown due to target orbit uncertainty. As expected, this relative state uncertainty grows over time, discernible from the spread in the initial relative positions (blue) to the spread in final relative positions (red) in Figure 5.23. This is an interesting result because a single linear simulation allows very large samples of possible relative states to be propagated efficiently, despite the fact that each of these points is for a different target orbit and would traditionally require its own linearization.

Overall, this method tends to work quite well for at least one target orbit period for un-

certainties in the target orbit corresponding to up to km-scale initial position error in low Earth orbits. The sensitivities enable efficient characterization of the evolving uncertain relative state for proximity operations in the vicinity of an uncertain target object. Additionally, they enable a direct study of which target orbit element uncertainties are the largest contributors to the relative state error at a future time of interest. Because it relies on linearized dynamics of the relative state's sensitivity to target orbit elements, it breaks down with both large separations in the nominal relative state and with sufficiently large differences between the nominal target orbit and the true orbit. As a result, the accuracy of the method will degrade for target orbit statistics with large standard deviations in the initial orbit elements. The method is fairly sensitive to errors in semimajor axis, which must be known to a certainty of kilometers or better. Nonetheless, it is quite useful for situations with modest uncertainty in the target object orbit.

5.2.4.2 Naïve Relative State Control

To test the influence of control on the sensitivities, this section explores simple examples of infinite-time LQR control with the CW dynamics. The following cost is minimized for symmetric positive-definite Q and R :

$$J = \int_{t_0}^{\infty} (\mathbf{x}^\top Q \mathbf{x} + \mathbf{u}^\top R \mathbf{u}) dt \quad (5.79)$$

The cost-minimizing feedback control is $\mathbf{u} = -R^{-1}B^\top P \mathbf{x}$ where P solves the algebraic Riccati equation:

$$A^\top P + PA - PBR^{-1}B^\top P + Q = 0 \quad (5.80)$$

Note that typical control maneuvers conducted in close-proximity exert only a small influence on the sensitivities. This is especially true if the control effort for the maneuvers is low. As an example, consider the case given by the data in Table 5.5.

The optimal control signal solving the infinite-time LQR problem parameterized by Table 5.5 is not very aggressive, taking about 2 nominal target orbit periods to settle 95% of the initial relative state error. The resulting nominal relative motion is given by the dotted line in Figure

Table 5.5: Simulation Parameters, CW Control Example 1

Parameters	Values
Nominal Target Orbit Elements	$a^* = 8000$ km, $\bar{\theta}_0^* = 37^\circ$, $i^* = 30^\circ$, $\Omega^* = 21^\circ$
Target Orbit Uncertainty	Normal dist., zero-mean, angle deviations $\times 10^{-5}$ degrees: $\sigma_a = 6.0$ m, $\sigma_i = 4.0$, $\sigma_\Omega = 1.9$, $\sigma_{\bar{\theta}_0} = 8.0$
Nominal Initial Relative State	$\boldsymbol{\rho}_0 = (-0.92, -2.92, -3.76)$ km, $\boldsymbol{\rho}'_0 = (1.27, 2.06, -5.22)$ m/s
Target Relative Motion	Bounded relative orbit, $x(0) = 0.5$ km, $\dot{y}(0) = -2n^*x(0)$
Control Parameters	$Q_{\boldsymbol{\rho}\boldsymbol{\rho}} = 2I_{3\times 3}$, $Q_{\boldsymbol{\rho}'\boldsymbol{\rho}'}$ = $100I_{3\times 3}$, $R = 10^{13}I_{3\times 3}$
Simulation Parameters	$t_f = 2.25 T^*$

5.24. The achieved nominal relative orbit is approximately 2 km by 1 km. To simulate the effects of uncertainty in the target orbit, a 1000-point Monte Carlo study is also propagated using the sensitivities for the CW case, whose dynamics are given by Eq. (5.69). None of the sensitivity-propagated controlled relative position errors exceed 5 cm from their true values in the 2.25 nominal orbit periods simulated. This demonstrates that the sensitivities remain effective for efficiently studying relative state outcomes for cases of controlled relative motion.

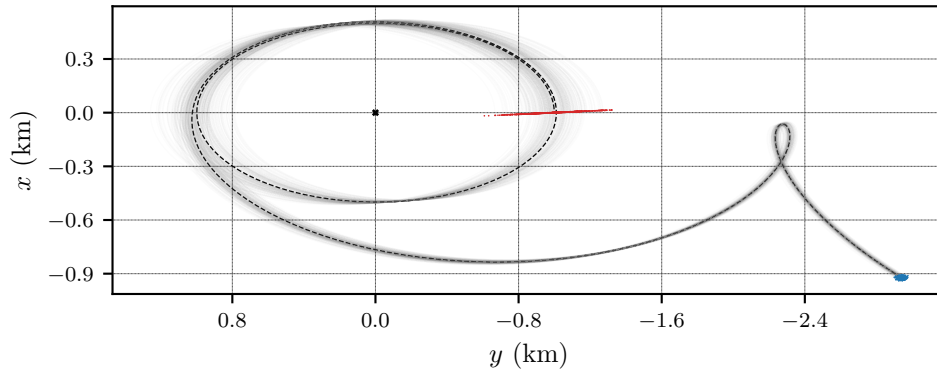


Figure 5.24: Controlled Relative State, Naïve Control Example

The most significant relative state sensitivities are given in Figures 5.25 and 5.26. Note that the sensitivities for relative state propagation without control are given as dotted black lines that are very close to their counterparts from the controlled example (colored). This shows that the control strategy explored for this example exerts only a small influence on the sensitivities. This is because the relative state sensitivities are more costly to significantly influence than the relative state. First, for the sensitivity to semimajor axis, Eqs. (5.69) and (5.71) show that the influence of

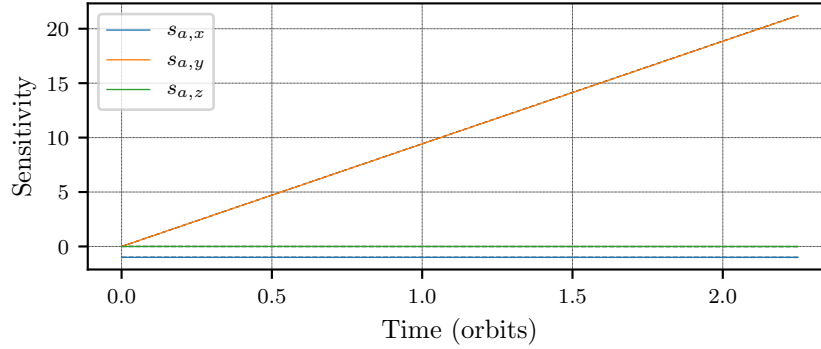


Figure 5.25: Sensitivity to Semimajor Axis, Naïve Control Example

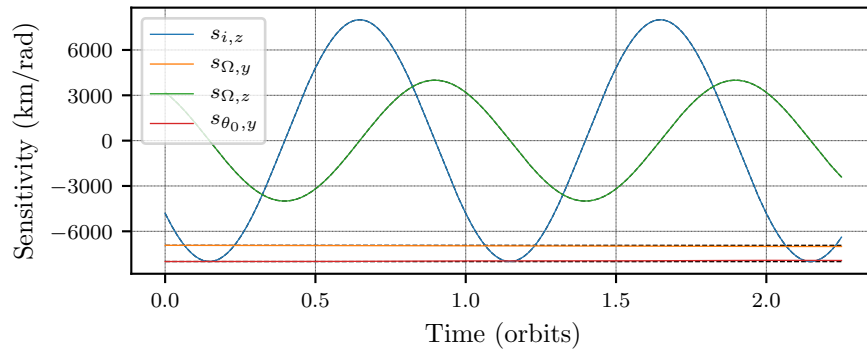


Figure 5.26: Sensitivities to Target Orbit Element Angles, Naïve Control Example

control on the dynamics is pre-multiplied by n^*/a , a very small quantity. For the sensitivities to Ω , i , and $\bar{\theta}_0$, the reason for the weak influence of control is due to the sheer scale of those sensitivity states, which are much larger than the relative state. Recall from Eq. (5.69) that these sensitivities obey forced CW dynamics, just like the relative state. There are actually comparable effects of control on the relative state and the sensitivities - the control exerts a km-scale influence on the relative state, and a km/rad scale influence on the sensitivities. The sensitivities are simply quite costly to influence significantly, at least in comparison to the cost of achieving desired regulation and tracking control of the relative state. This is an important point that will be discussed further in the next control example.

Note from Figures 5.25 and 5.26 that the simple predictions of Eqs. (5.72) - (5.74) and their associated discussions in Section 3 are accurate. In particular, for \mathbf{s}_i , the dominant component is a

large periodic oscillation in $s_{i,z}$, with the state components in the x and y directions of a negligible scale by comparison. For \mathbf{s}_Ω , there is a large y component, and the oscillatory z component is also large, whereas the x component is insignificant (not shown). Additionally, by inspection of Figure 5.25, the simple secular behavior given by Eq. (5.74) for \mathbf{s}_a is also shown to be accurate.

Comparing the curves in Figures 5.25 and 5.26 with their counterparts in Figures 5.19 - 5.22 for an eccentric target orbit, the qualitative differences in the sensitivity between the circular target and eccentric target orbit cases are fairly straightforward. First, the oscillations in $s_{a,x}$ and $s_{a,y}$ become more pronounced, but the secular growth in $s_{a,y}$ is retained for both. Next, because the target orbit is now circular, the in-plane sensitivities of the relative state to target elements Ω and θ_0 no longer vary considerably over time. Lastly, because the target orbit is assumed circular and the dynamic effects of nonzero target orbit eccentricity are not at all considered by the CW formulation, the sensitivities s_{q_1} and s_{q_2} are undefined here.

5.2.4.3 Augmented Relative State and Sensitivity Control

As an example of combined control of the relative state and a subset of the sensitivities, the strategy discussed in Section 3 is implemented. This strategy maneuvers the spacecraft to a desired final relative state, and in the process, reduces the planar relative state sensitivity to θ_0 while preserving the planar sensitivity to Ω . In general, this results in an exaggeration of the neutrally stable out-of-plane motion, while also potentially generating insignificant increases in the in-plane sensitivity of the relative state to the target inclination. For this example, the relevant simulation parameters are provided in Table 5.6.

In general, it has been determined that controlling the sensitivities is more costly than control of the relative state. As a simple demonstration of the possibility of controlling the relative state along with a subset of the sensitivities, a stationary along-track offset of 4 km is targeted, in a control maneuver that also yields a 10% reduction in the magnitude of $s_{\bar{\theta}_0,y}$, while keeping $s_{\bar{\theta}_0,x} \approx 0$ and preserving the values of the planar components of \mathbf{s}_Ω . Through this action, the contribution of uncertainty in the target orbit element $\bar{\theta}_0$ to uncertainty in the relative state is reduced. The purpose

Table 5.6: Simulation Parameters, CW Control Example 2

Parameters	Values
Nominal Target Orbit Elements	$a^* = 8000$ km, $\bar{\theta}_0^* = 37^\circ$, $i^* = 30^\circ$, $\Omega^* = 21^\circ$
Nominal Initial Relative State	$\boldsymbol{\rho}_0 = (-0.92, -2.92, -3.76)$ km, $\boldsymbol{\rho}' = (1.27, 2.06, -5.22)$ m/s
Control Goals	$\boldsymbol{\rho}_{2D} = (0, -4)$ km, $\boldsymbol{\rho}'_{2D} = (0, 0)$ m/s, $s_{\bar{\theta}_0,x} = 0$ km/rad, $s_{\bar{\theta}_0,y} = -7200$ km/rad (10% reduction)
Control Parameters	Preserve \mathbf{s}_Ω , ignore out-of-plane relative state and sensitivities $Q = \text{diag}(200, 200, 10^4, 10^4, 0.02, 0.02, 10, 10)$, $R = 10^{11} I_{2 \times 2}$, Out-of-plane control $u_3 = \frac{\cos i}{\sin i \sin \theta} u_1$, $ u_3 < 1$ m/s ²
Simulation Parameters	$t_f = 4.0 T^*$

of this control example is to demonstrate that the sensitivities can be meaningfully influenced by control action.

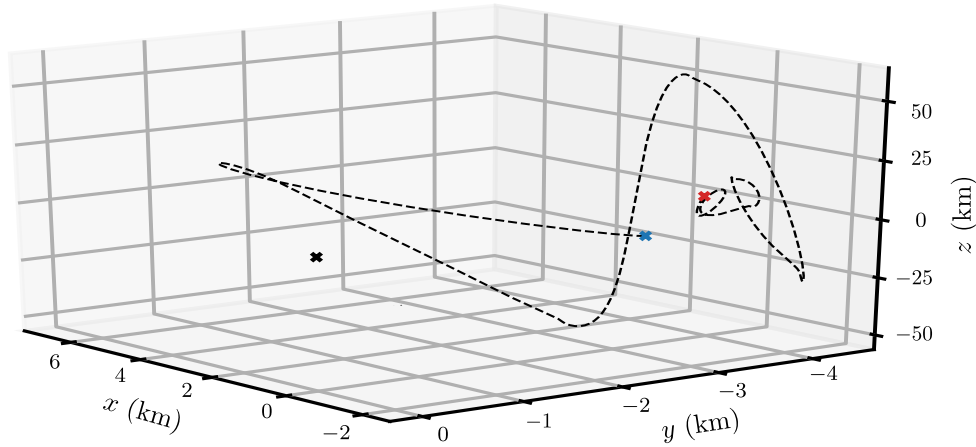


Figure 5.27: Relative Motion Trajectory, Augmented Control Example

Using the augmented control design discussed in Section 3 and the control parameters in Table 5.6, the control effect is simulated for 4 nominal target orbit periods. The resulting motion of the nominal trajectory is given in Figure 5.27. The initial point is given by a blue x and the final point is given by a red x, and the target is at the origin of the nominal LVLH frame, indicated with a black x. Note from Figure 5.27 that the relative state trajectory follows a very indirect path to the target relative position. This is because a lot of control effort has to be exerted to reduce the planar components of $\mathbf{s}_{\bar{\theta}_0}$ as specified. There is no way to exert this control effort without also affecting the relative state in the process.

The time-varying behaviors of each component of the controlled nominal relative position are given in Figure 5.28. Examining both Figures 5.27 and 5.28, the initial large change in the relative position is clear. There is an almost 8 km shift in x and a ~ 2 km shift in y . This maneuver seems necessary to initialize reduction in $s_{\bar{\theta}_0,y}$. Using other control simulations, it is determined that the size of this initial maneuver scales with the desired reduction in $s_{\bar{\theta}_0,y}$. Despite this large initial deviation, the relative state does eventually settle to the desired value, as can be seen from Figure 5.28. The planar relative position settles to the desired values $x = 0$, $y = -4$. These desired values are indicated by the two horizontal dashed lines.

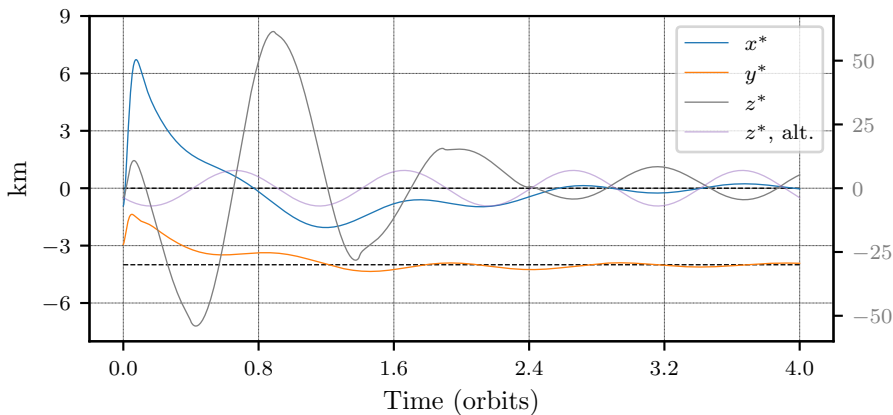


Figure 5.28: Relative Position, Augmented Control Example

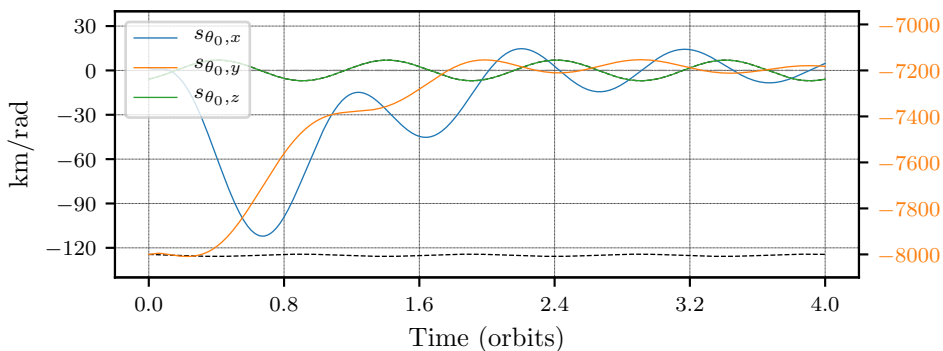


Figure 5.29: Controlled Sensitivity to θ_0 , Augmented Control Example

Note that as a consequence of the control compensation given by Eq. (5.78), the out-of-plane motion is highly affected, as indicated by the gray curve in Figure 5.28. The out-of-plane nominal

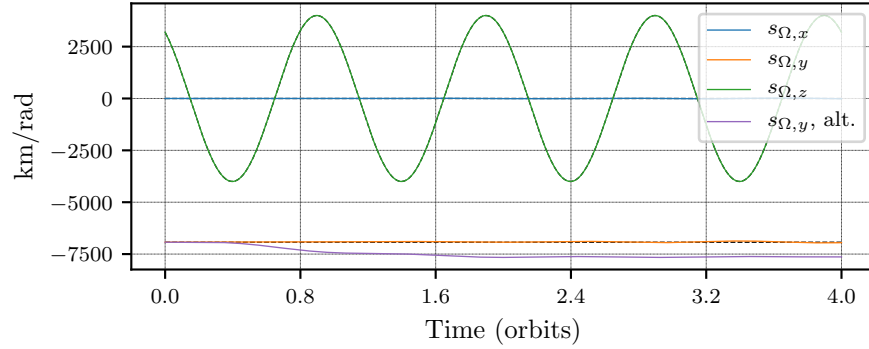


Figure 5.30: Stationary Sensitivity to Ω , Augmented Control Example

relative state oscillations would be limited to $|z| < 2$ km without this compensation strategy (purple curve), but grow to oscillations of up to $|z| < 9$ km, especially in the first 1.5 orbits. Note that the out-of-plane motion settles to smaller variations after 2.4 orbits. However, without the control compensation strategy, there would be larger changes in \mathbf{s}_Ω . This is clear from examining Figure 5.30. Without the control compensation, $u_3 = 0$, and $s_{\Omega,y}$ is heavily affected. This is given by the purple curve, while the properly stabilized behavior of $s_{\Omega,y}$ is shown by the orange curve.

The position components of $\mathbf{s}_{\bar{\theta}_0}$ are given in Figure 5.29. The 10% reduction in the absolute value of $s_{\bar{\theta}_0,y}$ is achieved. The uncontrolled $s_{\bar{\theta}_0,y}$ is given by the dashed horizontal curve towards the bottom of the plot, while the orange curve shows the effect of control on that component. Note the large scale of $s_{\bar{\theta}_0,y}$ necessitates that it be plotted with its own y axis, on the right side of the plot. This enables small details in the other two components to be discernible. The small oscillations in $s_{\bar{\theta}_0,z}$ are essentially unaffected, and the component $s_{\bar{\theta}_0,x}$ is successfully regulated.

Finally, the control components for this example are given in Figure 5.31. Note from Eq. (5.78) that $|u_3| \rightarrow \infty$ as $\sin \bar{\theta} \rightarrow 0$, but this is avoided by enforcing $|u_3| < 1$ m/s². Nonetheless, the control signal prescribed in Figure 5.31 might be a challenge to implement practically, due to the combination of small and medium accelerations needed, and especially by the challenging profile of $u_3(t)$. Additionally, a more ambitious control strategy than what is explored with this second example is probably possible. These things are beyond the scope of this work, which only introduces the sensitivity dynamics and does a preliminary investigation of whether or not they

can be influenced by control. From this second control example, it is clear that the sensitivities can be meaningfully influenced by control, but it is costly, and difficult to balance with relative state control requirements. As discussed previously, because the components of the sensitivities are so large, more control action must be exerted to significantly change these than to significantly change the relative state.

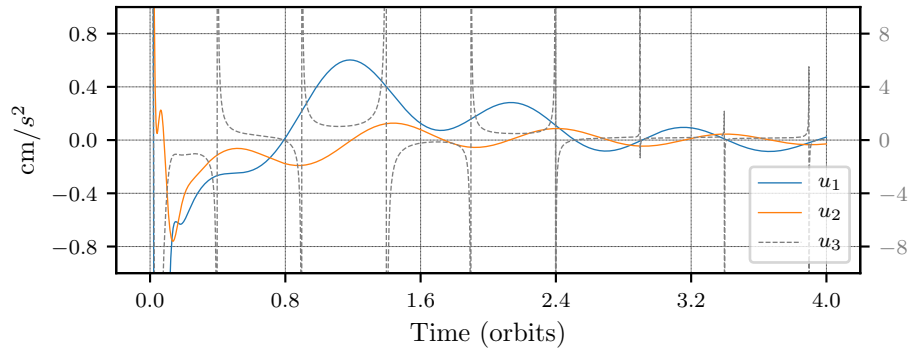


Figure 5.31: Control Accelerations, Augmented Control Example

This last point is an important insight of this work. It is an appealing concept to directly control some aspects of the evolving relative state uncertainty distribution, but it doesn't seem to always be practical. The most practical way to ensure safe relative motion is to design relative motion while being aware of the distribution of possible relative states for a chosen maneuver design. It is much easier to move the entire relative state distribution than it is to significantly contract it in particular directions. Inspecting Figure 5.24 for example, it is apparent that considering the nominal relative state alone in relative motion control design can be dangerous, because there is a risk for impact depending on how the uncertainty distribution evolves. Computing the sensitivities along with the nominal relative state response to a control action enables safe relative motion control in the presence of target orbit uncertainty to be executed very efficiently. Finally, note that there are limits to what control can achieve when influencing the relative state uncertainty distribution – changing the shape is possible, but greatly reducing the volume through the action of control alone should be impossible. Only measurements can effectively curb uncertainty growth.

5.2.5 Discussion

This section explores the sensitivities of the relative state to initial target orbit elements in the satellite relative motion problem. The initial values and the dynamics of the sensitivities are derived for the case of any target orbit eccentricity and for the special case that the target orbit is circular. Simulations performed show that the sensitivities can be used to efficiently study how the uncertain relative state distribution evolves with high accuracy. The sensitivities can be used to directly map from uncertainty distributions in the initial target orbit elements to the consequential evolving uncertainty distribution in the relative state. This enables rapid characterization of statistical risks of impact for the case of maneuvering in the vicinity of an uncertain target object. This would be especially useful in instances where the target object cannot be continuously tracked.

To explore the effects of relative state control on the sensitivities, infinite-time LQR control is implemented with the CW system. The effects of control on the sensitivities are determined to typically be fairly small, because the sensitivities to target elements tend to have much larger state values than those of the relative state, and are thus more difficult to significantly alter. The prospect of augmented control of a subset of the sensitivities with the nominal relative state is also briefly explored in this section, testing a formulation that controls planar relative state and planar sensitivity to the initial target of argument latitude while preserving sensitivity to target R.A.A.N. This simple control design is implemented with infinite-time LQR and achieves the desired control objectives. It is observed that inducing large changes in the sensitivities is fairly expensive, and in practice it would often be easier to simply control the relative state directly while computing the effects of such control actions on the uncertainty distribution via the sensitivities.

The concept of rendezvous and relative motion control in the vicinity of an uncertain orbit is not new. However, the formulation discussed in this section offers new perspectives. The sensitivity dynamics are shown to be rather simple, behaving like the relative motion dynamics but forced by control and by the relative state in some cases. There are several ways this work can be expanded on in the future. First, analytic solutions of the relative state sensitivities to the target orbit

elements could be derived. Combined with a suitable analytic formulation for propagating the relative state, such as by using the Tschauner-Hempel equations [126], this would remove the need for any numerical integration when studying the problem of maneuvering in the vicinity of a poorly tracked target object. Additionally, the full problem could be explored – including sensitivities of the relative state to both the initial target and chaser orbit elements. While maneuvering space objects are typically well-tracked, the small error in the chaser spacecraft’s orbital state can still be important in the uncertain relative motion problem. Additionally, more exploration of the limitations of the augmented control of the relative state and sensitivities would be useful. Lastly, the sensitivity formulation can in principle be used to design control that reduces the statistical risk of collision.

5.3 Conclusions

This chapter introduces the concept of the linear sensitivities for spacecraft formation flying and relative motion control. These are the derivative of the relative state with respect to an uncertain dynamically relevant parameter. It is shown that these vector quantities have their own well-defined dynamics, which prompts control and modeling exploration. The joint consideration of both the system state \boldsymbol{x} and its sensitivities \boldsymbol{s}_i allows for much more information about a system than just the relative state to be considered. This is demonstrated in section 5.1 with control that takes into account uncertainty in important dynamic parameters, and especially with the computationally efficient sensitivity-based uncertainty propagation shown in section 5.2. The sensitivities additionally encourage control explorations, but it is shown in section 5.1 that standard LQR with a sufficiently accurate relative motion model is already capable of achieving satisfactory regulation control. In section 5.2, the concept of controlling the sensitivities themselves is revisited for a different type of problem – in a case with navigational uncertainty instead of mere dynamic uncertainty. The relative state uncertainty distribution is shown to be partially controllable as well. This is revealed to be costly in terms of propellant – more costly than shifting the entire uncertainty distribution to minimize the statistical likelihood of an undesirable state value (such

as collision). While the implications of control of the sensitivities are interesting, this dissertation shows that their most promising application for the spacecraft relative motion problem seems to be in modeling of the future behavior of the relative state, as well as the evolving relative state uncertainty distribution. A desensitized control concept that was not explored is to design impulsive maneuvers that avoid exacerbating key sensitivities in the relative motion problem that could drive a need for large corrective maneuvers later in the future.

Chapter 6

Modal Decomposition of Spacecraft Relative Motion

To address the problem of efficiently studying the nature of relative motion in the vicinity of general orbits, this chapter leverages the classical idea of the modal decomposition, used extensively in the theory of vibrations [92]. All small deflections of a continuous and homogeneous body can be expressed as a linear weighted sum of independent mode shapes, which each have their own associated frequency. In the same manner for the satellite relative motion problem in the vicinity of a closed orbit, all possible motions are the sum of 6 independent fundamental motions with their own shapes and associated frequencies:

$$\mathbf{x}(t) = \sum_{i=1}^6 c_i \boldsymbol{\xi}_i(t) \quad (6.1)$$

where the c_i are constants for the unperturbed problem for which the $\boldsymbol{\xi}_i$ are solutions. A prudent choice of fundamental solutions enables the relative motion to be investigated and designed by simply varying the weighing constants, with the fundamental solutions designed such that their geometry is as simple as possible. In this manner, the constants perform a similar function to ROEs, by directly providing geometric insight. Figure 6.1 illustrates this conceptually with a depiction of relative motion decomposed into three simpler constituent modal motions. One benefit of the modal decomposition approach is that oscillatory, unstable, and drift motions are naturally isolated from one another. There are also many other benefits which will be discussed. Note that most of the work in this chapter can be found in Reference 26.

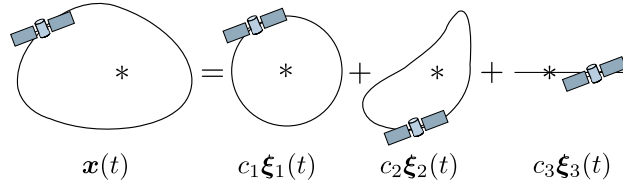


Figure 6.1: Example Satellite Relative Motion as a Sum of Individual Modes

6.1 Motivating Example

To motivate the arguments in this chapter, consider an introductory exercise using the simple well-known relative motion problem defined by Clohessy and Wiltshire [36]. This problem, discussed in [chapter 2](#), studies the dynamics of the relative state of a deputy spacecraft with respect to a chief, which is in a circular orbit. The relative state is augmented relative position and velocity $\mathbf{x} = (\boldsymbol{\rho}^\top, \boldsymbol{\rho}'^\top)^\top$ resolved in the chief-centered local vertical-local horizontal (LVLH) frame. The linearized unforced relative motion dynamics for the Clohessy Wiltshire (CW) problem are given below:

$$\ddot{x} - 2n\dot{y} - 3n^2x = 0 \quad (6.2a)$$

$$\ddot{y} + 2n\dot{x} = 0 \quad (6.2b)$$

$$\ddot{z} + n^2z = 0 \quad (6.2c)$$

for LVLH frame-resolved relative position $\boldsymbol{\rho} = x\hat{e}_r + y\hat{e}_t + z\hat{e}_n$ and velocity $\boldsymbol{\rho}' = x\dot{\hat{e}}_r + y\dot{\hat{e}}_t + z\dot{\hat{e}}_n$. The constant $n = \sqrt{\mu/a^3}$ is the mean motion. Recall that the out-of-plane z motion is a simple harmonic oscillator. The solutions to any linearized relative motion equations can generally given in an STM format as $\mathbf{x}(t) = [\Phi(t, t_0)]\mathbf{x}(t_0)$. Ignoring the simple and decoupled z component of the solution, the planar part of the STM is given below with epoch time $t_0 = 0$:

$$[\Phi(t)] = \begin{bmatrix} (4 - 3 \cos nt) & 0 & \frac{\sin nt}{n} & \frac{2}{n}(1 - \cos nt) \\ 6(\sin nt - nt) & 1 & -\frac{2}{n}(1 - \cos nt) & \frac{4}{n} \sin nt - 3t \\ 3n \sin nt & 0 & \cos nt & 2 \sin nt \\ -6n(1 - \cos nt) & 0 & -2 \sin nt & 4 \cos nt - 3 \end{bmatrix} \quad (6.3)$$

To illuminate the nature and types of planar relative motion permitted by Eq. (6.3), there are a few options. First, in the case of CW dynamics, the first two rows of the 4-state STM in Eq. (6.3) can be factored into a simple and geometrically insightful pair of expressions:

$$x(t) = A_0 \cos(nt + \alpha) + x_{\text{off}} \quad (6.4a)$$

$$y(t) = -2A_0 \sin(nt + \alpha) - \frac{3}{2}ntx_{\text{off}} + y_{\text{off}} \quad (6.4b)$$

where A_0 , α , x_{off} , and y_{off} are ROEs that are functions of the initial relative state conditions. These are defined in Reference 111. Eq. (6.4) shows that the planar relative motion is in a 2:1 ellipse when $x_{\text{off}} = 0$, and otherwise drifts in the along-track direction. This concise and highly specialized expression stems from the simplicity of the CW dynamics. In relative motion cases where the STM is more complicated than the form given in Eq. (6.3), an alternate and more general approach for understanding the relative motion is needed.

One alternate approach is to consider an expression of the relative motion in terms of the fundamental solutions ξ_i , as in Eq. (6.1). The most obvious fundamental solutions are the columns of the STM, i.e. $\xi_i = \phi_i$, for which $\mathbf{c} = \mathbf{x}_0$. These are typically inconvenient for geometric interpretation. For the case of the CW problem, two of the four columns of the planar STM given by Eq. (6.3) have drifting components, whereas the drifting part of the solution is one-dimensional. A superior parameterization would thus isolate the drifting motion to only one fundamental solution, with the associated constant c_i providing a no-drift constraint $c_i = 0$. Such a set of solutions is offered by the eigenvalue decomposition of the planar CW problem into independent modes. More generally, the modal decomposition serves as an attractive parameterization of the relative motion solution regardless of the dynamics and orbit geometry, for any periodic orbit. This will be discussed later.

For the planar CW problem, which has LTI dynamics, the decomposition is computed below:

$$[A_{2D}] = \begin{bmatrix} 0 & 0 & 1 & 0 \\ 0 & 0 & 0 & 1 \\ 3n^2 & 0 & 0 & 2n \\ 0 & 0 & -2n & 0 \end{bmatrix} = [V][J][V]^{-1} \quad (6.5)$$

$$[V] = \begin{bmatrix} 0 & -\frac{2}{3n} & -\frac{1}{2n} & -\frac{1}{2n} \\ 1 & 0 & -\frac{i}{n} & \frac{i}{n} \\ 0 & 0 & -\frac{i}{2} & \frac{i}{2} \\ 0 & 1 & 1 & 1 \end{bmatrix} \quad (6.6)$$

$$[J] = \begin{bmatrix} 0 & 1 & 0 & 0 \\ 0 & 0 & 0 & 0 \\ 0 & 0 & ni & 0 \\ 0 & 0 & 0 & -ni \end{bmatrix} \quad (6.7)$$

Using the theory of superposition, the solution to the in-plane dynamics is given below:

$$\mathbf{x}(t) = c_1 \mathbf{v}_1 e^{\lambda_{1,2}t} + c_2 (\mathbf{v}_1 t + \mathbf{v}_2) e^{\lambda_{1,2}t} + c_3 \mathbf{v}_3 e^{\lambda_3 t} + c_4 \mathbf{v}_4 e^{\lambda_4 t} \quad (6.8)$$

where \mathbf{v}_i is the i th column of $[V]$. Evaluating this at $t = 0$, let the solution constants be defined as $\mathbf{c} \equiv (c_1, c_2, c_3, c_4)^\top$. Solving $\mathbf{c} = [V]^{-1} \mathbf{x}_0$ yields the following values for the constants c_i :

$$\begin{aligned} c_1 &= y_0 - \frac{2}{n} \dot{x}_0 \\ c_2 &= -6nx_0 - 3\dot{y}_0 \\ c_3 &= 3nx_0 + i\dot{x}_0 + 2\dot{y}_0 \\ c_4 &= 3nx_0 - i\dot{x}_0 + 2\dot{y}_0 \end{aligned} \quad (6.9)$$

The solution given by Eq. (6.8) is written in a simpler form, noting $\lambda_{1,2} = 0$, and removing the imaginary part of the constants via the factorization $c_3 = c_{\mathbb{R}} + ic_{\mathbb{I}}$, and $\mathbf{v}_3 = \mathbf{v}_{\mathbb{R}} + i\mathbf{v}_{\mathbb{I}}$:

$$\begin{aligned} \mathbf{x}(t) &= c_1 \mathbf{v}_1 + c_2 (\mathbf{v}_1 t + \mathbf{v}_2) + 2c_{\mathbb{R}} (\mathbf{v}_{\mathbb{R}} \cos nt \\ &\quad - \mathbf{v}_{\mathbb{I}} \sin nt) - 2c_{\mathbb{I}} (\mathbf{v}_{\mathbb{R}} \sin nt + \mathbf{v}_{\mathbb{I}} \cos nt) \end{aligned} \quad (6.10)$$

Thus, $c_{\mathbb{R}} = 3nx_0 + 2\dot{y}_0$, $c_{\mathbb{I}} = \dot{x}_0$, and the fundamental modal solutions weighed by constants c_1 , c_2 , $c_{\mathbb{R}}$, and $c_{\mathbb{I}}$ are plotted in order in Figure 6.2. The initial positions of the oscillatory solutions are marked with an \mathbf{x} , and they are scaled such that they don't overlap.

The third and fourth modal solutions are simply two different phases, forming a basis on the 2:1 ellipse, and the first modal solution is a constant offset in the along-track direction, whose scale and direction is determined by the magnitude and sign of c_1 . Comparing this to Eq. (6.4), it is clear that the insights of the ROE-based solution have been recovered. For bounded relative motion, the relative orbit is a 2:1 ellipse which can be centered anywhere in the along-track direction. Inspecting the drift solutions in Eq. (6.10) and in Figure 6.2, the magnitude of c_2 determines the rate of along-track drift, and its sign determines the direction.

As demonstrated by the simple CW example, the strength of a modal decomposition for analysis is that it naturally separates out oscillatory, drifting, and stable/unstable components of the relative motion. For the Keplerian problem, there will always be one relative motion drift mode and no more than three in-plane oscillatory modes. For general periodic orbits, the nature of the relative motion varies based on the dynamics, and concise analytic solutions become impossible. It is in these settings where a modally decomposed solution resolved in favorable coordinates becomes most valuable to the astrodynamist. However, the application of the theory to the Keplerian case connects strongly to other literature on the topic.

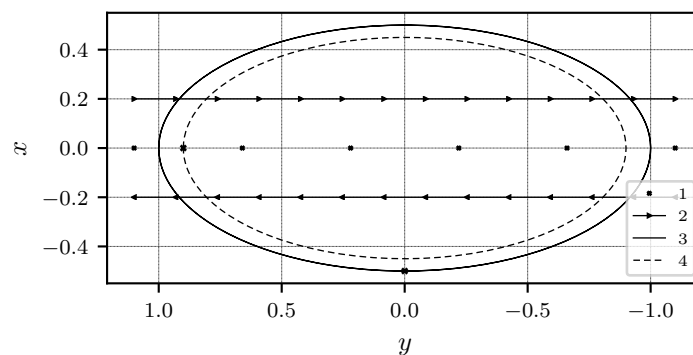


Figure 6.2: Planar Relative Motion Modes for the Clohessy-Wiltshire Problem

6.2 General Formulation

The modal decomposition concept in this chapter is enabled by Floquet theory, which is reviewed extensively in [chapter 2](#). The modal decomposition of solutions to a system of ODEs is traditionally defined for autonomous equations, but essentially all non-averaged relative motion except the CW problem is characterized by non-autonomous differential equations of the following form:

$$\dot{\mathbf{x}} = [A(t)]\mathbf{x} \quad (6.11)$$

The Lyapunov-Floquet transformation [97] can be used to equate a linear time-varying (LTV) dynamic system with periodic plant matrix $[A(t)] = [A(t + T)]$ to a linear time-invariant (LTI) counterpart via a periodic coordinate transformation:

$$\mathbf{x} = [P(t)]\mathbf{z} = [P(t + T)]\mathbf{z} \quad (6.12)$$

where \mathbf{z} represents the coordinate set for the LTI equivalent of the system in \mathbf{x} , with the following simple LTI dynamics:

$$\dot{\mathbf{z}} = [\Lambda]\mathbf{z} \quad (6.13)$$

The LF transformation and the LTI matrix are any pair of matrices $[P(t)]$, $[\Lambda]$ satisfying the following matrix differential equation:

$$[P(t)]^{-1} \left([A(t)][P(t)] - [\dot{P}(t)] \right) = [\Lambda] \quad (6.14)$$

In analytically solving this equation, which can be challenging, one seeks periodic solutions for the individual elements of $[P(t)]$ while also requiring the elements of $[\Lambda]$ to be constant. In practice, the periodicity conditions for all non-trivial elements of $[P(t)]$ constrain the admissible forms of $[\Lambda]$, but still allow for variations in the values of elements in $[\Lambda]$ depending on the form of $[P(t_0)]$. As a result, there can be more than a single pair of matrices satisfying Eq. (6.14).

A unique definition of the LF transformation is given below using the monodromy matrix. This transformation conveniently equals identity at the epoch time:

$$[P(t)] = [\Phi(t, t_0)]e^{-[\Lambda](t-t_0)} \quad (6.15)$$

$$[P(t_0)] = [P(t_0 + kT)] = [I] \quad (6.16)$$

$$[\Lambda] = \frac{1}{T} \ln(\Phi(t_0 + T, t_0)) \quad (6.17)$$

The difficulty of computing the LF transformation varies depending on the coordinates chosen to parameterize the problem. For example, for the Keplerian case, the LF transformation in orbit element differences will be shown to be identity except for a single row, whereas the transformation for local coordinates [120] is much more difficult to identify.

From the LF transformation above, the modal decomposition can be defined as a transformation from the LTI eigenvalue decomposition:

$$\mathbf{x}(t) = \sum_{i=1}^6 c_i [P_{\mathbf{x}}(t)] \mathbf{v}_i e^{\lambda_i(t-t_0)} \quad (6.18)$$

Because $[\Lambda]$ is a real matrix, any complex eigenvector $\lambda = \sigma + i\omega$ has a complex conjugate $\lambda = \sigma - i\omega$. The eigenvectors are also complex conjugates. Thus, for an eigenvalue $\lambda_1 = \sigma + i\omega$ with eigenvector $\mathbf{v}_1 = \mathbf{v}_{\mathbb{R}} + i\mathbf{v}_{\mathbb{I}}$, one can find complex conjugates $\lambda_2 = \sigma - i\omega$ and $\mathbf{v}_2 = \mathbf{v}_{\mathbb{R}} - i\mathbf{v}_{\mathbb{I}}$. Then, to enforce $\mathbf{z} \in \mathbb{R}^6$, one writes $c_1 = c_{\mathbb{R}} + ic_{\mathbb{I}}$ and $c_2 = c_{\mathbb{R}} - ic_{\mathbb{I}}$. The factorization $\mathbf{z}(t) = c_1 \mathbf{v}_1 e^{\lambda_1 t} + c_2 \mathbf{v}_2 e^{\lambda_2 t} + \dots$ is written in purely real form below:

$$\mathbf{z}(t) = 2c_{\mathbb{R}} (\mathbf{v}_{\mathbb{R}} \cos \omega t - \mathbf{v}_{\mathbb{I}} \sin \omega t) e^{\sigma t} - 2c_{\mathbb{I}} (\mathbf{v}_{\mathbb{R}} \sin \omega t + \mathbf{v}_{\mathbb{I}} \cos \omega t) e^{\sigma t} + \dots \quad (6.19)$$

Note from this equation that by specifying the values of $c_{\mathbb{R}}$ and $c_{\mathbb{I}}$, one is also choosing the initial condition of the system and the resultant behavior. Any choice of $c_{\mathbb{R}}$ and $c_{\mathbb{I}}$ is valid and results in a real solution $\mathbf{z} \in \mathbb{R}^6$ for complex-conjugate pairs $c_1 = c_{\mathbb{R}} + ic_{\mathbb{I}}$ and $c_2 = c_{\mathbb{R}} - ic_{\mathbb{I}}$.

One last note will illuminate how the constants c_i relate to the initial conditions of the system. Evaluating Eq. (6.18) at $t = t_0$ and defining $\mathbf{c} \equiv (c_1, c_2, c_3, c_4, c_5, c_6)^\top$, one obtains $\mathbf{x}_0 = [V]\mathbf{c}$. Thus, the appropriate constants may be obtained for given initial conditions via $\mathbf{c} = [V]^{-1}\mathbf{x}_0$.

As a result of the above discussion, the number of fundamental modes varies based on the nature of $[\Lambda]$. The number of geometrically distinct modes M is given in terms of the number of complex eigenvalue pairs p_c :

$$M = 6 - p_c \quad (6.20)$$

Additionally, it is useful to replace any complex-conjugate pair of modal constants c_1, c_2 with the associated components $c_{\mathbb{R}}, c_{\mathbb{I}}$ in the modal constant vector \mathbf{c} .

6.3 Analytic Results for the General Keplerian Relative Motion Problem

6.3.1 Relative Motion Dynamics

In a coordinate-based dynamics approach (as opposed to the coordinate-invariant approaches of geometric and variational mechanics [81]), the choice of coordinates for a system determines the form of the dynamics. For the relative motion problem, the two most common representations are (1) local coordinates of relative position and velocity and (2) the coordinates of orbit element differences. The first is easily physically interpreted, and the latter is often mathematically more convenient. The general perturbed linearized dynamics for both representations are important for this work and are both reviewed here.

Starting with local coordinates, consider the Cartesian relative state defined previously as $\mathbf{x} = (\boldsymbol{\rho}^\top, \boldsymbol{\rho}'^\top)^\top$. Dropping the c subscript for chief orbit parameters, the general linearized dynamics in these coordinates are given below in terms of the chief radial vector \mathbf{r} and angular velocity vector $\boldsymbol{\omega}$ and their derivatives [35]:

$$\dot{\mathbf{x}} = \begin{bmatrix} 0_{3 \times 3} & I_{3 \times 3} \\ \frac{\partial}{\partial \boldsymbol{\rho}} (\ddot{\mathbf{r}}_d - \ddot{\mathbf{r}}) - [\tilde{\boldsymbol{\omega}}] - [\tilde{\boldsymbol{\omega}}] [\tilde{\boldsymbol{\omega}}] & -2[\tilde{\boldsymbol{\omega}}] + \frac{\partial}{\partial \boldsymbol{\rho}} (\ddot{\mathbf{r}}_d - \ddot{\mathbf{r}}) \end{bmatrix} \mathbf{x} \quad (6.21)$$

$$\boldsymbol{\omega} = \frac{r}{h} (\ddot{\mathbf{r}} \cdot \hat{\mathbf{e}}_n) \hat{\mathbf{e}}_r + \frac{1}{r} (\dot{\mathbf{r}} \cdot \hat{\mathbf{e}}_t) \hat{\mathbf{e}}_n \quad (6.22)$$

$$\begin{aligned} \dot{\boldsymbol{\omega}} = & \frac{r}{h} \left(\frac{\dot{r}}{r} (\ddot{\mathbf{r}} \cdot \hat{\mathbf{e}}_n) - 2 \frac{r}{h} (\ddot{\mathbf{r}} \cdot \hat{\mathbf{e}}_t) (\dot{\mathbf{r}} \cdot \hat{\mathbf{e}}_n) + (\ddot{\mathbf{r}} \cdot \hat{\mathbf{e}}_n) \right) \hat{\mathbf{e}}_r \\ & + \frac{1}{r} \left((\ddot{\mathbf{r}} \cdot \hat{\mathbf{e}}_t) - 2 \frac{\dot{r}}{r} (\dot{\mathbf{r}} \cdot \hat{\mathbf{e}}_t) \right) \hat{\mathbf{e}}_n \end{aligned} \quad (6.23)$$

where the tilde on a symbol denotes the transformation of its vector into the cross-product matrix, and all matrices appear in square brackets. The above expressions are general, and apply to Keplerian and non-Keplerian dynamics. For the Keplerian case, they simplify significantly into a more common form that can be found in Reference 111. An inconvenience of these equations

is that they are time-varying if $\dot{\boldsymbol{\omega}} \neq \mathbf{0}$. Further, for the perturbed problem, they can assume a very complicated form and the effects of perturbations are almost irrevocably mixed in with the Keplerian contribution. Furthermore, computation of the plant matrix requires information about the derivative of the force model, shown here explicitly as the jerk, $\ddot{\mathbf{r}}$.

An alternative parameterization in terms of orbit element differences $\delta\boldsymbol{\text{oe}} = \boldsymbol{\text{oe}}_d - \boldsymbol{\text{oe}}_c$ separates out the effect of perturbations from the unperturbed linear dynamics, which are trivial except in one element. This work will use the differential quasi-nonsingular (QNS) elements given by $\delta\boldsymbol{\text{oe}} = (\delta a, \delta\theta, \delta i, \delta q_1, \delta q_2, \delta\Omega)^\top$. The Gauss planetary equations are provided below. Note $q_1 = e \cos \omega$, $q_2 = e \sin \omega$, $\theta = \omega + f$ is the argument of latitude, and the other elements are classical semimajor axis a , inclination i , and right ascension of the ascending node Ω .

$$\dot{a} = \frac{2a^2}{h} \left((q_1 \sin \theta - q_2 \cos \theta) a_r + \frac{p}{r} a_t \right) \quad (6.24a)$$

$$\dot{\theta} = \frac{h}{r^2} - \frac{r \sin \theta \cos i}{h \sin i} a_n \quad (6.24b)$$

$$\dot{i} = \frac{r \cos \theta}{h} a_n \quad (6.24c)$$

$$\dot{q}_1 = \frac{p \sin \theta}{h} a_r + \frac{(p+r) \cos \theta + r q_1}{h} a_t + \frac{r q_2 \sin \theta}{h \tan i} a_n \quad (6.24d)$$

$$\dot{q}_2 = -\frac{p \cos \theta}{h} a_r + \frac{(p+r) \sin \theta + r q_2}{h} a_t - \frac{r q_1 \sin \theta}{h \tan i} a_n \quad (6.24e)$$

$$\dot{\Omega} = \frac{r \sin \theta}{h \sin i} a_n \quad (6.24f)$$

In the absence of perturbations, the only nonzero term in Eq. (6.24) is the true latitude rate $\dot{\theta} = h/r^2$. Factoring the Keplerian component of the Jacobian of the right hand side of Eq. (6.24) into the mostly zero matrix $[A_{\delta\boldsymbol{\text{oe}},0}(t)]$, the complicated but typically sub-dominant perturbation-induced component of the Jacobian is written as $[\delta A_{\delta\boldsymbol{\text{oe}}}(t)]$ and the linearized differential QNS dynamics are written concisely below:

$$\delta\dot{\boldsymbol{\text{oe}}} = \left([A_{\delta\boldsymbol{\text{oe}},0}(t)] + [\delta A_{\delta\boldsymbol{\text{oe}}}(t)] \right) \delta\boldsymbol{\text{oe}} \quad (6.25)$$

The benefit of Eq. (6.25) over Eq. (6.21) is that the jerk no longer needs to be computed, the effects of perturbations are neatly separated out in the dynamics, and the remaining Keplerian

component is fairly simple. A disadvantage is that the differential QNS elements are not as well-suited for geometric interpretation.

References 50 and 111 discuss the *geometric method*, which relates the relative state in local coordinates to the relative state in differential QNS elements:

$$\mathbf{x}(t) = \left([G_0(t)] + [\delta G(t)] \right) \delta \mathbf{oe}(t) = [G(t)] \delta \mathbf{oe}(t) \quad (6.26)$$

where $[G_0(t)]$ captures the Keplerian component of the mapping. The $[\delta G(t)]$ matrix captures the perturbation-induced component of the mapping and is typically sub-dominant to $[G_0(t)]$. Reference 50 demonstrates the derivation of $[\delta G(t)]$ for the J_2 perturbation.

6.3.2 The Lyapunov-Floquet Transformation in any Coordinates

Motivated by the multitude of possible coordinates to parameterize the relative motion problem and the inconvenience of computing the LF transformation from scratch in a given coordinate set, a means to obtain the LF transformation in one set of relative motion coordinates from the transformation in any other set is derived here. For notational convenience, this is explored through the relationship between differential quasi-nonsingular (QNS) elements and local coordinates, but the same concept applies for any pair of coordinates.

Let \mathbf{x} denote the relative state in the desired local coordinates and $\delta \mathbf{oe}$ denote the relative state in the orbit element differences. As already shown with Eq. (6.26), these two representations are approximately related by an orbit-periodic linear mapping:

$$\mathbf{x} = [G(t)] \delta \mathbf{oe} \quad (6.27)$$

The following linear mapping between the STMs is obtained using Eq. (6.27):

$$[\Phi_{\mathbf{x}}(t, t_0)] = [G(t)][\Phi_{\delta \mathbf{oe}}(t, t_0)][G(t_0)]^{-1} \quad (6.28)$$

The following mapping between the plant matrices can also be shown:

$$[A_{\mathbf{x}}(t)] = [G(t)][A_{\delta \mathbf{oe}}][G(t)]^{-1} + [\dot{G}(t)][G(t)]^{-1} \quad (6.29)$$

Let $[P_{\mathbf{x}}(t)]$ and $[P_{\delta\mathbf{oe}}(t)]$ denote the LF transformations, transforming the two coordinate sets to their corresponding LTI coordinates:

$$\delta\mathbf{oe} = [P_{\delta\mathbf{oe}}(t)]\mathbf{z}_{\delta\mathbf{oe}} \quad (6.30)$$

$$\mathbf{x} = [P_{\mathbf{x}}(t)]\mathbf{z}_{\mathbf{x}} \quad (6.31)$$

These transformations are used to relate the plant matrices for the LTI forms of both coordinates, choosing $[P_{\mathbf{x}}(t_0)] = [P_{\delta\mathbf{oe}}(t_0)] = [I_{6 \times 6}]$:

$$\begin{aligned} [\Lambda_{\mathbf{x}}] &= \frac{1}{T} \ln ([\Phi_{\mathbf{x}}(t_0 + T, t_0)]) \\ &= \frac{1}{T} \ln ([G(t_0 + T)][\Phi_{\delta\mathbf{oe}}(t_0 + T, t_0)][G(t_0)]^{-1}) \end{aligned} \quad (6.32)$$

Noting $[G(t_0 + T)] = [G(t_0)]$, the matrix logarithm is factored as follows:

$$\begin{aligned} [\Lambda_{\mathbf{x}}] &= [G(t_0)] \cdot \frac{1}{T} \ln ([\Phi_{\delta\mathbf{oe}}(t_0 + T, t_0)]) \cdot [G(t_0)]^{-1} \\ &= [G(t_0)][\Lambda_{\delta\mathbf{oe}}][G(t_0)]^{-1} \end{aligned} \quad (6.33)$$

The LTI matrix for the local coordinate relative motion representation is simply a change-of-basis of the LTI matrix for the quasi-nonsingular element differences.

Using Eqs. (6.33) and (6.14), the following is obtained:

$$\begin{aligned} [P_{\mathbf{x}}]^{-1} \left([A_{\mathbf{x}}][P_{\mathbf{x}}] - [\dot{P}_{\mathbf{x}}] \right) &= \\ [G(t_0)][P_{\delta\mathbf{oe}}]^{-1} \left([A_{\delta\mathbf{oe}}][P_{\delta\mathbf{oe}}] - [\dot{P}_{\delta\mathbf{oe}}] \right) [G(t_0)]^{-1} \end{aligned} \quad (6.34)$$

Substituting Eq. (6.29) and expanding yields

$$\begin{aligned} [P_{\mathbf{x}}]^{-1} [G][A_{\delta\mathbf{oe}}][G]^{-1} [P_{\mathbf{x}}] + [P_{\mathbf{x}}]^{-1} [\dot{G}][G]^{-1} [P_{\mathbf{x}}] - [P_{\mathbf{x}}]^{-1} [\dot{P}_{\mathbf{x}}] \\ = [G(t_0)][P_{\delta\mathbf{oe}}]^{-1} [A_{\delta\mathbf{oe}}][P_{\delta\mathbf{oe}}][G(t_0)]^{-1} - [G(t_0)][P_{\delta\mathbf{oe}}]^{-1} [\dot{P}_{\delta\mathbf{oe}}][G(t_0)]^{-1} \end{aligned} \quad (6.35)$$

This equation is used to show the following relationship between the LF transformations for the two coordinates, assuming a periodic geometric relationship $[G(t)] = [G(t + T)]$:

$$[P_{\mathbf{x}}(t)] = [G(t)][P_{\delta\mathbf{oe}}(t)][G(t_0)]^{-1} \quad (6.36)$$

The LF transformation and LTI form in any set of coordinates can thus be obtained using the corresponding information in another set of coordinates along with the transformation between

coordinates via Eqs. (6.33) and (6.36). These relationships hold for linearization about any closed orbit, regardless of whether or not the dynamics are Keplerian.

Through the modal decomposition using the mapped LF transformation, the astrodynamist is freed to explore the choice of coordinates that is most desirable for a given application without having to do a prohibitive amount of work when switching coordinates. The only recurring analytic burden is in deriving the necessary linear mapping $[G(t)]$ for any new coordinate representation of interest.

The LF transformation is now obtained for Keplerian dynamics of any eccentricity in QNS element differences, and this is analytically transformed to LF transformations in Cartesian and spherical coordinates. It is shown that the modal solutions in Cartesian and spherical coordinates are different. This is an interesting result that illustrates how the choice of working coordinates can affect the complexity of the modal solutions.

6.3.3 Orbit Element Differences

For two-body dynamics, the relative motion dynamics in QNS elements can be shown to take the following simplified form by transforming the independent variable from t to θ :

$$\delta\mathbf{oe}' = \begin{bmatrix} 0 & 0 & 0 & 0 & 0 & 0 \\ -\frac{3}{2a} & \frac{2(q_2c\theta - q_1s\theta)}{\kappa} & 0 & \frac{3q_1}{\eta^2} + \frac{2c\theta}{\kappa} & \frac{3q_2}{\eta^2} + \frac{2s\theta}{\kappa} & 0 \\ 0 & 0 & 0 & 0 & 0 & 0 \\ 0 & 0 & 0 & 0 & 0 & 0 \\ 0 & 0 & 0 & 0 & 0 & 0 \\ 0 & 0 & 0 & 0 & 0 & 0 \end{bmatrix} \delta\mathbf{oe} \quad (6.37)$$

where $s = \sin(\)$, $c = \cos(\)$ and the shorthand quantities η , κ and κ_0 are defined below.

$$\eta = \sqrt{1 - q_1^2 - q_2^2} \quad (6.38)$$

$$\kappa = 1 + q_1 \cos \theta + q_2 \sin \theta \quad (6.39)$$

$$\kappa_0 = 1 + q_1 \cos \theta_0 + q_2 \sin \theta_0 \quad (6.40)$$

The dynamics are $\delta\mathbf{oe}' = \frac{d}{d\theta}(\delta\mathbf{oe}) = \frac{1}{\theta}\delta\mathbf{oe}$, so the plant matrix in Eq. (6.37) is $[\tilde{A}(\theta)] = \frac{1}{\theta}[A(\theta)]$. Note that there exists a relative motion state transition matrix (STM) that is obtained by integrating the differential equations in Eq. (6.37). This STM is given in Eq. (14.133) in Reference 111.

A Lyapunov-Floquet transformation of Eq. (6.37) is sought, because $[\tilde{A}(\theta)] = [\tilde{A}(\theta + 2\pi)]$. To differentiate the LTI system for this new choice of independent variable, let the LTI coordinates $\boldsymbol{\chi}$ be used instead of \mathbf{z} when θ is the independent variable, with associated LTI plant matrix $[R]$ instead of $[A]$, and LF transformation $[P(\theta)]$:

$$\delta\mathbf{oe} = [P(\theta)]\boldsymbol{\chi} \quad (6.41)$$

$$\boldsymbol{\chi}' = [R]\boldsymbol{\chi} \quad (6.42)$$

The LF transformation $[P(\theta)]$ solves an equivalent of Eq. (6.14):

$$[P(\theta)]^{-1} \left([\tilde{A}(\theta)][P(\theta)] - [P'(\theta)] \right) = [R] \quad (6.43)$$

The LF transformation sought is determined to have the following simple form:

$$[P(\theta)] = \begin{bmatrix} 1 & 0 & 0 & 0 & 0 & 0 \\ P_{21}(\theta) & P_{22}(\theta) & 0 & P_{24}(\theta) & P_{25}(\theta) & 0 \\ 0 & 0 & 1 & 0 & 0 & 0 \\ 0 & 0 & 0 & 1 & 0 & 0 \\ 0 & 0 & 0 & 0 & 1 & 0 \\ 0 & 0 & 0 & 0 & 0 & 1 \end{bmatrix} \quad (6.44)$$

This reduces the number of scalar differential equations in Eq. (6.43) to four:

$$\tilde{A}_{21} + \tilde{A}_{22}(\theta)P_{21} - P'_{21} = R_{21}P_{22}(\theta) \quad (6.45a)$$

$$\tilde{A}_{22}(\theta)P_{22} - P'_{22} = R_{22}P_{22}(\theta) \quad (6.45b)$$

$$\tilde{A}_{24}(\theta) + \tilde{A}_{22}(\theta)P_{24} - P'_{24} = R_{24}P_{22}(\theta) \quad (6.45c)$$

$$\tilde{A}_{25}(\theta) + \tilde{A}_{22}(\theta)P_{25} - P'_{25} = R_{25}P_{22}(\theta) \quad (6.45d)$$

These equations are solved, starting with $P_{22}(\theta)$, and enforcing a periodicity condition for each solution. This is demonstrated only for $P_{22}(\theta)$, whose general solution is given below:

$$P_{22}(\theta) = c_1 (1 + q_1 \cos \theta + q_2 \sin \theta)^2 e^{-R_{22}\theta} \quad (6.46)$$

where c_1 is an integration constant. The periodicity condition $P_{22}(\theta) = P_{22}(\theta + 2\pi)$ yields $R_{22} = 0$, and the resulting form for $P_{22}(\theta)$ is substituted into the other differential equations, which are solved for their own periodic solutions. An additional constraint is that $[P(\theta_0)] = [I]$ to obtain the desired LF transformation discussed in Section 2.3. The finalized nonzero components of the LF transformation are given below, along with the LTI matrix:

$$P_{21}(\theta) = \frac{\kappa^2}{2a} (\mathbb{F}_{21}(\theta_0) - \mathbb{F}_{21}(\theta)) \quad (6.47a)$$

$$\begin{aligned} \mathbb{F}_{21}(\theta) &= \frac{6}{\eta^3} \left(\tan^{-1} \left(\frac{q_2 + (1 - q_1) \tan(\frac{\theta}{2})}{\sqrt{1 - q_1^2 - q_2^2}} \right) - \frac{\theta}{2} \right) \\ &\quad + \frac{3(q_2 + (q_1^2 + q_2^2) \sin \theta)}{q_1(q_1^2 + q_2^2 - 1)\kappa} \end{aligned} \quad (6.47b)$$

$$P_{22}(\theta) = \frac{\kappa^2}{\kappa_0^2} \quad (6.47c)$$

$$P_{24}(\theta) = \frac{\kappa^2}{4(q_1^2 + q_2^2 - 1)} (\mathbb{F}_{24}(\theta_0) - \mathbb{F}_{24}(\theta)) \quad (6.47d)$$

$$\mathbb{F}_{24}(\theta) = \frac{4(q_2 + \sin \theta)}{\kappa^2} + \frac{4 \sin \theta}{\kappa} \quad (6.47e)$$

$$P_{25}(\theta) = \frac{\kappa^2}{4(q_1^2 + q_2^2 - 1)} (\mathbb{F}_{25}(\theta_0) - \mathbb{F}_{25}(\theta)) \quad (6.47f)$$

$$\mathbb{F}_{25}(\theta) = \frac{4(1 - q_1^2 + q_2 \sin \theta)}{q_1 \kappa^2} + \frac{4q_2 \sin \theta}{q_1 \kappa} \quad (6.47g)$$

$$[R] = \begin{bmatrix} 0 & 0 & 0 & 0 & 0 & 0 \\ -\frac{3a\eta}{2r_0^2} & 0 & 0 & 0 & 0 & 0 \\ 0 & 0 & 0 & 0 & 0 & 0 \\ 0 & 0 & 0 & 0 & 0 & 0 \\ 0 & 0 & 0 & 0 & 0 & 0 \\ 0 & 0 & 0 & 0 & 0 & 0 \end{bmatrix} \quad (6.48)$$

Note that there is a singularity in Eq. (6.47) for P_{25} for the case of $q_1 = 0$.

The Lyapunov-Floquet transformation and LTI form for the case that t is the independent variable instead of θ is now discussed. Due to the explicit appearance of the intermediate variable θ , this alternate form offers no computational advantages. It is however slightly simpler. First, the nonzero element of the new LTI matrix $[\Lambda_{\delta\mathbf{oe}}]$ is nR_{21} :

$$\Lambda_{21} = -\frac{3a\eta}{2r_0^2}n \quad (6.49)$$

where $n = \sqrt{\mu/a^3}$ is the mean motion. In this case, the Lyapunov-Floquet transformation takes on a slightly simpler form, with the $P_{21}(\theta)$ term in Eq. (6.44) reducing to zero, and all other components unaffected. With this modified transformation, the equation for $\delta\theta$ reduces to a familiar form:

$$\delta\theta = P_{22}(\theta)R_{21}n(t - t_0)\delta a + P_{22}(\theta)\delta\theta_0 + P_{24}(\theta)\delta q_1 + P_{25}(\theta)\delta q_2 \quad (6.50)$$

This expression is analytically equivalent to its counterpart in Eq. (14.129) of Reference 111, though derived by quite a different process. Exploiting the equivalence of Eq. (6.50) to Eq. (14.129) in Reference 111, alternate expressions can be obtained for $P_{24}(\theta)$ and $P_{25}(\theta)$ from Eq. (14.130). The alternate expression for $P_{25}(\theta)$ is notably nonsingular for $q_1 = 0$.

The mapping of LF transformations is to be applied for two alternate sets of relative motion coordinates. For this, Eqs. (6.33) and (6.36) are repeated with θ instead of t :

$$[R_{\mathbf{x}}] = [G(\theta_0)][R_{\delta\mathbf{oe}}][G(\theta_0)]^{-1} \quad (6.51)$$

$$[P_{\mathbf{x}}(\theta)] = [G(\theta)][P_{\delta\mathbf{oe}}(\theta)][G(\theta_0)]^{-1} \quad (6.52)$$

where $[R_{\delta\mathbf{oe}}]$ is given by Eq. (6.48) and $[P_{\delta\mathbf{oe}}(\theta)]$ is given by Eqs. (6.44) and (6.47).

6.3.4 Cartesian Coordinates

Let $\mathbf{x}_c = (x, y, z, \dot{x}, \dot{y}, \dot{z})^\top$ denote the state in local Cartesian coordinates. For these coordinates, the linearized coordinate transformation $[G(\theta)]$ from QNS orbit element differences is reproduced below [111]:

$$[G_{\mathbf{x}_c}] = \begin{bmatrix} \frac{r}{a} & \frac{v_r}{v_t} r & 0 & -\frac{r}{p}(2aq_1 + rc\theta) & -\frac{r}{p}(2aq_2 + rs\theta) & 0 \\ 0 & r & 0 & 0 & 0 & rci \\ 0 & 0 & rs\theta & 0 & 0 & -rc\theta si \\ -\frac{v_r}{2a} & \left(\frac{1}{r} - \frac{1}{p}\right) h & 0 & \frac{1}{p}(v_r a q_1 + hs\theta) & \frac{1}{p}(v_r a q_2 - hc\theta) & 0 \\ -\frac{3v_t}{2a} & -v_r & 0 & \frac{1}{p}(3v_t a q_1 + 2hc\theta) & \frac{1}{p}(3v_t a q_2 + 2hs\theta) & v_r ci \\ 0 & 0 & (v_t c\theta + v_r s\theta) & 0 & 0 & (v_t s\theta - v_r c\theta) si \end{bmatrix} \quad (6.53)$$

where $v_r = \dot{r}$ and $v_t = r\dot{\theta}$, and the shorthand s and c are sine and cosine. For the inverse of Eq. (6.53), see Reference 111.

Solving Eq. (6.51), the Cartesian LTI matrix $[R_{\mathbf{x}_c}]$ is obtained, which can be expressed in a highly compact form:

$$[R_{\mathbf{x}_c}] = \frac{2R_{21}a}{\gamma} \begin{bmatrix} A(B+2) & A^2 & 0 & A^2C & -A(B+1)C & 0 \\ -(B+1)(B+2) & -A(B+1) & 0 & -A(B+1)C & (B+1)^2C & 0 \\ 0 & 0 & 0 & 0 & 0 & 0 \\ B(B+2)/C & AB/C & 0 & AB & -B(B+1) & 0 \\ A(B+2)/C & A^2/C & 0 & A^2 & -A(B+1) & 0 \\ 0 & 0 & 0 & 0 & 0 & 0 \end{bmatrix} \quad (6.54)$$

where R_{21} is the nonzero (2,1) element of $[R_{\delta\mathbf{o}\mathbf{e}}]$ in Eq. (6.48) and the shorthand quantities γ , A , B , C are defined below:

$$\gamma = q_1^2 + q_2^2 - 1 = A^2 + B^2 - 1 \quad (6.55)$$

$$A = -\frac{v_{r,0}p}{v_{t,0}r_0} = q_2 \cos \theta_0 - q_1 \sin \theta_0 \quad (6.56)$$

$$B = \frac{p}{r_0} - 1 = q_1 \cos \theta_0 + q_2 \sin \theta_0 \quad (6.57)$$

$$C = \frac{hr_0^2}{a\mu\gamma} \quad (6.58)$$

The true and generalized eigenvectors of $[R_{\mathbf{x}_c}]$ are given as the columns of $[V_{R_{\mathbf{x}_c}}]$ below. The matrix

$[R_{x_c}]$ has six zero eigenvalues, with geometric multiplicity 5.

$$[V_{R_{x_c}}] = \begin{bmatrix} 0 & 0 & 0 & 0 & -\frac{2R_{21}a}{\gamma}A(B+1)C & 0 \\ 1 & 0 & 0 & 0 & \frac{2R_{21}a}{\gamma}(B+1)^2C & 0 \\ 0 & 1 & 0 & 0 & 0 & 0 \\ -\frac{1}{C} & 0 & 1 & 0 & -\frac{2R_{21}a}{\gamma}B(B+1) & 0 \\ 0 & 0 & \frac{A}{B+1} & 0 & -\frac{2R_{21}a}{\gamma}A(B+1) & 1 \\ 0 & 0 & 0 & 1 & 0 & 0 \end{bmatrix} \quad (6.59)$$

Note that both C and the scaling term on the fifth column of $[V_{R_x}]$ can be expressed in terms of A and B :

$$C = -\frac{(1 - A^2 - B^2)^{3/2}}{(B+1)^2n} \quad (6.60)$$

$$\frac{2R_{21}a}{\gamma} = \frac{3(B+1)^2}{(1 - A^2 - B^2)^{5/2}} \quad (6.61)$$

Because typically $|C| \gg 1$, the scaling of the fifth column of $[V_{R_x}]$ can be much larger than the others.

The general solution of the LTI form for the Cartesian coordinates is given below in terms of the columns of $[V_{R_{x_c}}]$ and the solution constants, to be defined shortly:

$$\boldsymbol{\chi}_{x_c}(\theta) = \sum_{i=1}^5 c_i \mathbf{v}_i + c_6 (\mathbf{v}_5(\theta - \theta_0) + \mathbf{v}_6) \quad (6.62)$$

The LF transformation for Cartesian coordinates maps the solution given by Eq. (6.62) back to Cartesian coordinates via $\mathbf{x}_c = [P_{x_c}]\boldsymbol{\chi}_{x_c}$. It is computed using the mapping from Eq. (6.47) given by Eq. (6.52), making use of Eq. (6.53). This is significantly easier than solving differential equations for its elements. The resulting LF transformation is a product of analytic matrices, and can be evaluated efficiently.

Using the inverse of Eq. (6.59), the constant vector $\mathbf{c} = (c_1, c_2, c_3, c_4, c_5, c_6)^\top$ is given by $\mathbf{c} = [V_{R_{x_c}}]^{-1}\boldsymbol{\chi}_{x_c}(\theta_0)$:

$$c_1 = -\frac{v_{t,0}}{v_{r,0}}x_0 + y_0 \quad (6.63a)$$

$$c_2 = z_0 \quad (6.63b)$$

$$c_3 = \frac{1}{C} \left(-\frac{v_{t,0}r_0}{v_{r,0}p} x_0 + y_0 + C\dot{x}_0 \right) \quad (6.63c)$$

$$c_4 = \dot{z}_0 \quad (6.63d)$$

$$c_5 = -\frac{(1-e^2)v_{t,0}}{3v_{r,0}} n \left(\frac{r_0}{p} \right)^2 x_0 \quad (6.63e)$$

$$c_6 = \frac{\left(\frac{p}{r_0} + 1 \right) \frac{p}{r_0} n}{(1-e^2)^{3/2}} x_0 + \frac{1}{C} \frac{v_{r,0}}{v_{t,0}} y_0 + \frac{v_{r,0}}{v_{t,0}} \dot{x}_0 + \dot{y}_0 \quad (6.63f)$$

The expression for c_6 reduces to the Clohessy-Wiltshire no-drift constraint $c_6 = 2nx_0 + \dot{y}_0$ when $e = 0$, so c_6 captures the degree of drift. It is better understood as a linearized measure of δa . In particular, if $\delta a = 0$, this quantity should be zero as well. The terms c_1 , c_3 , and c_5 are affiliated with the in-plane modes, and c_2 and c_4 are associated with the two out-of-plane oscillatory modes.

The analytic perspective offered by Eq. (6.63) is very useful. First, the out-of-plane motion is decoupled from the in-plane motion. Additionally, none of the in-plane constants except c_6 are functions of \dot{y}_0 . In the case that the degree of drift is specified via a fixed value of c_6 , a select initial in-plane component of the position (x_0, y_0) forms a point of intersection of all possible in-plane relative motions in a one-parameter variation, based on the value of \dot{x}_0 . The constants c_1 and c_5 are fixed by the choice of initial position, and only the value of c_3 varies as the value of \dot{x}_0 is varied. Additionally, only two of the in-plane mode constants, c_3 and c_6 , can be changed with a single impulsive maneuver. The constants c_1 and c_5 can only be changed with a two-burn sequence.

On the topic of maneuvers and the drift constant, an additional result can be determined from the constant c_6 . For single-maneuver changes to bounded relative motion, for which $c_6 = 0$, the in-plane component of the thruster direction is constrained to a line:

$$\Delta v_y = -\frac{v_{r,0}}{v_{t,0}} \Delta v_x \quad (6.64)$$

Any maneuver not satisfying this constraint will introduce drift to the relative motion. For two-burn maneuvers, the orbit must be parameterized in terms of two sets of constants \mathbf{c} and \mathbf{c}' at the two distinct maneuver points in the orbit. Note that the following equation can be used to map

constants \mathbf{c} for a choice of epoch anomaly θ_0 to a new epoch angle θ'_0 :

$$\mathbf{c}(\theta'_0) = [V(\theta'_0)]^{-1}[\Phi_{\mathbf{x}_c}(\theta'_0, \theta_0)][V(\theta_0)]\mathbf{c}(\theta_0) \quad (6.65)$$

The inverse of Eq. (6.59) becomes singular when $A = 0$. This is equivalent to whenever $e \sin f_0 = 0$, or whenever e and/or f_0 is equal to zero. However, the issue can be remedied by evaluating the expression with the offending terms set to a small number ϵ instead of exactly zero. For orbits of nonzero eccentricity, the singularity issue can also always be avoided by selecting $f_0 \neq k\pi$ for integers k .

For Keplerian orbits, the general linear relative motion problem in Cartesian coordinates are studied in terms of individual modes via the following:

$$\mathbf{x}_c(\theta) = \sum_{i=1}^5 c_i [P_{\mathbf{x}_c}(\theta)] \mathbf{v}_i + c_6 [P_{\mathbf{x}_c}(\theta)] (\mathbf{v}_5(\theta - \theta_0) + \mathbf{v}_6) \quad (6.66)$$

where the transformation $[P_{\mathbf{x}_c}]$ given by Eqs. (6.52) and (6.53) is required to evaluate this expression and the \mathbf{v}_i are the columns of Eq. (6.59). Compare Eq. (6.66) to Eqs. (6.1) and (6.18). The individual modal solutions for the Cartesian modal decomposition are plotted and studied in Section 3.4.

6.3.5 Spherical Coordinates

The local spherical coordinate representation is given by $\mathbf{x}_s = (\delta r, \theta_r, \phi_r, \delta \dot{r}, \dot{\theta}_r, \dot{\phi}_r)^\top$. It has the advantage over the local Cartesian coordinate representation of better capturing the curvature characteristic of large along-track separations and large out-of-plane motion. This makes it a more accurate representation for relative motion problems with large along-track separations.

The relative state in local spherical coordinates is obtained from local Cartesian coordinates as below:

$$\delta r = \sqrt{(r_c + x)^2 + y^2 + z^2} - r_c \quad (6.67a)$$

$$\theta_r = \tan^{-1} \left(\frac{y}{r_c + x} \right) \quad (6.67b)$$

$$\phi_r = \sin^{-1} \left(\frac{z}{\sqrt{(r_c + x)^2 + y^2 + z^2}} \right) \quad (6.67c)$$

$$\delta \dot{r} = \frac{(r_c + x)(\dot{r}_c + \dot{x}) + y\dot{y} + z\dot{z}}{\sqrt{(r_c + x)^2 + y^2 + z^2}} - \dot{r}_c \quad (6.67d)$$

$$\dot{\theta}_r = \frac{(r_c + x)\dot{y} - y(\dot{r}_c + \dot{x})}{(r_c + x)^2 + y^2} \quad (6.67e)$$

$$\dot{\phi}_r = \frac{(r_c + \delta r)\dot{z} - (\dot{r}_c + \delta \dot{r})z}{(r_c + \delta r)^2 \sqrt{1 - \frac{z^2}{(r_c + \delta r)^2}}} \quad (6.67f)$$

The position components of the inverse transformation are given below, for which the corresponding velocities can be obtained by differentiation:

$$x = (r_c + \delta r) \cos \theta_r \cos \phi_r - r_c \quad (6.68a)$$

$$y = (r_c + \delta r) \sin \theta_r \cos \phi_r \quad (6.68b)$$

$$z = (r_c + \delta r) \sin \phi_r \quad (6.68c)$$

The linearized transformation between the local spherical and Cartesian coordinate representations is given below:

$$\delta r \approx x \quad (6.69a)$$

$$\theta_r \approx y/r_c \quad (6.69b)$$

$$\phi_r \approx z/r_c \quad (6.69c)$$

$$\delta \dot{r} \approx \dot{x} \quad (6.69d)$$

$$\dot{\theta}_r \approx \dot{y}/r_c - (\dot{r}_c/r_c^2)y \quad (6.69e)$$

$$\dot{\phi}_r \approx \dot{z}/r_c - (\dot{r}_c/r_c^2)z \quad (6.69f)$$

The nonlinear transformation from orbit element differences to local spherical coordinates is discussed in Reference 54. For this work, the linearized transformation is derived for small angles θ_r ,

and ϕ_r . The result is given below:

$$[G_{\mathbf{x}_s}] = \begin{bmatrix} \frac{r}{a} & \frac{v_r}{v_t} r & 0 & -\frac{r}{p}(2aq_1 + rc\theta) & -\frac{r}{p}(2aq_2 + rs\theta) & 0 \\ 0 & 1 & 0 & 0 & 0 & ci \\ 0 & 0 & s\theta & 0 & 0 & -c\theta si \\ -\frac{v_r}{2a} & \left(\frac{1}{r} - \frac{1}{p}\right)h & 0 & \frac{1}{p}(v_r a q_1 + hs\theta) & \frac{1}{p}(v_r a q_2 - hc\theta) & 0 \\ -\frac{3\dot{\theta}}{2a} & -2\frac{v_r}{r} & 0 & \frac{\dot{\theta}}{p}(3aq_1 + 2rc\theta) & \frac{\dot{\theta}}{p}(3aq_2 + 2rs\theta) & 0 \\ 0 & 0 & \dot{\theta}c\theta & 0 & 0 & \dot{\theta}s\theta si \end{bmatrix} \quad (6.70)$$

Note the similarity of Eqs. (6.53) and (6.70). The first and fourth rows are identical.

Solving Eq. (6.51), the spherical coordinate LTI matrix $[R_{\mathbf{x}_s}]$ is obtained, expressed below in a form similar to Eq. (6.54):

$$[R_{\mathbf{x}_s}] = \frac{2R_{21}a}{\gamma} \begin{bmatrix} A(B+2) & 0 & 0 & A^2C & \gamma a AC & 0 \\ \frac{(B+1)^2(B+2)}{\gamma a} & 0 & 0 & \frac{AC(B+1)^2}{\gamma a} & (B+1)^2C & 0 \\ 0 & 0 & 0 & 0 & 0 & 0 \\ \frac{B(B+2)}{C} & 0 & 0 & AB & \gamma a B & 0 \\ -\frac{2A(B+1)(B+2)}{\gamma a C} & 0 & 0 & -\frac{2A^2(B+1)}{\gamma a} & -2A(B+1) & 0 \\ 0 & 0 & 0 & 0 & 0 & 0 \end{bmatrix} \quad (6.71)$$

The true and generalized eigenvectors of $[R_{\mathbf{x}_s}]$ are given as the columns of $[V_{R_{\mathbf{x}_s}}]$ below. Like the LTI matrix for QNS element differences and Cartesian coordinates, the matrix $[R_{\mathbf{x}_s}]$ has six zero eigenvalues, with geometric multiplicity 5.

$$[V_{R_{\mathbf{x}_s}}] = \begin{bmatrix} 0 & 0 & 0 & 0 & \frac{2R_{21}a}{\gamma} AC \gamma a & 0 \\ 1 & 0 & 0 & 0 & \frac{2R_{21}a}{\gamma} (B+1)^2 C & 0 \\ 0 & 1 & 0 & 0 & 0 & 0 \\ 0 & 0 & 1 & 0 & \frac{2R_{21}a}{\gamma} B \gamma a & 0 \\ 0 & 0 & -\frac{A}{\gamma a} & 0 & -\frac{4R_{21}a}{\gamma} A(B+1) & 1 \\ 0 & 0 & 0 & 1 & 0 & 0 \end{bmatrix} \quad (6.72)$$

Analogously as for Cartesian coordinates, the general solution of the LTI form for the spherical coordinates is given below in terms of the columns of $[V_{R_{\mathbf{x}_s}}]$. The constant vector $\mathbf{c} =$

$(c_1, c_2, c_3, c_4, c_5, c_6)^\top$ is given by $\mathbf{c} = [V_{R_{\mathbf{x}_s}}]^{-1} \boldsymbol{\chi}_{\mathbf{x}_s}(\theta_0)$:

$$c_1 = -\frac{v_{t,0}}{v_{r,0}r} \delta r_0 + \theta_{r,0} \quad (6.73a)$$

$$c_2 = \dot{\phi}_{r,0} \quad (6.73b)$$

$$c_3 = \frac{1}{C} \left(\frac{\left(1 - \frac{r_0}{p}\right) v_{t,0}}{v_{r,0}} \delta r_0 + C \delta \dot{r}_0 \right) \quad (6.73c)$$

$$c_4 = \dot{\phi}_{r,0} \quad (6.73d)$$

$$c_5 = -\frac{v_{t,0}}{3v_{r,0}a} n \left(\frac{r_0}{p} \right) \delta r_0 \quad (6.73e)$$

$$c_6 = \frac{\mu}{hr_0^2} \left(1 + \frac{p}{r_0} \right) \delta r_0 + \frac{v_{r,0}}{v_{t,0}r_0} \delta \dot{r}_0 + \dot{\theta}_{r,0} \quad (6.73f)$$

Note that the equation for c_6 in Eq. (6.73) is zero when $\delta a = 0$. It represents a more concise local coordinate no-drift condition than its counterpart in Eq. (6.63).

For Keplerian orbits, the general linear relative motion problem in spherical coordinates are studied in terms of individual modes via the following:

$$\mathbf{x}_s(\theta) = \sum_{i=1}^5 c_i [P_{\mathbf{x}_s}(\theta)] \mathbf{v}_i + c_6 [P_{\mathbf{x}_s}(\theta)] (\mathbf{v}_5(\theta - \theta_0) + \mathbf{v}_6) \quad (6.74)$$

where the transformation $[P_{\mathbf{x}_s}]$ given by Eq. (6.52) is required to evaluate this expression and the \mathbf{v}_i are the columns of Eq. (6.72). Note that the singularity properties of the Cartesian and spherical coordinate representations are the same.

To project the spherical coordinate results into Cartesian coordinates, there are two options. The nonlinear transformation given by Eq. (6.68) and its first derivative can be used, or the inverse of the linearized transformation given by Eq. (6.69) can be used. The former is a more accurate transformation that will capture the curvature of the relative motion missed by the Cartesian representation, while the latter transformation has the benefit of being linear, but lacks the additional accuracy offered by the nonlinear transformation. The results of the linearized Cartesian and spherical coordinate representations can be made completely equivalent via the linearized transformation Eq. (6.69) and its inverse. This coordinate equivalence has been discussed in past works [121, 31, 18]. As a result of the linear equivalence, the relative motion problem can be explored

from the linearized Cartesian perspective, if desired, then a linearized transformation to spherical coordinates followed by a nonlinear transformation back to Cartesian coordinates will reproduce the curvature correction offered by the spherical coordinate representation. However, the different modal representation in local spherical coordinates might offer benefits in some applications over the Cartesian representation. This is one of the topics explored in the numerical analysis in Section 3.4.

One interesting result from the preceding analysis is that the LTI form for spherical coordinates has a comprehensible physical interpretation with very simple dynamics. The LTI form for spherical coordinates is reproduced below, where $\boldsymbol{\chi}_{x_s} = [P_{x_s}(\theta)]^{-1} \mathbf{x}_s$ is the transformed state.

$$\boldsymbol{\chi}'_{x_s} = [R_{x_s}] \boldsymbol{\chi}_{x_s} \quad (6.75)$$

Examining the plant matrix, which is given by Eq. (6.71), a simple interpretation of the dynamics in the spherical LTI coordinates is possible, because the three nonzero columns of $[R_{x_s}]$ are linearly dependent. Factoring out $\alpha = 2R_{21}a/\gamma$, the following common column vector is defined:

$$\mathbf{R}_f = \alpha \begin{pmatrix} AC \\ \frac{C(B+1)^2}{\gamma^a} \\ 0 \\ B \\ -\frac{2A(B+1)}{\gamma^a} \\ 0 \end{pmatrix} \quad (6.76)$$

The common column vector is related to all nonzero columns of $[R_{x_s}]$ as below:

$$\mathbf{R}_1 = \frac{B+2}{C} \mathbf{R}_f, \quad \mathbf{R}_4 = A \mathbf{R}_f, \quad \mathbf{R}_5 = \gamma a \mathbf{R}_f \quad (6.77)$$

The relative motion state is resolved in the spherical LTI coordinates as the 6 component state vector $\boldsymbol{\chi}_{x_s}$. The coordinates χ_3 and χ_6 are stationary – see the zero 3rd and 6th rows of the plant matrix in Eq. (6.71). Defining $\boldsymbol{\rho} = (\chi_1, \chi_4, \chi_5)^\top$, the nonzero natural dynamics of the LTI coordinates are given below:

$$\boldsymbol{\rho}' = \alpha (\boldsymbol{\rho} \cdot \mathbf{n}) \zeta \quad (6.78)$$

$$\chi_2' = \alpha \frac{C(B+1)^2}{\gamma A} (\boldsymbol{\rho} \cdot \mathbf{n}) \quad (6.79)$$

$$\mathbf{n} = \begin{pmatrix} \frac{B+2}{C} \\ A \\ \gamma a \end{pmatrix} \quad (6.80)$$

$$\boldsymbol{\zeta} = \begin{pmatrix} AC \\ B \\ -\frac{2A(B+1)}{\gamma a} \end{pmatrix} \quad (6.81)$$

where $\boldsymbol{\zeta} \cdot \mathbf{n} = 0$ and $\frac{d}{d\theta} (\boldsymbol{\rho} \cdot \mathbf{n}) = 0$. From Eqs. (6.78) and (6.79), it is clear that the dynamics of χ_2 are influenced by $\boldsymbol{\rho}$, but the coordinate χ_2 does not influence $\boldsymbol{\rho}$. The 3D space in which $\boldsymbol{\rho}$ is embedded is by far the most important space for the transformed relative motion problem. When $\boldsymbol{\rho} \cdot \mathbf{n} = 0$, the dynamics are stationary. This is an equation of a plane passing through $\boldsymbol{\rho} = \mathbf{0}$. This plane is called the stationary plane. The vector field of the dynamics of $\boldsymbol{\rho}$ is parallel to the stationary plane, pointing along $\boldsymbol{\zeta}$ above the plane and along $-\boldsymbol{\zeta}$ below it. The magnitude of the vector field at any point is proportional to the distance off the plane, $\boldsymbol{\rho} \cdot \mathbf{n}$.

The coordinates χ_3 and χ_6 are related to the out-of-plane motion, and they are decoupled from the in-plane motion and stationary. Any periodic in-plane motion of interest can be parameterized by a unique choice of four constant state values $\chi_1, \chi_2, \chi_4, \chi_5$, where $\boldsymbol{\rho} = (\chi_1, \chi_4, \chi_5)^\top$ is constrained to the stationary plane to prevent movement of the χ_2 coordinate. The dynamics of $\boldsymbol{\rho}$ and χ_2 are easily described and visualized, as discussed above. By the LF transformation to the spherical LTI coordinates, the dimensionality of the Keplerian satellite relative motion problem is reduced to 3 active coordinates with very simple dynamics. The other coordinates are a steered coordinate χ_2 and the stationary out-of-plane coordinates.

Given the simplicity of the dynamics in the spherical LTI coordinates, a natural question is to explore control design in the context of this formulation. For example, low-thrust strategies for relative orbit reconfiguration will naturally maintain close proximity to the stationary plane, to minimize the degree to which the natural dynamics need to be countered by control. By contrast,

impulsive maneuver-based strategies will push ρ further from the stationary plane and will make greater use of the natural dynamics to achieve control objectives. Examining existing control strategies from the perspective of this special coordinate representation might provide new insights.

6.3.6 Numerical Simulations for the Keplerian Problem

In this section, the developments in this chapter are tested on unperturbed Earth orbits with $a = 26600$ km, $\Omega = 0^\circ$, $i = 63.4^\circ$, and $\omega = 270^\circ$, and the eccentricity is varied. In the case that $e \sim 0.74$, the resulting orbit is of the same type as the Molniya orbits used by the Soviets.

6.3.6.1 Modal Decomposition in Local Cartesian Coordinates

The modal decomposition concept discussed in this chapter enables any close-proximity relative motion to be expressed as the unique weighted combination of 6 or fewer modal motions. To introduce this concept, the 6 relative motion modes are computed for the Molniya orbit with $e = 0.74$. There are four in-plane modes (modes 1, 3, 5, 6), and two purely out-of-plane modes (2 and 4). These are normalized and plotted for three chief orbits in Figures 6.3 and 6.4, where the mode numbers correspond with the numbering of the constants in Eq. (6.63).

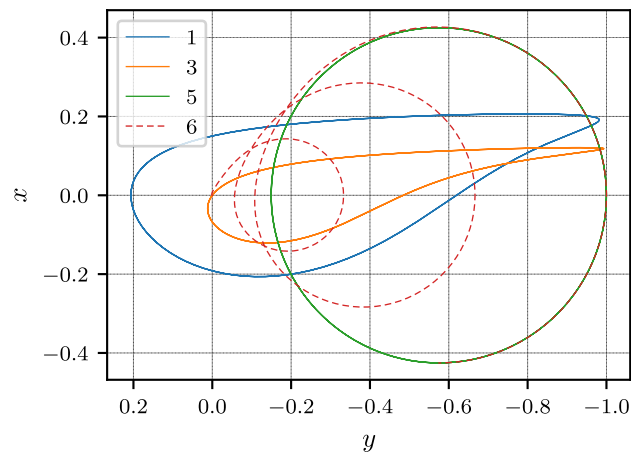


Figure 6.3: In-plane Normalized Relative Motion Modes, $e = 0.74$, $f_0 = 90^\circ$

The modes are numerically validated by comparing to propagation of their initial conditions

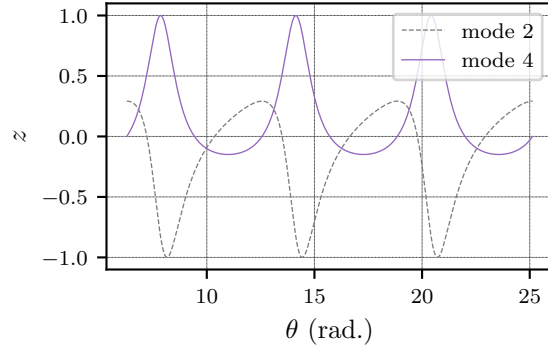


Figure 6.4: Out-of-plane Normalized Relative Motion Modes, $e = 0.74$, $f_0 = 90^\circ$

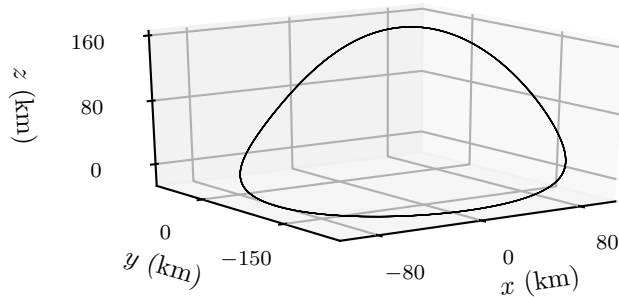


Figure 6.5: Example Relative Orbit, $e = 0.74$, $f_0 = 90^\circ$, $\delta e = 0.002$, $\delta i = 0.2^\circ$, $\delta f_0 = 0^\circ$

with the Tschauner-Hempel equations and ensuring a match [126]. All modes are periodic except the drift mode, mode 6. This mode is a composition of the motion of mode 5, but grows and drifts over time in the along-track direction. The 5th mode is an offset circle that is similar to a combination of fundamental solutions to the Tschauner-Hempel equations discussed in Reference 123.

To demonstrate how these relative motion modes combine to construct any close-proximity relative motion, consider an example of bounded relative motion with $\delta a = 0$, $\delta e = 0.002$, and $\delta i = 0.2^\circ$. The resulting relative motion is depicted in Figure 6.5. This is distorted from the traditional 2:1 relative orbit ellipse of the Clohessy-Wiltshire solution, due to the very high chief eccentricity. Because the motion starts out in the x - y plane, the out-of-plane motion is constructed entirely of mode 4. The in-plane motion is composed of three of the in-plane modes. Figure 6.6 shows the three modes that combine to construct the planar component of the relative motion,

which is given in black. The modes are scaled such that their linear combination produces the relative orbit, and this result is numerically confirmed. Note the absence of any contribution of the drift mode, as expected. The initial position is marked with an **x**, and the point after a true anomaly change of $\Delta f = \pi$ is marked with a filled circle. Using these points, it is possible for the reader to graphically verify that the sum of the individual modes reproduces the indicated motion. Note from Figure 6.6 that $c_3 < 0$, because mode 3 is flipped in comparison to its normalized form in Figure 6.3.

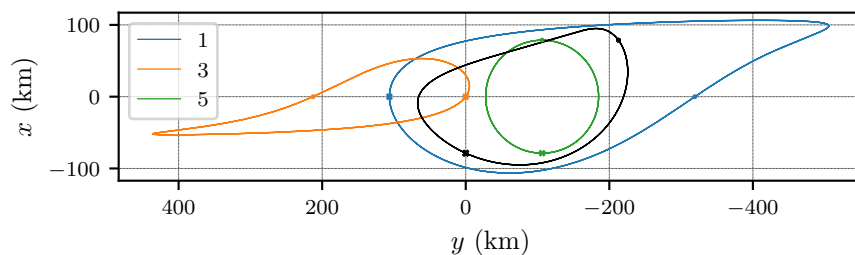


Figure 6.6: Example Modal Decomposition (Planar), $e = 0.74$, $f_0 = 90^\circ$, $\delta e = 0.002$, $\delta i = 0.2^\circ$

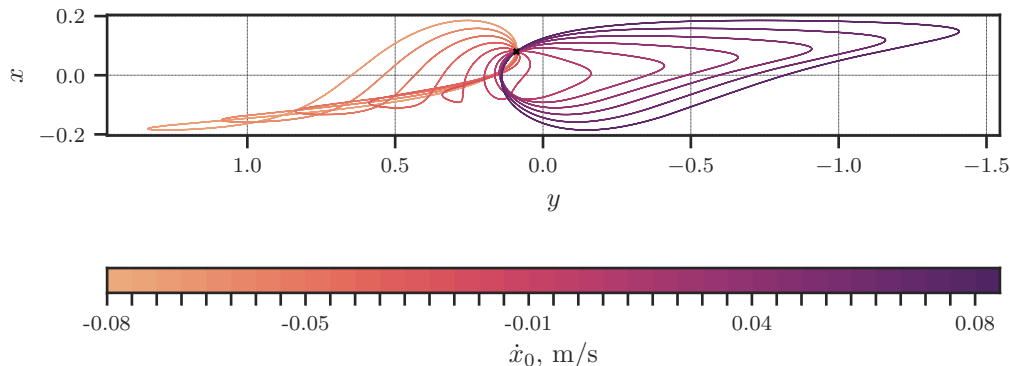


Figure 6.7: Bounded Planar Motion with (x_0, y_0) specified, $e = 0.74$, $f_0 = 90^\circ$

The analysis in this work enables analytic modal decomposition using Eqs. (6.52), (6.59), and (6.63). Furthermore, only Eq. (6.63) needs to be re-evaluated for each possible relative motion case – the eigenvectors of the LTI plant matrix and the periodic transformation only change with the chief orbit. In addition, Eq. (6.63) is simple enough to facilitate some interesting analysis that leverages the computational efficiency of this formulation. For example, recall that if the degree of

drift is specified via a fixed value of c_6 , a select initial in-plane component of the position (x_0, y_0) forms a point of intersection of all possible in-plane relative motions in a one-parameter variation, based on the value of \dot{x}_0 . To demonstrate this for the Molniya orbit, consider an initial planar relative position of $(x_0, y_0) = (0.08, 0.09)$ km, and the drift constant is set to $c_6 = 0$ to explore only bounded relative motion solutions. The variation of \dot{x}_0 yields the family of possible planar motions originating at the specified point (x_0, y_0) . The modes only need to be computed once using Eqs. (6.52) and (6.59), while repeated evaluation of expressions derived from Eq. (6.63) facilitates the computation of the families of relative orbits intersecting the point of interest. A subset of the possible relative orbits is computed and given in Figure 6.7, with the initial point indicated by an **x**.

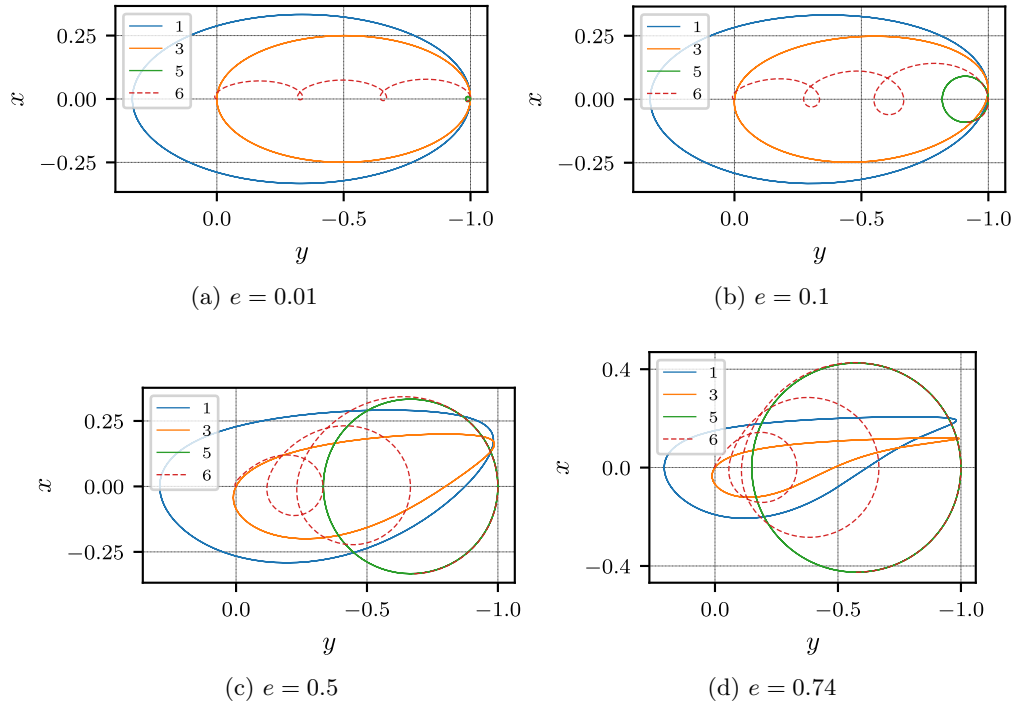


Figure 6.8: Normalized Relative Motion Modes vs. Eccentricity, Cartesian Coordinates

In Figure 6.8, the eccentricity is varied to show the evolution of the relative motion modes. The drift modes are plotted for three chief orbit periods. Because the model is linear, the scale of the modes is unimportant. All modes have been normalized in the figures so the maximum

relative distance is unit magnitude. Starting with $e = 0.01$, the four planar modes are two relative motion ellipses, a drift mode, and a small circular motion in the along-track direction. While the formulation explored in this chapter becomes singular for $e = 0$, it is still well-defined for small but nonzero values of eccentricity. The 2:1 centered relative motion ellipse from the classical relative motion problem with near-circular orbits would be constructed from modes 1, 3, and 5. Increasing the eccentricity to 0.1, the circular mode becomes larger, and as a result, the loops in the drift mode also grow more noticeably over time. Increasing the eccentricity to $e = 0.5$, the first and third modes have become distorted. The nature of this distortion varies with the choice of epoch true anomaly f_0 . For $e = 0.5$, mode 5 falls in the range $1/3 \leq x \leq 1$, with the center at $x = 2/3$. It is determined that mode 5 is a circle centered in the along-track direction, for which the eccentricity determines the ratio of the circle radius to the distance of its center from the origin. When the eccentricity is increased to that of the Molniya orbits, modes 1 and 3 become distorted significantly at their greatest along-track extent.

6.3.6.2 Analysis using Local Spherical Coordinates

Using the same Molniya orbit from the previous example, the epoch true anomaly is shifted to $f_0 = 145^\circ$. The normalized planar modes from decompositions in Cartesian and spherical coordinates are provided in Figure 6.9. The Cartesian modes 1 and 3 are distorted differently from the $f_0 = 90^\circ$ case, but modes 5 and 6 are still similar to before. In spherical coordinates, plotting $\delta r/r$ enables a visualization of the relative motion with the non-dimensional θ_r coordinate. Because r varies greatly over time for sufficiently eccentric orbits, the motion plotted in the figure is not representative of the modal motion in Cartesian coordinates. For this reason, linearly mapping the spherical coordinate modes to Cartesian coordinates may be preferable for visualization. However, when plotted in these normalized spherical coordinates, the first mode becomes just a single point, which could be a useful simplification.

A new relative motion example is parameterized by the initial orbit element differences $\delta e = 0.002$, $\delta i = \delta f_0 = 0.2^\circ$. The planar component of the resulting relative orbit is expressed in terms

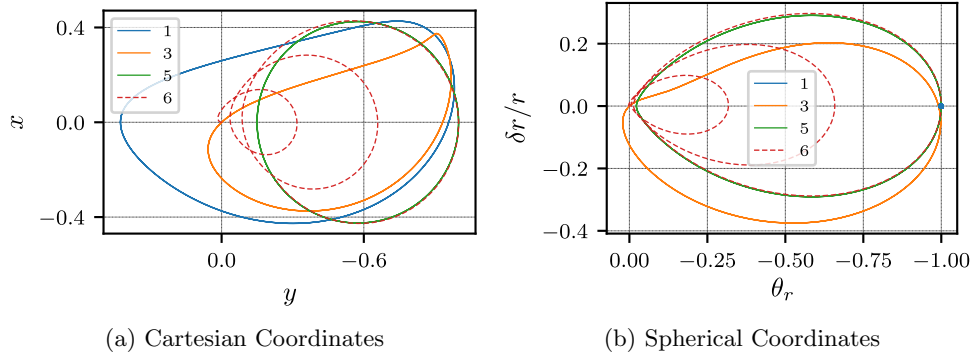


Figure 6.9: Normalized Relative Motion Modes, $e = 0.74$, $f_0 = 145^\circ$

of the Cartesian relative motion modes in Figure 6.10. The out-of-plane components of the motion are omitted from this analysis because they are comparatively uninteresting. In the same manner as the previous example, the initial point is marked with a \mathbf{x} and the point after half an orbit at $\Delta f_0 = 180^\circ$ is marked with a solid circle. In Figure 6.11, the same motion is plotted as a sum of the spherical coordinate modes expressed in Cartesian coordinates. As a result of this mapping, the stationary mode 1 in Figure 6.9 becomes an oscillatory motion in the along-track direction. By inspection of the linear transformation in Eq. (6.69), it is determined that the oscillatory along-track motion is due to rescaling by the chief orbit radius.

Comparing Figures 6.10 and 6.11, the mapped spherical coordinate parameterization of the relative motion offers some simplifications over the Cartesian coordinate parameterization. While modes 3 and 5 are similar, mode 1 has been reduced to a simpler one-dimensional motion. With this parameterization, the manner in which modes 1, 3, and 5 linearly combine to produce the example relative motion is easier to visualize than using the Cartesian representation. There are only two 2D motions, and mode 1 shifts their sum in the along-track direction.

Through the application of the modal decomposition technique and the convenient mapping of the LF transform and LTI solutions across coordinates to the Keplerian relative motion problem, a few things have been demonstrated. First, it is shown that the choice of coordinates influences the geometric complexity of the modal solutions. From the technique of deriving new LF transfor-

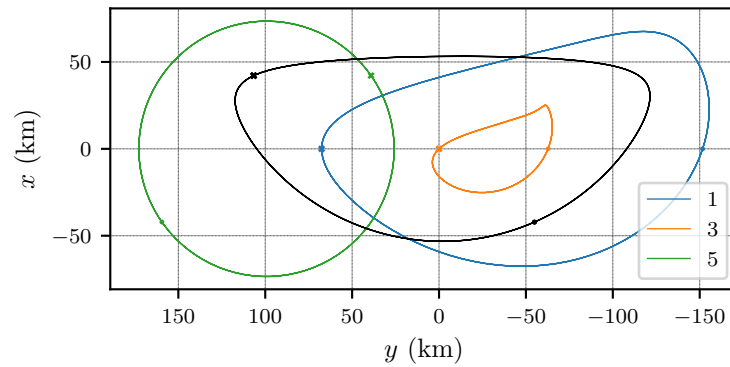


Figure 6.10: Example Modal Decomposition, Cartesian, $e = 0.74$, $f_0 = 145^\circ$, $\delta e = 0.002$, $\delta i = \delta f_0 = 0.2^\circ$

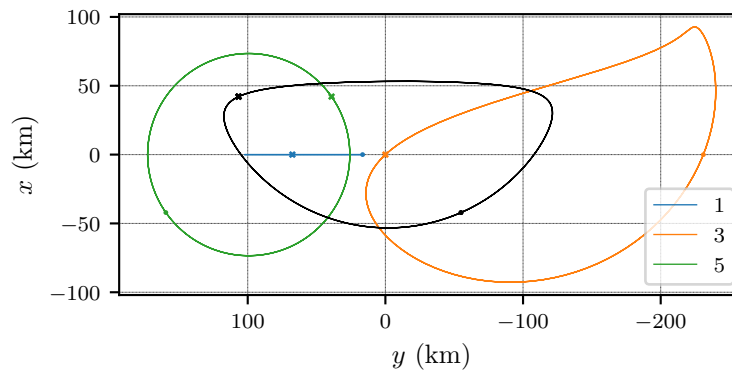


Figure 6.11: Example Modal Decomposition, Spherical, $e = 0.74$, $f_0 = 145^\circ$, $\delta e = 0.002$, $\delta i = \delta f_0 = 0.2^\circ$

mations from old, the exploration of relative motion modal decompositions derived from different coordinate representations is highly feasible. Additionally, simple conclusions have been obtained about the nature of relative motion in any bounded Keplerian orbit. Using the spherical coordinate modal decomposition, it is determined that any close-proximity natural relative motion can be expressed as the weighted sum of two purely out-of-plane modes, one in-plane drift mode, an offset circle mode, a 1D along-track oscillatory mode, and a “teardrop” shaped mode. This simple basis of relative motion solutions facilitates straightforward design of close-proximity relative motion in Keplerian orbits of any eccentricity. The six modal constants parameterize all possible motions, similarly to how the six LROEs for the CW solutions [10] can be used to explore all possible close-proximity relative motion for near-circular orbits.

6.4 Weakly Perturbed Orbits

In the case that the orbital dynamics are not Keplerian, the modal decomposition theory can still be applied using LF theory if the chief orbits are sufficiently close to periodic. This allows for a conceptually unifying description of circular unperturbed, eccentric unperturbed, and perturbed spacecraft relative motion using the modal method. This section briefly discusses the procedure for analytic application for a chief orbit subject to a small perturbation.

In the case of a sub-dominant non-Keplerian perturbation (such as J_2), the LTI matrix $[\Lambda]$, LF transformation $[P]$, and geometric transformation $[G]$ are all perturbed from their Keplerian forms $[\Lambda_0]$, $[P_0]$, and $[G_0]$:

$$[\Lambda] = [\Lambda_0] + [\delta\Lambda] \quad (6.82a)$$

$$[P] = [P_0] + [\delta P] \quad (6.82b)$$

$$[G] = [G_0] + [\delta G] \quad (6.82c)$$

Solving for a first-order correction in the LF transformation $[\delta P]$ from the deviation in the plant matrix $[\delta A]$, the following differential equation for these quantities is obtained:

$$[\delta \dot{P}] = -[\delta P][\Lambda_0] + [A_0][\delta P] - [P_0][\delta \Lambda] + [\delta A][P_0] \quad (6.83)$$

Eq. (6.83) is solved analytically using a specific $[\delta A]$ for the desired perturbative effects, analogously to how Eq. (6.14) is solved. For this, it is easiest to solve for the LF transformation in the space of orbit element differences, because $[\delta A]$ will be much simpler in this space than it is in local coordinates. Additionally, as is done in Reference 78, it may be convenient to examine only the secular variations induced by the perturbations, ignoring short-period effects. This will significantly simplify $[\delta A]$. Lastly, the deviation $[\delta G]$ in the geometric mapping from orbit element differences to local coordinates must also be obtained. Reference 50 discusses how this is obtained for the J_2 perturbation.

Once the above analysis has been performed, a modified modal decomposition will be obtained, with a modified vector of modal constants \mathbf{c} that is still a function of relative state initial

conditions. The same modal analysis as performed in this chapter for the Keplerian problem can then be explored for the perturbed problem of interest. The application of the modal decomposition method to perturbed cases is generally reserved for the next chapter.

6.5 Conclusions

This chapter introduces the modal decomposition concept for efficient and convenient parameterization of the spacecraft relative motion problem in the vicinity of any closed orbit. This approach is facilitated by Lyapunov-Floquet theory, enabling the LTV dynamics to be transformed into an LTI system. This chapter additionally introduces a means for computing the LF transformation for the decomposition in any set of coordinates using the LF transformation from another set of coordinates and the linearized mapping between coordinates. The procedure is applied to the Keplerian relative motion problem to obtain modal decompositions in local Cartesian and spherical coordinates using the LF transformation in orbit element differences, yielding novel analytic results. The resulting decompositions are analyzed for relative motion near a Molniya orbit. Numerical examples in the next chapter will show that the modal concept extends beyond the Keplerian case.

This work connects strongly to concepts from literature. First, it demonstrates the connection between the relative motion solution in orbit element differences explored by Reference 111 and the concept of the LF transformation applied to those coordinates. Additionally, it makes use of a similar geometric method concept to what was used to great effect in Reference 50. Finally, some of the modal solutions obtained are equivalent to previously explored special combinations of the Tschauner-Hempel fundamental solutions [123]. New results include the spherical coordinate modal decomposition, the numerically efficient exploration of bounded relative motion using the modal solutions, and the extension of the theory for perturbed settings.

The benefits of the modal relative motion perspective discussed by this chapter are numerous. First, the modal solution constants \mathbf{c} offer a simple state representation for relative motion that has clear geometric meaning through the associated modes, and allows for computationally efficient exploration of possible relative motion types. The dynamics of the modal solution con-

stants are functions only of control and perturbations. In the case of nominal dynamics without control, they are integral quantities, similar to the stationary ROE quantities explored elsewhere in literature. However, unlike traditional ROEs, modal constants can be computed beyond the Keplerian problem. For example, in periodic orbits in three-body environments, it would still be possible to compute a modal decomposition with associated modal constants that are stationary in the absence of additional perturbations or control. Thus, the modal decomposition perspective is a unified view that extends from the simple Clohessy-Wiltshire case to periodic orbits in exotic environments, with practical application extending even to the case of almost-periodic orbits encountered in real-world scenarios. This is discussed more in the following chapter.

Chapter 7

Applications of the Relative Motion Modal Decomposition

This chapter explores application of the modal decomposition concept in a variety of circumstances. First, the Lyapunov-Floquet (LF) transformation is numerically computed for a low-fidelity analytic linear model of perturbed spacecraft relative motion in the vicinity of an asteroid. Then, the perturbative application of LF theory to the case of an almost-periodic chief orbit is discussed (in other words, an orbit for which $\exists T \mid [A(t)] \approx [A(t+T)]$). This is satisfied, for example, for quasi-periodic orbits with a dominant frequency in the frequency vector. It extends the applicability of the LF transform-based modal decomposition to a wide variety of perturbed orbits. This facilitates an interesting numerical example for spacecraft relative motion in the vicinity of perturbed terminator orbits about the asteroid Ryugu. Lastly, this chapter discusses the use of the fundamental solution constants \mathbf{c} as a state description, which connects naturally to the modal decomposition concept and also allows for elegant control approaches. Much of the work in this chapter can be found in References [22](#), [23](#), [26](#), and [28](#).

7.1 Numerical Application to Analytic Model of Oblateness, Ellipticity, and SRP Perturbations

For the first application of the modal decomposition perspective to relative motion analysis, the analytic $C_{20} + C_{22} + \text{SRP}$ model from [chapter 3](#) is revisited. See Eqs. [\(3.48\)](#) - [\(3.51\)](#) and the associated discussion. In particular, the analytically approximated plant matrix for the linearized system is used to compute the monodromy matrix, which is then used to compute the LF transfor-

mation and the LTI plant matrix. Due to the fact that the linear model is an explicit function of time, the periodicity condition $[A(t)] = [A(t + T)]$ is easily satisfied. In reality, the linearized plant matrix is only approximate, so the chosen chief orbits are not actually periodic. Nonetheless, the effects of non-periodicity are secondary in the model plant matrix, and do not appear analytically. After the monodromy matrix has been computed, the analysis in this section uses it to study the stability of the LTI transformed system in \mathbf{z} , along with the fundamental relative orbital motion modes predicted by the linearized model. These provide a wealth of information about the system behavior throughout the explored parameter space.

For the results that follow, close-proximity formation dynamics about a rotating asteroid are considered, with important physical parameters given in Table 7.1. Note that this is the same simulation setup that was used for originally testing the model in chapter 3. The parameter R

Table 7.1: Physical Parameters for Modal Parameter Study

Parameters	Values
Asteroid Physical Parameters	$M = 4.9 \times 10^{14}$ kg, $R = 6$ km, Ellipsoidal semi-axes: 6, 3, 2.5 km
Gravity Parameters	$\mu = 3.271 \times 10^{-5}$ km ³ /s ² , $C_{20} = -0.0903$, $C_{22} = 0.0375$
Asteroid Orbit Radius	$R_O = 3.5904 \times 10^8$ km (2.4 AU)
Configuration Parameters	$\kappa = 15^\circ$, $\varphi_0 = 90^\circ$, $T_r = 18.0$ hr, $\psi_0 = 0$
Spacecraft Optical Constants	$\frac{A}{m} = 0.3$ m ² /kg, $\bar{B} = 0.6$, $\bar{s} = 0.25$, $\bar{\rho} = 0.3$

is the Brillouin sphere radius, the maximum extent of the body material from its center of mass. The linearized relative motion model in Eq. (3.48) is used to explore the parameter space for prograde and retrograde near-circular chief orbits. Namely, the inclination of prograde orbits in the terminator plane is $i_T = 75.0^\circ$, and the set of inclinations tested is between 70° and 105° in one degree increments. The range of Γ tested is from $\Gamma = 3/4$ to $\Gamma = 4$, with 25 evenly spaced values for non-modal analysis results. For the modal analysis, the range is the same but with even increments of $\delta\Gamma = 1/4$. The semimajor axis is related to Γ through the following equation, where $c = 2\pi/T_r$:

$$a = \left(\mu \frac{\Gamma^2}{c^2} \right)^{1/3} \quad (7.1)$$

For simplicity, the initial non-critical chief orbit elements $e_0, \omega_0, \Omega_0, f_0$ are all assumed to be zero.

Thus $\theta_0 = 0$ and the chief orbit is initially circular. Small initial nonzero values of chief eccentricity (e.g. $\mathcal{O}(10^{-3})$) do not significantly affect the results. The osculating chief orbit eccentricity is generally of this scale anyway, and can reach higher values in strongly perturbed cases.

While third body effects are ignored in this study, the radius of the asteroid sphere of influence is estimated assuming $m \ll M$ [8]:

$$r_{\text{SOI}} = R_O \left(\frac{m}{M} \right)^{2/5} \approx 205 \text{ km} \quad (7.2)$$

where M is the mass of the sun. Note that at $a = 38.2$ km (corresponding to $\Gamma = 4$), the sun's gravity would be a little less than 3% the strength of the asteroid gravity, so the third-body disturbance should be included in the approximate model for higher fidelity in actual applications.

In the studies that follow, for each point in the parameter space, the state transition matrix is computed using the linearized dynamics for one period of the $[A(t)]$ matrix. This enables any type of close-proximity relative motion to be studied without re-integrating each initial condition of interest, and also efficiently provides the monodromy matrix useful for all subsequent computations.

Figure 7.1 shows the variation of the modulus of the largest Floquet multiplier in the parameter space. Recall that the Floquet multipliers are eigenvalues of the monodromy matrix. Any Floquet multiplier with a modulus greater than 1 is an indicator of the potential for system instability. Stability can only be ensured only if $|\rho_j| \leq 1 \forall j$. The data in Figure 7.1 does not provide a complete parameterization of the degree of instability by itself. The figure does not show how many unstable modes exist; it only shows the severity of the most unstable mode. However, the figure still provides useful insights into the potential for instability depending on the value of Γ and i .

For weakly unstable systems with all $|\rho| \approx 1$, the destabilization that occurs by partial projections of the initial condition into the unstable subspace is less rapid than for systems with a multiplier $|\rho| \gg 1$. Furthermore, formation geometry selected to avoid exciting the unstable modes will enable the motion to remain within specified bounds for longer without corrective maneuvers. Thus, uncorrected formation stability will still be dependent on the initial conditions

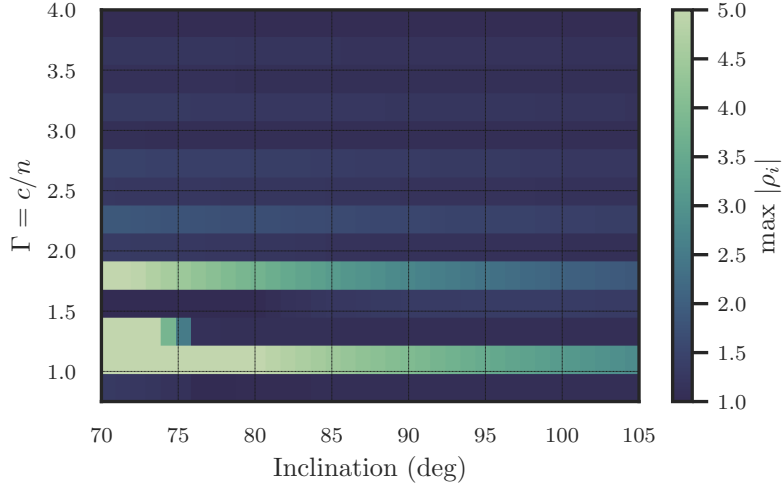


Figure 7.1: Modulus of Largest Floquet Multiplier

of relative states of the spacecraft. This would be very expensive to study with simulations using the truth model alone. However, parameter studies with the linear system can efficiently provide this insight, since the linear dynamics of the perturbed relative motion can be decomposed into linearly independent modes in \mathbf{z} space. Recall that since $\mathbf{x} = [P(t)]\mathbf{z}$ and $[P(t_0)] = [I_{6 \times 6}]$, the behavior of the fundamental modes can be represented in \mathbf{x} coordinates as well.

The approximate model is first used to determine how the number of relative motion modes varies in the parameter space. This data is presented in Figure 7.2(a).

It is also useful to consider how many of these modes are highly unstable. The approach in this work is to determine if the real part of any of the eigenvalues of $[A]$ exceeds a critical value λ^* , defined below as the minimum value required for the real exponential term in the $\mathbf{z}(t)$ solution to increase by a factor of e in N orbits:

$$\lambda^* = \frac{c}{2\pi\Gamma N} \quad (7.3)$$

Setting $N = 10$, this is of $\mathcal{O}(10^{-6})$ for much of the parameter space surveyed.

The critical value λ^* is used to create Figure 7.2(b). It is important to keep the limitations of the model in mind when interpreting these modal results. The relative duration of model accuracy is highly correlated with the relative magnitude of maximum deviation in the AMROS parameter.

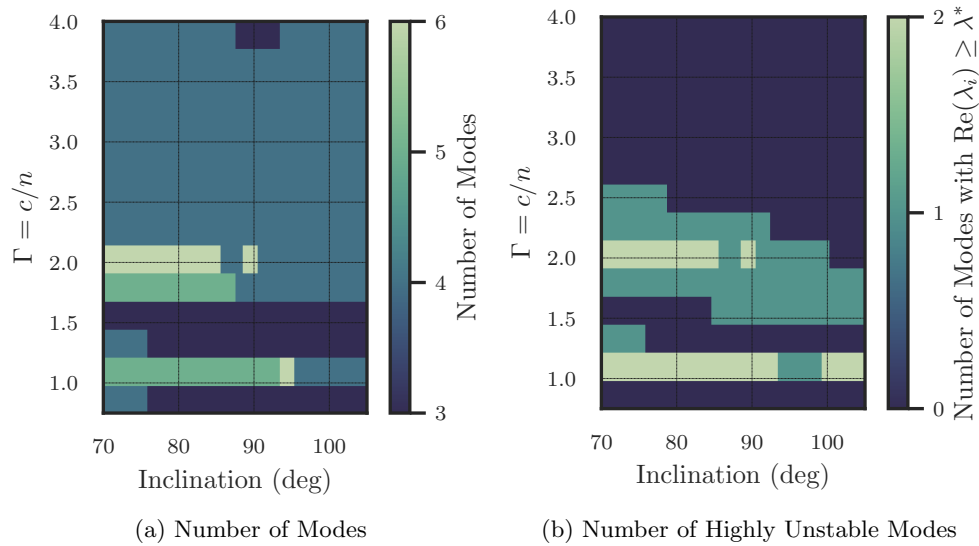
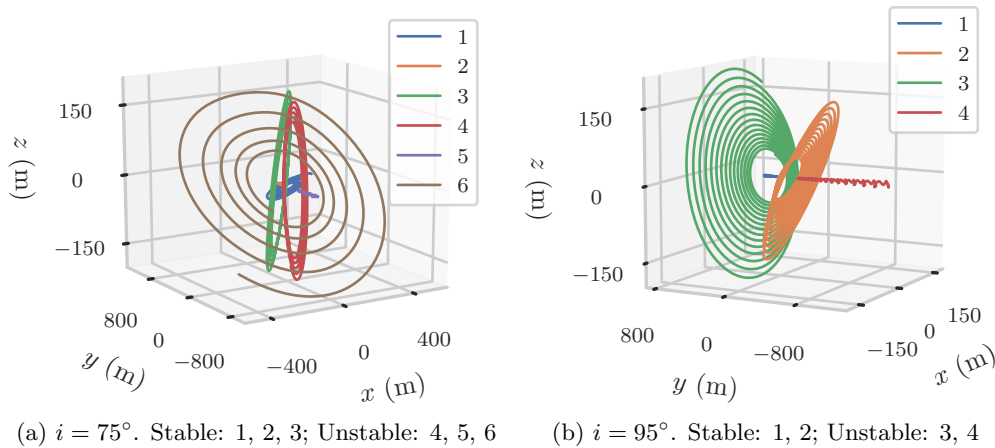


Figure 7.2: Relative Orbital Motion Modal Data

Figure 7.3: Relative Motion Modes for $\Gamma = 2$

In the most highly perturbed regions of the parameter space (lower values of Γ), the linear model only predicts initial behavior well without re-initialization and update of perturbed chief orbit parameters. The stability predictions below $\Gamma = 1.5$ are not consistently trustworthy. Figure 7.2(b) predicts that generally for high-altitude orbits, there are no highly unstable modes, and this property extends to progressively lower orbits as inclination is increased to polar and retrograde orbits.

Because all solutions of the linear model will be a superposition of the fundamental modes, variations in the modal behavior at intermediate levels of Γ are complex and worth investigating. At $\Gamma = 2$, the number of total modes and their stability properties vary with inclination. This is illustrated by Figure 7.3. Note that scale is irrelevant for these linear results. For relative motion centered in the orbit with $i = 75^\circ$, there are 6 unique modes, and all eigenvalues are real. These are plotted for 5 orbits. Three modes are unstable, and two are highly unstable (modes 5 and 6). Mode 4 is slightly unstable ($\lambda_4 = 5.07 \times 10^{-7}$) and mode 3 is stable ($\lambda_3 = -5.06 \times 10^{-7}$). Modes 1 and 2 are strongly stable. Modes 2 and 5 are distorted along-track motion. Such modes appear throughout much of the parameter space, but their eigenvectors are poorly scaled, and do not accurately represent the motion of the system for long time spans. However, modes such as 1, 3, 4, and 5 do reflect the actual formation dynamics. These modes (or mixtures of them) could be periodically re-computed and targeted by a guidance system to enforce desired relative motion behavior.

Figure 7.3(b) shows the modes for relative motion about a chief with $i = 95^\circ$, plotted for 15 chief orbits. These represent the fundamental modes of the same point in the parameter space used to generate Figure 3.7 in chapter 3. The eigenvalues corresponding to each mode are all of scale 10^{-7} , with multiplying factors $\lambda_1 = -9.1$, $\lambda_2 = -6.6 \pm 2.5i$, $\lambda_3 = 6.6 \pm 2.6i$, $\lambda_4 = 9.2$. From these results, it is evident that the initial condition of the motion in Figure 3.7 has partially excited the unstable third mode.

Long-term accurate prediction is possible without any model re-initialization for cases where the relative motion is not too perturbed to compromise model accuracy. This is incredibly useful, as it can be used to find relative motion conditions that would result in bounded formations with linearly predictable behavior for very long time spans without correction. Figure 7.2 shows that for values of $\Gamma > 2.5$, there are only 3 or 4 relative motion modes, and none are particularly unstable. Selecting $\Gamma = 4.0$ and $i = 75^\circ$, the modal results indicate that there are two along-track modes (one stable and one unstable) and two very similar modes with eigenvalues $\lambda_{2,3} = \pm 9.7 \times 10^{-9} \pm 6.1 \times 10^{-7}i$. This represents stable relative motion for long time spans, due to

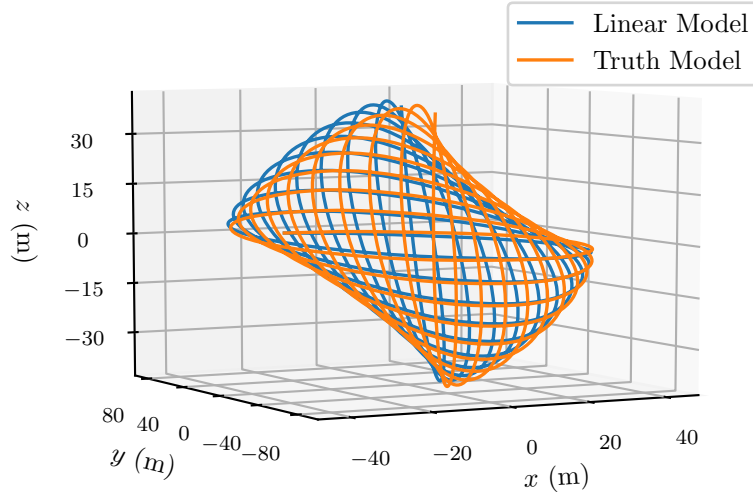


Figure 7.4: Long-Term Stable Relative Motion Mode

the very small real parts of the eigenvalues. Figure 7.4 is produced by initializing the mode with the eigenvalue with the slightly negative real part. The initial condition is just the associated eigenvector with a chosen scaling, given below in LVLH components in meters and meters/second:

$$\mathbf{x}_0 = c\mathbf{v} = \left(12.5, 7.90, 0.8, 9.69 \times 10^{-4}, 6.05 \times 10^{-4}, 7.27 \times 10^{-5} \right)^{\top} \quad (7.4)$$

The first half-period of behavior is shown, amounting to approximately 10 chief orbit periods. There is a positive rotation of the relative orbit about the $\hat{\mathbf{e}}_r$ vector and a shrinking of the relative position bounds along $\hat{\mathbf{e}}_r$. The approximate model agrees with the true behavior for 10 orbits (30 days), with some growing distortion visible. The dynamics in this region of the parameter space are clearly favorable for fuel-efficient close-proximity formation flying. Overall, the results of modal analysis provide a wealth of insight into the behavior of uncontrolled close-proximity relative motion.

7.2 Implementation for General Almost-Periodic Orbits

This section explores the application of the modal decomposition via LF theory to the case that the chief orbit is not exactly periodic. The method explored is to numerically compute a periodic matrix that is similar to the almost-periodic plant matrix, then to use the modes for the former system as an approximate basis for motions in the latter. In this case, conditions are provided

that need to be satisfied for the computed modes to correspond to the actual relative motions of the system. Additionally, there is some discussion of how the behavior of the true system will deviate from what is predicted from the approximate modal basis. Finally, the technique is applied to the problem of formation design in perturbed terminator orbits around the asteroid 162173 Ryugu.

The arguments in this section assume that the spacecraft are operating in sufficiently close proximity that nonlinear relative motion effects are negligible. This would be highly applicable to fractionated space systems, rendezvous and docking, and satellite servicing applications. For close-proximity relative motion in local rectilinear coordinates or orbit element differences, the linearized dynamics are of the form $\dot{\mathbf{x}} = [A(t)]\mathbf{x}$. It can be shown that $[A(t)] \approx [A(t + T)]$ if the chief spacecraft orbit is slowly varying or quasi-periodic such that there exists a “quasi-period” T for which the position and velocity are almost periodic, $\mathbf{r}(t) \approx \mathbf{r}(t + T)$, $\mathbf{v}(t) \approx \mathbf{v}(t + T)$, and furthermore $\frac{\partial \dot{\mathbf{r}}(t)}{\partial \mathbf{r}} \approx \frac{\partial \dot{\mathbf{r}}(t+T)}{\partial \mathbf{r}}$. This regularity is a desirable characteristic for spacecraft orbits in highly perturbed environments, and the resulting almost-periodicity of $[A(t)]$ also enables the analytic developments in this section. The analysis in this section notably applies broadly. First, it applies to the case that the plant matrix is truly quasi-periodic $[A(t)] = [A(\boldsymbol{\omega}t + \boldsymbol{\phi})]$ with frequency vector $\boldsymbol{\omega}$, assuming there exists a dominant frequency $\omega_j \in \boldsymbol{\omega}$ that is much more important to the behavior of $[A(t)]$ than the other frequencies. In such a case, the “quasi-period” is given simply by $T = \frac{2\pi}{\omega_j}$. The analysis also applies to $[A(t)]$ when the components have slow secular drift.

Instead of parameterizing the relative motion in coordinates along the radial, normal, and transverse directions $\hat{\mathbf{e}}_r = \mathbf{r}/r$, $\hat{\mathbf{e}}_n = \mathbf{h}/h$, $\hat{\mathbf{e}}_t = -\hat{\mathbf{e}}_r \times \hat{\mathbf{e}}_n$, orbit element differences are used. The quasi-nonsingular (QNS) elements linearize better than local rectilinear coordinate descriptions, without suffering the weakness for near-circular orbits inherent to the classical orbit elements.[111] They are given by $\boldsymbol{\alpha} = (a, \theta, i, q_1, q_2, \Omega)^\top$ where a is the semimajor axis, $\theta = \omega + f$ is the argument of latitude, i is inclination, $q_1 = e \cos \omega$ and $q_2 = e \sin \omega$ are defined in terms of the eccentricity e and argument of periapsis ω , and Ω is the right ascension of the ascending node (R.A.A.N.). Their differential equations are given below, where $r = p/(1 + q_1 \cos \theta + q_2 \sin \theta)$, $p = a(1 - q_1^2 - q_2^2)$, and

$h = \sqrt{\mu p}$, and the disturbance acceleration is resolved as $\mathbf{a}_P = a_r \hat{\mathbf{e}}_r + a_t \hat{\mathbf{e}}_t + a_n \hat{\mathbf{e}}_n$:

$$\dot{a} = \frac{2a^2}{h} \left((q_1 \sin \theta - q_2 \cos \theta) a_r + \frac{p}{r} a_t \right) \quad (7.5a)$$

$$\dot{\theta} = \frac{h}{r^2} - \frac{r \sin \theta \cos i}{h \sin i} a_n \quad (7.5b)$$

$$\dot{i} = \frac{r \cos \theta}{h} a_n \quad (7.5c)$$

$$\dot{q}_1 = \frac{p \sin \theta}{h} a_r + \frac{(p+r) \cos \theta + r q_1}{h} a_t + \frac{r q_2 \sin \theta}{h \tan i} a_n \quad (7.5d)$$

$$\dot{q}_2 = -\frac{p \cos \theta}{h} a_r + \frac{(p+r) \sin \theta + r q_2}{h} a_t - \frac{r q_1 \sin \theta}{h \tan i} a_n \quad (7.5e)$$

$$\dot{\Omega} = \frac{r \sin \theta}{h \sin i} a_n \quad (7.5f)$$

The differential equations for orbit element differences are obtained by linearizing Eq. (7.5) about the chief orbit as $\delta \dot{\mathbf{oe}} = \left. \frac{d\dot{\mathbf{oe}}}{d\mathbf{oe}} \right|_c \delta \mathbf{oe} = [A_{\mathbf{oe}}(t)] \delta \mathbf{oe}$, where $\delta \mathbf{oe} = (\delta a, \delta \theta, \delta i, \delta q_1, \delta q_2, \delta \Omega)^\top$, and the first row of $[A_{\mathbf{oe}}(t)]$ is given below:

$$A_{11} = \frac{3a}{h} (a_t + (q_1 a_t - q_2 a_r) \cos \theta + (q_1 a_r + q_2 a_t) \sin \theta) + \frac{2a^2}{h} ((q_1 \sin \theta - q_2 \cos \theta) \frac{da_r}{da} + \frac{p}{r} \frac{da_t}{da}) \quad (7.6a)$$

$$A_{12} = \frac{2a^2}{h} ((q_1 a_r + q_2 a_t) \cos \theta + (q_2 a_r - q_1 a_t) \sin \theta) + \frac{2a^2}{h} ((q_1 \sin \theta - q_2 \cos \theta) \frac{da_r}{d\theta} + \frac{p}{r} \frac{da_t}{d\theta}) \quad (7.6b)$$

$$A_{13} = \frac{2a^2}{h} ((q_1 \sin \theta - q_2 \cos \theta) \frac{da_r}{di} + \frac{p}{r} \frac{da_t}{di}) \quad (7.6c)$$

$$A_{14} = \frac{2a^3 \mu}{h^3} (q_1 a_t + (a_t - q_1 q_2 a_r - q_2^2 a_t) \cos \theta + (a_r + q_1 q_2 a_t - q_2^2 a_r) \sin \theta) + \frac{2a^2}{h} ((q_1 \sin \theta - q_2 \cos \theta) \frac{da_r}{dq_1} + \frac{p}{r} \frac{da_t}{dq_1}) \quad (7.6d)$$

$$A_{15} = \frac{2a^3 \mu}{h^3} (q_2 a_t + ((q_1^2 - 1) a_r + q_1 q_2 a_t) \cos \theta + (a_t + q_1 q_2 a_r - q_1^2 a_t) \sin \theta) + \frac{2a^2}{h} ((q_1 \sin \theta - q_2 \cos \theta) \frac{da_r}{dq_2} + \frac{p}{r} \frac{da_t}{dq_2}) \quad (7.6e)$$

$$A_{16} = \frac{2a^2}{h} ((q_1 \sin \theta - q_2 \cos \theta) \frac{da_r}{d\Omega} + \frac{p}{r} \frac{da_t}{d\Omega}) \quad (7.6f)$$

There are too many terms to show all other components here, but they are straightforward to obtain. These equations were adapted to write a generalized linearization toolbox valid for any perturbed orbit problem, which was used to perform the necessary computations for this section.

The nonlinear mapping between orbit element differences and the local vertical-local horizontal (LVLH) frame relative state is achieved by adding the element differences to the chief elements to obtain the deputy orbit elements, then the chief and deputy elements are mapped to inertial coordinates, then the chief state is subtracted from the deputy and the state differences are resolved in the LVLH frame. There also exists a linearized mapping between the local coordinate description and the QNS element differences, reproduced here:[2]

$$x = \frac{r}{a}\delta a + \frac{V_r}{V_t}r\delta\theta - \frac{r}{p}(2aq_1 + r\cos\theta)\delta q_1 - \frac{r}{p}(2aq_2 + r\sin\theta)\delta q_2 \quad (7.7a)$$

$$y = r(\delta\theta + \cos i\delta\Omega) \quad (7.7b)$$

$$z = r(\sin\theta\delta i - \cos\theta\sin i\delta\Omega) \quad (7.7c)$$

$$\dot{x} = -\frac{V_r}{2a}\delta a + \left(\frac{1}{r} - \frac{1}{p}\right)h\delta\theta + (V_r a q_1 + h\sin\theta)\frac{\delta q_1}{p} + (V_r a q_2 - h\cos\theta)\frac{\delta q_2}{p} \quad (7.7d)$$

$$\dot{y} = -\frac{3V_t}{2a}\delta a - V_r\delta\theta + (3V_t a q_1 + 2h\cos\theta)\frac{\delta q_1}{p} + (3V_t a q_2 + 2h\sin\theta)\frac{\delta q_2}{p} + V_r\cos i\delta\Omega \quad (7.7e)$$

$$\dot{z} = (V_t\cos\theta + V_r\sin\theta)\delta i + (V_t\sin\theta - V_r\cos\theta)\sin i\delta\Omega \quad (7.7f)$$

where V_r and V_t are given below. Note that the given mapping to velocity components does not account for the effects of perturbations, but the position mapping is accurate because it is just geometric [50].

$$V_r = \frac{h}{p}(q_1\sin\theta - q_2\cos\theta) \quad (7.8a)$$

$$V_t = \frac{h}{p}(1 + q_1\cos\theta + q_2\sin\theta) \quad (7.8b)$$

7.2.1 Almost-Periodic Linear Systems

Consider a linear time-varying system $\dot{\mathbf{x}} = [A(t)]\mathbf{x}$, for which $[A(t)] \approx [A(t+T)]$ but a perturbing term $[\delta A(t)]$ stops the plant matrix from being exactly periodic:

$$\dot{\mathbf{x}} = ([\bar{A}(t)] + [\delta A(t)])\mathbf{x} \equiv [A(t)]\mathbf{x} \quad (7.9)$$

where $[\bar{A}(t)] = [\bar{A}(t+T)]$, which can be computed by a Fourier series fit of $[A(t)]$ over an interval $t_0 < t < t_0 + T$ for some choice of T . A Fourier series naturally only captures the T -periodic component

of $[A(t)]$. In this discussion, Eq. (7.9) represents the linearized dynamics of relative motion about an orbiter in a perturbed environment, in either LVLH frame coordinates or differential QNS elements. The term $[\delta A(t)]$ represents the known non-periodic data in the plant matrix, but the influence of dynamic uncertainty due to low-fidelity modeling or navigational errors in the chief orbit can additionally be incorporated into this term for other analyses.

Let $\mathbf{x}_u(t)$ be the solution to the following uncorrected dynamics for which the plant matrix is exactly periodic:

$$\dot{\mathbf{x}}_u = [\bar{A}(t)]\mathbf{x}_u \quad (7.10)$$

For this system, the constant matrix $[\bar{\Phi}(t_0 + T, t_0)]$ is the monodromy matrix, with $[\bar{\Phi}(t, t_0)]$ being the solution of the following differential equation for the state transition matrix (STM) of \mathbf{x}_u :

$$[\dot{\bar{\Phi}}(t, t_0)] = [\bar{A}(t)][\bar{\Phi}(t, t_0)] \quad (7.11)$$

with the initial condition $[\bar{\Phi}(t_0, t_0)] = [I]$. Note the following transformation of the monodromy matrix due to a shift of the epoch time from t_0 to t_c :

$$[\bar{\Phi}(t_c + T, t_c)] = [\bar{\Phi}(t_c, t_0)][\bar{\Phi}(t_0 + T, t_0)][\bar{\Phi}(t_c, t_0)]^{-1} \quad (7.12)$$

Standard Floquet theory applies to the linear system with $[\bar{A}(t)]$ as its plant matrix. First, there exists a T -periodic coordinate transformation $\mathbf{x}_u = [P(t)]\mathbf{z}_u$, with $[P(t)]$ given below:

$$[P(t)] = [\bar{\Phi}(t, t_0)]e^{-[\bar{\Lambda}](t-t_0)} \quad (7.13)$$

$$[P(t_0)] = [P(t_0 + T)] = [I] \quad (7.14)$$

Furthermore, by differentiating $\mathbf{x}_u = [P(t)]\mathbf{z}_u$ and substituting Eq. (7.10), it can be shown that the dynamics of \mathbf{z}_u obey the following equation with a *constant* plant matrix $[\bar{\Lambda}]$:

$$\dot{\mathbf{z}}_u = \left([P(t)]^{-1}[\bar{A}(t)][P(t)] - [P(t)]^{-1}[\dot{P}(t)] \right) \mathbf{z}_u = [\bar{\Lambda}]\mathbf{z}_u \quad (7.15)$$

Note in addition that $[\bar{\Lambda}]$ is computed directly from the monodromy matrix:

$$[\bar{\Lambda}] = \frac{1}{T} \ln([\bar{\Phi}(t_0 + T, t_0)]) \quad (7.16)$$

For the perturbed system given by Eq. (7.9), let a new corresponding system \mathbf{z} be constructed as $\mathbf{z} = [P(t)]^{-1}\mathbf{x}$ using the same T -periodic transformation $[P(t)]$ in Eq. (7.13). In other words, this new system will be dynamically equivalent to the system in \mathbf{x} , with the states mapped using the same periodic transformation that maps between the uncorrected systems. This is illustrated in Figure 7.5.

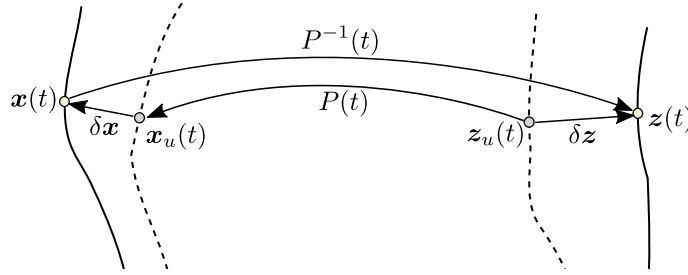


Figure 7.5: Transformation Between \mathbf{x} and \mathbf{z} Spaces

The dynamics of \mathbf{x} differ from those of \mathbf{x}_u by the addition of the $[\delta A(t)]$ term in the plant matrix, and the dynamics in \mathbf{z} will correspondingly differ from those of \mathbf{z}_u . The corresponding deviation in \mathbf{z} space dynamics must be characterized. Differentiating $\mathbf{x} = [P(t)]\mathbf{z}$ and substituting Eq. (7.9), the following equation is obtained for the dynamics in \mathbf{z} :

$$\dot{\mathbf{z}} = \left([P]^{-1}[\bar{A}][P] + [P]^{-1}[\delta A][P] - [P]^{-1}[\dot{P}] \right) \mathbf{z} \quad (7.17)$$

Here, the term $[\bar{\Lambda}] = [P]^{-1}[\bar{A}][P] - [P]^{-1}[\dot{P}]$ is recognized, and the dynamics of \mathbf{z} are rewritten:

$$\dot{\mathbf{z}} = ([\bar{\Lambda}] + [\delta\Lambda(t)]) \mathbf{z} \equiv [\Lambda(t)]\mathbf{z} \quad (7.18)$$

$$[\delta\Lambda(t)] = [P(t)]^{-1}[\delta A(t)][P(t)] \quad (7.19)$$

Thus, on the interval $\mathcal{S} = [t_0, t_0 + T]$, the linear time-varying system in \mathbf{x} with almost-periodic plant matrix $[A(t)] \approx [A(t + T)]$ has been transformed into a system in \mathbf{z} with an almost constant plant matrix $[\Lambda(t)]$ subject to small oscillations $[\delta\Lambda(t)]$ about a constant $[\bar{\Lambda}]$. Eqs. (7.18) and (7.19) are of fundamental importance in this discussion, as is the \mathbf{z} space in which they operate.

7.2.2 Persistence and Robustness of Modes

The properties of desirable modes are now outlined. To facilitate this discussion, introduce the factorization $\mathbf{z} = \mathbf{z}_u + \delta\mathbf{z}$, for which \mathbf{z}_u obeys the following modal decomposition:

$$\mathbf{z}_u = \sum_{i=1}^k c_i \mathbf{v}_i e^{\lambda_i(t-t_0)} \quad (7.20)$$

Here \mathbf{v}_i is the i th eigenvector of $[\bar{\Lambda}]$. It is also possible to modally decompose the motion in \mathbf{x}_u due to the existence of the transformation $\mathbf{x}_u(t) = [P(t)]\mathbf{z}_u(t)$. Let \mathbf{z} be initialized in a single mode, such that $\delta\mathbf{z}(t_0) = \mathbf{0}$, and then evolve subject to the full plant matrix via Eq. (7.18):

$$\mathbf{z}_l = \mathbf{z}_{u,l} + \delta\mathbf{z} = c_l \mathbf{v}_l e^{\lambda_l(t-t_0)} + \delta\mathbf{z} \quad (7.21)$$

For simplicity, the mode is assumed to consist of a single unique eigenvalue, but this analysis could be repeated with a complex-conjugate pair of eigenvalues. Substitute Eq. (7.21) into Eq. (7.18), and consider a time range $t_0 \leq t < t^*$ such that $\delta\mathbf{z}$ is small enough to neglect in comparison to \mathbf{z}_u . In this time range, the state evolves as:

$$\dot{\mathbf{z}}_l = \dot{\mathbf{z}}_{u,l} + \delta\dot{\mathbf{z}} \approx [\bar{\Lambda}]\mathbf{z}_{u,l} + [\delta\Lambda(t)]\mathbf{z}_{u,l} \quad (7.22)$$

From Eq. (7.22), during the time $t_0 \leq t < t^*$, the condition that the initial modal motion be closely followed by the perturbed system is that the flow of the uncorrected mode $\dot{\mathbf{z}}_{u,l}$ dominates that of the deviation $\delta\dot{\mathbf{z}}$, where $\|\cdot\|$ is the operator norm or 2-norm:

$$\|[\delta\Lambda(t)]\mathbf{v}_l\| \ll \|\lambda_l \mathbf{v}_l\| \quad (7.23)$$

In other words, only the sub-eigenspace of $[\bar{\Lambda}]$ that is *robust* to the small perturbations due to $[\delta\Lambda(t)]$ will be closely reflected by the true dynamics for an appreciable period of time.

Consider two intervals $\mathcal{T}_k = [t_0 + kT, t_0 + (k+1)T]$ and $\mathcal{T}_{k+1} = [t_0 + (k+1)T, t_0 + (k+2)T]$, on which the matrices $[\bar{\Lambda}_k]$ and $[\bar{\Lambda}_{k+1}]$ are computed from the monodromy matrices associated with the periodic parts of the plant matrix on the two intervals, themselves obtained via Eq. (7.11):

$$[\bar{\Lambda}_k] = \frac{1}{T} \ln([\bar{\Phi}(t_0 + (k+1)T, t_0 + kT)]) \quad (7.24)$$

$$[\bar{\Lambda}_{k+1}] = \frac{1}{T} \ln([\bar{\Phi}(t_0 + (k+2)T, t_0 + (k+1)T)]) \quad (7.25)$$

Let $[\Delta\bar{\Lambda}_{k+1}] = [\bar{\Lambda}_{k+1}] - [\bar{\Lambda}_k]$. It can be said that the i th mode is *persistent* in the transition from interval \mathcal{T}_k to \mathcal{T}_{k+1} so long as the changes in the eigenvalue are small, $|\Delta\lambda_i| \ll |\lambda_i|$, and the changes in the eigenvector are small.

The desirable modes for spacecraft relative motion guidance are thus those which satisfy two criteria: (1) robustness, meaning that any disturbances $[\delta\Lambda(t)]$ have only secondary effects, and (2) persistence, meaning that they change only slightly with each interval. Most importantly, these two properties are expected to go hand-in-hand, because they both are indicators of the robustness of a given eigenvalue and eigenvector to arbitrary small matrix perturbations. Thus, modes that are persistent over multiple intervals should also generally be robust.

7.2.3 Dynamics of the Deviation

Factoring Eq. (7.18) into the uncorrected component and the deviation, the following is obtained:

$$(\dot{z}_u + \delta\dot{z}) = ([\bar{\Lambda}] + [\delta\Lambda(t)])(z_u + \delta z) \quad (7.26)$$

It has already been established that for initialization in an appropriately chosen robust and persistent mode (or similarly, a combination of such modes), $z(t) \approx z_u(t)$ for some time range $t_0 \leq t < t^*$. On this time range, an approximate expression for the deviation $\delta z(t)$ is sought. This can be obtained with a straightforward perturbation expansion, by introducing the scalings $[\Lambda(t)] = [\Lambda_0] + \epsilon[\Lambda_1]$ and $z = z_0 + \epsilon z_1$, where the zeroth-order terms are $[\Lambda_0] = [\bar{\Lambda}]$ and $z_0 = z_u$, and the first-order terms are $\epsilon[\Lambda_1] = [\delta\Lambda]$ and $\epsilon z_1 = \delta z$. Substituting these expansions into Eq. (7.26) and isolating the $\mathcal{O}(\epsilon^0)$ and $\mathcal{O}(\epsilon^1)$ components, the following two equations are obtained:

$$\dot{z}_0 = [\Lambda_0]z_0 \quad (7.27)$$

$$\dot{z}_1 = [\Lambda_0]z_1 + [\Lambda_1]z_0 \quad (7.28)$$

Multiplying Eq. (7.28) by ϵ , substituting in $z_0 = z_u(t)$ and the other scaling definitions, and allowing for a small nonzero initial condition on the deviation $\delta z(t_0) = \Delta z$, the solution to the

approximate dynamics of the deviation are given below, where $[\bar{\Phi}_z(t, \tau)] = \exp([\bar{\Lambda}](t - \tau))$:

$$\delta \mathbf{z}(t) \approx \int_{t_0}^t [\bar{\Phi}_z(t, \tau)] [\delta \Lambda(\tau)] [\bar{\Phi}_z(\tau, t_0)] d\tau \cdot \mathbf{z}_u(t_0) + [\bar{\Phi}_z(t, t_0)] \Delta \mathbf{z} \quad (7.29)$$

This equation is valid so long as the deviation remains sufficiently small that the deriving assumptions are not violated. The term $\Delta \mathbf{z}$ represents a small targeting error, $\mathbf{z}(t_0) - \mathbf{z}_u(t_0)$. The derivation of Eq. (7.29) concludes the analytic prerequisites for discussing the use of approximate modes computed via the numerical application of LF theory.

7.2.4 Spacecraft Relative Motion Near Terminator Orbits

The numerical approximate modal decomposition is now applied to the problem of design and control of close-proximity spacecraft relative motion around an asteroid. This is a useful problem of study because of both the growing popularity of asteroid missions and the potential for future spacecraft missions to trend more towards low-cost fractionated designs [5, 86]. In addition, there is an availability of nearby asteroids which are good targets for scientific study, yet reachable by small, low-cost spacecraft [45].

The application in this work is the study of relative motion modes in terminator orbits about the asteroid 162173 Ryugu, a near-Earth asteroid which was the target of the recent Hayabusa2 mission. The rotating gravity field and the combined effects of solar gravity and radiation pressure make this a dynamically complex target for formation design or any other multi-spacecraft proximity operations, and the natural close-proximity spacecraft relative motion modes in this environment will be interesting to characterize. This example also helps to illustrate that the modal decomposition tools and techniques introduced in this dissertation can be applied even to very complex orbits.

For this work, periodic terminator orbits computed in the Augmented Normalized Hill Three-Body Problem (ANH3BP) serve as the nominal orbit conditions for the chief orbit in the formation, but the true orbit is perturbed by the rotating irregular gravity field of the asteroid. Thus, the nominal orbit design is periodic, but the actual orbits will be generally quasi-periodic. Under the

influence of perturbations, regular long-term stable motion can still be found in the vicinity of nominal periodic terminator orbits [14].

Past studies have demonstrated that so long as the semimajor axis is above a 1.5 resonance radii limit and below a corresponding upper limit characterized by the third-body and SRP perturbations, the orbit will be more likely to persist for long time spans [63, 113, 115]:

$$\frac{3}{2} \left(\frac{T_r^2 \mu}{4\pi^2} \right)^{1/3} < a < \frac{1}{4} \sqrt{\frac{\mu B}{G_1}} d \quad (7.30)$$

Here T_r is the rotation period of the asteroid, μ is its gravitational parameter, B is the spacecraft mass-to-area ratio in kg/m^2 , $G_1 \approx 10^8 \text{kg} \cdot \text{km}^3/\text{s}^2 \text{m}^2$ is the solar constant, and d is the distance from the asteroid to the sun in km. Note also that the semimajor axis can be expressed as a function of the parameter $\Gamma = c/n$, where c is the rotation rate of the asteroid and n is the mean motion of the spacecraft orbit:

$$a = \Gamma^{2/3} \left(\frac{T_r^2 \mu}{4\pi^2} \right)^{1/3} \quad (7.31)$$

thus the rotation rate ratio inequality to guard against the effects of the rotating gravity field is $\Gamma > (3/2)^{3/2} \approx 1.8$. With the nominal orbit designed as a periodic orbit with size satisfying the constraints of Eq. (7.30), the effect of the perturbations can be minimized to some degree. Furthermore, a useful degree of regularity can be introduced to the orbit by choosing the value of Γ to be rational and of the following form:

$$\Gamma^*(j, k, l) = \frac{kl + j}{k} \quad (7.32)$$

where j , k , and l are integers chosen such that Γ is greater than the lower limit, $j \leq k$. This choice of Γ results in $l + j/k$ rotations of the asteroid with after each spacecraft orbit period T_s . Thus, the sun-orbiter-asteroid geometry for time t and time $t + T_s$ will be the same, except the longitude of the asteroid will have advanced by $2\pi j/k$. This regularity helps to ensure that the plant matrix for relative motion will obey $[A(t)] \approx [A(t + T)]$ so that the relative motion modes can be easily characterized, and in this case $T = T_s k$. It could also be potentially useful for scientific studies by providing regularly reproducible and highly predictable lighting conditions.

The ANH3BP describes motion in the vicinity of a sun-orbiting asteroid, and the dynamics are given by the following dimensionless equations of motion for a circular asteroid heliocentric orbit [15]:

$$\mathbf{r}'' + \hat{\mathbf{z}} \times \mathbf{r}' + (\hat{\mathbf{z}} \cdot \mathbf{r}) \hat{\mathbf{z}} = \frac{\partial U}{\partial \mathbf{r}} \quad (7.33)$$

$$U(\mathbf{r}) = \frac{1}{\|\mathbf{r}\|} + \beta \hat{\mathbf{d}} \cdot \mathbf{r} + \frac{3}{2} (\hat{\mathbf{d}} \cdot \mathbf{r})^2 \quad (7.34)$$

where $\hat{\mathbf{d}}$ is the unit vector pointing from the sun to the asteroid and β is the non-dimensional SRP acceleration in terms of the solar constant G_1 , mass-to-area ratio B , solar gravitational parameter μ_s , and asteroid gravitational parameter μ :

$$\beta = \frac{G_1}{B \mu_s^{2/3} \mu^{1/3}} \quad (7.35)$$

Note that β is the only parameter of interest in the non-dimensional problem. The terms \mathbf{r} and \mathbf{r}' are the dimensionless orbiter position and velocity about the asteroid in the rotating asteroid-fixed Hill frame, related to the dimensionalized position \mathbf{R} and velocity $\dot{\mathbf{R}}$ in the rotating frame by the expressions given below:

$$\mathbf{r} = \frac{1}{\epsilon d} \mathbf{R} \quad (7.36)$$

$$\mathbf{r}' = \frac{1}{\epsilon d \Omega_n} \dot{\mathbf{R}} \quad (7.37)$$

where d is the sun-asteroid distance, $\epsilon = (\mu/\mu_s)^{1/3}$, and $\Omega_n = \sqrt{\mu_s/d^3}$. These equations are adapted from more general eccentric orbit equations, and Eqs. (7.33) and (7.37) change for the general elliptic case [115]. Note that Eq. (7.33) admits a Jacobi integral, which is conserved for any orbit, and given below in terms of the potential $U(\mathbf{r})$ and $v = \|\mathbf{r}'\|$ and $z = \mathbf{r} \cdot \hat{\mathbf{z}}$

$$C_J = \frac{1}{2} (v^2 + z^2) - U(\mathbf{r}) \quad (7.38)$$

Periodic orbits are found using a multiple-shooting predictor-corrector algorithm, which breaks the trajectory into q segments with initial states \mathbf{X}_i for $i = 1, \dots, q$, and these states are combined with the segment time duration $t_{\text{seg}} = T_s/q$ into the state vector \mathbf{Z} [15]:

$$\mathbf{Z} = \left[\mathbf{X}_1^\top, \mathbf{X}_2^\top, \dots, \mathbf{X}_q^\top, t_{\text{seg}} \right]^\top \quad (7.39)$$

By driving the following vector $\mathbf{G}(\mathbf{Z})$ to zero, the algorithm drives an initial guess of the orbit towards a nearby periodic orbit, if it exists. The zero constraint on the three select components of \mathbf{X}_1 and the Jacobi integral value constraint restrict the search space for the periodic orbit:

$$\mathbf{G}(\mathbf{Z}) = \left[\mathbf{X}_2^\top - \mathbf{F}_{t_{\text{seg}}}^\top(\mathbf{X}_1), \mathbf{X}_3^\top - \mathbf{F}_{t_{\text{seg}}}^\top(\mathbf{X}_2), \dots, \mathbf{X}_q^\top - \mathbf{F}_{t_{\text{seg}}}^\top(\mathbf{X}_{q-1}), \right. \\ \left. \mathbf{X}_1^\top - \mathbf{F}_{t_{\text{seg}}}^\top(\mathbf{X}_q), y_1, \dot{x}_1, \dot{z}_1, C(\mathbf{X}_1) - C_0 \right]^\top = \mathbf{0} \quad (7.40)$$

The resulting correction to \mathbf{Z} is of the form $\mathbf{Z}_{k+1} = \mathbf{Z}_k - \delta\mathbf{Z}$, with $\delta\mathbf{Z}$ given as:

$$\delta\mathbf{Z} = \gamma \left([H]^\top [H] \right)^{-1} [H]^\top \mathbf{G}(\mathbf{Z}) \quad (7.41)$$

where $[H] = \partial\mathbf{G}/\partial\mathbf{Z}|_{\mathbf{Z}_k}$ and $\gamma \leq 1$ is a variable step size for better convergence of the algorithm.

In order to determine the family of periodic terminator orbits applicable to this study, the value of β for this problem must be determined, and the size of appropriate admissible dimensionless orbits must also be obtained. The former problem is a straightforward computation given B, μ, μ_s , and the latter can be solved by choosing orbits that ensure that the previously mentioned inequality $\Gamma > (3/2)^{3/2}$ is satisfied. It turns out that using $z(0) = \tilde{a}$, $\dot{y}(0) = 1/\tilde{a}^{1/2}$ as an initial guess tends to yield periodic terminator orbits with dimensionless periods very close to $\tilde{T} = 2\pi\tilde{a}^{3/2}$. It is thus straightforward to find the conditions for a periodic orbit with an acceptable value of dimensionless period $\tilde{T} = \Omega T_s = \Omega\Gamma T_r$, derived from a given asteroid rotation period T_r and an acceptable choice of Γ . Re-dimensionalizing the computed initial conditions will result in a satisfactory terminator orbit. Important information for this problem is summarized in Table 7.2, along with the semimajor axis for select values of Γ .

In Table 7.2, note that d is the distance from the sun to the asteroid at the beginning of the simulation, R denotes the maximum radius, and the C_{ij} terms are the low degree and order gravitational harmonics generated from the Ryugu shape model using a constant-density assumption [44]. The rotation period of Ryugu is $T_r = 7.6326$ hrs, so admissible semimajor axes fall in the range $1.246 < a < 3.691$ km, and the given semimajor axis values all fall within this range. In the provided orientation data, the terms λ_p and β_p are the ecliptic longitude and latitude

Table 7.2: Physical Parameters for Ryugu Simulation

Parameters	Values
Geometric	$d = 1.1466$ AU, $B = 24.7$ kg/m ²
Nondimensional	$\beta = 50$, $\Omega_n = 1.62334 \times 10^{-7}$, $\epsilon = 6.0873 \times 10^{-5}$
Asteroid properties [46, 44]	$\mu = 3 \times 10^{-8}$ km ³ /s ² , $T_r = 7.6326$ hrs, $R = 0.4484$ km
Asteroid orbit	$C_{20} = -0.0539$, $C_{22} = 0.0027$, $C_{30} = 0.00307$, $C_{40} = 0.04209$
Asteroid orientation [46]	$a = 1.1896$ AU, $e = 0.1902$, $\Omega = 251.589^\circ$, $i = 5.884^\circ$, $\omega = 211.436^\circ$, $f_0 = \pi/2$
Semimajor axis, $a(\Gamma)$	$\lambda_p = 179.3^\circ$, $\beta_p = -87.44^\circ$, $\phi_p = 153.9^\circ$, $v_p = 171.64^\circ$, $\psi_{p,0} = 0^\circ$ $a(2) = 1.319$, $a(5/2) = 1.531$, $a(3) = 1.728$, $a(7/2) = 1.916$ km $a(4) = 2.094$, $a(6) = 2.744$ km

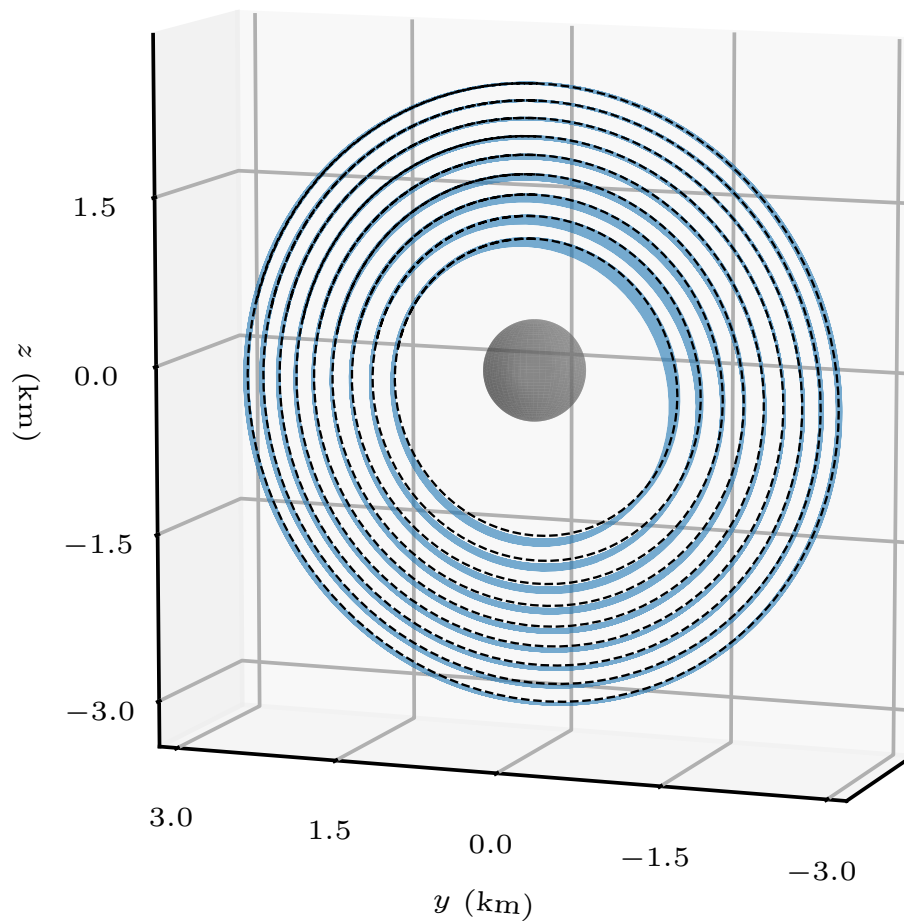


Figure 7.6: Nominal and Perturbed Terminator Orbits at Ryugu

to the spin axis. These yield an obliquity of the spin axis of 171.64° , so Ryugu rotates retrograde with respect to its orbit. The parameters $\phi_p, v_p, \psi_{p,0}$ are derived sequential Euler angles for the

3-1-3 rotation from the asteroid orbit perifocal frame to the asteroid body frame parameterized by the principal axes. Note $\psi_p(t) = \psi_{p,0} + ct$ for uniform rotation.

While the gravitational coefficients given in Table 7.2 are sufficient to capture the dominant dynamics, the effects of higher-order gravitational perturbations are added in the simulations by artificially generating higher order C_{lm} coefficients for even $l \geq m$ from C_{20} and C_{22} using the following generating function valid for constant-density ellipsoidal bodies [12, 17]:

$$C_{lm} = 3\chi(2 - \delta_{0m}) \frac{5^{\frac{l}{2}} \left(\frac{l}{2}\right)! (l-m)!}{(l+3)(l+1)!} \sum_{i=0}^{\text{int}\left(\frac{l-m}{4}\right)} \frac{C_{20}^{\frac{l}{2} - (\frac{m}{2} + 2i)} C_{22}^{\frac{m}{2} + 2i}}{\left(\frac{l}{2} - \frac{m}{2} - 2i\right)! \left(\frac{m}{2} + i\right)!} \quad (7.42)$$

where χ is a multiplier introduced because the value of C_{40} from Table 7.2 is greater than predicted with this equation, thus $\chi = |C_{40,\text{true}}/C_{40,\text{comp}}|$. In reality, Ryugu is not a constant-density ellipsoid, so these generated coefficients won't match the true values. In future work it would be possible to obtain more accurate values for the higher-order coefficients using the Ryugu shape model data.

A subset of the family of periodic terminator orbits is computed for $\beta = 50$ and given in Figure 7.6. The black curves are generated by scaling the ANH3BP-predicted periodic orbit initial conditions and propagating with only the asteroid point-mass gravity, solar gravity, and cannonball solar radiation pressure. The light blue curves are the perturbed terminator orbits, propagated for 20 orbits from the same nominal periodic orbit initial condition, but subject to the additional disturbances of a rotating 12th degree and order gravity field generated from the data in Table 7.2 and Eq. (7.42). From the figure, it is evident that the effects of the perturbations are larger for orbits closer to Ryugu. Nonetheless, these orbits are still far more regular than orbits generated by other means, such as propagation from a circular orbit initial condition in the terminator plane.

7.2.5 Mode-Computing Algorithm Validation

As a preliminary test of the code for computing the modal decomposition code in orbit element differences, a 1.531 km orbit about Ryugu is tested with only the J_2 perturbation. For the J_2 -only problem, the code predicts a relative motion mode with a zero eigenvalue corresponding to relative motion consisting only of the z_6 coordinate, and the bottom row of $[P(t)]$ is zero except for

the last element, thus $\delta\Omega = z_6$. In other words, the numerical modal decomposition has successfully identified that relative motion in orbit element space consisting only of a RAAN difference will not drift or change at all over time due to the axial symmetry in the dynamics.

In addition, note that while the computed $[P(t)]$ matrix has a highly complex form when \mathbf{x} is in local rectilinear coordinates, that is not the case when \mathbf{x} is in QNS element differences. In this case, numerical results show that the numerically computed LF transformation is a perturbed form of the Keplerian case (Eq. (6.50)), with smaller additional time-varying oscillations about zero in many components, represented by $[P_\epsilon(t)]$:

$$\begin{pmatrix} \delta a \\ \delta\theta \\ \delta i \\ \delta q_1 \\ \delta q_2 \\ \delta\Omega \end{pmatrix} \approx \begin{bmatrix} 1 & 0 & 0 & 0 & 0 & 0 \\ 0 & P_{2,2}(t) & 0 & P_{2,4}(t) & P_{2,5}(t) & 0 \\ 0 & 0 & 1 & 0 & 0 & 0 \\ 0 & 0 & 0 & 1 & 0 & 0 \\ 0 & 0 & 0 & 0 & 1 & 0 \\ 0 & 0 & 0 & 0 & 0 & 1 \end{bmatrix} \begin{pmatrix} z_1 \\ z_2 \\ z_3 \\ z_4 \\ z_5 \\ z_6 \end{pmatrix} + [P_\epsilon(t)]\mathbf{z} \quad (7.43)$$

This result further agrees with Eq. (6.82) and the associated discussion in the end of [chapter 6](#). Because the plant matrix is not exactly periodic for the provided numerical examples, the computed LF transformation and the resulting modal decomposition will form an approximate basis of possible close-proximity relative motion, and not an exact one as in the Keplerian case. However, if the discarded component $[\delta A(t)]$ is sufficiently small, the errors will be quite small. In some cases, the plant matrix $[A(t)]$ will be quasi-periodic, and it could be worthwhile to explore computing the quasi-periodic Lyapunov-Perron (LP) transformation [66] that reduces the linearized dynamics to an LTI form. There are practical challenges to reducing the linearized dynamic equations with quasi-periodic coefficients. The decomposition based on the LF transformation, however, is numerically straightforward, analytically promising, and provides insights into the types of relative motion for a large range of potential applications.

7.2.6 Applying the Mode-Computing Algorithm to Ryugu Terminator Orbits

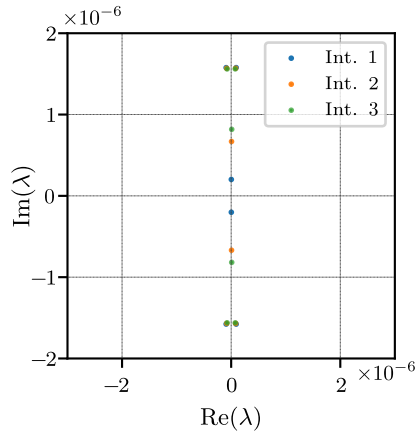
The modal decompositions obtained for the perturbed terminator orbit with $\Gamma = 3$ are discussed next. The quasi-period for the perturbed orbit is determined as the time between chief orbit crossings of the plane $y = 0$ in Figure 7.6. The result is approximately 1% greater than the result predicted by the dimensionless system using $T = \tilde{T}/\Omega_n$. The eigenvalues of $[\bar{\Lambda}]$ are listed in Table 7.3 and plotted in Figure 7.7(a) for three successive intervals \mathcal{T}_1 , \mathcal{T}_2 , and \mathcal{T}_3 . Also included are the initial conditions for a slowly-changing mode on the three subsequent intervals, in QNS orbit element differences $\delta\mathbf{oe}_0 = \mathbf{z}_0 = [\delta a_0, \delta\theta_0, \delta i_0, \delta q_{1,0}, \delta q_{2,0}, \delta\Omega_0]$, with δa_0 in km and all angle differences in radians. It is worth noting that the pair of eigenvalues $\lambda_{5,6}$ closest to zero for interval \mathcal{T}_1 moved around significantly depending on the value of the quasi-period used to compute $[\bar{A}(t)]$, whereas the other four eigenvalues are comparatively unaffected by small changes to the quasi-period. The other four eigenvalues $\lambda_{1,2}$ and $\lambda_{3,4}$ also change very little between intervals, as can be seen by examining the two complex-conjugate pairs farthest from the real line. Note that the points for these four eigenvalues on intervals 1, 2, and 3 lie almost on top of one another in Figure 7.7. The mode corresponding to the pair $\lambda_{1,2}$ is selected, and the corresponding motion is given in the LVLH frame for 12 orbits in Figure 7.7(b). Note that the original space of this mode is in \mathbf{z}_u coordinates, computed using the methods introduced earlier in the chapter, and its motion is mapped to LVLH coordinates by first using $[P(t)]$ to map to QNS element differences, followed by the approximate linear mapping to LVLH given by Eq. (7.7). The relative motion analysis was performed in QNS element differences, and the plots in this section are given in LVLH coordinates only as a visual aid to the reader.

Note that the differences between $[A(t)]$ and $[\bar{A}(t)]$ are small for most components, and furthermore the differences between $[\bar{A}(t)]$ for successive intervals are small. This is demonstrated by Figure 7.8, in which a representative component of $[\bar{A}(t)]$ from interval \mathcal{T}_1 is overlaid on the same component of $[A(t)]$ for interval \mathcal{T}_2 , and there is still close agreement.

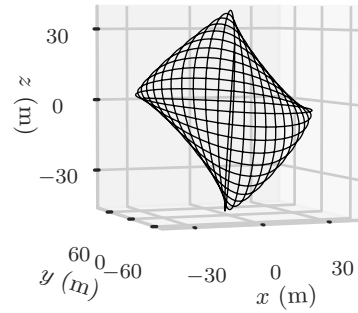
In a control implementation, desired combinations of the persistent linearly predicted modes

Table 7.3: Spacecraft Relative Motion Modal Data for Terminator Orbit, $\Gamma = 3$

Parameters	Values
Interval \mathcal{T}_1 eigenvalues	$\lambda_{1,2} = 9.16 \times 10^{-8} \pm 1.58 \times 10^{-6}i$, $\lambda_{3,4} = -9.21 \times 10^{-8} \pm 1.58 \times 10^{-6}i$ $\lambda_{5,6} = 0.27 \times 10^{-8} \pm 2.02 \times 10^{-7}i$
Interval \mathcal{T}_1 mode initial conditions	$\delta\mathbf{oe}_0 = [-0.001, 0.039, 0.0007, 0.015, 0.016, -0.002]$
Interval \mathcal{T}_2 eigenvalues	$\lambda_{1,2} = 8.21 \times 10^{-8} \pm 1.57 \times 10^{-6}i$, $\lambda_{3,4} = -8.24 \times 10^{-8} \pm 1.57 \times 10^{-6}i$ $\lambda_{5,6} = 0.66 \times 10^{-8} \pm 6.69 \times 10^{-7}i$
Interval \mathcal{T}_2 mode initial conditions	$\delta\mathbf{oe}_0 = [-0.001, 0.039, -0.0004, 0.014, 0.016, -0.003]$
Interval \mathcal{T}_3 eigenvalues	$\lambda_{1,2} = 7.46 \times 10^{-8} \pm 1.56 \times 10^{-6}i$, $\lambda_{3,4} = -7.46 \times 10^{-8} \pm 1.56 \times 10^{-6}i$ $\lambda_{5,6} = 0.99 \times 10^{-8} \pm 8.18 \times 10^{-7}i$
Interval \mathcal{T}_3 mode initial conditions	$\delta\mathbf{oe}_0 = [-0.001, 0.037, -0.0017, 0.014, 0.018, -0.005]$



(a) Eigenvalues for Three Intervals



(b) Select Modal Motion, Interval 1, 12 Orbits

Figure 7.7: Modal Results for Formations in $\Gamma = 3$ Terminator Orbit

would serve as the guidance solution for the formation to follow. Multiple close-proximity spacecraft could safely occupy modal structures similar to the type depicted in Figure 7.7(b), either through a phasing difference or by targeting different scalings of the motion, since the structure is nearly scale-invariant in the linear regime of orbit element differences. This would enable close-proximity relative motion of many spacecraft despite the highly complex orbital dynamics. However, the trajectories eventually come close to the chief, so before that time the other spacecraft would have to reconfigure and target a new modal motion.

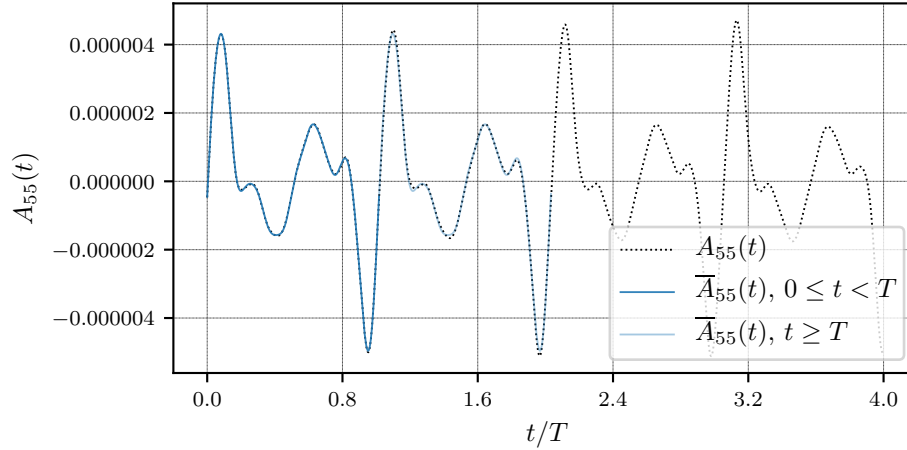


Figure 7.8: Select Component of Plant Matrix, $\Gamma = 3$, $[\bar{A}(t)]$ Computed from Interval \mathcal{I}_1

7.3 Relative Motion Dynamics and Control Using the Fundamental Solution Constants

This section explores the use of the fundamental solution constants as state variables for satellite relative motion. The fundamental modes can be computed for a given Keplerian or non-Keplerian problem, then the influence of perturbations and/or control will cause the relative motion to deviate from a linear sum of constant scalings of the fundamental relative motion modes. Despite this, the modes can still be used to describe the motion, and the modal constants will vary over time in that case.

7.3.1 The Modal Constants as State Variables

The Keplerian case will be used to facilitate this discussion, but the findings of this section apply for any modal decomposition. For the Keplerian problem, any uncontrolled close-proximity relative motion $\mathbf{x}(t)$ can be expressed as a *constant* weighted sum of the fundamental Keplerian modal motions. In the event that the orbital dynamics are perturbed, or control is active, the general behavior can still be represented by a time-varying weighted sum of the modal motions:

$$\dot{\mathbf{x}} = \mathbf{f}(\mathbf{x}, \mathbf{u}, t) \quad (7.44a)$$

$$\mathbf{x}(t) = [\Psi(t)]\mathbf{c}(t) \quad (7.44b)$$

where the first equation gives the general true nonlinear dynamics, and $\mathbf{c}(t)$ is made to vary such that these dynamics are satisfied. The vector of constants is allowed to vary in time as $\mathbf{c}(t)$ such that any motion $\mathbf{x}(t)$ can be represented. This is enabled by the following osculating condition:

$$\dot{\mathbf{x}}(t) = \frac{\partial \mathbf{x}}{\partial t} + \frac{\partial \mathbf{x}}{\partial \mathbf{c}} \dot{\mathbf{c}} = \mathbf{f}(\mathbf{x}, \mathbf{u}, t) \quad (7.45a)$$

$$\frac{\partial \mathbf{x}}{\partial t} = [A(\boldsymbol{\alpha}^*, t)]\mathbf{x} \quad (7.45b)$$

where $[A(\boldsymbol{\alpha}^*, t)]$ is the plant matrix for the original linearized dynamics used to compute the fundamental modal solutions $[\Psi(t)]$. The following dynamics satisfy the osculating condition:

$$\dot{\mathbf{c}} = [\Psi(t)]^{-1} (\mathbf{f}(\mathbf{x}, \mathbf{u}, t) - [A(\boldsymbol{\alpha}^*, t)]\mathbf{x}) \quad (7.46)$$

Assuming that $\mathbf{x}(t)$ remains in the linear regime, Eq. (7.47) reduces to linear dynamics in \mathbf{c} :

$$\dot{\mathbf{c}} = [\Psi(t)]^{-1} \left([A(t)] - [A^*(t)] \right) [\Psi(t)]\mathbf{c} + [\Psi(t)]^{-1} [B_{\mathbf{x}}]\mathbf{u} \quad (7.47)$$

where $[B_{\mathbf{x}}] = [0_{3 \times 3} \ I_{3 \times 3}]^T$ if \mathbf{x} is in Cartesian coordinates, and $[A(t)]$ is the plant matrix for linearization about the true (deviated) chief orbit. Note in the case that the orbital dynamics are unchanged, Eq. (7.47) obtains a form where \mathbf{c} is only influenced by control:

$$\dot{\mathbf{c}} = [\Psi(t)]^{-1} [B_{\mathbf{x}}]\mathbf{u} \quad (7.48)$$

Because \mathbf{c} has no linearized plant matrix, it is possible in this case to design control to track a desired natural reference trajectory $\mathbf{x}_r(t)$ using a regulation controller in \mathbf{c} space, because the dynamics of the error $\delta \mathbf{c} = \mathbf{c} - \mathbf{c}_r$ are of the same form as Eq. (7.48).

In the case that the true orbit is weakly perturbed in comparison to the orbit used to develop the modal decomposition, one may write the true plant matrix in terms of the nominal plus a small deviation:

$$[A(t)] \approx [A^*(t)] + \varepsilon [\delta \tilde{A}(t)] \quad (7.49)$$

where $|\varepsilon| \ll 1$ is a small parameter. In this case, Eq. (7.47) is rewritten:

$$\begin{aligned} \dot{\mathbf{c}} &= \varepsilon [\Psi(t)]^{-1} [\delta \tilde{A}(t)] [\Psi(t)]\mathbf{c} + [\Psi(t)]^{-1} [B_{\mathbf{x}}]\mathbf{u} \\ &\equiv \varepsilon [\Omega(t)]\mathbf{c} + [B_{\mathbf{c}}(t)]\mathbf{u} \end{aligned} \quad (7.50)$$

Eq. (7.50) is interesting because as the relative state is written as $\mathbf{x}(t) = [\Psi(t)]\mathbf{c}(t)$, the perturbed close-proximity dynamics of relative motion can be factored into a traditional slow-fast dynamical system:

$$[\dot{\Psi}] = [A^*(t)]\Psi \quad (7.51a)$$

$$\dot{\mathbf{c}} = \varepsilon[\Omega(t)]\mathbf{c} + [B_{\mathbf{c}}(t)]\mathbf{u} \quad (7.51b)$$

where from Eq. (7.50), the matrices $[\Omega]$ and $[B_{\mathbf{c}}]$ are also functions of the modal solutions, and the equations change from LTV to autonomous nonlinear equations if one adds t as a fast variable, with dynamics $\dot{t} = 1$. The “slowness” of the dynamics in \mathbf{c} implies that for weakly perturbed cases, the state $\mathbf{c}(t)$ will change slowly from $\mathbf{c}(t_0)$ in comparison to how the $\psi_i(t)$ change from $\psi_i(t_0)$ and how $\mathbf{x}(t)$ changes from $\mathbf{x}(t_0)$. This allows interpretation of the evolving relative motion using the osculating modal constants, similarly to how the osculating orbital elements are used to study general perturbed satellite orbits.

7.3.2 Continuous Control Using the Fundamental Solution Constants

Consider the classical Linear Quadratic Tracking (LQT) problem in the dynamics of local coordinates, such as the Cartesian representation. Both the close-proximity controlled relative state $\mathbf{x}(t)$ and the reference state $\mathbf{x}_r(t)$ are solutions of Eq. (7.52):

$$\dot{\mathbf{x}} = [A(t)]\mathbf{x} + [B_{\mathbf{x}}]\mathbf{u} \quad (7.52)$$

Consider the case that the dynamics are Keplerian and the desired trajectory $\mathbf{x}_r(t)$ is a natural trajectory, thus $\mathbf{u}_r = \mathbf{0}$. The cost function for LQT is given below, along with the optimal control $\mathbf{u}(t)$ in terms of time-varying gain $[K(t)]$ and co-state $\mathbf{s}(t)$:

$$J = \frac{1}{2} (\mathbf{x}(t_f) - \mathbf{x}_r(t_f))^\top [S] (\mathbf{x}(t_f) - \mathbf{x}_r(t_f)) + \frac{1}{2} \int_{t_0}^{t_f} \left((\mathbf{x}(t) - \mathbf{x}_r(t))^\top [Q] (\mathbf{x}(t) - \mathbf{x}_r(t)) + \mathbf{u}^\top [R] \mathbf{u} \right) dt \quad (7.53)$$

$$\mathbf{u}(t) = -[R]^{-1}[B]^\top [K]\mathbf{x}(t) - [R]^{-1}[B]^\top \mathbf{s}(t) \quad (7.54)$$

$$[\dot{K}] = -[K][A] + [K][B][R]^{-1}[B]^\top[K] - [Q] - [A]^\top[K], \quad [K(t_f)] = [S] \quad (7.55)$$

$$\dot{\mathbf{s}} = -\left([A]^\top - [K][B][R]^{-1}[B]^\top\right)\mathbf{s} + [Q]\mathbf{x}_r, \quad \mathbf{s}(t_f) = -[S]\mathbf{x}_r(t_f) \quad (7.56)$$

Thus to execute the tracking control, the 6×6 matrix $[K]$ must first be propagated backwards via the Riccati equation, Eq. (7.55) (requiring simultaneous back-propagation of the chief orbit and computation of the plant matrix $[A]$), and the 6-dimensional co-state $\mathbf{s}(t)$ must also be back-propagated via Eq. (7.56).

Consider instead that the fundamental solution constants \mathbf{c} are used as the state representation, and the desired trajectory to track is natural, thus $\mathbf{u}_r = \mathbf{0}$ and $\mathbf{c}_r(t) = \mathbf{c}_r(t_0)$. The state error is $\delta\mathbf{c} = \mathbf{c} - \mathbf{c}_r$ with the following simple dynamics, assuming that the chief orbit is unperturbed:

$$\delta\dot{\mathbf{c}} = [B_c(t)]\mathbf{u} \quad (7.57)$$

Furthermore, the LQT problem in \mathbf{x} space reduces to the Linear Quadratic Regulator (LQR) problem in \mathbf{c} space, with cost function, optimal control, and simplified Riccati equation below:

$$\tilde{J} = \frac{1}{2}\delta\mathbf{c}(t_f)^\top[S]\delta\mathbf{c}(t_f) + \frac{1}{2}\int_{t_0}^{t_f} \left(\delta\mathbf{c}(t)^\top[Q]\delta\mathbf{c}(t) + \mathbf{u}^\top[R]\mathbf{u}\right)dt \quad (7.58)$$

$$\mathbf{u}(t) = -[R]^{-1}[B_c]^\top[K]\delta\mathbf{c}(t) \quad (7.59)$$

$$[\dot{K}] = [K][B_c(t)][R]^{-1}[B_c(t)]^\top[K] - [Q], \quad [K(t_f)] = [S] \quad (7.60)$$

With this formulation, the controlled $\mathbf{x}(t)$ will track natural trajectory $\mathbf{x}_r(t)$ through control in \mathbf{c} space – where there is no need to back-propagate any co-state dynamics, and the Riccati equation is also greatly simplified by the absence of an $[A]$ matrix. However, a complication is that the choice of satisfactory gains is not as straightforward in \mathbf{c} space as it is in \mathbf{x} space.

7.3.3 Impulsive Control Using the Fundamental Solution Constants

Instead of continuous control strategies, the relative motion parameterization in terms of fundamental solution constants is particularly well-suited for impulsive maneuver-based control

strategies. Returning to Eq. (7.51), in the absence of disturbances, $[\Omega(t)] = [0_{6 \times 6}]$, and the solution for \mathbf{c} can be expressed solely in terms of a series of impulsive maneuvers $\Delta \mathbf{v}_i = \Delta \mathbf{v}(t_i)$:

$$\mathbf{c} = \mathbf{c}_0 + \sum_{i=1}^N [B_c(t_i)] \Delta \mathbf{v}_i \quad (7.61)$$

Consider the optimal control problem of minimizing the total delta-V subject to the dynamics in Eq. (7.68):

$$J = \sum_{i=1}^N \Delta v_i \quad (7.62)$$

where $\Delta v_i = \|\Delta \mathbf{v}(t_i)\|$. Also, let $\Delta \mathbf{c} = \mathbf{c} - \mathbf{c}_0$. Some useful results are borrowed from Reference 52. First, consider the sets of control inputs $\mathbf{u}(t) \in \mathcal{U}$ and the reachable variations $\Delta \mathbf{c} \in \mathcal{C}$ with cost less than or equal to J :

$$\mathcal{U}(J) = \left\{ \mathbf{u}(t) : \mathbf{u}(t) = \sum_{i=1}^N \Delta \mathbf{v}_i, \sum_{i=1}^N \Delta v_i \leq J \right\} \quad (7.63)$$

$$\mathcal{C}(J) = \left\{ \Delta \mathbf{c} : \Delta \mathbf{c} = \sum_{i=1}^N [B_c(t_i)] \Delta \mathbf{v}_i, \sum_{i=1}^N \Delta v_i \leq J \right\} \quad (7.64)$$

As discussed in Reference 52, the set \mathcal{C} is compact and convex, and scales linearly with J . Furthermore, for a minimum cost J_{\min} to achieve a desired variation, the desired difference in constants $\Delta \mathbf{c}^* = \mathbf{c}^* - \mathbf{c}_0$ lies on the boundary of the set. The minimum delta-V to reach this goal in N maneuvers can be obtained in terms of the unit vector $\hat{\boldsymbol{\eta}}$, which is normal to the boundary of \mathcal{C} at $\Delta \mathbf{c}^*$:

$$J_{\min} = \frac{\hat{\boldsymbol{\eta}}^\top \Delta \mathbf{c}^*}{\max_{t_i \in [t_0, t_f]} \|\hat{\boldsymbol{\eta}}^\top [B_c(t_i)]\|} \quad (7.65)$$

Reference 52 described a means of numerically obtaining $\hat{\boldsymbol{\eta}}$ using a convex solver, then linearly solving for an optimal sequence of $N \leq n$ impulsive maneuvers for a dynamic system with n state variables. In general, for the formation flying problem, a minimum of two maneuvers are required. For the unperturbed problem, only control action induces movement in \mathcal{C} – the flow of the integrable dynamics has no effect. This property, combined with the compactness and convexity of \mathcal{C} , allows for powerful geometric interpretations for the fuel-optimal impulsive maneuver problem. However, any significant perturbations will play a disruptive role, inducing drifts in $\Delta \mathbf{c}$ that would need to be accounted for.

The algorithm for solving for an optimal maneuver sequence is given below for the unperturbed problem [52]:

- (1) Solve the following second-order cone program for the optimal value $\boldsymbol{\eta}^*$:

$$\begin{aligned} & \text{maximize} && \tilde{J} = \boldsymbol{\eta}^\top \Delta \mathbf{c}^* \\ & \text{subject to} && \|[B_c](t)^\top \boldsymbol{\eta}\| \leq 1 \text{ for } t \in [t_0, \dots, t_j, \dots, t_f] \end{aligned} \quad (7.66)$$

where $[t_0, \dots, t_j, \dots, t_f] \in \mathbb{R}_{\geq 0}^k$ is a chosen discretization of the control interval.

- (2) Determine all times $t_i \in [t_0, \dots, t_j, \dots, t_f]$ for which $||[B_c(t)^\top \boldsymbol{\eta}^*] - 1| < \epsilon$ for some tolerance $\epsilon \ll 1$. This will yield an N -maneuver sequence, with $N \ll k$, for which the i^{th} impulse is directed along the unit vector:

$$\hat{\mathbf{u}}_i = [B_c](t)^\top \boldsymbol{\eta}^* \quad (7.67)$$

- (3) The set of delta-V maneuvers $\{\Delta v_i\}$ needs to satisfy the linear system of equations:

$$\sum_{i=1}^N [B_c(t_i)] \hat{\mathbf{u}}_i \cdot \Delta v_i = \Delta \mathbf{c}^* \quad (7.68)$$

A traditional relative motion control approach is to use a factorization of the STM to uniquely solve for a 2-burn delta-V sequence given some specified initial and final times. This could also be used, with the desired target relative orbit efficiently identified in \mathbf{c} space. This \mathbf{c}^* would then be mapped to \mathbf{x}^* via the fundamental solutions. To control to a future target condition $\mathbf{x} = [\Delta \mathbf{r}^\top, \Delta \mathbf{r}'^\top]^\top$ at time t from a maneuver initial condition $\mathbf{x}_m = [\Delta \mathbf{r}_m^\top, \Delta \mathbf{r}'_m^\top]^\top$ at time t_m , the following factoring of the state transition matrix is used:

$$[\Phi(t, t_m)] = \begin{bmatrix} \Phi_{rr}(t, t_m) & \Phi_{rv}(t, t_m) \\ \Phi_{vr}(t, t_m) & \Phi_{vv}(t, t_m) \end{bmatrix} \quad (7.69)$$

from which the final state may be expressed in terms of the state at the initial time:

$$\Delta \mathbf{r} = [\Phi_{rr}(t, t_m)] \Delta \mathbf{r}_m + [\Phi_{rv}(t, t_m)] \Delta \mathbf{r}'_m \quad (7.70)$$

$$\Delta \mathbf{v} = [\Phi_{vr}(t, t_m)] \Delta \mathbf{r}_m + [\Phi_{vv}(t, t_m)] \Delta \mathbf{r}'_m \quad (7.71)$$

Using the desired position $\Delta \mathbf{r}^*$ and velocity $\Delta \mathbf{r}'^*$ in Eqs. (7.70) and (7.71), the two needed delta-Vs δ_1 and δ_2 can be uniquely determined:

$$\delta_1 = [\Phi_{rv}(t, t_m)]^{-1} (\Delta \mathbf{r}^* - [\Phi_{rr}(t, t_m)] \Delta \mathbf{r}_m) - \Delta \mathbf{r}'_m^- \quad (7.72)$$

$$\delta_2 = \Delta \mathbf{r}'^* - ([\Phi_{vr}(t, t_m)] \Delta \mathbf{r}_m + [\Phi_{vv}(t, t_m)] \Delta \mathbf{r}'_m^+) \quad (7.73)$$

where $\Delta \mathbf{r}'_m^-$ is the velocity at time t_m before the first delta-V, and $\Delta \mathbf{r}'_m^+ = \Delta \mathbf{r}'_m^- + \delta_1$. By necessity, a two-burn solution using either approach will obtain the same answer. Later in this section, the optimal maneuver approach from Reference 52 is tested with the modal constant approach via numerical simulation.

7.3.4 Using the Modal Constants to Explore Relative Orbits

Consider the example of a bounded relative orbit in the vicinity of an eccentric chief orbit, given by the data listed in Table 7.4. Note that while $\delta a = 0$, the drift constant c_6 does not exactly equal zero. This is because $\delta a = 0$ is the nonlinear no-drift requirement, and it is not perfectly captured by the linearized no-drift condition. This is a well-known property of linearized solutions – consider for example that the linearized no-drift condition for the CW system is $\dot{y} + 2nx = 0$, which only linearly approximates $\delta a = 0$. From the data in Table 7.4, the resulting Keplerian relative orbit is depicted in 3D in Figure 7.9, and the planar projection appears as a black closed curve in Figures 7.10 – 7.12.

Table 7.4: Simulation Parameters – Final Keplerian Modal Example

Parameter	Value
Chief Orbit Elements	$\mathbf{oe} = (a, e, i, \Omega, \omega, f_0) = (8600 \text{ km}, 0.2, 25^\circ, 0^\circ, 270.001^\circ, 90^\circ)$
Deputy Relative Orbit	$\delta \mathbf{oe} = \mathbf{oe}_d - \mathbf{oe}_c = (0.0, 0.0002, 0.02^\circ, 0^\circ, 0^\circ, 0.003^\circ)$
Modal Constants	$\mathbf{c} = (4.3, 0.0, 7.07, 3.60, 3.61, -0.014)$

Figure 7.10 shows the modal decomposition of the in-plane component of the relative motion using the modes developed in Cartesian coordinates. Figure 7.11 shows the modal decomposition of the in-plane motion using the modes developed in spherical coordinates and linearly mapped to

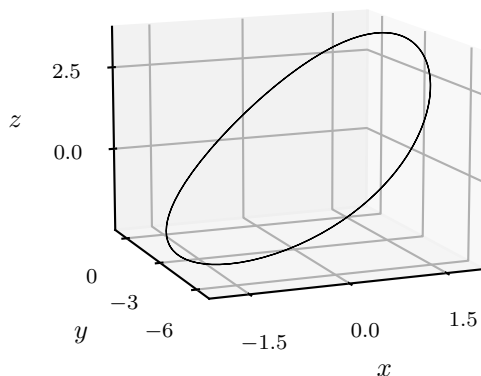


Figure 7.9: Example Relative Orbit

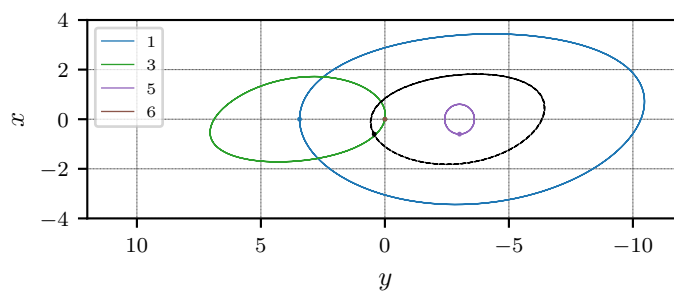


Figure 7.10: Cartesian Planar Modes

Cartesian coordinates. For both plots, the initial point of the orbiter and the initial point in each mode are given by dots. Because the relative orbit is non-drifting, the drift mode contribution is zero – thus the mode appears as a non-moving point at the origin. For both modal decompositions, the modes shown sum linearly to reproduce the observed relative motion in black. In other words, $\mathbf{x}_{2D}(t) = c_1\boldsymbol{\psi}_{2D,1} + c_3\boldsymbol{\psi}_{2D,3} + c_5\boldsymbol{\psi}_{2D,5}$. Recall that the out-of-plane modes (2 and 4) have no in-plane component – they exist only in z , and are completely decoupled from the in-plane modes.

Comparing Figures 7.10 and 7.11, the spherical coordinate-based modal decomposition reproduces the true relative orbit in a much more straightforward and intuitive manner than the Cartesian coordinate-based counterpart. The motion is represented as a sum of a rectilinear along-track motion (mode 1), a distorted elliptical motion (mode 3), and the offset circular trajectory

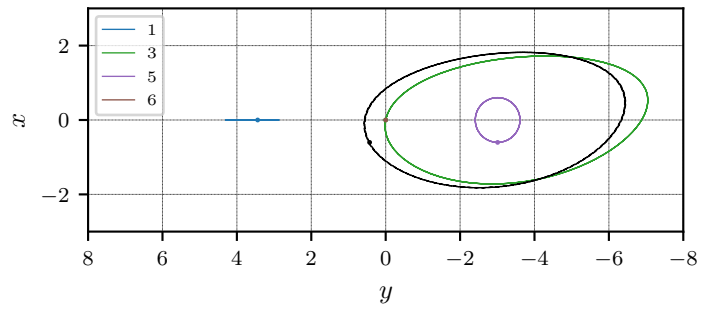
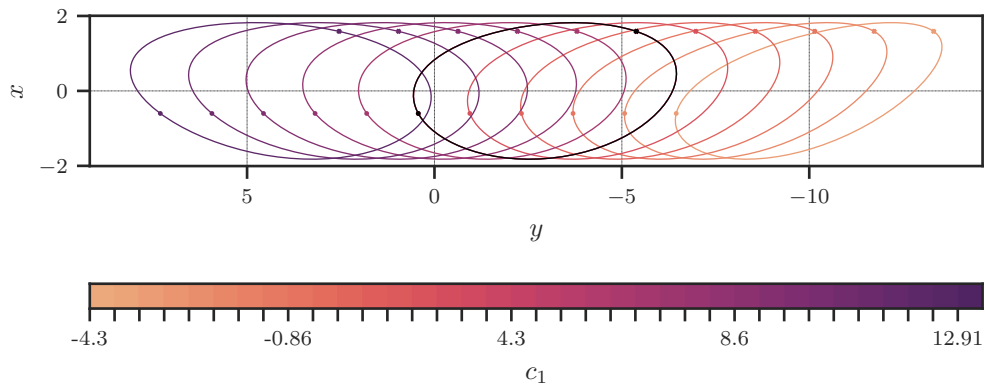
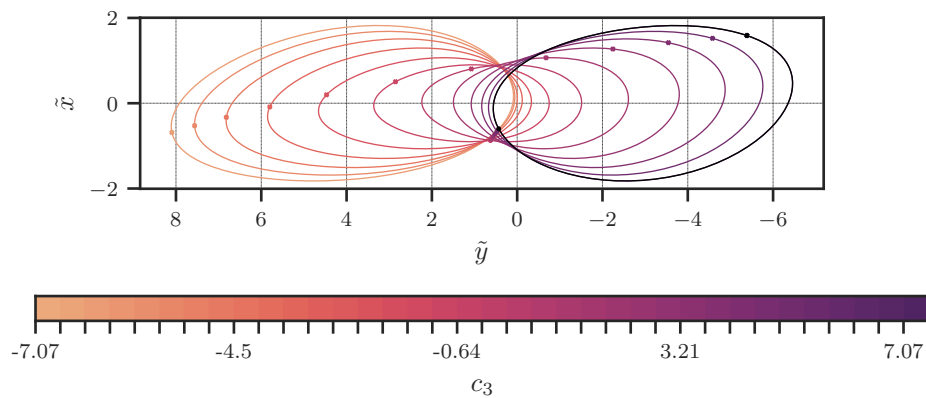


Figure 7.11: Spherical Planar Modes

(mode 5). This is the simplest geometric representation possible for general Keplerian relative motion, with two of the three bounded in-plane motions given as basic shapes.

Figure 7.12: Variations of the Planar Relative Motion with c_1 Figure 7.13: Variations of the Planar Relative Motion with c_3 (Re-scaled)

Because the fundamental modal motions only need to be computed once, variations in the

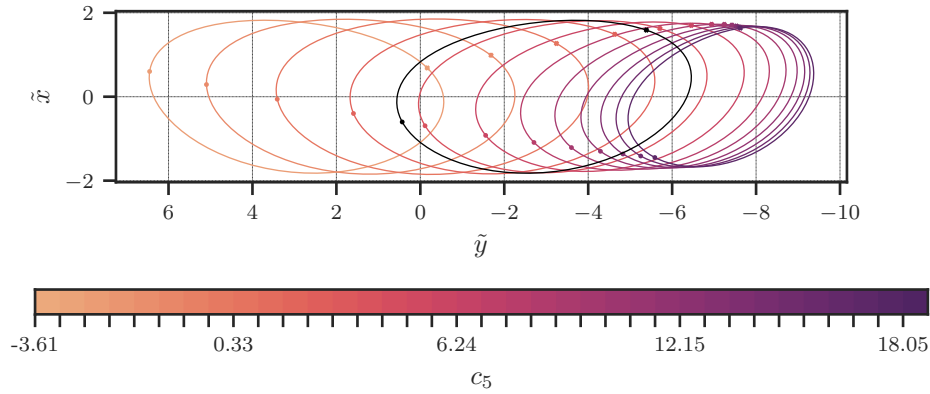


Figure 7.14: Variations of the Planar Relative Motion with c_5 (Re-scaled)

relative motion due to changes in the modal constants can be explored with a minimal amount of numerical computation. For example, exploring a range of variations in c_1 , Figure 7.12 is produced. The initial ($t = t_0$) and mid-orbit ($t = t_0 + \frac{T}{2}$) points are denoted with a “•” and with an “x”, respectively, and the original relative orbit is given in black. The effect of isolated changes in c_1 is to shift the motion further along in the along-track direction as c_1 is increased, with the additional effect of rotating and distorting the planar component of the relative orbit. Note that the x scale of the relative orbit is not affected at all. Similar figures can be generated to isolate the effects of changes in c_3 and c_5 on the relative orbit shape and location. However, changing the scales of c_3 and c_5 also change the size of the relative orbit. To display the characteristic changes in relative orbits with these parameters clearly on individual plots, the relative orbits are computed across desired ranges for these parameters, as was done for Figure 7.12, then the orbits are re-scaled such that $\|\mathbf{c}_{\text{new}}\| = \|\mathbf{c}_{\text{old}}\|$ to preserve the original relative orbit scale. The resulting plots are given in Figure 7.13 for variations in c_3 and Figure 7.14 for variations in c_5 .

In Figure 7.13, as c_3 is decreased from its original value of 7.07, the re-scaled relative orbit shifts from the original relative orbit (given in black) to more centered and symmetric relative motion in the middle of the range (near $c_3 = 0$), to an essentially reversed version of the original for $c_3 < 0$. Note that there would also be accompanying relative orbit scale changes with changing value of c_3 , but the re-scaled orbit plot sacrifices this information to better show the variations

in the relative orbit geometry. Figure 7.14 shows the variations in re-scaled relative orbit due to changes in c_5 , with an original value of $c_5 = 3.61$. The negative value is essentially flipped about the x -axis, and as the value is increased, the re-scaled relative orbits gradually circularize as the contribution of the circular mode 5 is increased in relative scale.

Figures 7.12 – 7.14 show that the parameter space for the in-plane component of bounded relative orbits is only three-dimensional. The two out-of-plane modes add an additional two dimensions – completely decoupled from the in-plane design. From the perspective of the modal constants, it is conceptually easy and numerically efficient for the astrodynamist to explore all possible useful types of relative motion that can exist. In this manner, the vector of modal constants \mathbf{c} serves as the design space, and also uniquely determines the relative motion state when combined with a given time since epoch $t - t_0$. As discussed earlier, it is also possible to compute how the constants vary under the influence of non-Keplerian dynamics. With such a study, the influence of perturbations on relative motion can be viewed as an evolving alteration of the relative scales of the constituent Keplerian relative motion modes that form the basis for the unperturbed problem.

7.3.5 Effects of Perturbations – Modeling with J_2

To demonstrate the behavior of the Keplerian modal constants under the influence of perturbations, consider the ubiquitous example of J_2 -perturbed relative motion, which highly relevant for Earth orbits. To compute the perturbed dynamics of the Keplerian modal constants, Eq. (7.47) is used with Eqs. (6.21) – (6.23) providing the linearized perturbed relative motion dynamics, evaluated using the following equations for the acceleration, differential acceleration, and jerk induced by the J_2 -perturbed Keplerian dynamics:

$$\ddot{\mathbf{r}} = -\frac{\mu}{r^3}\mathbf{r} - \frac{3\mu J_2 R^2}{2r^4} \left(\left(1 - 5(\hat{\mathbf{r}} \cdot \hat{\mathbf{K}})^2\right) \hat{\mathbf{r}} + 2(\hat{\mathbf{r}} \cdot \hat{\mathbf{K}}) \hat{\mathbf{K}} \right) \quad (7.74)$$

$$\begin{aligned} \nabla_{\mathbf{r}} \ddot{\mathbf{r}} = & -\frac{3\mu J_2 R^2}{2r^5} \left[\left(1 - 5(\hat{\mathbf{K}} \cdot \hat{\mathbf{r}})^2\right) \mathbf{I} + 2\hat{\mathbf{K}}\hat{\mathbf{K}}^\top + 5\left(7(\hat{\mathbf{K}} \cdot \hat{\mathbf{r}})^2 - 1\right) \hat{\mathbf{r}}\hat{\mathbf{r}}^\top \right. \\ & \left. - 10(\hat{\mathbf{K}} \cdot \hat{\mathbf{r}}) \left(\hat{\mathbf{K}}\hat{\mathbf{r}}^\top + \hat{\mathbf{r}}\hat{\mathbf{K}}^\top\right) \right] \end{aligned} \quad (7.75)$$

$$\ddot{\mathbf{r}} = (\nabla_{\mathbf{r}} \ddot{\mathbf{r}}) \dot{\mathbf{r}} \quad (7.76)$$

where $\hat{\mathbf{K}}$ denotes the polar axis unit vector, R is the equatorial radius, \mathbf{I} is the 3×3 identity matrix, and $\hat{\mathbf{r}} = \mathbf{r}/r$. The dynamics given by Eq. (7.47) are integrated in parallel with the J_2 -perturbed chief orbit.

The same initial chief orbit and deputy relative orbit conditions from Table 7.4 are selected, but with Earth's J_2 perturbation active. As a result of this perturbation, variations are induced in the Keplerian modal constants. Figure 7.15 shows the result of integrating the dynamics in \mathbf{c} for 3 unperturbed chief orbit periods. The effect of J_2 is limited to small oscillations in the modal constants, but these oscillations grow over time, which is an unfortunate but unavoidable property. For the case of J_2 , it seems that the modified orbital frequency due to the perturbation requires that the secular drift mode (mode 6) be used to fully describe the perturbed state. This is because all other modes are periodic on the interval $[0, T]$, and variations in their sums would be unable to describe a relative orbit on the shortened interval $[0, T - \Delta T_{J_2}]$. Additionally, the J_2 perturbation induces slow long-term drift in the relative orbit. The drift mode is used to describe the perturbed solution, and it grows and shifts over time, so variations in other modes (primarily mode 5) are induced to compensate for these variations. This yields the opposing behaviors of c_5 and c_6 seen in Figure 7.15. Despite these growing oscillations, the long-term drift in c_5 and c_6 and in the other c_i parameters is quite slow. This suggests that the averaged dynamics in \mathbf{c} could be a useful lens for studying relative motion in the perturbed problem, especially for even zonal harmonics like J_2 , but such a study is not explored here. Lastly, the growing oscillations are not a major problem for modeling, because the fundamental solutions can always be re-initialized as needed by re-defining the epoch time, i.e. $t_{0,\text{new}} \triangleq t$.

7.3.6 Impulsive Maneuver Control in the Keplerian Relative Motion Problem

To demonstrate unperturbed control using the Keplerian modal constants, consider the problem of changing from the initial relative motion dictated by the data in Table 7.4 to a new planar non-drifting relative orbit parameterized by $c_5 = 3.61$. In this test case, the contribution of all

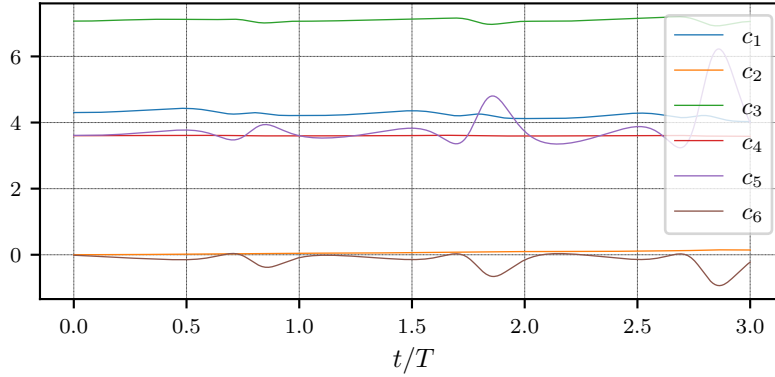


Figure 7.15: Variation of Modal Constants with J_2

modes except mode 6 in the initial relative motion are removed. To implement this test, the previously discussed impulsive maneuver-based control solution strategy is implemented in Python using `cvxpy`.

In the first example, a two-burn maneuver achieves the desired relative orbit, with the first burn at $t = t_0 + 1590.6$ s with maneuver magnitude $\Delta v = 2.3$ m/s, and the second burn at $t = t_0 + 5567.1$ s with $\Delta v = 4.7$ m/s. To enforce that only two maneuvers are performed, the control interval was discretized into just the initial and end times. As expected, both the convex optimization-based approach and the STM-based approach yield the same maneuvers. The resulting change in modal constant space and the relative position evolution are given in Figures 7.16 and 7.17, with vertical dotted lines indicating each maneuver. Figure 7.17 shows the sizable discontinuities in the velocity, particularly in the z component – indicating that the maneuver is not particularly efficient.

By contrast, allowing for more than two maneuvers and expanding the interval of control time, the multi-maneuver impulsive control strategy can achieve the same relative motion objectives but with a reduced delta-V. For a second example, time is discretized into 100 points on the interval $t_i \in [t_0 + 1590.6 \text{ s}, t_0 + 12724.7 \text{ s}]$. This increases the number of constraints given by Eq. (7.66) from 2 for the previous example to 100, but does not noticeably increase solver time. The resulting impulsive control solution consists of 5 maneuvers for a combined delta-V of only 2.7 m/s, compared to 7.0 m/s for the previous example. The changes in \mathbf{c} with each maneuver are plotted in Figure

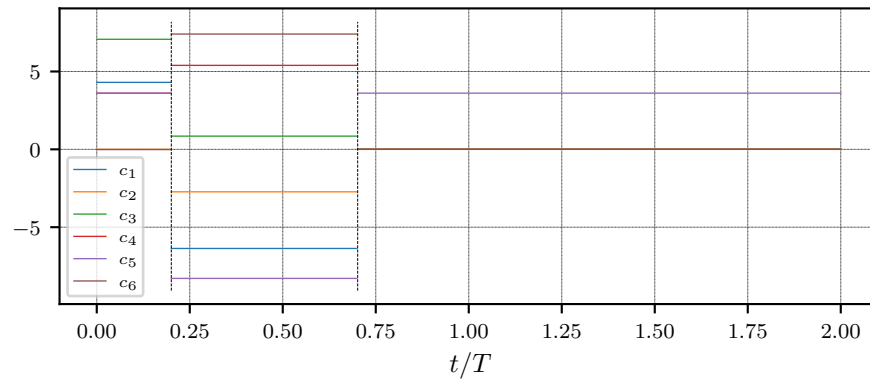


Figure 7.16: Two-Burn Maneuver, Modal Constants

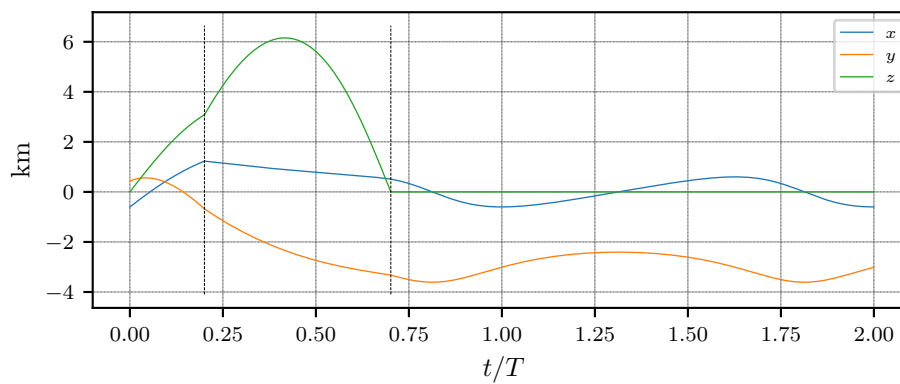


Figure 7.17: Two-Burn Maneuver, Local Cartesian Coordinates

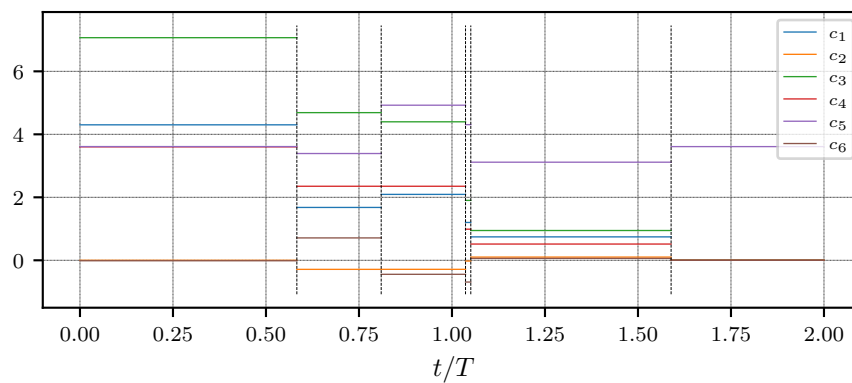


Figure 7.18: Five-Burn Maneuver, Modal Constants

7.18, with vertical dotted lines indicating each maneuver. The relative position components are plotted in Figure 7.19. In comparison to Figure 7.17, 7.19 shows a more gradual change in the

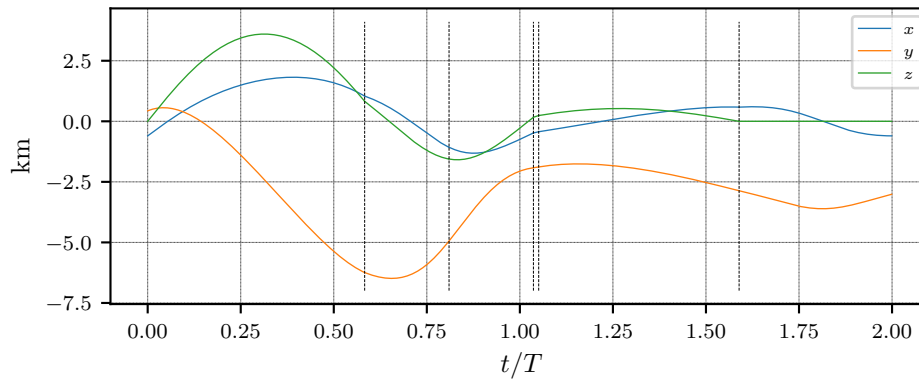


Figure 7.19: Five-Burn Maneuver, Local Cartesian Coordinates

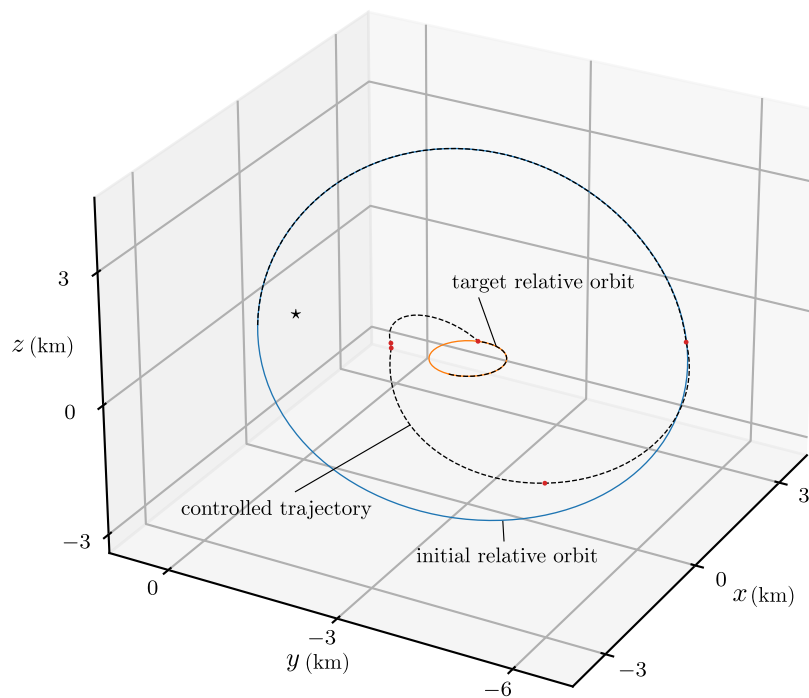


Figure 7.20: Relative Orbit Transfer Using Modal Constants

relative state to achieve the desired relative motion. Note that the last ~ 0.4 orbit periods of the simulation show the same behavior in \mathbf{c} and in \mathbf{x} for both examples, because they both target the same desired \mathbf{c}^* .

For the second controlled example, the initial, transfer, and final relative motions are shown in 3D in Figure 7.20. The initial relative orbit is the large blue closed curve, and the final relative orbit is the small orange planar circular trajectory. The transfer trajectory is given by the dashed

black line, and the maneuver points are indicated with red dots.

Control using the modal solution constants is highly convenient, due to both the straightforward geometric interpretation of the c_i parameters and the efficient means by which multi-maneuver impulsive control schedules can be obtained. This is demonstrated by the preceding simple examples with Keplerian dynamics. However, extending this control design to account for the effect of perturbations on \mathbf{c} is necessary for elegant flight implementation – particularly for long-duration control maneuver sequences. This is not explored, but mitigating the effects of perturbations in control design in \mathbf{c} space should be straightforward, because even in the perturbed relative motion case, the \mathbf{c} parameters do not lose their geometric meaning. This is highly convenient, and generally does not hold for most other perturbed integral representations. For example, for relative motion parameterizations using orbit element differences $\delta\mathbf{oe} = \mathbf{oe}_d - \mathbf{oe}_c$, the perturbations modify \mathbf{oe}_c , and as a result, the resulting exact local coordinate behavior mapped from a particular desired $\delta\mathbf{oe}$ changes over time.

7.4 Modal Decomposition and Modal Control in the Earth-Moon Three-Body Problem

7.4.1 The Circular Restricted Three Body Problem

7.4.1.1 Basics of the CR3BP

Here, the basics of the CR3BP are briefly reviewed. For a more in-depth review, see e.g. Ref. 79. The circular restricted three-body problem (CR3BP) is a normalized three-body problem using the following dimensionalization parameters m^* , l^* , t^* :

$$m^* = \tilde{M}_1 + \tilde{M}_2 \quad (7.77)$$

$$l^* = \tilde{R}_1 + \tilde{R}_2 \quad (7.78)$$

$$t^* = \left(\frac{(l^*)^3}{\tilde{G}m^*} \right)^{1/2} \quad (7.79)$$

where \tilde{M}_1 and \tilde{M}_2 are the masses of bodies 1 and 2, \tilde{R}_1 and \tilde{R}_2 are their distances from the origin. Via these parameters, one can convert the dimensional quantities into their nondimensional counterparts:

$$X = \frac{\tilde{X}}{l^*}, \quad Y = \frac{\tilde{Y}}{l^*}, \quad Z = \frac{\tilde{Z}}{l^*} \quad (7.80)$$

$$\tau = \frac{t}{t^*} \quad (7.81)$$

$$G = \frac{\tilde{G}m^*(t^*)^2}{(l^*)^3} = 1 \quad (7.82)$$

where \tilde{G} is the gravitational constant, t is the dimensional time, τ is the nondimensional time, and all quantities with a tilde are dimensional.

The mass ratio μ is the only special value appearing in the non-dimensional equations of motion:

$$\mu = \frac{\tilde{M}_2}{\tilde{M}_1 + \tilde{M}_2} \quad (7.83)$$

Lastly, note that when $l^* = a$ where a is the semimajor axis of the orbit between the two large bodies 1 and 2, the parameter t^* reduces to the following:

$$t^* = \frac{T}{2\pi} \quad (7.84)$$

where T is the period of the orbit between the two primary bodies. For reference, the equations of motion for the CR3BP and the Jacobi constant equation are provided below:

$$\ddot{x} = 2\dot{y} + x - \frac{(1-\mu)(x+\mu)}{r_1^3} - \frac{\mu(x-1+\mu)}{r_2^3} \quad (7.85a)$$

$$\ddot{y} = -2\dot{x} + y - \frac{(1-\mu)y}{r_1^3} - \frac{\mu y}{r_2^3} \quad (7.85b)$$

$$\ddot{z} = -\frac{(1-\mu)z}{r_1^3} - \frac{\mu z}{r_2^3} \quad (7.85c)$$

$$r_1 = \sqrt{(x+\mu)^2 + y^2 + z^2} \quad (7.86a)$$

$$r_2 = \sqrt{(x-1+\mu)^2 + y^2 + z^2} \quad (7.86b)$$

$$C = 2U^* - v^2 = (x^2 + y^2) + \frac{2(1-\mu)}{r_1} + \frac{2\mu}{r_2} - \dot{x}^2 - \dot{y}^2 - \dot{z}^2 \quad (7.87)$$

where $(\dot{}) = \frac{d}{dt}()$. The x , y , and z are the coordinates in a frame rotating with the two primary bodies (in the case of this work, the Earth and the moon), $z = 0$ defines the plane in which the primary bodies orbit, and x is the direction from the larger to smaller primary.

7.4.1.2 Periodic Orbits in the CR3BP

There are a variety of periodic orbits in the Earth-Moon CR3BP. These are generally found via shooting methods or collocation schemes, and families of periodic orbits are readily computed via continuation methods. These concepts are briefly reviewed here, and the orbits of interest for this work are numerically obtained.

To compute a general three-dimensional periodic orbit in the CR3BP, a single-shooting scheme will often suffice. An initial guess of the orbit is provided and iterated on. The implementation is built on the premise of generating a vector of free variables \mathbf{V} to be altered iteratively until a constraint vector function $\mathbf{F}(\mathbf{V}) = \mathbf{0}$ is satisfied. For the general 3D single-shooting case, the free variables are the initial condition for the trajectory $\mathbf{x}_0 = (x, y, z, \dot{x}, \dot{y}, \dot{z})^\top$ and the period of the orbit T – the length of time for which the trajectory is integrated. The constraint vector is that the final state and initial state match at time T (a periodicity condition). This is all restated below:

$$\mathbf{V} = \begin{pmatrix} \mathbf{x}_0 \\ T \end{pmatrix} \quad (7.88)$$

$$\mathbf{F}(\mathbf{V}) = \mathbf{x}_f - \mathbf{x}_0 \quad (7.89)$$

To solve these types of problems, assume that the initial guess is sufficiently close to a periodic orbit that a first-order expansion of the constraint condition approximately satisfies the desired value of the constraint vector \mathbf{V}_d :

$$\mathbf{F}(\mathbf{V}_d) \approx \mathbf{F}(\mathbf{V}_i) + \left. \frac{d\mathbf{F}(\mathbf{V})}{d\mathbf{V}} \right|_{\mathbf{V}_i} (\mathbf{V}_d - \mathbf{V}_i) \equiv \mathbf{F}(\mathbf{V}_i) + [G](\delta\mathbf{V}_i) \approx \mathbf{0} \quad (7.90)$$

Because this is only approximately true, successive iteration is needed in a Newton method ap-

proach. Simplifying and dropping the approximation notation, we obtain the linear system below:

$$[G](\delta \mathbf{V}_i) = -\mathbf{F}(\mathbf{V}_i) \quad (7.91)$$

The dimensions of $[G]$ matter greatly here. Let $\mathbf{F}(\mathbf{V}_i) \in \mathbb{R}^m$ and $\delta \mathbf{V}_i \in \mathbb{R}^n$. For the general 3D solver case, $m = 6$ and $n = 7$. Thus, $[G]$ is an $m \times n$ matrix (in the general 3D case, 6×7). If $m < n$ (as in the general 3D case), the system is underdetermined and infinitely many solutions for $\delta \mathbf{V}_i$ exist. The desired solution is the minimum-norm, which minimizes $\|\delta \mathbf{V}_i\|^2$ subject to the constraint that $[G](\delta \mathbf{V}_i) = -\mathbf{F}(\mathbf{V}_i)$. The solution is given by the right-inverse:

$$\delta \mathbf{V}_i = -[G]^\top \left([G][G]^\top \right)^{-1} \mathbf{F}(\mathbf{V}_i) \quad (7.92)$$

If $m = n$, the direct solution is given by the direct inverse:

$$\delta \mathbf{V}_i = -[G]^{-1} \mathbf{F}(\mathbf{V}_i) \quad (7.93)$$

Lastly, if $m > n$, the system is overdetermined and no unique solution exists. Minimizing the norm of the residual squared $\|[G](\delta \mathbf{V}_i) + \mathbf{F}(\mathbf{V}_i)\|^2$ is obtained via the left-inverse:

$$\delta \mathbf{V}_i = -\left([G]^\top [G] \right)^{-1} [G]^\top \mathbf{F}(\mathbf{V}_i) \quad (7.94)$$

In all cases, the update proceeds via the following equation:

$$\mathbf{V}_{i+1} = \mathbf{V}_i + \delta \mathbf{V}_i \quad (7.95)$$

By this method (using the underdetermined solution), the initial conditions for the periodic orbit \mathbf{x}_0 and the period T itself are successively updated via this equation, the updated trajectory is computed, the constraint vector is evaluated, and the Jacobian $[G]$ of the constraint function is evaluated, then a new update is done. This is done repeatedly until a norm constraint $\|\mathbf{F}(\mathbf{V}_i)\| < \varepsilon$ is satisfied, where ε should be sufficiently small that it corresponds to minimal discontinuity in $\mathbf{x}_f - \mathbf{x}_0$ and minimal error in the computed period T .

For the general 3D single-shooter method, the matrix $[G] = \left. \frac{d\mathbf{F}(\mathbf{V})}{d\mathbf{V}} \right|_{\mathbf{V}_i}$ is given below using Eqs. (7.88) and (7.89) along with the definition of the STM:

$$[G] = \left. \frac{d\mathbf{F}(\mathbf{V})}{d\mathbf{V}} \right|_{\mathbf{V}_i} = \left[\begin{array}{cc} \frac{d}{d\mathbf{x}_0} (\mathbf{x}_f - \mathbf{x}_0) & \left. \frac{d\mathbf{x}_f}{dt} \right|_{t=T} \end{array} \right] = \left[\begin{array}{cc} \Phi(t_0 + T, t_0) - I_{6 \times 6} & \dot{\mathbf{x}}_f \end{array} \right] \quad (7.96)$$

where $\dot{\mathbf{x}}_f$ is the augmented final velocity and acceleration at time $t = T$, because the derivative of the state at T with respect to the trajectory duration T will simply be the state rate at time T .

Once a periodic orbit is found, the other periodic orbits in the same family can be obtained by a continuation scheme. For this work, pseudo arc-length continuation is used to compute a family of Earth-Moon L_2 halo orbits. The pseudo-arc length method is based on the idea that if the constraint Jacobian $[G]$ has a one-dimensional null space, there is a direction in which changes in the free variable vector \mathbf{V} still satisfy $\mathbf{F}(\mathbf{V}) = \mathbf{0}$, thus the distinct orbits defined by those other choices of free variables are also periodic. In other words, $\dim(\ker(G)) = 1$ and there exists a unit vector $\hat{\mathbf{n}}^* \in \ker(G)$ which informs the direction in \mathbf{V} space for the family:

$$\mathbf{V} \approx \mathbf{V}^* + \Delta s \hat{\mathbf{n}}^* \quad (7.97)$$

Because it is only a linearization, Eq. (7.97) is only approximately true, and only valid at all for sufficiently small Δs . Nonetheless, it informs an update equation yielding a good initial guess for the next orbit after one periodic orbit is computed:

$$\mathbf{V}_0 = \mathbf{V}^* + \Delta s \hat{\mathbf{n}}^* \quad (7.98)$$

With this initial guess, a new pseudo arc-length constraint is given by $(\mathbf{V} - \mathbf{V}^*) \cdot \hat{\mathbf{n}}^* = \Delta s$. Thus, a new constraint vector is constructed for iterating on the initial guess \mathbf{V}_0 in pseudo-arc length continuation for the general 3D solver:

$$\tilde{\mathbf{F}}(\mathbf{V}_i) = \begin{pmatrix} \mathbf{x}_f - \mathbf{x}_0 \\ (\mathbf{V}_i - \mathbf{V}^*)^\top \hat{\mathbf{n}}^* - \Delta s \end{pmatrix} \quad (7.99)$$

The constraint Jacobian is given for the general 3D solver below:

$$[\tilde{G}] = \left. \frac{d\tilde{\mathbf{F}}(\mathbf{V})}{d\mathbf{V}} \right|_{\mathbf{V}_i} = \begin{bmatrix} \Phi(t_0 + T, t_0) - I_{6 \times 6} & \dot{\mathbf{x}}_f \\ \hat{\mathbf{n}}^{*\top} & \end{bmatrix} \quad (7.100)$$

This matrix is 7×7 so the update $\delta \mathbf{V}_i$ on \mathbf{V}_i should be obtained by direct inversion, Eq. (7.93). The iteration is applied until the next orbit is found. At that point, the general 3D constraint Jacobian $[G]$ given by Eq. (7.96) is evaluated on the satisfactory solution, yielding a new null space vector $\hat{\mathbf{n}}^*$ and re-initializing the iterative solver process just described.

7.4.1.3 The L_2 Halo Orbits

This work focuses on satellite relative motion in the vicinity of northern L_2 halo orbits – including computation of the relative motion modes, and use of the modes for control. The family of northern halo orbits is computed, and the result is given in Figure 7.21.

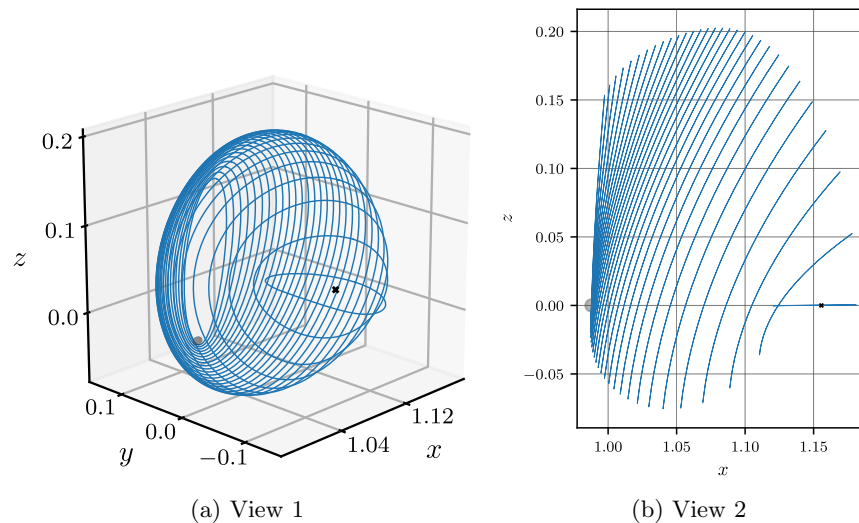


Figure 7.21: L_2 Northern Halo Orbits

Some of the halo orbits are *stable*, i.e. no small deviations from the periodic orbit result in unbounded departures in the linearized dynamics. Stability of the orbits is computed via *stability indices*. Computing the relative motion modes would provide insight about the stability and nature of local behavior. However, it would be tedious to perform modal analysis in the vicinity of each orbit along a family, examining how the eigenvalues and eigenvectors change over time. The classical stability indices $s = \lambda_i + \lambda_j$ ease the analysis for examining a large number of orbits. Because the reference orbit is periodic, the monodromy matrix has a “trivial” pair of eigenvalues $+1, +1$, yielding a trivial stability index $s_0 = 2$. It turns out that one can examine the evolution of the two non-trivial stability indices stepping along a periodic orbit family, and the value of these indices determines the dimensionality of the stable ($|\lambda| < 1$), unstable ($|\lambda| > 1$), and center ($|\lambda| = 1$) subspaces. Note that the critical values $s = \pm 2$ have special importance, which is

now briefly discussed.

For the monodromy matrix, the eigenvalues occur in reciprocal pairs because the matrix is symplectic. For each λ_i , there exists $\lambda_j = \frac{1}{\lambda_i}$. The other eigenvalues provide insight in the stability of the periodic orbit to small departures from the periodic reference motion. The stability index is defined for a pair of eigenvalues λ and $1/\lambda$ as below:

$$s = \lambda_1 + \lambda_2 = \lambda + \frac{1}{\lambda} \quad (7.101)$$

In all cases except $|\lambda_1| = |\lambda_2| = 1$, the stability of λ_2 requires the instability of its reciprocal λ_1 . An eigenvalue inside the unit circle implies that its reciprocal is outside, and vice-versa.

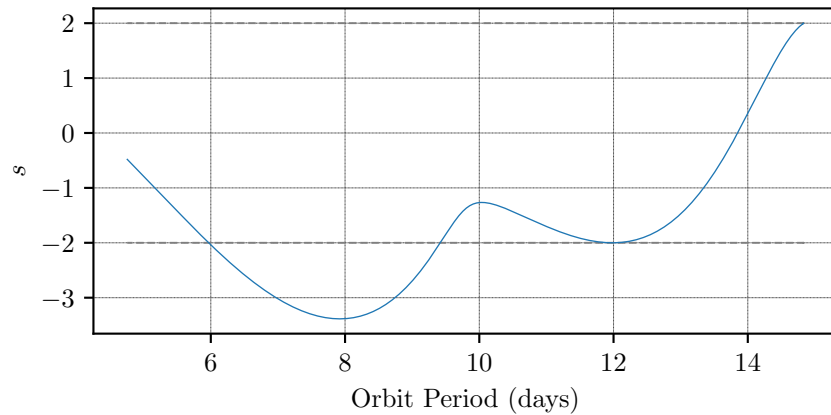
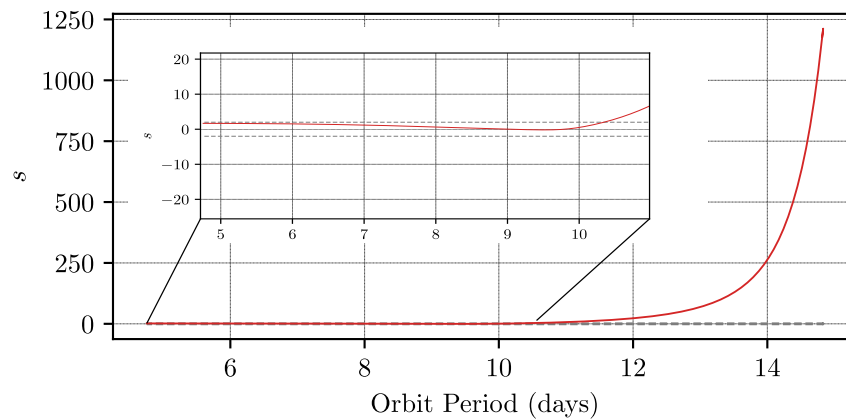
The stability index s_1 is given as a function of orbit period in Figure 7.22, and s_2 is in Figure 7.23. Note again that the trivial index is $s_0 = 2$, which is numerically confirmed to high accuracy. Figure 7.23 provides the second stability index s_2 for the halo orbit family. For the orbits with longer periods (towards the planar orbit with the longest period), s_2 achieves a very high value, indicating the existence of unstable and stable eigenvalues on the order of 10^3 and 10^{-3} , respectively. For the orbits with shorter periods, there is $-2 < s_2 < 2$, indicating stability of the associated modes because the eigenvalues are constrained to the unit circle.

The stability characteristics of the halo orbit family are summarized over the range of orbit periods in Table 7.5. Here summarized are the number of stable ($|\lambda| < 1$), unstable ($|\lambda| > 1$), and “center” ($|\lambda| = 1$) modes. Note that there are always at least two eigenvalues with $\lambda = +1$ because the problem is linearized about a periodic orbit. The table summarizes the non-trivial modes.

Table 7.5: Stability Properties of L₂ Halo Orbits vs. Orbit Period

Orbit Period	Mode Classification
$12.0 < T < 14.83$ days	1 unstable, 1 stable, 2 center, 2 trivial
$11.96 < T < 12.0$ days	2 unstable, 2 stable, 2 trivial
$10.3 < T < 11.96$ days	1 unstable, 1 stable, 2 center, 2 trivial
$9.4 < T < 10.3$ days	4 center, 2 trivial
$5.97 < T < 9.4$ days	1 unstable, 1 stable, 2 center, 2 trivial
$T < 5.97$ days	4 center, 2 trivial

Noting the presence of only stable modes in the vicinity of halo orbits with periods $9.4 <$

Figure 7.22: Stability Index s_1 , L_2 Halo Orbit FamilyFigure 7.23: Stability Index s_2 , L_2 Halo Orbit Family

$T < 10.3$ days, these orbits could be convenient targets for spacecraft formation flying. This work computes the modal decomposition for sample orbits from this stable range, then derives a control methodology for changing the relative motion as desired. Note for this work that the relative motion modes are not computed in an LVLH frame, but are instead computed in the rotating CR3BP frame for convenience. Alternate parameterizations are possible, including LVLH frame coordinates and moon-centered osculating orbit element differences. In fact, one or both of these might yield a more geometrically insightful basis of modal motion than the CR3BP coordinates. However, that is left for future work.

7.4.2 Relative Motion Modes and Modal Control in the CR3BP

In this work, the relative motion modes in the vicinity of an L_2 Northern Halo orbit are computed using the same procedure used in chapters 6 and 7 of the dissertation. In particular, the LF transformation of the relative motion and the plant matrix for the LTI system are computed in terms of the monodromy matrix for a given periodic orbit:

$$[P(\tau)] = [\Phi(\tau, \tau_0)]e^{-[\Lambda](\tau-\tau_0)} \quad (7.102)$$

$$[P(\tau_0)] = [P(\tau_0 + kT)] = [I] \quad (7.103)$$

$$[\Lambda] = \frac{1}{T} \ln (\Phi(\tau_0 + T, \tau_0)) \quad (7.104)$$

The relative motion in the vicinity of the periodic orbit is studied in CR3BP rotating coordinates and is given as $\delta \mathbf{x} = [P(\tau)]\mathbf{z}$ (where the delta differentiates this from the usual LVLH frame relative state), and $\dot{\mathbf{z}} = [\Lambda]\mathbf{z}$.

Due to the Hamiltonian nature of the CR3BP, the monodromy matrix has a repeated eigenvalue of $\lambda_{m,1} = \lambda_{m,2} = +1$. Furthermore, it can be shown that the state rate $\dot{\mathbf{x}}(t_0) = \dot{\mathbf{x}}(t_0 + T)$ is an eigenvector corresponding to the unity eigenvalue. There is not a second eigenvector – the unity eigenvalue has algebraic multiplicity two and geometric multiplicity one. Solving for the generalized eigenvector \mathbf{v}_2 is a straightforward linear algebra problem:

$$([\Phi(t_0 + T, t_0)] - [I_{6 \times 6}])\mathbf{v}_2 = \mathbf{v}_1 \quad (7.105)$$

Then, the resulting Jordan decomposition of the monodromy matrix is as below:

$$[\Phi(t_0 + T, t_0)] = [V_m][J_m][V_m]^{-1} = [\mathbf{v}_1 \ \mathbf{v}_2 \ \dots \ \mathbf{v}_6] \begin{bmatrix} 1 & 1 & 0 & \dots \\ 0 & 1 & 0 & \dots \\ 0 & 0 & \lambda_{m,3} & \\ \vdots & \vdots & & \ddots \end{bmatrix} [\mathbf{v}_1 \ \mathbf{v}_2 \ \dots \ \mathbf{v}_6]^{-1} \quad (7.106)$$

The LTI matrix is given by $[\Lambda] = \frac{1}{T} \ln(\Phi(t_0 + T, t_0))$:

$$[\Lambda] = \frac{1}{T} [V_m] \ln(J_m) [V_m]^{-1} = \frac{1}{T} [\mathbf{v}_1 \ \mathbf{v}_2 \ \dots \ \mathbf{v}_6] \begin{bmatrix} 0 & 1 & 0 & \dots \\ 0 & 0 & 0 & \dots \\ 0 & 0 & \ln(\lambda_{m,3}) & \\ \vdots & \vdots & & \ddots \end{bmatrix} [\mathbf{v}_1 \ \mathbf{v}_2 \ \dots \ \mathbf{v}_6]^{-1} \quad (7.107)$$

The solution to linearized relative motion in the CR3BP has the following form, with a drift mode as a result of the defectiveness:

$$\mathbf{x}(t) = c_1 [P(t)] \mathbf{v}_1 + c_2 [P(t)] (\mathbf{v}_1 t + \mathbf{v}_2) + c_3 \psi_3(t) + \dots + c_6 \psi_6(t) \quad (7.108)$$

where the trivial mode is the first listed mode, being periodic in CR3BP coordinates, and the drift mode is listed second. Then there are four other modes (stable, unstable, or center) starting with ψ_3 .

The defectiveness of the LTI form, its double-zero eigenvalues, and the resulting secular drift mode might remind the reader of the Keplerian relative motion modal decomposition. The drift mode has a simple physical interpretation: bounded relative motion must satisfy a period-matching condition, so motion on nearby orbits of different periods would violate this condition and result in nonzero projection into a local drift mode in the linearized system. For the CR3BP, the relationship between the trivial mode and the drift mode is geometrically illustrated by Figure 7.24, resolved in the rotating frame of the standard CR3BP coordinates, but centered on the spacecraft in the Halo orbit (given by the \mathbf{x}). Examining Figure 7.24 and Eq. (7.108), the geometric relationship between the bounded trivial mode and the drift mode is revealed. This relationship also appears in the Keplerian relative motion problem: bounded purely along-track relative motion is possible (representing points of a different phase along the orbit), and in the case that the no-drift condition is violated, the drift occurs along this same along-track direction.

The above discussion of the defectiveness of the monodromy matrix (and the underlying LTI form) and the resulting drift mode enables a fully analytic view of the relative motion modes. First, consider the case of relative motion in the vicinity of a stable orbit, where all the relative motion

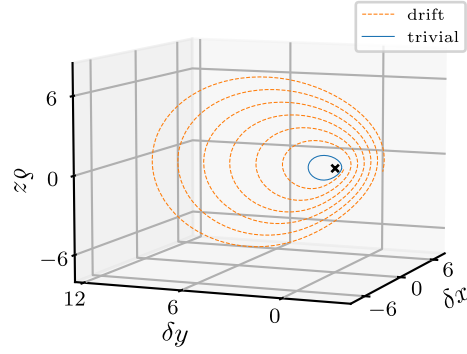


Figure 7.24: Trivial Mode and Drift Mode in Vicinity of L_2 Halo Orbit

modes are bounded (i.e. all eigenvalues of $[\Lambda]$ have zero real part). In this case, there is one pair of trivial eigenvalues and there are two non-trivial pairs of eigenvalues:

$$\lambda_{1,2} = 0 \quad (7.109a)$$

$$\lambda_{3,4} = \pm i\omega_1 \quad (7.109b)$$

$$\lambda_{5,6} = \pm i\omega_2 \quad (7.109c)$$

Let the complex-conjugate eigenvector pairs associated with the frequencies ω_1 and ω_2 be written as $\mathbf{v}_{3,4} = \mathbf{v}_{\mathbb{R}_1} \pm i\mathbf{v}_{\mathbb{I}_1}$ and $\mathbf{v}_{5,6} = \mathbf{v}_{\mathbb{R}_2} \pm i\mathbf{v}_{\mathbb{I}_2}$, respectively. Re-factoring, the following form is obtained for the modal decomposition of the relative motion:

$$\delta \mathbf{x}(\tau) = \sum_{i=1}^6 c_i \psi_i(\tau) \quad (7.110a)$$

$$\psi_i = [P(\tau)] \boldsymbol{\eta}_i(\tau) \quad (7.110b)$$

$$\boldsymbol{\eta}_1(\tau) = \mathbf{v}_1 \quad (7.111a)$$

$$\boldsymbol{\eta}_2(\tau) = \mathbf{v}_1 t + \mathbf{v}_2 \quad (7.111b)$$

$$\boldsymbol{\eta}_3(\tau) = 2(\mathbf{v}_{\mathbb{R}_1} \cos(\omega_1 \tau) - \mathbf{v}_{\mathbb{I}_1} \sin(\omega_1 \tau)) \quad (7.111c)$$

$$\boldsymbol{\eta}_4(\tau) = -2(\mathbf{v}_{\mathbb{R}_1} \sin(\omega_1 \tau) + \mathbf{v}_{\mathbb{I}_1} \cos(\omega_1 \tau)) \quad (7.111d)$$

$$\boldsymbol{\eta}_5(\tau) = 2(\mathbf{v}_{\mathbb{R}_2} \cos(\omega_2 \tau) - \mathbf{v}_{\mathbb{I}_2} \sin(\omega_2 \tau)) \quad (7.111e)$$

$$\boldsymbol{\eta}_6(\tau) = -2(\mathbf{v}_{\mathbb{R}_2} \sin(\omega_2\tau) + \mathbf{v}_{\mathbb{I}_2} \cos(\omega_2\tau)) \quad (7.111f)$$

where the \mathbf{c} is given as a function of $\delta\mathbf{x}_0$:

$$\mathbf{c} = [\bar{\mathbf{V}}]^{-1} \delta\mathbf{x}_0 \quad (7.112)$$

$$[\bar{\mathbf{V}}] = [\mathbf{v}_1, \mathbf{v}_2, 2\mathbf{v}_{\mathbb{R}_1}, -2\mathbf{v}_{\mathbb{I}_1}, 2\mathbf{v}_{\mathbb{R}_2}, -2\mathbf{v}_{\mathbb{I}_2}] \quad (7.113)$$

Because modes $\boldsymbol{\psi}_3 - \boldsymbol{\psi}_6$ are generally composed of multiple incommensurate frequencies, they trace out complex and unintuitive shapes on long timespans. The trivial modes associated with the double-zero eigenvalues of $[\Lambda]$ are comparatively simple, because they are T -periodic. Together, these modes form the basis of all close-proximity relative motion in the vicinity of the periodic orbit.

Another example is the case of two trivial modes, two center modes, a stable mode, and an unstable mode. The modal decomposition is given as below, where $\mathbf{v}_{3,4} = \mathbf{v}_{\mathbb{R}_1} \pm i\mathbf{v}_{\mathbb{I}_1}$:

$$\delta\mathbf{x}(\tau) \approx \sum_{i=1}^6 c_i \boldsymbol{\psi}_i(\tau) \quad (7.114a)$$

$$\boldsymbol{\psi}_i = [P(\tau)] \boldsymbol{\eta}_i(\tau) \quad (7.114b)$$

$$\boldsymbol{\eta}_1(\tau) = \mathbf{v}_1 \quad (7.115a)$$

$$\boldsymbol{\eta}_2(\tau) = \mathbf{v}_1 t + \mathbf{v}_2 \quad (7.115b)$$

$$\boldsymbol{\eta}_3(\tau) = 2(\mathbf{v}_{\mathbb{R}_1} \cos(\omega_1\tau) - \mathbf{v}_{\mathbb{I}_1} \sin(\omega_1\tau)) \quad (7.115c)$$

$$\boldsymbol{\eta}_4(\tau) = -2(\mathbf{v}_{\mathbb{R}_1} \sin(\omega_1\tau) + \mathbf{v}_{\mathbb{I}_1} \cos(\omega_1\tau)) \quad (7.115d)$$

$$\boldsymbol{\eta}_5(\tau) = \mathbf{v}_5 e^{\lambda_5 \tau} \quad (7.115e)$$

$$\boldsymbol{\eta}_6(\tau) = \mathbf{v}_6 e^{\lambda_6 \tau} \quad (7.115f)$$

$$[\bar{\mathbf{V}}] = [\mathbf{v}_1, \mathbf{v}_2, 2\mathbf{v}_{\mathbb{R}_1}, -2\mathbf{v}_{\mathbb{I}_1}, \mathbf{v}_5, \mathbf{v}_6] \quad (7.116)$$

In this case, the existence of an unstable mode generally results in relative motion being unstable if there is any projection of $\delta\mathbf{x}$ into the unstable subspace.

With the modal decomposition, it is possible to efficiently explore the types of relative motion permitted and also to do relative motion control with impulsive maneuvers. For the linearized system, the dynamics in \mathbf{c} space are stationary except for the action of control. For the true nonlinear dynamics, the state in \mathbf{c} space is not constant, but is only very weakly perturbed if the relative motion is in sufficiently close proximity. The action of the nonlinear dynamics can be computed using Eq. (7.47).

7.4.3 Example Simulations

7.4.3.1 Control Near a Stable Orbit

Consider a stable northern L_2 halo orbit with an orbit period of $T = 9.504$ days. This orbit is given in Figure 7.25. For this orbit, there are 4 center modes and two trivial modes (ψ_1 and ψ_2) in its vicinity. The center modes are composed of incommensurate frequencies, so they trace out complex shapes over long timespans. This is demonstrated with plots of ψ_3 and ψ_5 propagated with the linearized dynamics for 240 chief orbits. The scale shown corresponds to relative motion on the km scale, but is plotted in the dimensionless CR3BP length scale. The dimensionless frequencies are $\omega_1 = 1.2511$ and $\omega_2 = 0.7604$. Not shown is the trivial mode, which traces a closed curve with each chief orbit.

As a demonstration of the impulsive control strategy discussed in section 7.3, consider the control case summarized in Table 7.6. The initial motion is bounded but irregular, and the bounded trivial mode is targeted. The resulting relative motion is plotted in Figure 7.27. The uncontrolled trajectory is given in blue for two chief orbits, the target trajectory is in orange, and the controlled trajectory is given by the dashed line, with impulsive maneuver points marked by red dots. The chief is shown as a star. This figure is plotted in the rotating CR3BP coordinates, not the LVLH frame. The figure shows that the impulsive maneuver-based control strategy is successful in achieving the desired relative motion.

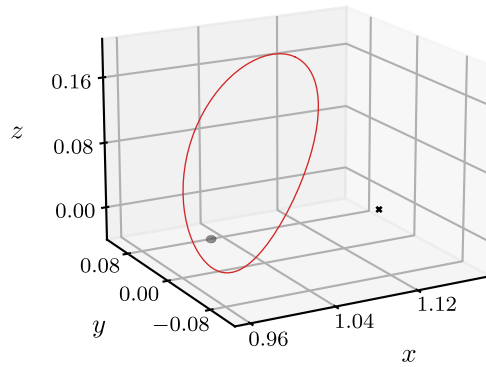
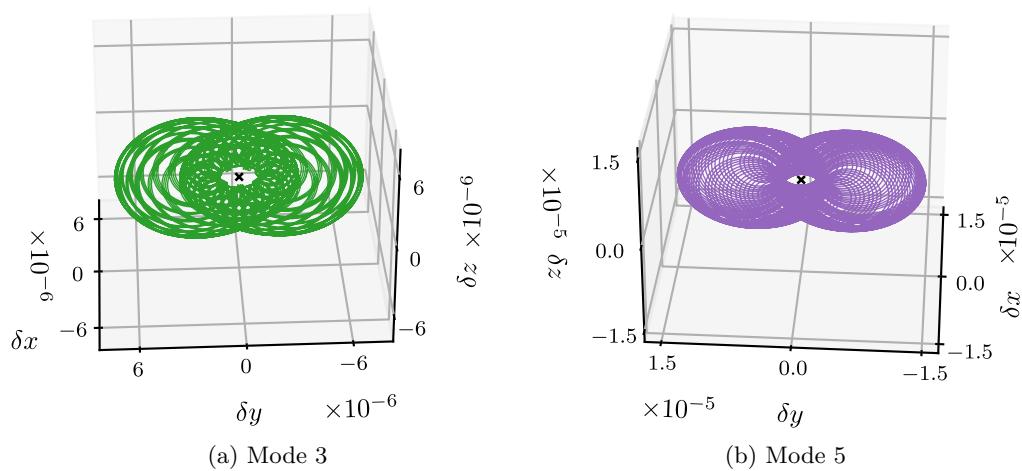
Figure 7.25: Stable L_2 Halo OrbitFigure 7.26: Center Modes, Stable L_2 Northern Halo Orbit

Table 7.6: Halo Orbit Control Simulation Parameters, Example 1

Parameter	Value
Initial relative motion	$\mathbf{c}_0 = (0, 0, 0.2, 0.1, 0.08, 0)\alpha$, $\alpha = 5.2 \times 10^{-6}$
Initial state	$\delta \mathbf{x}_0 = (-0.01, 0.309, -0.005, 0.168, -0.002, 0.362)\alpha$
Desired relative motion	$\mathbf{c}^* = (0.2, 0, 0, 0, 0, 0)\alpha$
Maneuver interval	$\tau \in [1.23, 3.29]$, Interval disc. 14 samples
Maneuver times	$\tau_1 = 1.37$, $\tau_2 = 2.876$, $\tau_3 = 3.013$
Resulting maneuvers	$\Delta \mathbf{v}_1 = (-0.281, 0.094, 0.161)\alpha$ $\Delta \mathbf{v}_2 = (-0.131, -0.027, 0.085)\alpha$ $\Delta \mathbf{v}_3 = (-0.221, -0.064, 0.121)\alpha$

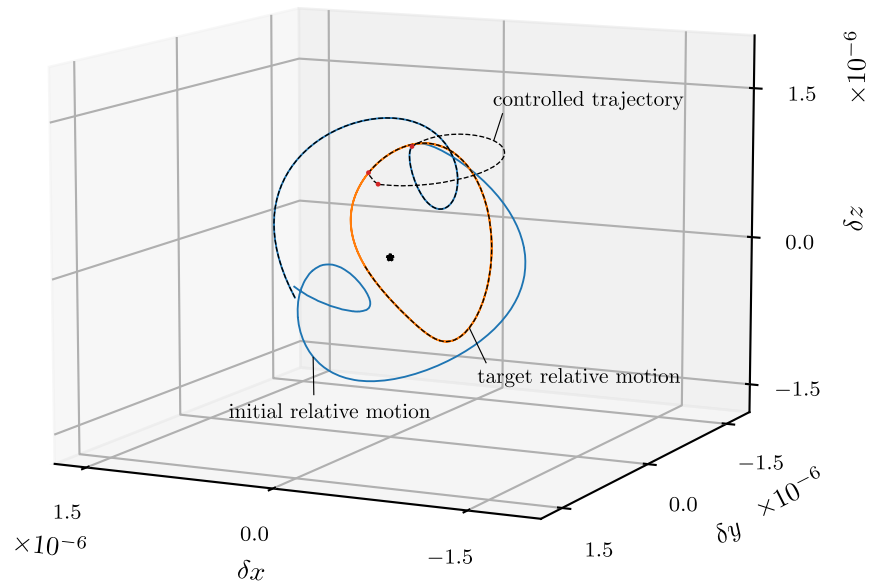


Figure 7.27: Halo Orbit Relative Motion with Impulsive Control, Example 1

7.4.3.2 Control Near an Unstable Orbit

Now, consider an unstable northern L_2 halo orbit with a period of $T = 14.676$ days. This orbit is given in Figure 7.28. For this orbit, there are the trivial bounded and drift modes ψ_1 and ψ_2 , two center modes ψ_3 and ψ_4 , a stable mode ψ_5 , and an unstable mode ψ_6 . The center mode ψ_3 is propagated for many orbits and given also in Figure 7.28. Its dimensionless frequency is $\omega_1 = 0.1288$.

For this orbit, two relative motion control examples are provided. First is control from the chief point $\delta\mathbf{x} = \mathbf{0}$ to target one of the center modes. The second is an example of regulation from the trivial mode to the chief point. Tables 7.7 and 7.8 contain the data for these. Starting with the example given by Table 7.7 and Figure 7.29, the initial point is at $\delta\mathbf{x} = \mathbf{0}$ and the target motion is in orange. The controlled trajectory is given by the dashed line, and the control maneuvers are labeled on the plot with red points. The control successfully targets the quasi-periodic mode ψ_3 , but small residual error projected into the unstable subspace results in a subsequent need for correction, so the trajectory departs from the target mode. This is a fundamental property of relative motion control in the vicinity of an unstable halo orbit: corrective maneuvers will always

be necessary on some timescale, due to the combined effects of nonlinearity and instability.

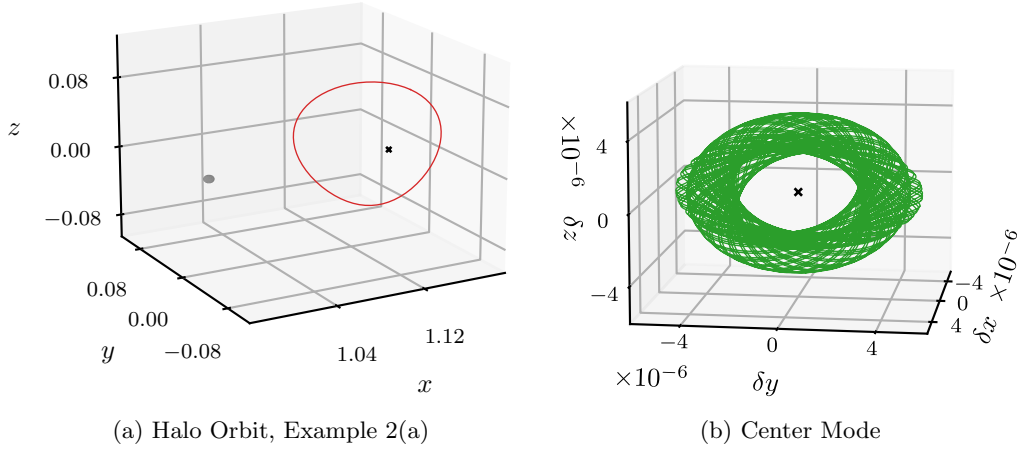


Figure 7.28: Unstable L_2 Northern Halo Orbit and a Center Mode

Table 7.7: Halo Orbit Control Simulation Parameters, Example 2(a)

Parameter	Value
Initial relative motion	$\mathbf{c}_0 = (0, 0, 0, 0, 0, 0)$
Initial state	$\delta \mathbf{x}_0 = (0, 0, 0, 0, 0, 0)$
Desired relative motion	$\mathbf{c}^* = (0, 0, 0.3, 0, 0, 0)\alpha$, $\alpha = 5.2 \times 10^{-6}$
Maneuver interval	$\tau \in [1.90, 5.08]$, Interval disc. 15 samples
Maneuver times	$\tau_1 = 1.903$, $\tau_2 = 2.538$, $\tau_3 = 3.595$, $\tau_4 = 3.807$, $\tau_5 = 4.864$
Resulting maneuvers	$\Delta \mathbf{v}_1 = (-0.035, -0.007, 0.052)\alpha$ $\Delta \mathbf{v}_2 = (-0.148, 0.278, 0.052)\alpha$ $\Delta \mathbf{v}_3 = (0.028, 0.002, -0.068)\alpha$ $\Delta \mathbf{v}_4 = (0.028, -0.035, -0.101)\alpha$ $\Delta \mathbf{v}_5 = (-0.001, 0, 0.0005)\alpha$

The second example is given by the data in Table 7.8 and the trajectory in Figure 7.30. The initial trivial modal motion is given in blue, the controlled trajectory is given by the dashed line, and the control maneuvers are labeled with red dots. This example demonstrates regulation control in this environment, with the chief at $\delta \mathbf{x} = \mathbf{0}$ successfully targeted to a high degree of numerical precision. A similar strategy could be used for orbit regulation, keeping the spacecraft on the unstable periodic orbit.

This example with the CR3BP demonstrates that the previously developed modal decompo-

Table 7.8: Halo Orbit Control Simulation Parameters, Example 2(b)

Parameter	Value
Initial relative motion	$\mathbf{c}_0 = (0.2, 0, 0, 0, 0, 0)\alpha$, $\alpha = 5.2 \times 10^{-6}$
Initial state	$\delta\mathbf{x}_0 = (0., -0.127, 0, -0.117, 0, -0.1)\alpha$
Desired relative motion	$\mathbf{c}^* = (0, 0, 0, 0, 0, 0)$
Maneuver interval	$\tau \in [1.90, 5.08]$, Interval disc. 15 samples
Maneuver times	$\tau_1 = 1.903$, $\tau_2 = 2.538$, $\tau_3 = 2.749$, $\tau_4 = 4.018$, $\tau_5 = 4.230$, $\tau_6 = 4.864$
Resulting maneuvers	$\Delta\mathbf{v}_1 = (-0.008, 0.0005, -0.004)\alpha$ $\Delta\mathbf{v}_2 = (-0.002, -0.003, 0.002)\alpha$ $\Delta\mathbf{v}_3 = (-0.044, 0.084, 0.081)\alpha$ $\Delta\mathbf{v}_4 = (-0.045, -0.086, 0.081)\alpha$ $\Delta\mathbf{v}_5 = (-0.0007, -0.001, 0.0006)\alpha$ $\Delta\mathbf{v}_6 = (-0.008, -0.0004, -0.004)\alpha$

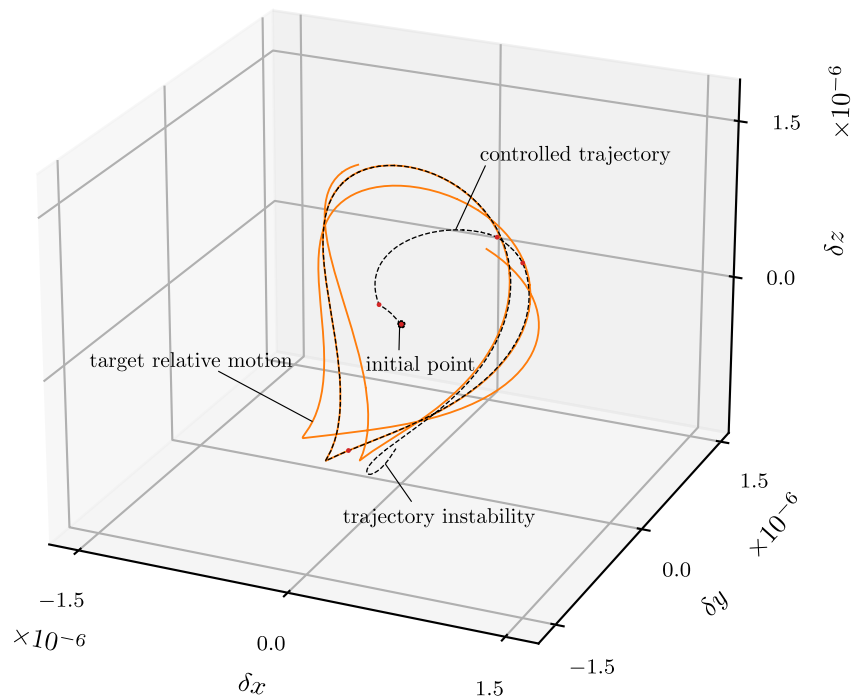


Figure 7.29: Halo Orbit Relative Motion with Impulsive Control, Example 2(a)

sition concept and the highly efficient associated impulsive control strategies can be readily applied beyond Keplerian relative motion with no modification of the concept. Using a control scheme facilitated by the modal decomposition, necessary corrective maneuvers can be computed with any desired frequency for stationkeeping, orbit regulation, and relative motion control. This work could be extended with a search for superior coordinates for linearization or for visualization of the modal

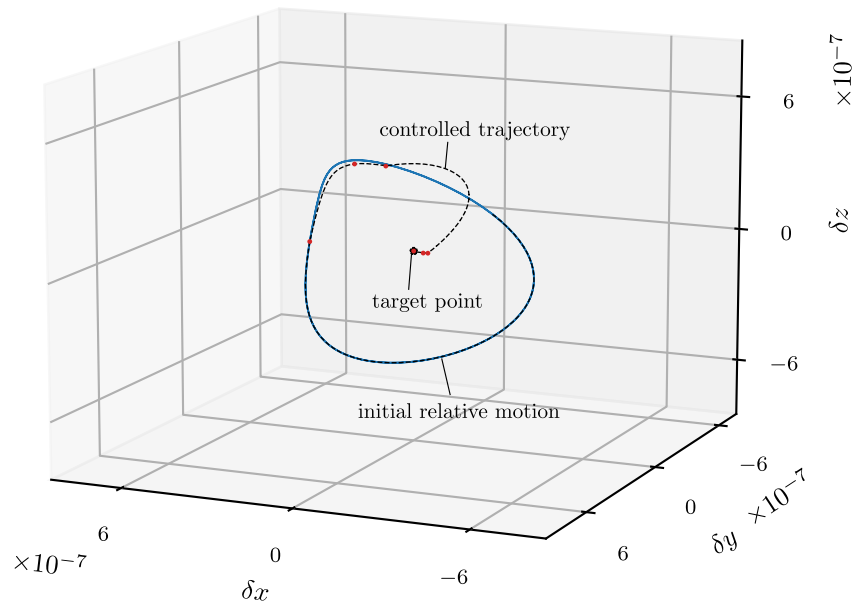


Figure 7.30: Halo Orbit Relative Motion with Impulsive Control, Example 2(b)

motion. Both the LVLH frame Cartesian/curvilinear coordinates could be explored, and so could the moon-centered osculating orbit elements. Additionally, by applying the tools for the reducibility of more general quasi-periodic linear systems [65] (in the case that they are reducible), this approach could theoretically be extended to control in the vicinity of quasi-periodic orbits in the Earth-Moon three-body problem as well. In such a case, the LF transformation would be replaced with a more general quasi-periodic transformation, and an underlying LTI form can also be found.

7.5 Conclusions

This chapter explores various applications of the modal decomposition method for close-proximity spacecraft relative motion. First, in section 7.1, the method is numerically applied to the relative motion model developed in chapter 3. With this, the parameter space for relative motion about a near-circular orbit at a variety of altitudes and inclinations is explored. It is revealed that below $\Gamma = c/n_0 = 2$, the relative motion is unstable, indicated by the high number of unstable modes. At higher altitudes, the motion is more stable, and the predicted modes of the linear model match the propagation of the true dynamics for long timespans. Then, in section 7.2, the numerical

application of modal decomposition to almost-periodic orbits is explored, revealing conditions that must be satisfied for the motion predicted by the approximate modal basis to be accurate. The numerical methodology is applied to perturbed terminator orbits about the asteroid Ryugu in a high-fidelity dynamic model. It is shown that some of the approximate modal basis is preserved across multiple orbits, evolving only slowly.

In section 7.3, the modal constants \mathbf{c} are treated as state variables for the case of additional perturbations and control via the variation-of-parameters method, and this methodology allows for a modal description to still remain valid beyond the dynamic case for which it is derived. This is demonstrated by showing how the Keplerian modes combine in a time-varying sum to produce the J_2 -perturbed relative motion. Additionally, this section shows how the modal constants can be used with the modes to explore different relative motions efficiently. Lastly, the dynamics in the modal constants facilitate an elegant relative motion control approach using the modal decomposition and convex optimization to solve for a delta-V optimal impulsive maneuver sequence.

Lastly, section 7.4 applies the same concepts from section 7.3 and earlier to the Earth-Moon circular restricted three-body problem (CR3BP). In particular, the section explores modal decompositions and modal control in the vicinity of periodic L_2 Halo orbits. The underlying modal form in the vicinity of periodic 3-body orbits is shown to have a secular drift mode, highly analogous to what is found in the Keplerian relative motion problem. Overall, this chapter shows that the modal decomposition approach provides interesting and useful insights in a variety of circumstances, and also utility for powerful relative motion control approaches.

Chapter 8

Conclusions and Future Work

8.1 Overview and Contributions of this Work

In future spaceflight applications, it will be a common requirement for spacecraft to operate in close proximity to one another in a variety of dynamical environments, from low-Earth orbit (LEO) to cislunar space and orbits in the vicinity of asteroids. This dissertation explores extensions of traditional dynamics and control approaches for formation flying to more challenging dynamical environments and applications. The overall goals of this work are:

- (1) Develop approximations of perturbed relative orbital motion dynamics (Chapter 3)
- (2) Derive, investigate, and demonstrate formation control using differential solar radiation pressure (Chapter 4)
- (3) Investigate robust formation flying/rendezvous control techniques subject to significant disturbances (Chapter 5)
- (4) Develop, test, and apply a methodology for modal decomposition approximations of spacecraft relative motion in a variety of orbital scenarios (Chapters 6, 7)

The novel contributions of this work begin with [chapter 3](#), which focuses on deriving accurate state transition matrix (STM) models of relative motion subject to various perturbations, particularly J_2 , with a focus on low-complexity high-accuracy models. The efficacy of these models is

compared with others in literature for the J_2 problem, and shows favorable performance – outperforming the Schweighart-Sedwick model [116] and showing almost comparable accuracy to the Gim-Alfriend state transition matrix [50], despite a favorable massive reduction in model complexity. The same techniques are used to derive corrective terms for the J_3 perturbation as well, which are tested numerically. Additionally, chapter 3 derives and tests various tools and techniques that can be used to further improve relative motion model accuracy. The chapter also derives a linear model of relative motion subject to some of the dominant disturbances encountered in orbits about large asteroids. The model enables efficient exploration of the parameter space of possible chief orbits, and is revisited in chapter 7. Lastly, the chapter briefly explores the problem of approximating the J_2 -perturbed chief orbit in more general orbital settings, which is necessary for more accurate and globally valid J_2 -perturbed relative motion models.

The same principles discussed in chapter 3 are further applied in chapter 4 to study the SRP-perturbed satellite relative motion problem in detail. A simple analytic linear model of relative motion is obtained and tested numerically, demonstrating high accuracy. The chapter also explores satellite relative motion control with differential SRP accelerations. The chapter includes controllability analysis and insights for achieving full regulation control with the differential SRP in a closed-loop fashion, which is demonstrated to be feasible for spacecraft with modest area-to-mass ratio, given sufficient control time.

The dissertation pivots to the topic of relative motion sensitivities in chapter 5. This chapter explores the dynamics of sensitivities of the relative state to error in dynamical parameters and in the chief orbit. The main accomplishments of this chapter are spacecraft orbit control in asteroid environments using the linear model developed in chapter 3, including both Linear Quadratic Regulator (LQR) and a desensitized control approach, expected to be more robust to poorly known dynamical parameters. It is shown that LQR control is already quite robust to uncertainties in dynamical parameters. Also in this chapter is a study in efficient propagation of satellite relative state uncertainty in the vicinity of a poorly tracked target object. It is shown that sensitivities of the relative state to initial target orbit elements have their own simple linearized dynamics, and

the relative state uncertainty distribution is a sum of the products of the initial distributions in target orbit elements and their associated sensitivity vectors. Overall, this approach could have applications to on-board uncertainty-aware control strategies.

Chapters 6 and 7 explore the modal decomposition of close-proximity spacecraft relative motion in a variety of applicable orbits. In [chapter 6](#), the theory is introduced, and exact analytic Lyapunov-Floquet (LF) transformations are computed for spacecraft relative motion in Cartesian and curvilinear coordinates. The fundamental modal solutions produced by this derivation are shown to be convenient for efficiently exploring the parameter space of possible relative motions. Some of the fundamental modal solutions connect to earlier solutions of the Tschauner-Hempel equations explored previously in literature. Chapter 6 also includes discussion of the analytic extension to weakly-perturbed orbits such as orbits perturbed by J_2 . Chapter 7 explores other applications of the modal decomposition, including satellite relative motion modes in an asteroid orbital environment, with some new contributions for how to apply the modal decomposition procedure numerically in orbits that are not exactly periodic. It is shown that a subset of the numerically computed approximate relative motion modes change slightly from orbit to orbit, while some change more drastically. The oscillatory and weakly unstable modes form convenient targets for long-term bounded relative motion. Additionally, the modal constants (affiliated with the fundamental modes) are used to design a highly computationally efficient impulsive maneuver-based control strategy that switches between desired relative motion modes or combinations of modes. This is demonstrated for both the Keplerian relative motion problem and for relative motion in the Earth-Moon circular restricted three-body problem (CR3BP).

8.2 Recommendations for Future Work

In the course of this research, numerous opportunities were identified for future work. First, further applications of and improvements to the J_2 model developed in [chapter 3](#) could be explored. The application of the existing model to J_2 -perturbed rendezvous, circumnavigation, and proximity operations is a logical extension. There are various authors at work on the general linearized

J_2 -perturbed relative motion modeling problem, with recent work including Reference 128 and references therein. Higher-fidelity differential SRP relative motion control is another possible area of future work. There are additionally some possibilities for future work with desensitized control – including developing the theory for desensitized control with impulsive maneuvers.

Much of the possibility for future work lies in the concept of the satellite relative motion modal decomposition. First, an analytic J_2 -perturbed modal could be obtained by applying the procedure discussed in the end of chapter 6. Numerical results with the J_2 perturbation in chapter 7 suggest that this could be a tractable problem. The analysis would certainly be possible with an averaging of the J_2 perturbation, but a model that accounts for instantaneous effects is perhaps more desirable. Additionally, the numerical modal decomposition of relative motion in the vicinity of periodic terminator orbits (in the unperturbed augmented Hill three-body problem) could reveal some new insights about the types of relative motion possible in that environment. There might also be some opportunities for analytic work for that problem. For the problem of relative motion in the vicinity of periodic terminator orbits, exact relative motion control between the modes could be achieved by numerical application of the modal constant impulsive control strategy developed in chapter 7. Similar applications and investigations are possible for the cislunar environment, and some were demonstrated in the end of chapter 7.

The impulsive relative motion control procedure needs to be extended to correct for non-periodicity of the plant matrix – right now it would only work accurately for relative motion control in the vicinity of exactly periodic chief orbits. Additionally, an interesting idea would be to convert the computed delta-V optimal impulsive maneuver solution into a corresponding low-thrust solution. Relevant work for such a problem includes Reference 88 and references therein. Because the dynamics in the space of the modal constants are only functions of control (for the unperturbed case), and due to the compactness and convexity of the set of \mathbf{c} states reachable by a given total delta-V, there are strong applications for delta-V reachability analysis. References 49, 52, and especially 60 are relevant for this. Revisiting the modal decomposition concept but with the computation of the more general Lyapunov-Perron transformation for the quasi-periodic plant

matrix case could be interesting, but would likely be very challenging. Relevant discussions can be found in Reference 65 and references therein. There might also be possibilities for application of the modal decomposition concept to other challenging problems in celestial mechanics, such as the development of algorithms for the efficient computation of invariant tori for spacecraft relative motion [6].

Bibliography

- [1] Kyle T. Alfriend and Hanspeter Schaub. Dynamics and control of spacecraft formations: Challenges and some solutions. Journal of the Astronautical Sciences, 48(2 and 3):249–267, April–Sept. 2000.
- [2] Kyle T. Alfriend, Hanspeter Schaub, and Dong-Woo Gim. Gravitational perturbations, nonlinearity and circular orbit assumption effect on formation flying control strategies. In Proceedings of the Annual AAS Rocky Mountain Conference, pages 139–158, Breckenridge, CO, Feb. 2–6 2000.
- [3] Kyle T. Alfriend, Srinivas R. Vadali, Pini Gurfil, Jonathan P. How, and Louis S. Breger. Spacecraft Formation Flying. Elsevier, Oxford, U.K., 2010.
- [4] P. Anderson, D. S. McKnight, F. Di Pentino, and H. Schaub. Operational Considerations of GEO Debris Synchronization Dynamics. In 66th International Astronautical Conference, October 12 - 16, 2015. Jerusalem, Israel. International Astronautical Federation, 2015.
- [5] Carles Araguz, Elisenda Bou-Balust, and Eduard Alarcon. Applying autonomy to distributed satellite systems: Trends, challenges, and future prospects. Systems Engineering, 21(5):401–416, 2018.
- [6] Nicola Baresi. Spacecraft Formation Flight on Quasi-periodic Invariant Tori. PhD thesis, University of Colorado Boulder, 2017.
- [7] R. Bate, D. D. Mueller, and J. E. White. Fundamentals of Astrodynamics. Dover Publications, Inc., New York, NY, 1971.
- [8] Richard H. Battin. An Introduction to the Mathematics and Methods of Astrodynamics. AIAA Education Series, New York, USA, 1987.
- [9] Carl M. Bender and Steven A. Orszag. Advanced Mathematical Methods for Scientists and Engineers: Asymptotic Methods and Perturbation Theory. Springer-Verlag, New York, USA, 1991.
- [10] Trevor Bennett and Hanspeter Schaub. Continuous-time modeling and control using non-singular linearized relative-orbit elements. Journal of Guidance, Control, and Dynamics, 39(12):2605–2614, 2016.
- [11] A. D. Biria and R. P. Russell. A Satellite Relative Motion Model Including J_2 and J_3 via Vinti’s Intermediary. Celestial Mechanics and Dynamical Astronomy, 130(23), 2018.

- [12] W. Boyce. Comment on a Formula for the Gravitational Harmonic Coefficients of a Triaxial Ellipsoid. Celestial Mechanics and Dynamical Astronomy, 67(2):107–110, 1997.
- [13] Louis Breger and Jonathan P. How. Safe Trajectories for Autonomous Rendezvous of Spacecraft. Journal of Guidance, Control, and Dynamics, 31(5):1478–1489, 2008.
- [14] S. B. Broschart and B. Villac. Identification of Non-Chaotic Terminator Orbits near 6489 Golevka. In AAS/AIAA Spaceflight Mechanics Meeting. American Astronautical Society, 2009.
- [15] Stephen B. Broschart, Gregory Lantoine, and Daniel J. Grebow. Quasi-terminator orbits near primitive bodies. Celestial Mechanics and Dynamical Astronomy, 120:195–215, 2014.
- [16] Dirk Brouwer. Solution of the Problem of Artificial Satellite Theory Without Drag. The Astronomical Journal, 64(1274):378–397, 1959.
- [17] E. R. Burnett and E. A. Butcher. Linearized Relative Orbital Motion Dynamics in a Rotating Second Degree and Order Gravity Field, AAS 18-232. Advances in the Astronautical Sciences, 167:3463–3482, 2018.
- [18] E. R. Burnett, E. A. Butcher, A. J. Sinclair, and T. A. Lovell. Linearized Relative Orbital Motion Model About an Oblate Body Without Averaging, AAS 18-218. Advances in the Astronautical Sciences, 167(AAS 18-218):691–710, 2018.
- [19] E. R. Burnett and H. Schaub. Spacecraft Formation and Orbit Control Using Attitude-Dependent Solar Radiation Pressure, IWSCFF 19-28. In International Workshop on Satellite Constellations and Formation Flying. IAF Astrodynamics Committee, 2019.
- [20] Ethan Burnett. Relative Orbital Motion Dynamical Models for Orbits about Nonspherical Bodies. Master’s thesis, University of Arizona, 2018.
- [21] Ethan Burnett, Andrew Harris, and Hanspeter Schaub. Desensitized Optimal Spacecraft Rendezvous Control with Poorly Known Gravitational and Solar Radiation Pressure Perturbations. In AAS/AIAA Astrodynamics Specialist Conference, number AAS 19-685. American Astronautical Society, 2019.
- [22] Ethan Burnett and Hanspeter Schaub. Modal Decomposition of Spacecraft Relative Motion in Quasi-Periodic Orbits. In AAS/AIAA Astrodynamics Specialist Conference, number AAS 20-506. American Astronautical Society, 2020.
- [23] Ethan R. Burnett and Hanspeter Schaub. Spacecraft formation and orbit control using attitude-dependent differential solar radiation pressure. Advances in Space Research, 2020.
- [24] Ethan R. Burnett and Hanspeter Schaub. Study of highly perturbed spacecraft formation dynamics via approximation. Advances in Space Research, 2020.
- [25] Ethan R. Burnett and Hanspeter Schaub. Approximating Orbits in a Rotating Gravity Field with Oblateness and Ellipticity Perturbations. Celestial Mechanics and Dynamical Astronomy (Under Review), 2021.
- [26] Ethan R. Burnett and Hanspeter Schaub. Geometric Perspectives on Fundamental Solutions in the Linearized Satellite Relative Motion Problem. Acta Astronautica (Under Review), 2021.

- [27] Ethan R. Burnett and Hanspeter Schaub. Satellite Relative State Uncertainty Dynamics in the Vicinity of a Poorly Tracked Target Object. In AIAA/AAS Astrodynamics Specialist Conference, number AAS 21-511. American Astronautical Society, 2021.
- [28] Ethan R. Burnett and Hanspeter Schaub. Spacecraft Relative Motion Dynamics and Control Using Fundamental Solution Constants. In AAS Spaceflight Mechanics Meeting, 2022.
- [29] E. A. Butcher, E. R. Burnett, and T. A. Lovell. Comparison of Relative Orbital Motion Perturbation Solutions in Cartesian and Spherical Coordinates. In AAS/AIAA Spaceflight Mechanics Meeting, 2017.
- [30] E. A. Butcher, E. R. Burnett, J. Wang, and T. A. Lovell. A New Time-Explicit J_2 -Perturbed Nonlinear Relative Orbit Model with Perturbation Solutions. In AAS/AIAA Astrodynamics Specialist Conference, number AAS 17-758. American Astronautical Society, 2017.
- [31] Eric A. Butcher and T. Alan Lovell. Spherical Coordinate Perturbation Solutions to Relative Motion Equations: Application to Double Transformation Spherical Solution. In AIAA/AAS Spaceflight Mechanics Meeting, Napa, CA, 2016. American Astronautical Society.
- [32] S. M. Byram and D. J. Scheeres. Stability of Sun-Synchronous Orbits in the Vicinity of a Comet. Journal of Guidance, Control, and Dynamics, 32(5):1550–1559, 2009.
- [33] T. Carter and M. Humi. Clohessy-Wiltshire Equations Modified to Include Quadratic Drag. Journal of Guidance, Control, and Dynamics, 25(6):1058–1063, November-December 2002.
- [34] Thomas E. Carter. State transition matrix for terminal rendezvous studies: Brief survey and new example. AIAA Journal of Guidance, Control, and Dynamics, 21(1):148–155, 1998.
- [35] S. Casotto. The Equations of Relative Motion in the Orbital Reference Frame. Celestial Mechanics and Dynamical Astronomy, 124(3):215–234, 2016.
- [36] W. H. Clohessy and R. S. Wiltshire. Terminal Guidance System for Satellite Rendezvous. Journal of the Aerospace Sciences, 27(9):653–658, Sept. 1960.
- [37] Howard D. Curtis. Orbital Mechanics for Engineering Students. Elsevier Aerospace Engineering Series, Burlington, MA, 2nd edition, 2010.
- [38] Bernd Dachwald. Solar sail dynamics and control. In Encyclopedia of Aerospace Engineering. John Wiley & Sons, New York, NY, Dec. 2010.
- [39] S. D’Amico, J. S. Ardaens, and R. Larsson. In-flight demonstration of formation control based on relative orbit elements. In 4th International Conference on Spacecraft Formation Flying Missions and Technologies, August 18-20 2011.
- [40] Simone D’Amico and Oliver Montenbruck. Proximity operations of formation-flying spacecraft using an eccentricity/inclination vector separation. Journal of Guidance, Control, and Dynamics, 29(3):554–563, 2006.
- [41] H. Dankowicz. Some Special Orbits in the Two-Body Problem with Radiation Pressure. Celestial Mechanics and Dynamical Astronomy, 58(4):353–370, 1994.

- [42] V. S. Deshmukh and S. C. Sinha. Control of Dynamic Systems with Time-Periodic Coefficients via the Lyapunov-Floquet Transformation and Backstepping Technique. Journal of Vibration and Control, 10(10):1517–1533, 2004.
- [43] J. Peiter DeVries. Elliptic elements in terms of small increments of position and velocity components. AIAA Journal, 1(9):2626–2629, Nov. 1963.
- [44] D. J. Scheeres et al. Comparing the Estimated Dynamical Environments and Mass Distributions of Bennu and Ryugu. In Asteroid Science, 2019.
- [45] Gianluca Benedetti et al. Interplanetary CubeSats for asteroid exploration: Mission analysis and design. Acta Astronautica, 154:238–255, 2019.
- [46] S. Watanabe et al. Hayabusa2 arrives at the carbonaceous asteroid 162173 Ryugu—A spinning top-shaped rubble pile. Science, 364(6437):268–272, April 2019.
- [47] A. Farrés, D. Folta, and C. Webster. Using Spherical Harmonics to Model Solar Radiation Pressure Accelerations, AAS 17-780. In AAS/AIAA Astrodynamics Specialist Conference, August 20 - 24, Stevenson, WA, USA. American Astronautical Society, 2017.
- [48] Cyrus Foster, James Mason, Vivek Vittaldev, Lawrence Leung, Vincent Beukelaers, Leon Stepan, and Rob Zimmerman. Constellation Phasing with Differential Drag on Planet Labs Satellites. Journal of Spacecraft and Rockets, 55(2), 2018.
- [49] E. Gilbert and G. Harasty. A class of fixed-time fuel-optimal impulsive control problems and an efficient algorithm for their solution. IEEE Transactions on Automatic Control, 16(1):1–11, 1971.
- [50] Dong-Woo Gim and Kyle T. Alfriend. The state transition matrix of relative motion for the perturbed non-circular reference orbit. AIAA Journal of Guidance, Control, and Dynamics, 26(6):956–971, 2003.
- [51] Gerard Gómez, Kathleen Howell, Josep Masdemont, and Carles Simó. Station-Keeping Strategies for Translunar Libration Point Orbits. In AAS/AIAA Spaceflight Mechanics Meeting, number AAS 98-168. American Astronautical Society, 1998.
- [52] Tommaso Guffanti and Simone D’Amico. Integration Constants as State Variables for Optimal Path Planning. In 2018 European Control Conference (ECC), pages 1–6, 2018.
- [53] Tommaso Guffanti and Simone D’Amico. Linear Models for Spacecraft Relative Motion Perturbed by Solar Radiation Pressure. Journal of Guidance Control, and Dynamics, 42(9):1962–1980, 2019.
- [54] Chao Han, Huan Chen, Gustavo Alonso, Yinrui Rao, Javier Cubas, Jianfeng Yin, and Xiaohui Wang. A linear model for relative motion in an elliptical orbit based on a spherical coordinate system. Acta Astronautica, 157:465 – 476, 2019.
- [55] Andrew Harris, Ethan Burnett, and Hanspeter Schaub. Desensitized Optimal Attitude Guidance for Differential-Drag Rendezvous. In AAS/AIAA Astrodynamics Specialist Conference, 2019.

- [56] Casey R. Heidrich, Marcus J. Holzinger, and Robert D. Braun. Optimal information filtering for robust aerocapture trajectory generation and guidance. Journal of Spacecraft and Rockets, pages 1–14, 2021.
- [57] S. G. Hesar, D. J. Scheeres, and J. W. McMahon. Stability Analysis of the OSIRIS-REx Terminator Orbits to Maneuver Errors. Journal of Guidance, Control, and Dynamics, 40(1):81 – 95, January 2017.
- [58] E. J. Hinch. Perturbation Methods. Cambridge University Press, Cambridge, England, 1991.
- [59] M. Holzinger, J. DiMatteo, J. Schwartz, and M. Milam. Passively safe Receding Horizon Control for satellite proximity operations. In 2008 47th IEEE Conference on Decision and Control, pages 3433–3440, Dec 2008.
- [60] Marcus J. Holzinger, Daniel J. Scheeres, and John Hauser. Reachability Using Arbitrary Performance Indices. IEEE Transactions on Automatic Control, 60(4):1099–1103, 2015.
- [61] K. C. Howell and B. G. Marchand. Natural and non-natural spacecraft formations near the L1 and L2 libration points in the Sun–Earth/Moon ephemeris system. Dynamical Systems, 20(1):149–173, 2005.
- [62] Steve B. Howell, Charlie Sobeck, Michael Haas, Martin Still, and Thomas Barclay. The K2 Mission: Characterization and Early Results. Publications of the Astronomical Society of the Pacific, 126:398 – 408, 2014.
- [63] W. Hu and D. J. Scheeres. Numerical determination of stability regions for orbital motion in uniformly rotating second degree and order gravity fields. Planetary and Space Science, 52:685–692, 2004.
- [64] Imre G. Izsak. On Satellite Orbits with Very Small Eccentricity. The Astronomical Journal, 66(3):129 – 131, April 1961.
- [65] Àngel Jorba. Numerical computation of the normal behaviour of invariant curves of n-dimensional maps. Nonlinearity, 14(5):943–976, Jul 2001.
- [66] Àngel Jorba and Carles Simó. On the reducibility of linear differential equations with quasiperiodic coefficients. Journal of Differential Equations, 98(1):111–124, 1992.
- [67] John L. Junkins. Adventures on the Interface of Dynamics and Control. AIAA Journal of Guidance, Control, and Dynamics, 20(6):1058–1071, Nov.–Dec. 1997.
- [68] John L. Junkins, Maruthi R. Akella, and Kyle T. Alfriend. Non-gaussian error propagation in orbital mechanics. Journal of the Astronautical Sciences, 44(4):541–563, Oct.–Dec. 1996.
- [69] John L. Junkins, Maruthi R. Akella, and Rush D. Robinett. Nonlinear adaptive control of spacecraft maneuvers. AIAA Journal of Guidance, Control, and Dynamics, 20(6):1104–1110, 1997.
- [70] John L. Junkins and Puneet Singla. How nonlinear is it? a tutorial on nonlinearity of orbit and attitude dynamics. Journal of the Astronautical Sciences, 52(1-2):7–60, Jan 2004.
- [71] M. Kaasalainen and J. Torppa. Optimization Methods for Asteroid Lightcurve Inversion. I. Shape Determination. Icarus, 153:24–36, 2001.

- [72] Stephen Kahne. Low-Sensitivity Design of Optimal Linear Control Systems. IEEE Transactions on Aerospace and Electronic Systems, 4(3):374–379, May 1968.
- [73] C. D. Karlgaard and F. H. Lutze. Second Order Relative Motion Equations. Journal of Guidance, Control, and Dynamics, 26(1):41–49, 2003.
- [74] Christopher D. Karlgaard and Haijun Shen. Desensitized optimal filtering. In AIAA Guidance, Navigation and Control Conference, Portland, OR, Aug. 8–11, 2011 2011. Paper AIAA 2011-6617.
- [75] William M. Kaula. Theory of Satellite Geodesy : Applications of Satellites to Geodesy. Dover Publications, New York, Nov. 1966.
- [76] J. Kechichian. Motion in general elliptic orbit with respect to a dragging and precessing coordinate frame. Journal of Astronautical Sciences, 46(1):25 – 45, 1998.
- [77] S. Kikuchi, K. C. Howell, Y. Tsuda, and J. Kawaguchi. Orbit-attitude coupled motion around small bodies: Sun-synchronous orbits with sun-tracking attitude motion. Acta Astronautica, 140:34–48, 2017.
- [78] Adam W. Koenig, Tommaso Guffanti, and Simone D’Amico. New State Transition Matrices for Spacecraft Relative Motion in Perturbed Orbits. Journal of Guidance, Control, and Dynamics, 40(7):1749–1768, 2017.
- [79] Wang S. Koon, Martin W. Lo, Jerrold E. Marsden, and Shane D. Ross. Dynamical Systems, The Three-Body Problem, and Space Mission Design. Marsden Books, 2006.
- [80] Toshihiro Kubo-oka and Arata Sengoku. Solar radiation pressure model for the relay satellite of SELENE. Earth, Planets and Space, 51(9):979–986, 1999.
- [81] C. Lanczos. The Variational Principles of Mechanics. Dover Books On Physics. Dover Publications, 1986.
- [82] D. Lantukh, R. P. Russell, and S. B. Broschart. Heliotropic Orbits at Oblate Asteroids: Balancing Solar Pressure and J2 Perturbations. Celestial Mechanics and Dynamical Astronomy, 121(171-190), 2015.
- [83] Robin Larsson, Joseph Mueller, Stephanie Thomas, Björn Jakobsson, and Per Bodin. Orbit constellation safety on the PRISMA in-orbit formation flying test bed. In Proceedings of the 3rd International Symposium on Formation Flying, Missions and Technologies, ESA-ESTEC, number 654 SP in European Space Agency, (Special Publication) ESA SP, November 2008. 3rd International Symposium on Formation Flying, Missions and Technologies, ESA-ESTEC ; Conference date: 23-04-2008 Through 24-04-2008.
- [84] Sangjin Lee, Hao Lyu, and Inseok Hwang. Analytical Uncertainty Propagation for Satellite Relative Motion Along Elliptic Orbits. Journal of Guidance, Control, and Dynamics, 39(7):1593–1601, 2016.
- [85] Zhan Li, Xuebo Yang, and Huijun Gao. Autonomous impulsive rendezvous for spacecraft under orbital uncertainty and thruster faults. Journal of the Franklin Institute, 350(9):2455–2473, 2013.

- [86] Paulett C. Liewer, Andrew T. Klesh, Martin W. Lo, Neil Murphy, Robert L. Staehle, Vasilis Angelopoulos, Brian D. Anderson, Manan Arya, Sergio Pellegrino, James W. Cutler, E. Glenn Lightsey, and Angelos Vourlidas. A Fractionated Space Weather Base at L5 using CubeSats and Solar Sails, pages 269–288. Springer Berlin Heidelberg, Berlin, Heidelberg, 2014.
- [87] M. Macdonald, G. Hughes, and C. McInnes. Geosail: an elegant solar sail demonstration mission. Journal of Spacecraft and Rockets, 44(4):784 – 796, 2007.
- [88] Michele Maestrini, Pierluigi Di Lizia, and Francesco Topputo. Analytical Impulsive-to-Continuous Thrust Conversion in Linearized Relative Dynamics. Journal of Guidance, Control, and Dynamics, 44(4):862–871, 2021.
- [89] Colin R. McInnes. Solar Sailing: Technology, Dynamics, and Mission Applications. Springer-Verlag, Berlin, 1999.
- [90] C.R. McInnes, M. MacDonald, V. Angelopolous, and D. Alexander. Geosail: exploring the geomagnetic tail using a small solar sail. Journal of Spacecraft and Rockets, 38(4):622–629, 2001.
- [91] J. W. McMahon and D. J. Scheeres. New Solar Radiation Pressure Force Model for Navigation. Journal of Guidance, Control, and Dynamics, 33(5):1418–1428, 2010.
- [92] L. Meirovitch. Fundamentals of Vibrations. McGraw-Hill higher education. McGraw-Hill, 2001.
- [93] Robert G. Melton. Time-explicit representation of relative motion between elliptical orbits. AIAA Journal of Guidance, Control, and Dynamics, 23(4):604–610, 2000.
- [94] G. Misra, M. Izadi, A. Sanyal, and D. J. Scheeres. Coupled Orbit-Attitude Dynamics and Relative State Estimation of Spacecraft Near Small Solar System Bodies. Advances in Space Research, 57(8):1747–1761, 2016.
- [95] Pierre Montagnier, Raymond J. Spiteri, and Jorge Angeles. The control of linear time-periodic systems using Floquet–Lyapunov theory. International Journal of Control, 77(5):472–490, 2004.
- [96] A.H. Nayfeh. Perturbation Methods. Wiley, 2000.
- [97] Ali H. Nayfeh and Dean T. Mook. Nonlinear Oscillations. John Wiley & Sons, Inc., New York, USA, 1979.
- [98] Ayansola D. Ogundele and Olufemi A. Agboola. Development of approximate solution of lf transformation of spacecraft relative motion with periodic coefficients. In AAS/AIAA Astrodynamics Specialist Conference. American Astronautical Society, 2020.
- [99] K. Oguri and J. W. McMahon. SRP-based Orbit Control with Application to Small Body Landing, AAS 18-375. In AAS/AIAA Astrodynamics Specialist Conference, August 19 - 23, 2018. Snowbird, Utah, USA, volume 167 of Advances in the Astronautical Sciences. American Astronautical Society, 2018.

- [100] D. J. O’Shaughnessy, J. V. McAdams, K. E. Williams, and B. R. Page. Fire Sail: Messenger’s use of Solar Radiation Pressure for Accurate Mercury Flybys, AAS 09-014. In AAS Spaceflight Mechanics Meeting, February 8 - 12, 2009. Savannah, GA, USA. American Astronautical Society, 2009.
- [101] K. Parsay and H. Schaub. Designing solar sail formations in sun-synchronous orbits for geomagnetic tail exploration. Acta Astronautica, 107:218 – 233, 2015.
- [102] K. Parsay and H. Schaub. Drift-free solar sail formations in elliptical sun-synchronous orbits. Acta Astronautica, 139:201 – 212, 2016.
- [103] K. Parsay and H. Schaub. Establishment of natural solar sail formation using solar electric propulsion. AIAA Journal of Guidance, Control, and Dynamics, 39(6):1417–1425, 2016.
- [104] J. E. Prussing and B. A. Conway. Orbital Mechanics. Oxford University Press, New York, NY, 2013.
- [105] Joaquim Puig. Reducibility of linear differential equations with quasi-periodic coefficients: a survey. Dept. de Matemàtica Aplicada i Anàlisi, Univ. de Barcelona, 2002.
- [106] Lucas Riggi and Simone D’Amico. Optimal impulsive closed-form control for spacecraft formation flying and rendezvous. In 2016 American Control Conference (ACC), pages 5854–5861, 2016.
- [107] D. Romagnoli and Stephan Theil. De-orbiting satellites in LEO using solar sails. In International Symposium on Space Flight Dynamics, Sao Jose dos Campos, Brasil, Feb. 28 – March 4, 2011 2011.
- [108] Hanspeter Schaub. Relative orbit geometry through classical orbit element differences. AIAA Journal of Guidance, Control, and Dynamics, 27(5):839–848, Sept.–Oct. 2004.
- [109] Hanspeter Schaub and Kyle T. Alfriend. Impulsive feedback control to establish specific mean orbit elements of spacecraft formations. AIAA Journal of Guidance, Control, and Dynamics, 24(4):739–745, July–Aug. 2001.
- [110] Hanspeter Schaub and Kyle T. Alfriend. J_2 Invariant Relative Orbits for Spacecraft Formations. Celestial Mechanics and Dynamical Astronomy, 79(2):77–95, 2001.
- [111] Hanspeter Schaub and John L. Junkins. Analytical Mechanics of Space Systems. AIAA Education Series, Reston, VA, 4th edition, 2018.
- [112] D. J. Scheeres. The dynamical evolution of uniformly rotating asteroids subject to YORP. Icarus, 188:430–450, 2007.
- [113] D. J. Scheeres. Orbit Mechanics About Asteroids and Comets. Journal of Guidance, Control, and Dynamics, 35(3):987–997, May 2012.
- [114] D. J. Scheeres. Orbital Motion in Strongly Perturbed Environments. Springer-Verlag, Berlin, 2012.
- [115] D. J. Scheeres and F. Marzari. Spacecraft dynamics in the vicinity of a comet. Journal of the Astronautical Sciences, 50(1):35–52, January 2002.

- [116] Samuel A. Schweighart and Raymond J Sedwick. High-fidelity linearized J model for satellite formation flight. AIAA Journal of Guidance, Control, and Dynamics, 6(25):1073–1080, Nov. 2002.
- [117] H. Seywald and R. Kumar. Desensitized optimal trajectories. Advances in the Astronautical Sciences, 93:103–106, 1996.
- [118] H. Seywald and K. L. Seywald. Desensitized optimal control. AIAA Scitech Forum, 2019.
- [119] Ryan E. Sherrill. Dynamics and Control of Satellite Relative Motion in Elliptic Orbits Using Lyapunov-Floquet Theory. Ph.D. dissertation, University of Auburn, April 2013.
- [120] Ryan E. Sherrill, A. J. Sinclair, S. C. Sinha, and T. A. Lovell. Lyapunov-floquet control of satellite relative motion in elliptic orbits. IEEE Transactions on Aerospace and Electronic Systems, 51:2800–2810, 2015.
- [121] A. J. Sinclair. Calibrated and Decalibrated Approximations of Nonlinear Dynamic Systems. Nonlinear Dynamics, 87:281–290, 2017.
- [122] A. J. Sinclair, R. E. Sherrill, and T. A. Lovell. Calibration of Linearized Solutions for Satellite Relative Motion. Journal of Guidance, Control, and Dynamics, 37(4):1362–1367, 2014.
- [123] Andrew J. Sinclair, Ryan E. Sherrill, and T. Alan Lovell. Geometric interpretation of the tschauner–hempel solutions for satellite relative motion. Advances in Space Research, 55(9):2268 – 2279, 2015.
- [124] Eduardo Sontag. Mathematical Control Theory: Deterministic Finite Dimensional Systems. Springer-Verlag, New York, NY, 1998.
- [125] Byron D. Tapley, Bob E. Schutz, and George H. Born. Statistical Orbit Determination. Elsevier Academic Press, Burlington, MA, 2004.
- [126] J. Tschauner and P. Hempel. Rendezvous zu einem in elliptischer bahn umlaufenden ziel. Astronautica Acta, 11(5):104–109, 1965.
- [127] D. A. Vallado. Fundamentals of Astrodynamics and Applications. Microcosm Press, Hawthorne, CA, 3rd edition, 2007.
- [128] Matthew Willis and Simone D’Amico. Cartesian Relative Motion on Perturbed Eccentric Orbits and Closed-Form Solution for J_2 Effects at Low Inclinations. In AIAA/AAS Astrodynamics Specialist Conference, number 21-602. American Astronautical Society, 2021.
- [129] K Yamanaka and F. Ankersen. New State Transition Matrix for Relative Motion on an Arbitrary Elliptical Orbit. AIAA Journal of Guidance, Control, and Dynamics, 25(1):60 – 66, Jan. – Feb. 2002.
- [130] C. Zhang, P. Melin, Shu-Nan Wu, Wen-Ya Zhou, Shu-Jun Tan, and Guo-Qiang Wu. Robust H-Infinity Control for Spacecraft Rendezvous with a Noncooperative Target. The Scientific World Journal, 2013:579703, 2013.